Growth and characterization of semiconductor/superconductor core/shell nanowires for quantum technologies

An-Hsi A.-H. Chen

THÈSE

Pour obtenir le grade de

DOCTEUR DE L'UNIVERSITÉ GRENOBLE ALPES

École doctorale : PHYS - Physique
Spécialité : Nanophysique
Unité de recherche : Institut Néel

Croissance et caractérisation de nanofils coeur/coquille semiconducteur/supraconducteur pour les technologies quantiques

Growth and characterisation of semiconductor/superconductor core/shell nanowires for quantum technologies

Présentée par :

An-Hsi CHEN

Direction de thèse :

Moïra HOCEVAR CRCN, Université Grenoble Alpes	Directrice de thèse

Rapporteurs :

Oussama MOUTANABBIR
PROFESSEUR, École Polytechnique de Montréal
Thomas SCHÄPERS
PROFESSEUR, Forschungszentrum Jülich GmbH

Thèse soutenue publiquement le **16 décembre 2022**, devant le jury composé de :

Oussama MOUTANABBIR PROFESSEUR, École Polytechnique de Montréal	Rapporteur
Thomas SCHÄPERS PROFESSEUR, Forschungszentrum Jülich GmbH	Rapporteur
Cécile NAUD CHARGE DE RECHERCHE, CNRS	Examinatrice
Laetitia VINCENT DIRECTEUR DE RECHERCHE, CNRS	Examinatrice
Daniel BELLET PROFESSEUR DES UNIVERSITES, GRENOBLE INP	Examinateur

Invités :

Jesper Nygård
PROFESSEUR, Niels Bohr Institute, University of Copenhagen

Abstract

Recently, new quantum phenomena have been the subject of intense research, notably for the development of quantum computers. Many quantum electronic devices use Josephson junctions. In these junctions, two superconductors are separated by a weak link (oxide tunnel barrier or thin layer of a normal metal) allowing the superconducting current to pass. By replacing the normal metal with a semiconductor, new electronic transport regimes become accessible. Due to a low critical temperature, traditional aluminum-based hybrid superconductor-semiconductor devices cannot be used under high magnetic fields. Therefore, research is moving towards the use of superconducting materials with higher critical temperatures. Yet, changing the materials constituting a device requires the development of new manufacturing processes. This takes place through a thorough understanding of the synthesis of materials and their interfaces.

In this regard, the objective of my thesis was to develop and characterize hybrid interfaces based on InAs and InSb semiconductors to realize Josephson junctions. I first studied the growth of tilted InAs nanowires by molecular beam epitaxy. I used the gold-catalyzed "vapor-liquid-solid" mechanism for the growth of InAs nanowires. I explored the different growth parameters available. I then deposited superconductors by different techniques on these nanowires and analyzed their interfaces. I showed that the annealing temperature before growth is a key parameter to producing homogeneous nanowires with low size dispersion and high density. By optimizing the annealing temperature and the V/III ratio, I was able to reduce the size dispersion and better control the growth rate. I then developed a process to deposit an amorphous MoGe superconductor around the nanowires. I obtained ultra-thin, smooth and homogeneous shells.

I then analyzed the crystalline structure of Sn/InSb hybrid interfaces. I studied Sn thin films prepared on InSb by X-ray diffraction (XRD). Then, I participated in a fully *in situ* experiment at the European Synchrotron Radiation Facility. I deposited Sn shells at cryogenic temperatures on InSb nanowire. I used grazing incidence XRD to study the crystal structure of the wires before and after deposition at 80 K. I observed that Sn films deposited on InSb substrates at cryogenic temperatures are in the cubic α crystalline phase. The tetragonal β phase of Sn appears in the thin films after the deposition of a protective AlO_x layer. This suggests that the deposition of AlO_x by electron beam evaporation provides sufficient heat to initiate the transformation of α- into β-Sn. In contrast to the thin-film geometry, the study conducted at ESRF showed that the shells formed at 80 K around InSb nanowires are in the β-Sn crystalline structure.

In conclusion, the research presented here is crucial for three reasons. (1) I have developed tilted nanowire arrays, those are necessary for the creation of etch-free Josephson junctions; (2) I have developed a superconductor deposition process that preserves the InAs crystal structure. (3) I have determined the crystalline phases of Sn deposited under different experimental conditions at 80 K on InSb substrates and nanowires. These new insights are a step forward the understanding of hybrid materials and interfaces and their integration into quantum devices.

Contents

CHAPTER 1

Introduction

1.1 Topological superconductivity and Majorana bound states

Topological phenomenon has attracted enormous interest since last century, while today our technology is sufficiently advanced to scale down the material dimensions to the nanoscale. In the late 20^{th} century, the experimental discovery of the quantum Hall effect in 2D material system is now considered as the first breakthrough in topological quantum physics [93]. The quantum Hall effect corresponds to a quantized electron current flowing along the edge of a 2D material where it is applied under a strong magnetic field at a low temperature. This signifies that a non-trivial topological phase presents close to the surface and differs from the bulk phase and that they exist at the same time in the material. We can engineer and operate these surface states for quantum computing purpose, such as qubits, and explore deeper fundamental physics, such as topological superconductivity [53].

Topological superconductivity is considered the path to achieve quantum computing through proximity-induced Cooper pairs in normal condensed matter systems, such as superconductor-semiconductor heterostructures [191, 75, 50, 17]. It requires a gapped superconductor or topological insulator to achieve non-trivial and gapless edge or surface states [175]. The edge of the material hosting this novel superconductivity can be the ends of one dimensional (1D) nanowire, the edge of two dimensional (2D) film and the surface of three dimensional (3D) materials, as seen in Figure 1.1.1. In the simplest 1D case, the Cooper pairs in a conventional superconductor are fully paired. Contrarily, topological superconductivity can arise when two unpaired electrons at both ends of the nanowire are connected by a chain of Cooper pairs [32]. These two unpaired electrons are insensitive to the local environment and are known as Majorana bound states (MBS). Thus, MBS are expected to contribute to the development of fault-tolerant quantum information [129, 34].

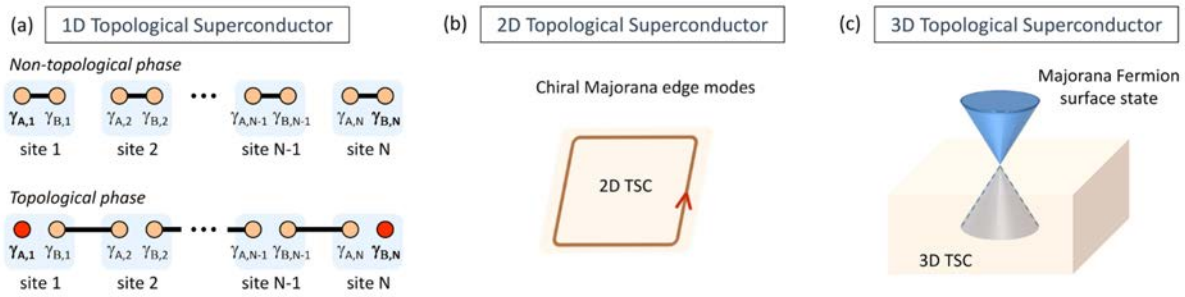

Figure 1.1.1: Illustration of topological superconductivity [32]. (a) 1D topological superconductivity (TSC) phase emerges at the edge of a nanowire as MBS. (b) TSC emerges chiral Majorana edge states along the edge of material. (c) 3D TSC reveals MBS at the surface.

MBS were proposed by Ettore Majorana from the real solution of the Dirac equation in the early 20$^{\text{th}}$ century [191]. In theory, the neutral Majorana quasiparticle is its own antiparticle $\psi = \psi^*$ in non-Abelian class [32, 17]. Non-Abelain is a mathematical concept in non-commutative algebra ($a * b \neq b * a$) and can be used to describe Dirac point braiding [107]. These self-conjugated ($\psi = \psi^*$) particles are locally insensitive and can transport encoded information through the braiding process, representing exchange of MBS [160, 214].

Although, these ideal quasiparticles are mathematically proven, there is currently no experimental evidence of their existence. In 2008, L. Fu and C. L. Kane proposed mathematically a hybrid interfaces to realize MBS, which consists of an s-wave conventional superconductor and a 1D topological insulator nanowire with strong spin-orbit coupling [76]. Therefore, the important ingredients for realizing MBS includes (1) a 1D semiconductor nanowire with strong spin-orbit coupling, (2) the presence of a finite magnetic field B parallel to nanowire, (3) a s-wave superconductor contact to nanowire, (4) a clean interface for well introducing proximity effect [142, 165, 158, 75, 32].

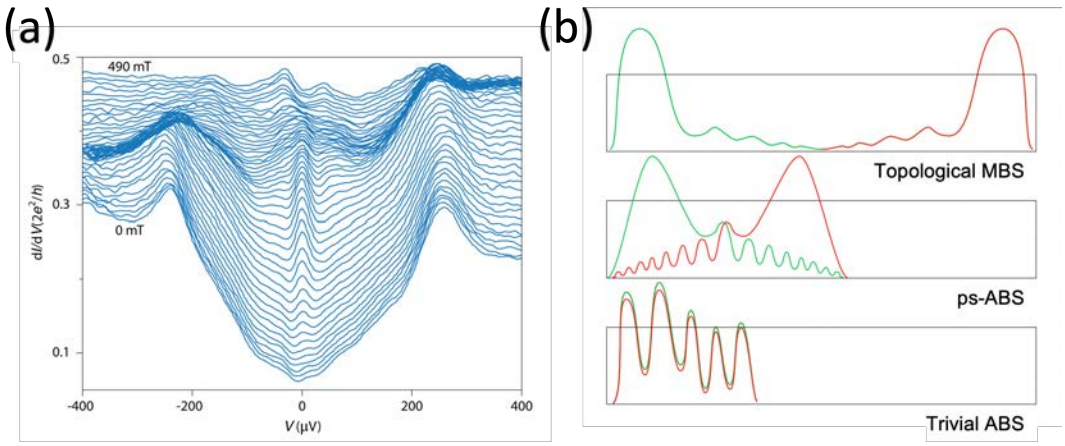

Figure 1.1.2: Examples of zero bias peaks. (a) At a finite magnetic field, the conductance peaks at zero bias appear [158]. (b) Subgap wave functions decomposed in nanowire into left Majorana (green) and right Majorana (red) basis [75].

There have been lots of attempts or proposals to search for MBS in hybrid nanowires. Yet, there is no determined evidence of the appearance of MBS, because some other quantum mechanisms can also produce similar phenomenon. Figure 1.1.2 demonstrates examples of zero bias peaks, one of the evidences of MBS. Mourik et al. demonstrated a conducting peak appearing at V = 0 under a finite magnetic field in InSb nanowire covered with NbTiN (Figure 1.1.2 (a)). Both Andreev bound states (ABS) and MBS can be represented in two Majorana wave functions, as seen in Figure 1.1.2 (b). In a nanowire with a finite length, these two waves can be fully separated in the case for topological MBS, partially separated for ps-ABS or quasi-Majorana states, and fully overlapped for trivial ABS [75]. Both ABS and MBS can give zero-bias peak, which is considered as a piece of determined evidence in the past [158]. Hence we need more criteria to identify the presence of MBS: (1) the $2e^2/h$ quantized conductance, (2) the superconducting gap closing in a finite magnetic field, (3) the Zeeman energy affected topological phase diagram, (4) the conductance peak at zero-bias voltage, and (5) the zero-bias pinning as a function of segment length [75, 162, 45, 46, 235].

1.2 Advantages of nanowire geometry

1.2.1 General presentation of nanowires

1D semiconductor nanowires have unique features such as high surface area-to-volume geometry, high crystal quality, and large strain tolerance [109, 150]. For decades, epitaxial growth on foreign substrates, crystal structure control, and the shape of NWs have been studied and explored for different purposes, such as optics, mechanics, and transport [121, 74, 8, 221]. We can create axial structures with materials of large lattice mismatch, such as GaAs/InAs heteronanowire used as a single-photon source regardless of a 7% lattice mismatch [190]. Lateral heterojunction, like core-shell nanowires, can efficiently relax the strain at the heterointerface [178, 92]. Tapered nanowires exhibit varying sub-band gaps due to diameter evolution, which can be an advantage when searching for MBS [202]. The electronic properties can be easily tunned by controlling the doping during nanowires growth. For example, doped GaAs nanowires show a longer photoconductivity lifetime than undoped ones [26]. The flexibility of nanowires intergration on foreign substrates, such as III-V nanowire-based devices on Si wafer serving as high-electron mobility transistors in conventional CMOS techniques [114, 211], is a significant advantage.

The synthesis of nanowires can be categorized into either bottom-up processes or top-down processes. Top-down fabrication utilizes etching or sculpting bulk materials into low-dimensional structures. This way, the density of nanowires can be scaled up for potential integration in the microelectronic industry [219]. Top-down fabrication has drawbacks such as complicated fabrication processes, large amounts of materials waste, and barely reaching high-aspect ratio nanostructures [62]. Bottom-up fabrication is the inverse of top-down fabrication,

which builds structures from the molecular or atom scale to the nano or micro scale [132, 176]. Bottom-up approaches have advantages such as flexible material combinations, tunable composition, and tailored geometry [150]. The disadvantages of bottom-up fabrication are large dispersion of size, contamination with gold while using Au-assist vapor-liquid-solid (VLS), and the requirement of compatible surfaces or molecules [62].

One of the most conventional bottom-up methods is the VLS mechanism. It was described for the first time by R. S. Wagner and W. C. Ellis in 1964 [227, 135, 95]. The VLS mechanism allows the crystallization of semiconductor at a lower temperature through a liquid metal catalyst and Au is the most common option [87].

VLS mechanism can be implanted in several high quality synthesizing techniques such as molecular beam epitaxy (MBE), chemical beam epitaxy (CBE), and metalorganic chemical vapor deposition (MOCVD) [74, 77, 128]. In this thesis, I focus on nanowires grown by MBE VLS growth protocol with Au nanoparticles.

1.2.2 The context of quantum transport

Semiconductor nanowires are fundamental blocks for building up electronic devices [109]. Firstly, their conductivity can be tuned electrostatically and they can be used as channels in transistors. Secondly, their quasi-1D morphology provides several advantages over planar materials. M. D. Kelzenberg et al. demonstrated Si wire arrays can reach 96% peak absorption of bulk Si, requiring only a 5% area fraction of nanowires, which significantly reduces materials consumption [117]. Ö. Gül et al. suggested that low disorder nanowires are the key to access topological properties such as ballistic electronic transport [86].

For quantum computing, it is attractive for low-disordered nanowire to serve as qubit, the basic unit of quantum information. The electronic state of quantum dots embedded in nanowires, such as Ge/Si core/shell nanowire quantum dots, is controllable by external perpendicular electric field and can be used as a spin qubit [120]. F. Luthi et al. showed that transmon qubits (superconducting charge qubits) based on nanowire Al-InAs-Al junctions have low sensitivity to charge noise, which gives high selectivity for qubits control [143]. In addition, as previously stated, III-V nanowire is the most likely candidate for MBS discovery [76].

1.3 Superconductor/semiconductor system for topological superconductivity

Topological superconductivity can be discovered in devices with hybrid interfaces, but it is strongly affected by material properties and interface quality. These devices demonstrate superconducting hard gap with a zero bias peak under a finite magnetic field, which is considered one of the MBS features [55]. Gating semiconductor nanowires allows us to control the chemical potential. According to several superconductor/semiconductor systems studies, indium arsenide

(InAs) and indium antimonide (InSb) are the most popular platforms for inducing superconducting gaps. They are III-V semiconductors with strong spin-orbit coupling, large Lande g-factor, small electron effective mass and long mean free path [27, 189, 181].

1.3.1 Hybrids based on InAs nanowires

All *in situ* fabrication is possible only by MBE via transfer channels, and there are lots of studies on combining InAs nanowires with superconductors. In 2015, hybrid devices based on epitaxial Al shell on InAs nanowires demonstrated induced superconducting hard gap and Cooper pair charging [112, 126, 59]. Their clean and impurity-free hybrid interface is achieved by *in situ* MBE. However, Al-based nanowire devices have a low critical temperature $T_c = 1.2\,K$, which limits their future application.

Bulk lead (Pb) is a superconductor with a high critical temperature ($T_c = 7\,K$) and a high critical field ($B_c = 8.5\,T$). It can potentially extend the superconductor-semiconductor parameter space. In 2021, T. Kanne et al. reported that Pb shell on InAs nanowire devices exhibit a large hard gap, $\Delta = 1250\,\mu eV$, as well as field-dependent Cooper pair charging [115]. This monocrystalline Pb shell on each facet of InAs nanowire is achieved by an *in situ* low temperature deposition.

Another attempt to enlarge the hybrid parameter space is using niobium (Nb), which has a high critical temperature ($T_c = 9.3\,K$), one of the highest critical temperatures among elemental superconductors. In 2017, the continuous Nb shell on InAs nanowires was achieved by tunning the deposition angle in *in situ* MBE [88]. However, the devices based on Nb/InAs nanowires have a soft gap, which is probably caused by native oxides on the Nb surface [40].

In 2020, D. J. Carrad et al. demonstrated that tantalum (Ta)/InAs nanowire devices with superconducting hard gap ($\Delta = 130\,\mu eV$) fabricated by the shadowing platform in *in situ* MBE [40]. Without post-process chemical etching, the hybrid devices show better conductance in low temperature transport measurements. In 2019, M. Bjergfelt et al. reported vanadium (V)/InAs hybrid nanowires since they are lattice matched materials, but single crystalline V is obtained at a high temperature 940 K, which can decompose InAs [23, 225]. A polycrystalline V-shell on InAs nanowires was obtained, yet their interface is mixed and alloyed, albeit the *in situ* MBE fabrication.

In 2021, M. S. Bjergfelt et al. reported that single crystalline indium (In) island/InAs devices manifest a high switching field of 2e-to-1e charging around $B_\perp \sim 0.7\,T$ and remain 2e periodic till $T = 1.2\,K$. This new combination extends the possibility of hybrid materials. Depositing a continuous In shell is challenging, because it is not thermodynamically favorable. The deposited granular In shell on an InAs nanowire deposited by diffusion cell in MBE or e-beam and the size of crystalline In islands ranging from 10 nm to 500 nm at 120 K [24].

	Superconductor (SC)	T_c (K)	Crystalline / Fabrication process	Superconducting gap, Δ ($\pm\mu$eV)	2e periodic transport	Ref.
InAs	Al	1.2 K	Polycrystalline/ *in situ*	Hard gap, 200	Yes	[112, 59, 41, 7, 126]
	Nb	9.3 K	Nanocrystalline/ *in situ*	Soft gap	No	[40, 88]
	Ta	4.4 K	Nanocrystalline/ *in situ*	Hard gap, 130	No	[40]
	V	5.4 K	Polycrystalline/ *in situ*	-	No	[23]
	Pb	7.2 K	Monocrystalline/ *in situ*	Hard gap, 1250	Yes	[115]
	In	3.4 K	Single crystal/ *in situ*	-	Yes	[24]
InSb	NbTiN	10.6 K - 11.8 K	Polycrystalline/*ex situ*	Hard gap, 400	Yes	[158, 46, 240]
	Al	1.2 K	Polycrystalline/ *ex situ*	Hard gap, 200	Yes	[29, 198]
	Sn	3.7 K	Polycrystalline/ *ex situ*	Hard gap, 700	Yes	[168]

Table 1.3.1: Recent scientific research on hybrid nanowires. Low temperature shortens the diffusion length of adatoms, resulting in the formation of a continuous superconductor shell on a nanowire. All the superconductors in the list are deposited at low temperature, except Nb deposited at room temperature to 270 K, NbTiN deposited at room temperature, and V deposited above 370 K.

1.3.2 Hybrids based on InSb nanowires

High aspect ratio InSb nanowires can be grown in metal organic vapor-phase epitaxy (MOVPE) which is not compatible with *in situ* fabrication. A clean hybridinterface is possible with the proper cleaning process, such as H_2 molecular cleaning prior to superconductor deposition. In 2012, V. Mourik et al. reported that devices based on NbTiN/InSb nanowire have a $\Delta \approx 250\,\mu$eV induced gap and a zero-bias peak in a finite magnetic field [158]. These features of topological superconductivity can be accomplished via devices with clean NbTiN/InSb interfaces and reduced disorder. Therefore, the chemical treatments that can cause damage to nanowires in device fabrication should be minimized.

In 2018, J. Shen et al. reported that Al/InSb nanowire devices have a field-resilient hard gap till B = 2 T with a polycrystalline Al shell [198]. To avoid the damaging risk from chemical etching during device fabrication, the shadowing platform is preferable to create the Al/InSb nanowire junction. In 2019, M. Pendharkar et al. reported that devices based on a polycrystalline Sn shell on InSb nanowire have a large superconducting hard gap, $\Delta = \pm 700\,\mu$eV, and

can withstand a magnetic field of B = 4 T [168]. The clean Sn/InSb interface is the key regardless of the polycrystalline shell. Noteworthily, Sn is allotropic, and its two crystal phases are of interest in topological studies, which we will discuss later.

1.4 Properties of selected semiconductors and superconductors

1.4.1 Semiconductors

The wurzite or zinc-blende are the types of crystal structure, that the former is hexagonal and the later is cubic, as seen in Figure 1.4.1.

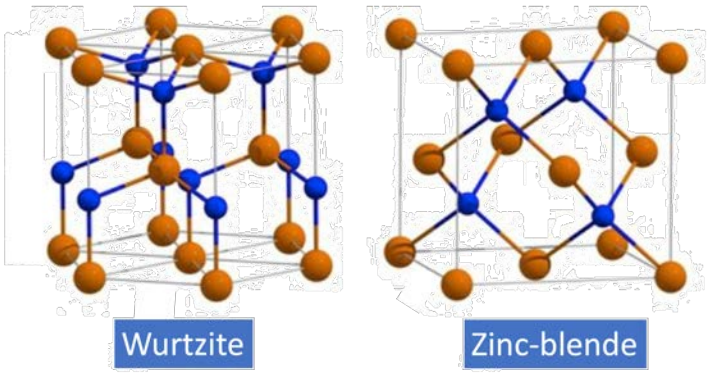

Figure 1.4.1: Crystal structures of wurtzite (hexagonal) and zinc-blende (cubic) [230].

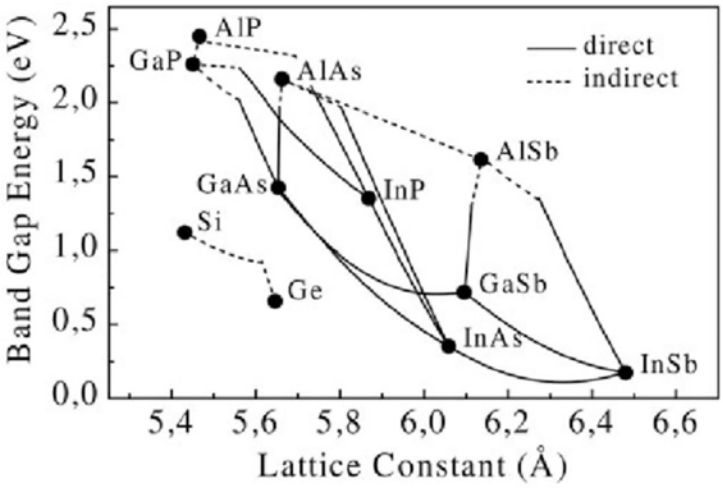

Figure 1.4.2: Band gap of III-V elements versus their lattice constant [19].

The local atomic arrangements in a ternary alloy are responsible for the presence of disorder in the potential field of the crystal. This deviation from the average composition gives to the bandgap a bowing character[78].

InAs

InAs is a crystalline III-V semiconductor and has a lattice constant 6.058 Å. Its large lattice parameter makes growing a high quality epitaxial layer on Si in CMOS technology difficult [79]. InAs has a zinc-blende (ZB) crystal structure in bulk, but it is mostly grown in the wurtzite (WZ) hexagonal phase in nanowires (Figure 1.4.1). Bulk InAs has a small effective mass 0.025 m_e (m_e: electron mass) and a high electron mobility of 30 000 cm^2/V/s [182]. It is also a strong spin-orbit coupling material and has a small direct band gap energy of $\sim$ 0.36 eV at 300 K [85] (Figure 1.4.2). Epitaxial InAs structures can be synthesized in MBE, liquid phase epitaxy (LBE), and MOVPE. For application, InAs is widely used in infrared detectors [183] and diode lasers [51] for its small gap. Some studies show that it has better emission efficiency than InSb as a terahertz radiation source [85]. In addition, InAs can be used in electronic transistors for its high electron mobility [52]. InAs/GaAs quantum dots can be an optimal single photon source for their narrow emitted photon linewidth and high emission rate [133].

InSb

Bulk indium antimony (InSb) is a cubic semiconductor in the III-V group and has the zinc-blende (ZB) crystal structure. Unlike InAs, grown InSb nanowires stay mostly in the ZB crystal structure. Its lattice constant is 6.476 Å, which makes it also difficult to fabricate or integrate in CMOS [138]. It is one of the semiconductors with the strongest spin-orbit coupling and a higher g-factor ($g \sim 50$). At 300 K, InSb has a small effective mass (0.0155 m_e) [182] and a high electron mobility (77 000 cm^2/V/s) [182]. Therefore, its ballistic length can be up to 0.7 μm at 300 K. Moreover, it has the smallest direct band gap energy 0.17 eV among III-V materials, as seen in Figure 1.4.2. Epitaxial InSb structures can be synthesized in MBE, LBE, MOVPE, etc. InSb is widely used in quantum transport research, such as using proximitized InSb nanostructures in the studies of ballistic measurements for its high electron mobility and small effective mass [81]. Moreover, its small band gap is attractive in the applications of infrared detectors [44], and terahertz radiation source [85].

1.4.2 Superconductors

Sn

Sn is an important metal in human history, for example, bronze is an alloy of copper and 5% of Sn, which had been used since 3000 BC. Around 600 BC, pure metallic Sn was fabricated and has been found in China and Machu Picchu [5]. Bulk Sn is an allotropic element with a phase transition at 286 K; its α-phase is stable at low temperatures and its β-phase is stable at high temperatures. α-Sn is a cubic topological insulator and hasa face-centered diamond crystal structure. β-Sn is a tetragonal superconductor and has a body-centered crystal structure. The lattice parameters are very different from α-Sn to β-Sn; a = b = c = 6.489 Å for α-Sn and

a = b = 5.809 Å, c = 3.169 Å for β-Sn. Importantly, α-Sn is lattice-matched material with InSb, with only 0.17% lattice mismatch, and this brings out the interest of research on the Sn/InSb system.

Sn is used often in our daily life, including as a corrosion-resistant coating on steel for food preservation and as an alloy with Pb for soldering electrical circuit junctions. For studying topological phases, both phases of Sn are interesting. Epitaxial α-Sn thin film is considered a zero-gap topological insulator for hosting quantum spin Hall effect [184, 134, 47]. Stanene, a few atomic layers of α-Sn, reveals strong quantum confinement and graphene-like electronic states, i.e. a Dirac point near the Fermi level [144]. The Dirac cone band structure is useful for high mobility transport applications. At the edges of 2D stanene, the surface states are gapless and insensitive to local disorders, which can be used for observing quantum Hall effect [91, 231].

β-Sn is a metallic superconductor with a rather high critical temperature, $T_c = 3.73\,K$ [91, 61]. Due to electron confinement effects, single-crystal β-Sn nanowires exhibit broadening T_c and higher critical field up to $H_c = 0.3\,T$ [210]. K. Houben et al. reported the increasing T_c ($> T_{c,bulk} = 3.73\,K$) in Sn nanoislands due to photon softening and enforcing electron-phonon coupling [140, 97]. D.Lozano et al. demonstrated there are several resistance drops in thin Sn nanowires below T_c, which is speculatively related to long-range superconductivity between grains. Electrodeposition in nanoporous polycarbonate membranes can be used to create high crystalline β-Sn nanowires at room temperature [141, 140].

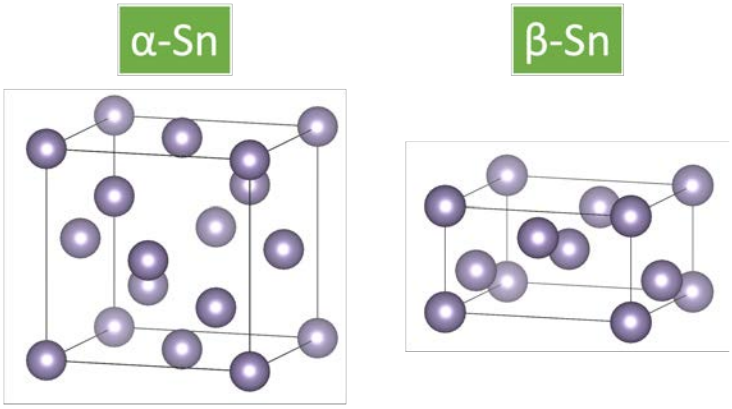

Figure 1.4.3: Sn crystal structures in α- and β-phases.

Al

Aluminum (Al) is a face-centered cubic metal from the 13th column of the periodic table. The first usage of Al can be traced back to the 5th century in Greek history records as a dyeing mordant. Pure Al is a light (2.70 g/cm^3, 7.85 g/cm^3 for steel) and soft (yield strength 7−11 MPa) metal in comparison to steel (yield strength 350 MPa) [1]. This is the reason why it is used to serve as tableware, foils, kitchen utensils. It has a high chemical affinity for oxygen and forms

a thin layer of native Al oxides ($\sim$ 3 nm) on the surface in the presence of oxygen. This oxide passivates the Al surface as it is resistive to oxygen, water, and diluted acid [11]. ^{27}Al is the only stable isotope and the third most abundant element on Earth after oxygen and silicon. As a metal, it has excellent thermal and electrical conductivity. We can wire bond for chip fabrication [194]. Al is also a metallic superconductor whose critical temperature T_c = 1.2 K and critical field H_c = 0.01 T [54]. Its applications include food packaging because of its non-toxicity, transportation crafts because of the low density, and electricity-related wires because of its good conductivity.

MoGe

Amorphous molybdenum germanium (MoGe) has received very few attention, and one of the early scientific reports about its synthesis was in 1953 by A. W. Searcy and R. Peavler [111]. It is a non-crystalline superconductor whose bulk critical temperature is up to T_c = 7.36 K [217]. Using magnetron sputtering from a $Mo_{0.75}Ge_{0.25}$ source is a practical approach for depositing an homogenous MoGe thin film with a very low surface roughness 0.27 nm [161]. In 1985, J. M. Graybeal reported a reduction of T_c and an increase of resistivity while decreasing MoGe layer thickness [84]. After that, in 2020, S. Mandal et al. studied the origin of superconductivity via amorphous MoGe thin films [147]. Roy et al. used amorphous MoGe thin film to study the superconducting phase transition of a 2D superconductor for fundamental research [186]. MoGe is used in different applications thanks to its superconductivity, such as quantum phase slip nanowire devices [9], superconducting memory [223], and superconducting nanowire single photon detectors [217].

1.5 Justification of the work performed in the thesis

I started my PhD thesis by growing inclined InAs nanowires in MBE for the realization of *in situ* shadowed hybrids in the framework of the international project ANR-NSF PIRE HYBRID. The samples were sent to collaborators for superconductor depositions, device fabrications and transport measurements. In particular, my nanowires samples were the first ones to be tested for the development of Sn thin film at cryogenic temperature at UCSB in the cluster of C. Palmstrøm (Section 2.3.2). Nevertheless, growing inclined InAs nanowires for shadowing nanowire networks requires a different growth process than vertical nanowires. There is a limited number of studies on the growth of inclined InAs nanowires on (001) substrates. Therefore, my first goal was to develop reliable InAs nanowires on InAs(001) substrates in MBE and to construct hybrids with standard and novel superconductors, such as MoGe, Sn, Al, either with collaborators or in our own system.

In parallel to InAs, Sn was also deposited on InSb nanowire networks from Eindhoven University of Technology. InSb nanowire networks have been developed for several years, the

focus evolved naturally towards a completed Sn/InSb system whose electronic properties had previously been validated [38, 71]. In this context, I studied the crystal structure of the Sn film by X-ray diffraction prepared at the University of California Santa Barbara (UCSB) to complement the transport data.

The transport properties of the Sn/InSb nanowires were studied by S. Frolov's group at Pittsburgh University. The superconductivity measurements are done on different nanowire devices at base temperature, such as normal metal-superconductor (N-S), superconductor-superconductor (S-S), and normal metal-superconductor-normal metal (N-S-N). The nanowire devices are made from shadowed Sn/InSb nanowires without post-deposition chemical etching. The contacts and the gates are defined by electron-beam lithography (EBL) and covered with 10/150 nm of titanium/gold (Ti/Au).

Figure 1.5.1 shows a Sn/InSb nanowire device [168]. The bare InSb nanowire sections without Sn are defined as a tunneling barrier between the superconductor Sn and the normal contact Ti/Au. We see that the conductance drops dramatically to a near-zero value at V = $\pm 680\,\mu$eV and this suppressed conductance region is called superconducting gap. It shows a larger hard gap than Al-based devices, which indicates a wider coherent range of Cooper pairs in nanowire. Besides, this superconducting gap is resistive in a parallel magnetic field till 4 Tesla and only starts softening above 2 Tesla. It is a good sign for applications requiring both superconductivity and magnetic fields, such as superconducting qubits operating in a magnetic field. I did not perform the experiments demonstrated in this study but took part in the structural investigations that confirmed the crystalline phase of Sn.

High resolution transmission electron microscope (HRTEM) analysis was performed on the Sn/InSb nanowire to evaluate the crystalline quality and the epitaxial relationship between the Sn shell and the InSb nanowire. We see in Figure 1.5.2 that the Sn shell is polycrystalline, and the interface is sharp. Via fourier transformation analysis, we learned that very few Sn grains are epitaxial on the InSb facet of the nanowire. We discovered that 11 of the 13 grains on the Sn shell are in the superconducting β-phase after examining them. The presence of β-Sn grains supports the transport data, but as a material scientist, it is puzzling. Indeed, most of Sn thin films grown on InSb reported in the literature are in the α-phase (not superconducting). Therefore, this is the original motivation for studying the crystal structure of Sn/InSb in 2D and 1D in my thesis.

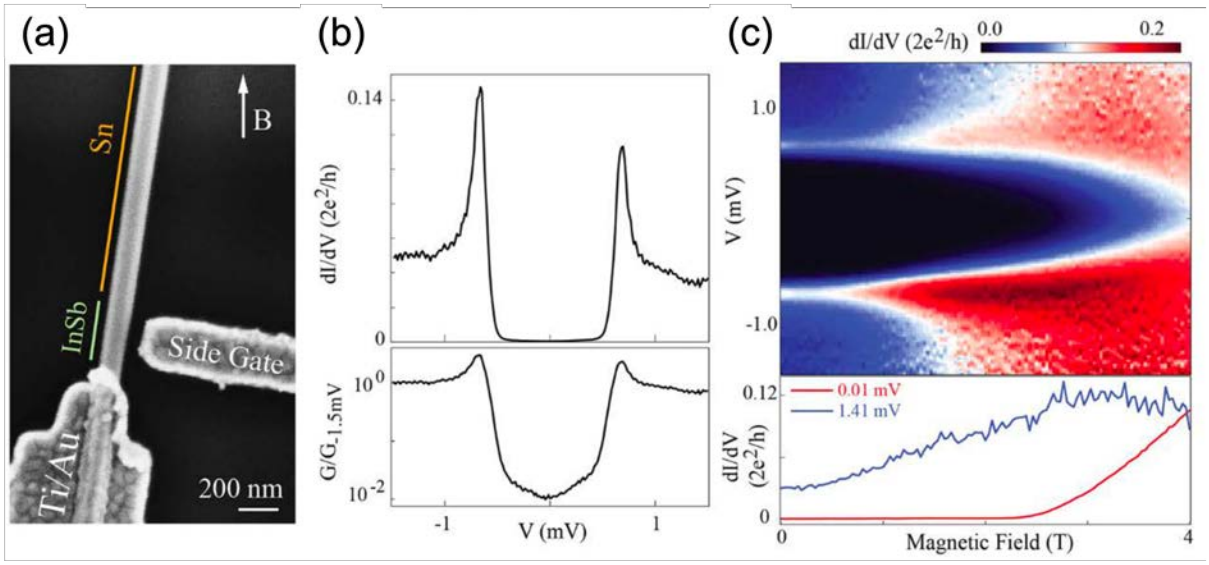

Figure 1.5.1: Superconductivity measurements of N-S Sn/InSb device. (a) SEM image of N-S device A shows Sn shell on shadowed InSb nanowire with the Ti/Au contact and the side gate. (b) Conductance of device A at zero magnetic field reveals a superconducting gap, shown in linear scale at the top and in logarithmic scale at the bottom. (c) The gap evolution with applied magnetic field shown as 2D transport map and the cutlines are extracted from high and low sweeping V [168].

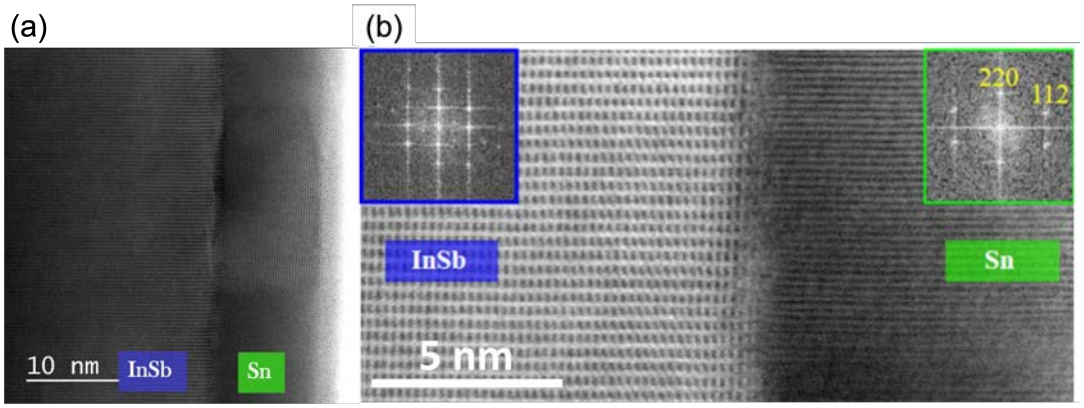

Figure 1.5.2: HRTEM analysis of Sn/InSb nanowire [168]. (a) Low magnification of a clean interface of a hybrid nanowire and polycrystalline Sn shell. (b) HRTEM image of Sn/InSb interface. The inset shows the fourier transform of an epitaxial Sn grain.

1.6 Thesis outline

The objective of my thesis is to develop reliable hybrid structures based on InAs and InSb. Over these years, it has become more and more important to focus on the quality of the materials if one wants to one day observe MBS in nanowires and thus create reliable fault-tolerant qubits using topological superconductivity.

In the first part of my thesis ⟨**Part I: Development of inclined hybrid InAs nanowires**⟩, I focus on the development of a reliable recipe for growing inclined InAs nanowires in MBE and

ex situ superconductor deposition approaches. I first describe the influence on Au-assist VLS nanowire growth from each growth parameters in MBE, such as annealing temperature, growth temperature, V/III ratio, and growth time in **Chapter 3: Growth of inclined InAs nanowires**. By optimizing the annealing step, the high density of inclined InAs nanowires is obtained. With further optimization of growth temperature and V/III ratio, I achieved non-tapered inclined InAs nanowires grown on InAs(001). Besides, I investigate the growth mechanism via a growth time study with the optimal growth parameters.

Then I describe the superconductors deposition on InAs nanowires via an *in situ* or *ex situ* procedure in **Chapter 4: Superconductor deposition on InAs nanowires**. *In situ* deposition is performed in MBE after nanowire growth, and *ex situ* deposition requires As-capping on nanowires to prevent oxidation during sample transfer. I established the procedures of the As capping at low temperature in MBE and the As decapping at high temperature in either MBE or sputtering. The selected superconductors are Al, MoGe, and Sn, whose deposition strategies are different according to their material properties. Metallic superconductors such as Al and Sn require a low depositing temperature to prevent nucleation of big grains. Amorphous MoGe is deposited by sputtering at room temperature, and the optimized As decapping is required prior to MoGe deposition.

In the second part of my thesis ⟨**Part II: Decoding the properties of Sn thin films on InSb**⟩, I focus on the crystalline study of Sn on the InSb system by X-ray diffraction technique. **Chapter 5: 2D Sn thin film on InSb substrate** focuses on the crystal structure and the crystalline quality of 2D Sn thin film on InSb substrate with different fabrication parameters, such as Sn layer thickness and capping layer methods. β-Sn grains appear while InSb substrate cannot stabilize epitaxial α-Sn layer by strain. I also studied the Sn thin film morphology by AFM and EDS to compare with the XRD results. In addition, the electrical properties of thin films are studied via low transport measurements performed by the collaborators at the University of Pittsburgh. This supports the presence of β-Sn grains in Sn thin films, which make the thin film superconducting.

Chapter 6: Sn shell on InSb nanowire describes the crystalline study of *in situ* Sn shell deposition on InSb nanowire (1D) by grazing incident X-ray diffraction. I will discuss the as-deposit Sn phase at cryogenic temperature and its evolution with increasing deposited Sn thickness and increasing temperature. *ex situ* XRD and low transport measurements help to verify the phase of Sn on InSb nanowires and complete the 1D Sn/InSb study.

Finally, I conclude on the outcomes of my studies on these two hybrid systems: the establishment of inclined InAs nanowires growth and the crystallography of Sn film/shell on InSb in **Chapter 7: Conclusions and perspectives**. These contributed to achieving better and more reliable hybrid systems in quantum transport. By discussing the difficulties that have been overcame, a next step from a material science perspective is proposed.

CHAPTER 2

Methodology and approach

2.1 Nanowire growth by VLS mechanism

We use the VLS mechanism to grow free-standing InAs nanowires. This mechanism is reported by R.S. Wagner and W.C. Ellis while using Au particles to assist Si whisker (nanowire) growth on Si(111) [218]. VLS is flexible and has vast applications for various nanowire structures, such as branched nanowire [86], nanowire junction [222], crystalline structure control [108, 237, 125], growth direction [238] etc. Notably, it is compatible with most epitaxial growth techniques, such as metal organic vapor-phase epitaxy (MOVPE) [195], molecular beam epitaxy (MBE) [207], and chemical beam epitaxy (CBE) [89].

The VLS mechanism is based on a liquid metallic droplet that changes the chemical potential at interfaces following the Gibbs-Thomson theory and favors unidirectional growth [113, 80]. The liquid-phase droplet collects atoms/molecules coming from the direct impingement and the diffusion from the substrate surface. Once the metallic droplet reaches the supersaturation at the eutectic temperature, the crystals precipitate at the interface of the liquid droplet and solid substrate surface. In short, the metallic droplet has two important roles in VLS: receiver of species and catalyst. The metallic catalyst can be inert metals, such as Au and Ag [121, 136, 64], or self-catalyzed metals, such as Ga and In for III-As nanowire growth [236, 157, 83], Sn for SnO_2 nanowire [48].

During VLS nanowire growth, atoms/molecules have several ways to reach the catalyst droplet on the top of the nanowire, (1) direct impingement to the droplet, (2) sidewall diffusion and (3) diffusion from substrates to the nanowire sidewalls, as illustrated in Figure 2.1.1 [63]. The 1^{st} path, the atoms/molecules arrive directly and diffuse into the metallic droplet via the vapor-liquid transition. The 2^{nd} path, the atoms/molecules arrive on the sidewalls of nanowires and diffuse along the nanowire. The 3^{rd} path, the atoms/molecules impinge to the substrate and then diffuse to the nanowires.

All three paths contribute to the axial growth of nanowires, and the 3^{rd} path is especially important for the beginning of the growth [146, 66]. The 2^{nd} path is highly related to the diffusion

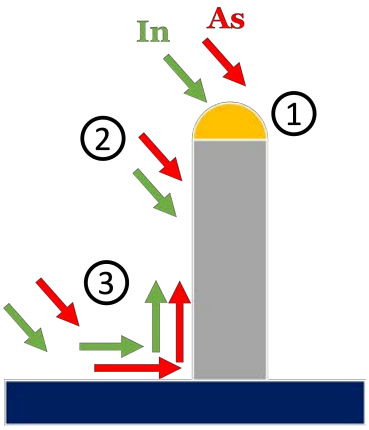

Figure 2.1.1: The kinetic paths of nanowire growth. (1) Direct impingement to the metallic catalyst, (2) sidewall diffusion, and (3) substrate diffusion.

length of adatoms on the sidewall, which can vary from few 10 nms as in II-VI materials [166] to few μms as in III-V materials [146]. The axial growth of nanowires is mainly driven by the adatoms collection from the sidewall diffusion instead of from the direct impingement [67, 65].

The 2^{nd} and 3^{rd} paths can also attribute to the radial growth of nanowires. The adatoms diffusing along the sidewalls can cooperate to nanowires via the vapor-solid transition. Notably, the desorption of adatoms happens at anytime and any phase transition, such as vapor-liquid, and vapor-solid transitions. The balance of these kinetic paths under certain experimental conditions leads to nanowire growth.

The Au droplet is one of the most commonly used metallic catalysts for growing III-V nanowires because it can form an eutectic liquid droplet at nanowire growth temperature with most III-group elements. There're several ways to seed Au droplets on a clean substrate depending on growth technique: (1) *in situ* deposit a few-nanometer Au thin film and anneal at a certain temperature in order that the film dewets into Au droplets [207], (2) *in situ* monodisperse aerosol Au nanoparticles [196], (3) *ex-situ* deposit directly monodisperse Au nanoparticles from colloïde solution [82], (4) *ex-situ* electron lithography patterning [30]. To obtain a lower dispersion in nanowire diameter and avoid a time-consuming nanofabrication process, we chose to seed Au nanoparticles on an InAs substrate from monodisperse Au colloid option (3) for InAs nanowire growth (Figure 2.1.2 (a)).

After transferring the seeded III-As substrate, Au nanoparticles become liquid hemisphere droplets (Figure 2.1.2 (b)) at a high-temperature annealing procedure ($\geq$ 420 °C) prior to nanowire growth. An overpressure As_2 flux is supplied in the annealing step to prevent roughening the substrate surface because of the As desorption at high temperature. It has been reported that As_2 starts to leave from III-As substrate at a substrate temperature > 300 °C [57, 139]. Meanwhile, Au decomposes the beneath InAs substrate and form Au-In alloy [216, 215].

After opening indium (In) shutters and starting the growth, In and As atomic fluxes reach the surface and diffuse to Au droplets, as seen in Figure 2.1.2 (c). With continuous diffusion

of species, the Au droplet reaches the supersaturation point and then the nucleation happens at the interface of the Au-In droplet and the substrate. The supersaturation and the precipitation of Au-In-As occur alternatively during the growth, which drives the axial development of the nanowire, as seen in Figure 2.1.2 (d). The concentration of the In in Au droplet is around 30%, whereas the As concentration is rather low and can be ignored [20].

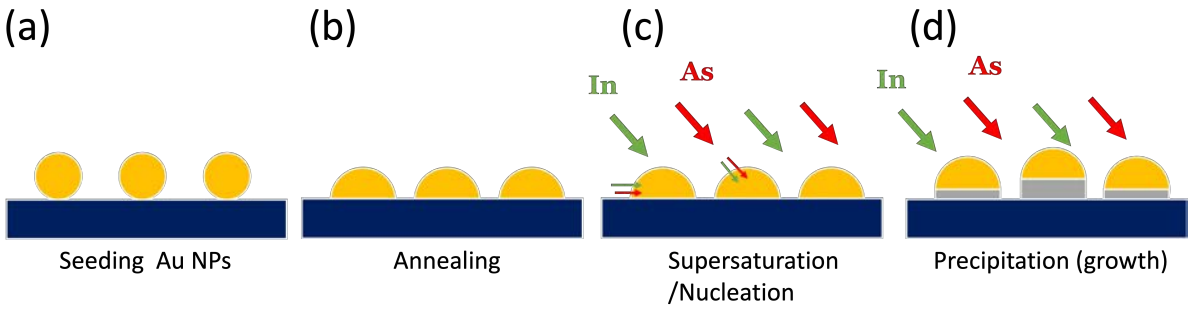

Figure 2.1.2: The steps of Au-assist nanowire growth via vapor-liquid-solid mechanism.

Nanowire growth follows successively layer-by-layer at the solid-liquid interface. F. Glas et al. showed that the nucleus of III-V nanowire in the Au droplet follows the lowest enthalpy, leading to wurtzite (WZ) or zinc blende (ZB) of the crystal structure [80]. Eq. 2.1 expresses the change in enthalpy ΔG during nucleation. For a solid nucleus geometry, A is its upper surface, h is its height, and P is its perimeter length in liquid. $\Delta\mu > 0$ is the chemical potential change of III-V compounds between liquid and solid phases per unit nucleus volume. $\gamma_{\ell L}$ is the energy per unit area of lateral surface between nucleus and liquid, γ_{NL} denotes the energy between nucleus and liquid at upper surface, γ_{SL} denotes the energy between substrate and liquid, and γ_{SN} denotes the energy between substrate and nucleus. According to ΔG, the crystal structure of nucleus is determined by the nucleation position in the Au droplet, i.e. the WZ nucleus occurs at triple-phase (vapor-liquid-solid) and the ZB nucleus occurs at center of the Au droplet.

$$\Delta G = -A \cdot h\Delta\mu + P \cdot h\gamma_{\ell L} + A(\gamma_{NL} - \gamma_{SL} + \gamma_{SN}) \tag{2.1}$$

J. Harmand et al. showed that the atomic step flow occurs at the interface of the catalyst and the GaAs nanowire by *in situ* TEM [90]. After the Au-Ga droplet reaches supersaturation, the crystalline nucleus starts from the boundary with nanofacets and propagates progressively to complete a monolayer of GaAs, which is illustrated in Figure 2.1.3 (a) and (b). The nuclei of a new monolayer appears after completing the previous monolayer (Figure 2.1.3 (c)).

We aim to create a crossed Au-assist InAs nanowires network on InAs(001) substrates using VLS mechanism. The complete description of my goal can be found in Chapter 1. As mentioned before, monodisperse Au colloidal solution is chosen for the seeding catalyst on the substrate. In the next section, we are going to present a MBE machine where VLS InAs nanowires grow.

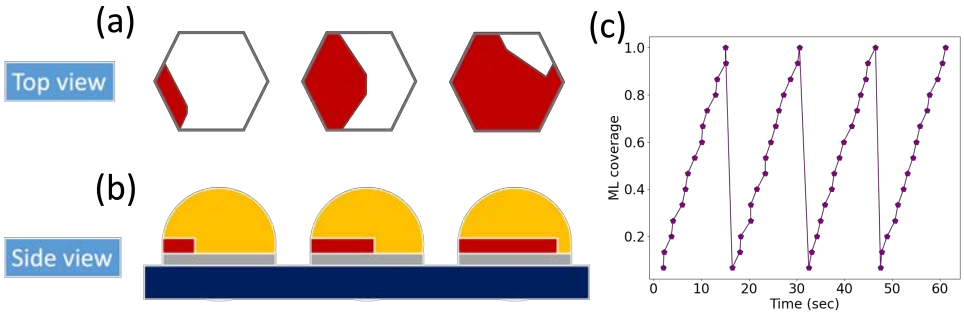

Figure 2.1.3: The monolayer growth of wurtzite nanowire progressing at solid-liquid interface. (a) is the top view of progression and (b) is the side view. (c) is the coverage of monolayer versus growth time. The illustration is inspired by [90].

2.2 MBE characteristics

Molecular beam epitaxy (MBE) has been used for high crystalline material in nanostructure synthesis. A classical MBE growth chamber provides an ultra-high vacuum environment, which can achieve $\sim 1 \times 10^{-12}$ torr leading to atoms with a long mean free path (>> 10 m) [212]. The material deposition rate is rather low (one monolayer per second) compared to other deposition techniques, which guarantees an epitaxial growth with low impurity. The excess amount of particles which do not reach the sample surface is removed immediately from growth chamber by a pumping system.

In our RIBER-32 MBE system, there is an intro chamber for inserting samples, a degassing chamber for prior degassing procedure at 250 °C and also a growth chamber for crystalline nanowire growth. All the chambers are connected by transfer chambers with a high vacuum of around $1 \times 10^{-9} \sim 1 \times 10^{-8}$ torr. The schematic of the growth chamber is illustrated in Figure 2.2.1. There are two pressure gauges in the growth chamber: one at the bottom for background pressure and the other at the center for flux measurement. The sample rotor can switch the positions of the gauge for measuring the flux, the manipulator for nanowire growth, and the transfer for transferring the sample. The background pressure of the growth chamber is around 1×10^{-9} torr while being cooled down by liquid nitrogen. The motor on the sample holder can simultaneously rotate the substrate during growth for homogeneity over a large surface in terms of the fluxes from diffusion cells.

The material sources with the highest achievable purity (>> 99.99999%) are loaded into the crucible of source cells. There are two types of cells used in our MBE for different materials: (1) Knudsen effusion cell and (2) valved cracker cell. A functional Knudsen effusion cell provides a uniform and directional atomic flux controlled by a heating filament. There is a controlling shutter in front of each effusion cell for initiating and terminating the deposition. Also, the effusion cells are facing the substrate to effectively evaporate materials onto the substrate. In and Al sources are loaded into Knudsen effusion cells. The 2nd type of cell, the valved cracker cell, is for evaporating As source. This type of cell composes of two zones, one is the evaporation zone

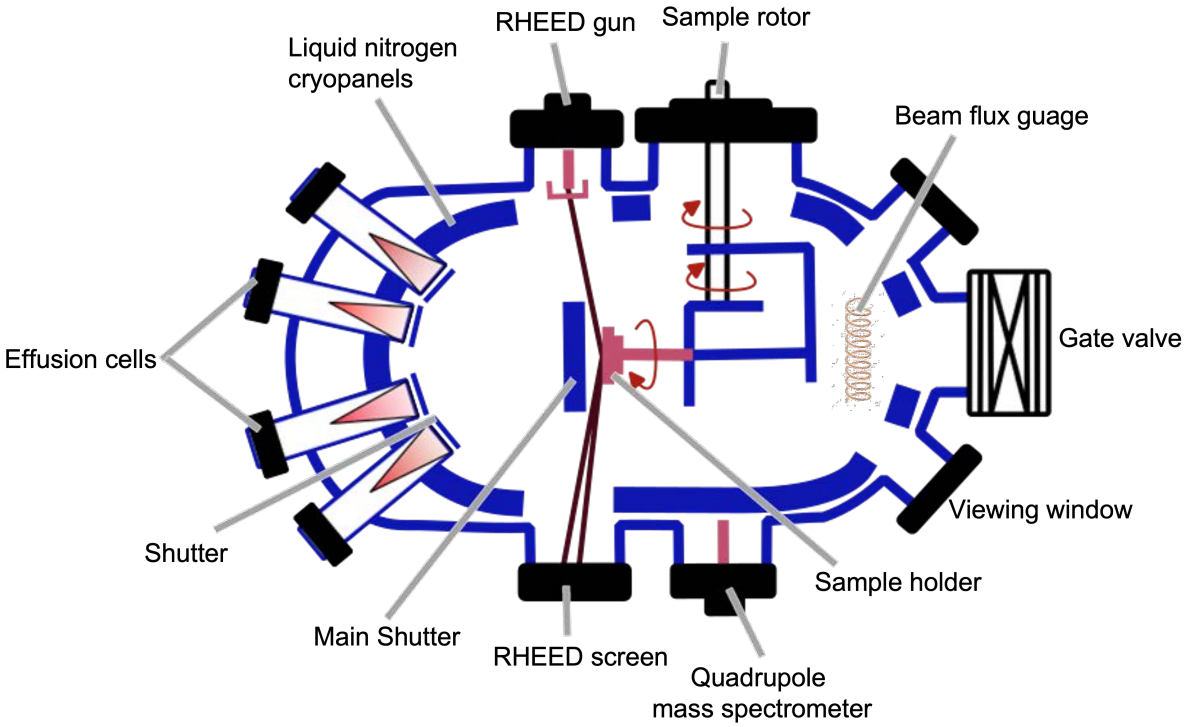

Figure 2.2.1: Schematic of the growth chamber in RIBER-32 molecular beam epitaxy.

and the other is the cracking zone. The evaporation zone heats up the As source, creating As_4 at 350 °C, then the cracker zone decomposes As_4 into As_2 above 600 °C. The flux is controlled by the valve of the cell. Notably, a valved cracker cell has a high capacity for containing As source for an extended period of time without the need for frequent refilling. The illustrations of cells are depicted in Figure 2.2.2.

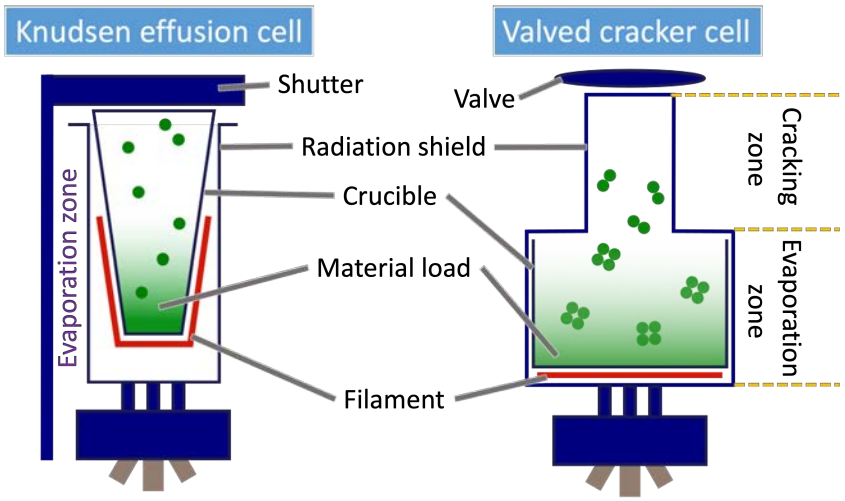

Figure 2.2.2: 2 types of cells used in MBE, Knudsen effusion cell and valved cracker cell [177].

The temperatures of the manipulator and cells are controlled by a heating filament ramping

rate of around 30 °C/min for the manipulator, 1 °C/min for the Al cell while > 700 °C to avoid aggressive thermal expansion due to the phase transition breaking the cell. The advantages of growing a high crystalline quality nanostructure in a MBE are the compatible real-time observations, such as RHEED and mass spectroscopy. The purity of the atmosphere in the chamber is monitored by mass spectroscopy. RHEED reflects the *in situ* structure of the crystalline surface. It is a grazing electron beam which is sensitive to the substrate surface and gets scattered by the crystalline morphology of the surface. This real-time observation leads to a high degree of manipulation during epitaxial growth. We will elaborate more about RHEED in the next section.

2.2.1 RHEED

Reflection high energy electron diffraction (RHEED) is an *in situ* analytical tool for characterizing the crystalline surface during MBE growth [33]. The basic elements of RHEED include a grazing incident electron beam (< 2°) as the source and a fluorescent screen as the signal receiver. The energy of an e-beam ranges from 20 – 30 keV. The probing range of RHEED is limited to the top-most few atomic layers of the sample because of the low incident angle, which hardly penetrates into bulk material. The wavevector of the incident beam is $\overrightarrow{k_{in}}$ and that of the diffracted beam is $\overrightarrow{k_{out}}$, and they construct an Ewald's sphere, illustrated in Figure 2.2.3.

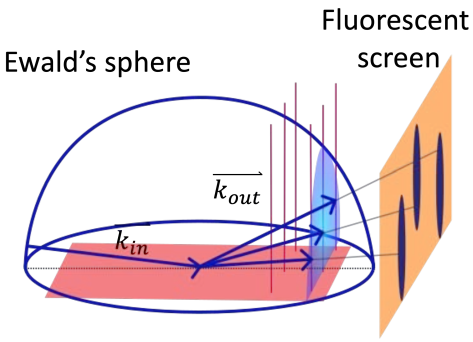

Figure 2.2.3: RHEED is a technique based on kinetic scattering of electron beam on sample surface. The wavevector of grazing incident e-beam $\overrightarrow{k_{in}}$ and the diffracted e-beam $\overrightarrow{k_{out}}$ construct a reciprocal Ewald's sphere. The pattern and the intensity evolution of reflected beam reflect the crystalline surface at different stage, such as elongated streaks coming from atomic flat and crystalline surface. The illustration is inspired by [73].

There are 2 kinds of output beams: (1) a reflected beam and (2) a diffracted beam. We can obtain a 2D growth rate during epitaxial growth by RHEED intensity oscillation from a reflected beam and the real space morphology by diffracted RHEED pattern from a diffracted beam. During 2D epitaxial layer growth, the intensity of the reflected beam oscillates periodically according to the coverage of the substrate surface, as seen in Figure 2.2.4 (a). In one period of oscillation, the maximal intensity is a fully covered surface, and the minimum intensity is half-covered surface, which is the roughest morphology. One complete period of RHEED intensity

oscillation means one monolayer (ML) formation. Therefore, we can obtain the growth rate of the 2D layer by measuring the period of oscillating fringes.

For InAs epitaxial layer growth, the growth rate is associated with In flux. Thus, we measured RHEED intensity oscillation period with different In flux at 530 °C on a InAs(001) substrate. Figure 2.2.4 (a) shows the RHEED oscillation curves related to different In fluxes. We observe that the faster growth rate of the 2D layer leads to a shorter oscillation period. We can thus plot the growth rate versus In flux (Figure 2.2.4 (b)) as a reference for further InAs nanowire growth studies.

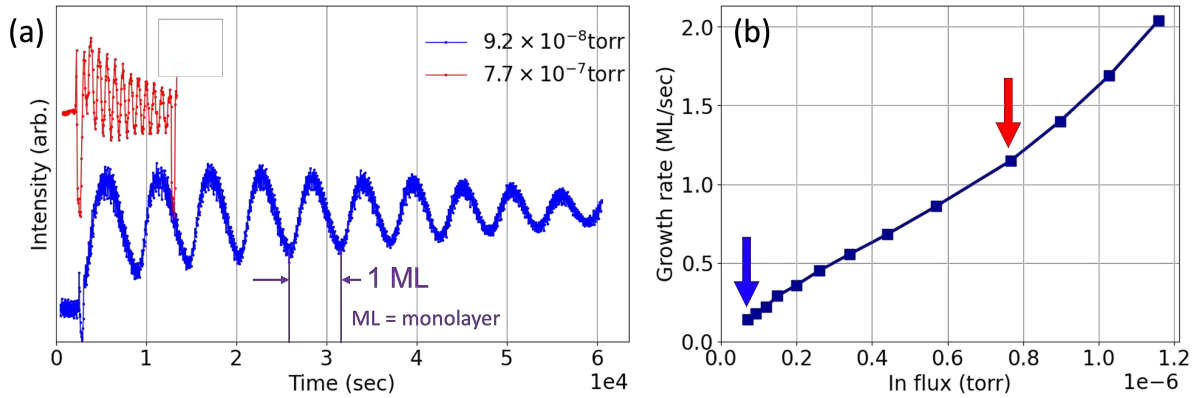

Figure 2.2.4: RHEED intensity oscillation. (a) The oscillation intensity of the reflected beam with different In flux measured at 530 °C versus time. (b) The growth rate of InAs(001) surface versus In flux. The arrows indicates the fluxes used in (a) with relevant color.

The diffracted RHEED beam gives information about the crystalline nanostructure on the surface. The surface morphology in real space causes the diffracted beams to interfere, resulting in various RHEED patterns in reciprocal space [96]. For a 2D layer, the diffracted pattern composes of clear and thin streaks with a certain spacing, as seen in Figure 2.2.5 (a)(c). The spacing between streaks is inversely proportional to the interplanar distance d of detected in-plane cyrstalline planes. For 3D objects, the emergence of bright spots corresponds to the diffraction of different family planes. Notably, different oriented nanowires surfaces result in different RHEED diffraction patterns. The vertical nanowire surface has flat spots along the azimuth [111] direction (Figure 2.2.5 (b)), and the inclined nanowire surface has spots along the $[1\bar{1}1]$ and the $[\bar{1}11]$ directions (Figure 2.2.5 (d)). In Figure 2.2.5 (d), we can see 2D surfaces and 3D objects at the same time.

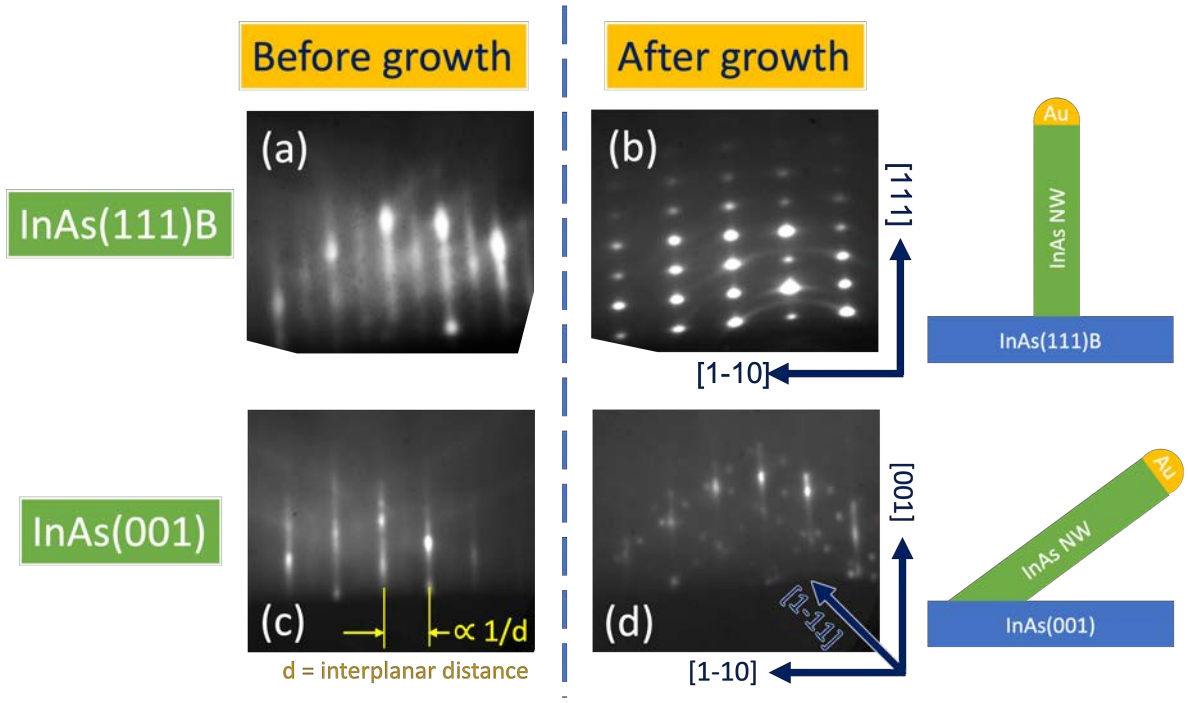

Figure 2.2.5: Evolution of the RHEED pattern before and after InAs nanowire growth on different orientational substrates. (a)(c) Cleaved surfaces of InAs(111)B and InAs(001) before nanowire growth, respectively. The RHEED pattern in (b) corresponds to vertical nanowire grown on an InAs(111)B substrate, and in (d)corresponds to tilted nanowire growth on an InAs(001) substrate. The schemes at right show the relevant sample orientation after growth.

In situ RHEED is a powerful tool for epitaxial growth in MBE that directly reflects the dynamical evolution of the sample surface. We use RHEED to monitor the *in situ* deoxidation process. A blurry RHEED pattern indicates the substrate surface being covered with oxides and contamination; a clear RHEED pattern with elongated streaks indicates the substrate surface being atomic flat and oxide-free. Another powerful usage of RHEED is calibrating the temperature of the sample in MBE chamber. The surface reconstruction of III-V material is sensitive with temperature, which can alter the elemental composition of the surface. This evolution can be observed by the RHEED pattern, which will be elaborated precisely in Section 3.3.

2.3 Superconductor deposition

To have a clean and contamination-free interface between superconductor and semiconductor, the cleaning process prior to the superconductor deposition is necessary and required. Also, the deposition technique is important for obtaining a smooth and continuous deposition of superconductors, which depends on their material properties. In this section, we present procedures for 2 different superconductor depositions, Sn deposition in MBE with prior H_2 cleaning on InSb, and MoGe deposition on InAs nanowire by sputtering.

Peak name	Binding energy (eV)
$Sb3d_{3/2}Ox$	539.60
$Sb3d_{5/2}Ox$	530.48
$Sb3d_{3/2}$	537.17
$Sb3d_{5/2}$	527.83

Table 2.3.1: Binding energy of Sb3d spectra for XPS measurements [208, 174].

2.3.1 Atomic hydrogen cleaning and XPS

Atomic hydrogen cleaning is used for the reduction of surface contamination and native oxides for semiconductors. It is a dry cleaning process and can be done *in situ* prior to epitaxial growth or metal deposition. Atomic hydrogen cleaning uses chemically reactive atomic hydrogen to decompose contamination/oxides on the surface at a low temperature $< 300\,^{\circ}C$, which avoids high temperature damage [36, 226]. The flux of molecular H_2 is controlled by the electron beam power, which thermally cracks to produce atomic hydrogen.

To monitor the cleaning process of atomic hydrogen cleaning, X-ray photoelectron spectroscopy (XPS) is useful as an *in situ* analytical technique which observes the elemental compositions and their chemical states of the substrate surface, such as oxides. It is based on the photoelectron phenomenon that an X-ray beam excites a sample surface, and a detector collects those photo-emitted electrons. XPS is a surface sensitive technique with an analysis depth of 5 nm. A classical XPS setup includes an X-ray source, a high vacuum analysis chamber, an electron focusing system, a spectrometer and an electrons detector.

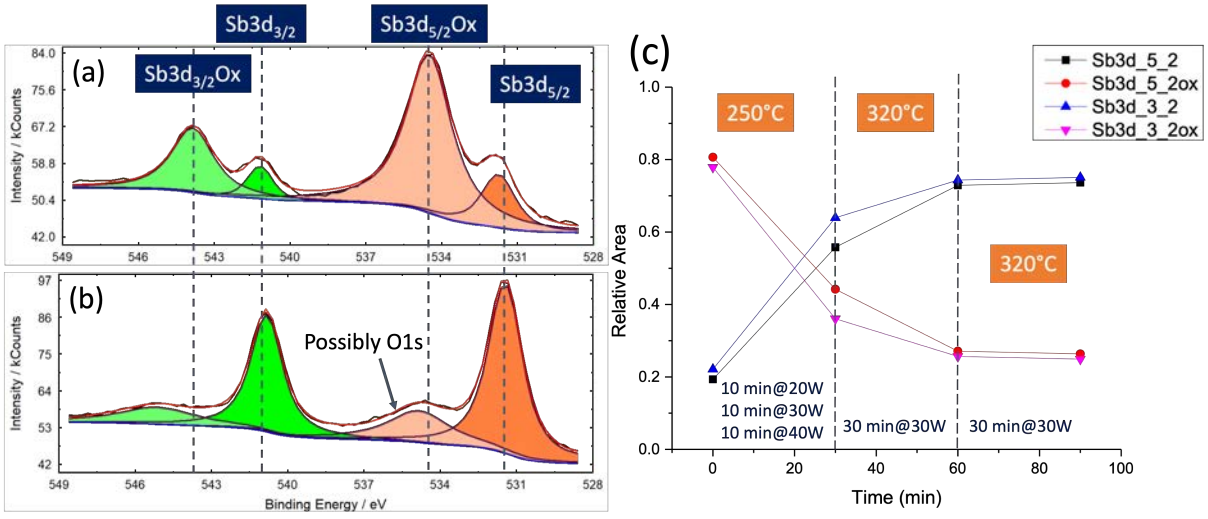

Figure 2.3.1: The XPS monitoring H_2 cleaning process on InSb(110) substrate. The binding energy profiles identify elemental compositions and their chemical states on sample surface (a) before and (b) after deoxidation. (c) Evolution of the relative area of $Sb3d_{3/2}Ox$, $Sb3d_{3/2}$, $Sb3d_{5/2}Ox$, $Sb3d_{5/2}$ for different atomic hydrogen cleaning cleaning step. Black dashed lines identify the position of each chemical state.

We are interested in the oxide-free interface of the Sn/InSb heterostructure so eliminating native oxides of InSb prior to Sn deposition is essential. Atomic hydrogen cleaning is reported to remove native InSb oxide at a surface temperature of 250 °C without supplementary Sb flux, which is verified by XPS analysis [208]. Under XPS monitoring, our oxide removal procedure is optimized on the InSb(110) substrate, which corresponds to one of InSb nanowire facets. The H-atoms flux is controlled by the power of the filament of the H_2 cell. We heat up the substrate to 250 °C and increase the H_2 source from 20 to 40 W for 10 minutes at each 10 W increment. Then, we increase the substrate temperature to 320 °C with an H_2 source at 30 W for 60 minutes to reinforce the oxides removal. Each step of atomic hydrogen cleaning is recorded by XPS.

The binding energy profile of the InSb(110) substrate surface before and after atomic hydrogen cleaning cleaning is shown in Figure 2.3.1 (a) and (b). We see that Sn oxide peaks, $Sb3d_{3/2}O_x$ and $Sb3d_{5/2}O_x$ are significantly reduced after the atomic hydrogen cleaning process. Meanwhile, $Sb3d_{3/2}$ and $Sb3d_{5/2}$ pure Sb peaks are increasing. The peaks are identified by the binding energy value listed in Table 2.3.1. Figure 2.3.1 (c) shows the evolution of the relative area of Sb3d peaks versus the atomic hydrogen cleaning process. We observe oxides peaks reaching their minimum after 60 minutes of atomic hydrogen cleaning cleaning. This signifies that the top-most native Sb oxide layer was mostly removed and replaced by an oxide-free InSb surface through the atomic hydrogen cleaning procedure. The final surface still has 25% residual oxide.

We use atomic hydrogen cleaning and XPS prior to Sn deposition in our *in situ* GIXRD study of Sn/InSb nanowire, and both equipments are installed at Beamline 25 (BM25) in Europe synchrotron radiation facility (ESRF). The optimized recipe for cleaning the InSb nanowires is fixed at a sample temperature of 300 °C with a 30 W H_2 source for 90 minutes in order to effectively remove all the oxide without harming nanowires. Furthermore, our collaborators at UCSB use the atomic hydrogen cleaning process on InSb substrates with their optimized recipe in their system, with a 360 °C substrate temperature and a 1700 °C hydrogen cracking temperature for 1 hour. The following Sn deposition details are described in the next section.

2.3.2 Sn evaporation

We have two types of Sn samples: 2D Sn/InSb substrates and 1D Sn/InSb nanowires, both of which are deposited from the Knudsen diffusion cell in an MBE but in different locations. The fabrication steps of 2D Sn/InSb substrate used at UCSB are as followed:

1. Cleave 2" InSb(001) or InSb(110) wafer into small pieces.
2. Glue pieces on a 3" molybdenum sample holder by gallium.
3. Load, transfer the samples to atomic hydrogen cleaning procedure.
4. Cool down the sample to < –160 °C in cryostats.

5. Sn cell temperature 1100 °C gives 2D deposition rate 0.60 nm/min.

6. Open the shutter of Sn cell and start deposition to determined thickness.

7. Stop Sn deposition and then *in situ* transfer to evaporator chamber for capping layer deposition while sample is still cold.

In the case of the 1D Sn/InSb nanowire, done in ESRF BM25, the steps for the Sn deposition are as followed:

1. Mount InSb nanowire sample fabricated by collaborator in Eindhoven on molybdenum sample holder by fixing with tungsten clamps.

2. Load sample into the chamber and perform atomic hydrogen cleaning procedure.

3. Sn cell temperature 1100 °C gives a 2D deposition rate 0.45 nm/min calibrated by quartz balance.

4. Cool down the sample to –190 °C for Sn deposition.

5. No rotation applied and the sample is tilted during Sn deposition for lateral Sn deposition on one-side of InSb nanowire.

2.3.3 MoGe sputtering

We use the sputtering deposition for the amorphous superconductor MoGe. Sputtering deposition is a type of physical vapor deposition that involves hitting a target material with charged gas particles, and the ejected target material's particles are then deposited on the substrate. As seen in Figure 2.3.2, a charged inert gas (such as Ar^+) is supplied into the deposition chamber, and it attacks the material target by following the direction of the magnetic field. The charged gas (plasma) is confined by the magnetic field, which also regulates the plasma density above the target surface and the rate of material deposition. The ejected uncharged material particles then fly to the substrate surface and deposit there. The substrate temperature can be controlled by the filament behind the sample holder without contact. The background vacuum in sputtering is around 5×10^7 mbar. The extra Ar^+ gas is expelled by the pumping system.

MoGe is sputtered at room temperature on InAs nanowires with a DC source in the sputtering. To create a clean and contamination-free interface, we use As-capped InAs nanowire and decap it in the sputtering by heating. The details will be elaborated in Section 4.5. Besides, a half-covering MoGe shell can be realized on inclined InAs nanowires in non-directional sputter deposition. This is an advantage for creating nanowire junctions without extra fabrication steps. The deposition rate is that 120 seconds deposition can attain a 15 nm half-covering MoGe shell on inclined InAs nanowires.

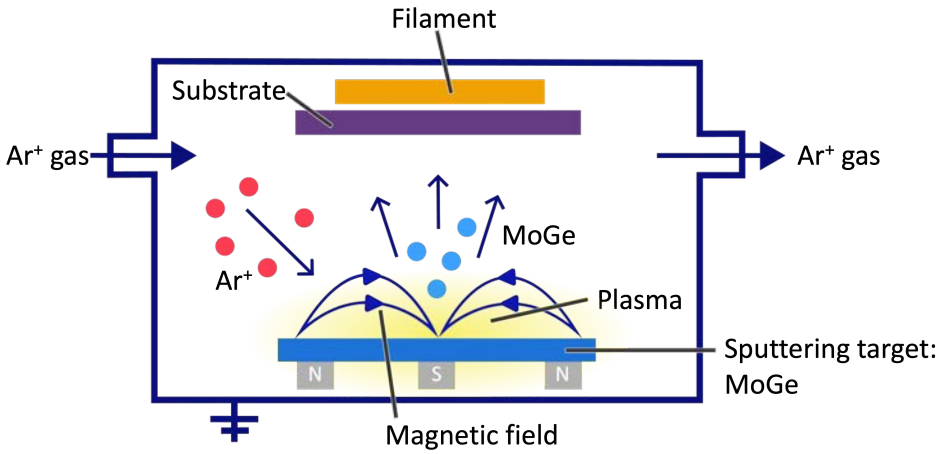

Figure 2.3.2: Schematic of sputtering deposition in the case of MoGe deposition.

2.4 Structural characterization techniques

In this section, the techniques of characterizing materials' morphology and crystalline structure are introduced, such as X-ray diffraction (XRD), transmission electron microscopy (TEM), atomic force microscopy (AFM), etc. These characterizations allow a deeper insight into the material crystalline properties, morphological evolution and interface quality.

2.4.1 XRD principle

X-ray diffraction (XRD) is a technique widely used in crystal phase analysis since its wavelength is similar to the size of lattice space and ranges from 0.03 to 3 nm [56]. A crystal is a solid material whose constitutional atoms are arranged in a highly ordered structure with repetitive motives. Lattice vectors are used to describe this repetitive crystalline arrangement, or crystal planes. The crystal family planes in material can be revealed through XRD patterns and are usually expressed in the Miller index notation system, as shown in Eq. 2.2. The g is a vector that is perpendicular to the (hkl) plane. The crystal family planes g_{hkl} can be expressed with three non-collimating lattice vectors (a_1, a_2, a_3) of the real space with 3 Miller indices (h, k, l) respectively. For a simple cubic system, the lattice vectors are mutually orthogonal. The Miller index is expressed in integers.

$$g_{hkl} = ha_1 + ka_2 + la_3 \tag{2.2}$$

A metallic anode is frequently used to produce X-ray source, such as copper, molybdenum, and silver. An accelerated electron beam bombards a metallic anode and ejects the electrons at the inner shell of the metal atoms. The vacancies are created at the inner shell and then filled by the electrons from higher energy levels at the outer shells of the atoms, and X-rays are emitted. Once the X-ray beam emitted, it is necessary to define its divergence and its wavelength. According to the type of experiment performed, it is possible to use slits, or monochromator. Then, this X-ray beam incidents on the sample and its reflected beam is captured by a detector.

Diffraction angle 2θ is defined as the angle between incident beam and reflected beam, and ω is defined as the angle between incident beam and sample surface, as seen in Figure 2.4.1. The diffraction of crystal planes fulfills Bragg's law $2d\sin\theta = n\lambda$ in real space. d is the crystal interplanar distance, n is an arbitrary integer, λ is the wavelength of incident X-ray beam and θ is the diffraction angle. At Bragg condition, the incident beam diffracted by the lattice undergoes constructive interference.

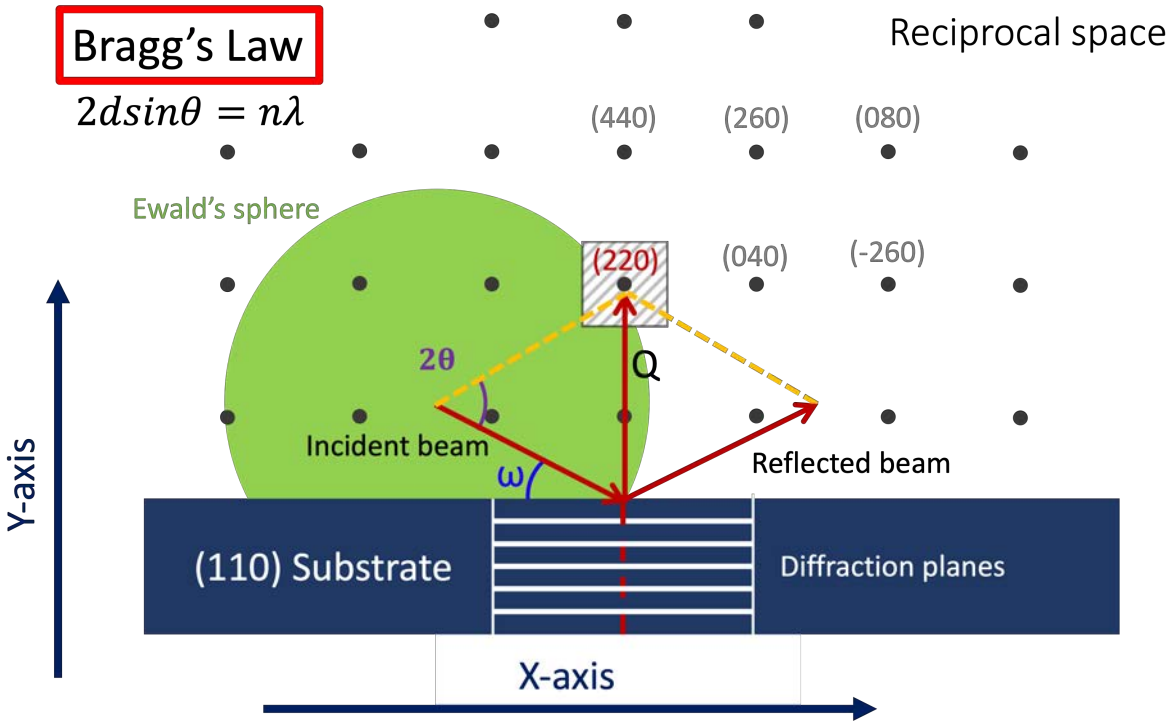

Figure 2.4.1: Illustration of reciprocal space of (110) substrate and symmetrical diffraction from planes parallel to the surface. The vertical axis corresponds to the [110] direction, and the x-axis corresponds to the [-110] direction. The incident X-ray beam makes an angle ω with the sample surface and the reflected beam makes an angle 2θ with the incident beam. The momentum transfer is Q.

It is practical to express crystal planes in reciprocal space which is the Fourier transform of real space. Each reciprocal point represents a family plane (*hkl*). In reciprocal space, the incident beam vector and the reflected vector define the momentum transfer vector Q, pointing towards a reciprocal point. Ewald's sphere is a geometric construction in reciprocal space and determines the detectable diffraction planes at a given incident wavelength. The symmetrical diffraction along the y-axis reveals crystal planes parallel to the sample surface, like (220) as an example in Figure 2.4.1. In this direction, the XRD measurements are sensitive to the thin film thickness and to the out-of-plane crystalline quality. Also, it is possible to consider the asymmetrical diffraction, like (040) in Figure 2.4.1. In this direction, the XRD measurements contain out-of-plane and in-plane crystal components. It is sensitive to the thin film strain and the lattice constant, such as in reciprocal space map (RSM) analysis.

Grazing incident X-ray diffraction (GIXRD) is one of the XRD techniques majorly probing the in-plane direction. In-plane measurement probes the crystal planes perpendicular to the surface (along the x-axis) and is sensitive to lateral grain size. Basically, the incoming X-ray beam, the diffracted beam and Q vector are nearly parallel to the surface, as seen in Figure 2.4.2. The vector is composed of a major Q_H in-plane component and a small Q_L out-of-plane component. The in-plane Bragg's angle corresponds to the $2\theta_\chi$ angle. The low-angle incident angle makes GIXRD surface sensitive, and its X-ray penetration depth into the material is limited to the order of nanometers. In laboratory, the configurations provided by Rigaku SmartLab for different purposes would be explained in the next section.

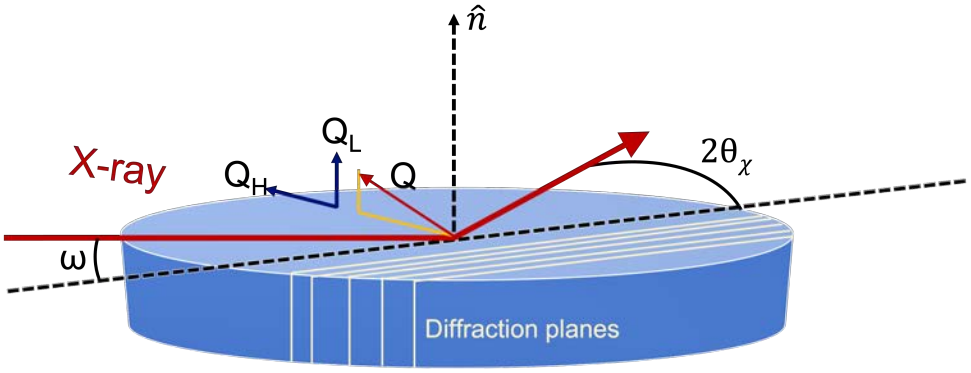

Figure 2.4.2: Schematic of GIXRD. The diffraction planes are perpendicular to sample surface. n̂ is normal vector of sample surface.

2.4.2 Laboratory setups

In this section, we present the diffractometer setup used in this manuscript as well as the main analysis methods of the X-ray data. The illustrations of configuration are shown in Figure 2.4.3. All the used optics for each kind of measurement are in Table 2.4.1.

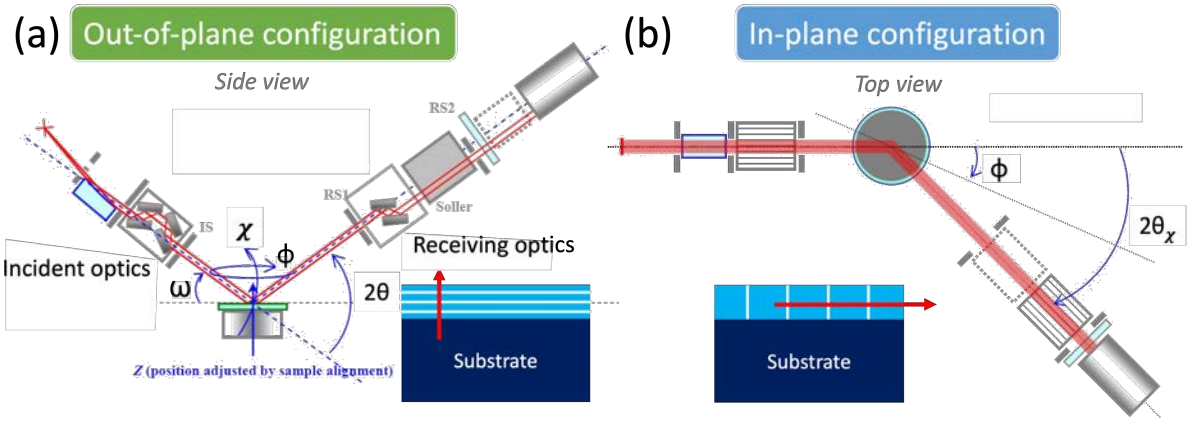

Figure 2.4.3: Two configurations of Rigaku SmartLab XRD for different probing directions. (a) Side view of out-of-plane configuration [153]. (b) Top view of in-plane configuration [199].

We use rotating copper anode in our laboratory setup as an X-ray source, whose main components are Cu κ_α and Cu κ_β. In the out-of-plane configuration, we use a monochromator to keep only the high intensity Cu κ_α and suppress the Cu κ_β. For the in-plane configuration, only a Ni filter is used for suppressing the κ_β to keep the intensity of signal at the same time.

Measurement type	**Incident optics**	**κ_β filter**	**Crystalline information**
	Receiving optics	**Irradiated dimensions (mm^2)**	
Out-of-plane	Ge(220)×2 monochromator	No	growth direction planes, thin film thickness, out-of-plane crystal quality
	PSA-0.228° analyzer	10 × 5	
In-plane	PSC-0.5°	Yes	in-plane direction planes, in-plane grain size, different phase or orientation
	PSA-0.5° analyzer	10 × 20	
Reciprocal space map	Ge(220)×2 monochromator	No	thin film strain, lattice constant
	PSA-0.114° analyzer	10 × 5	
temperature-dependent XRD	Ge(220)×2 monochromator	No	thermostability of thin film
	PSA-0.228° analyzer	10 × 5	

Table 2.4.1: List of optics used for each kind of XRD measurement, including incident optics, receiving optics, if used κ_β filter and which crystalline information and the irradiated dimensions (width×length). PSA stands for the parallel slit analyzer and and PSC stands for the parallel slit collimator, which can improve the resolution.

Out-of-plane and RSM configurations

We aim to separate the α-Sn and InSb with a small lattice parameter difference, so the high resolution XRD measurements are required. As the samples are of a high quality, we are able to perform the experiments with a high resolution. The out-of-plane configuration are shown in Figure 2.4.3 (a). The configuration of Ge(220)×2 monochromator plus PSA-0.228° gives a X-ray beam with a size 1 mm in height, 10 mm in width, and 0.01° divergence. As Bragg's angle are around 20–30°, the irradiated length of the sample is around 5 mm^2 long and the penetration depth is around micrometer [199]. The irradiation width is determined by the sample size, for example, I use a mask of 5 mm in width. The sample can be rotated around the sample normal direction (ϕ angle).

We aim to know if α-Sn films are in the epitaxial relationship with InSb substrates. The use of RSM measurements can give the strain of the α-Sn thin films. To get even higher resolution, we employ a Ge(220)×2 monochromator and a finer PSA-0.114 degree analyzer.

In-plane configurations

We are interested in the thin film analyses of the planes perpendicular to the sample surface. The in-plane configuration probes the in-plane Bragg's angle $2\theta_\chi$ and is surface sensitive because of a low incident angle $\omega < 1^\circ$. As we are in the grazing configuration, the irradiated length is very long. We choose to decrease the height of the incoming beam to have an irradiated length of about 20 mm, while keeping the same beam width around 10 mm.

Figure 2.4.4 shows the X-ray penetration depth on different materials versus the incident angle. We use a grazing incident angle around 0.3° which gives a penetration depth around few 10 nms. This signifies a surface sensitive measurement feature that the signal of thin films is maximized and that of the substrate is minimized. As we probe only few monolayers, we use a medium resolution configuration to maximize the intensity. The vertical PSC- and PSA-0.5° are used and only a κ_β filter for eliminating the Cu κ_β. The filter gives a cutoff edge to the peak, which needs to be taken into account.

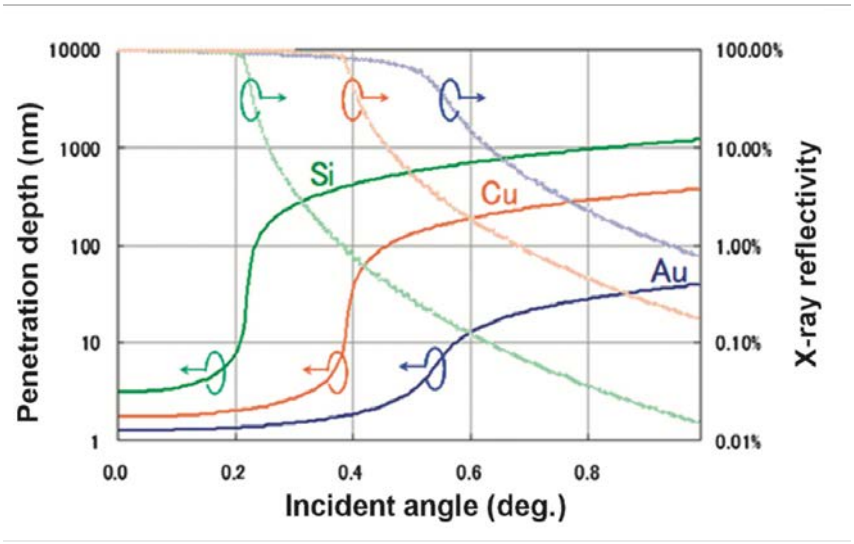

Figure 2.4.4: Plot of the penetration depth and the X-ray reflectivity versus the grazing incident angle of the X-ray beam [199]. Different materials have their own unique penetration depth profile. In general, the penetration is limited at a lower incident angle, which means the surface sensitive region.

temperature-dependent XRD configuration

We aim to see the stability of α-Sn thin films versus the temperature. As we only see the α-Sn peak in the out-of-plane direction, we perform the temperature-dependent XRD in the out-of-plane configuration. Its configuration is the basic out-of-plane configuration, combined with a heating plate and a graphite dome. The sample is placed and fixed at the center of the heating plate and covered with the dome. The heating plate can heat the sample up from 25 to 1100 °C while measuring the diffraction. A N_2 flux can be injected into the hemisphere dome to protect

the sample from oxidation. These thermal accessories give some weak and broad diffraction peaks but won't disturb our diffraction peaks of interest. We perform the temperature-dependent XRD measurement with a 10 °C increment starting from room temperature up to 130 °C.

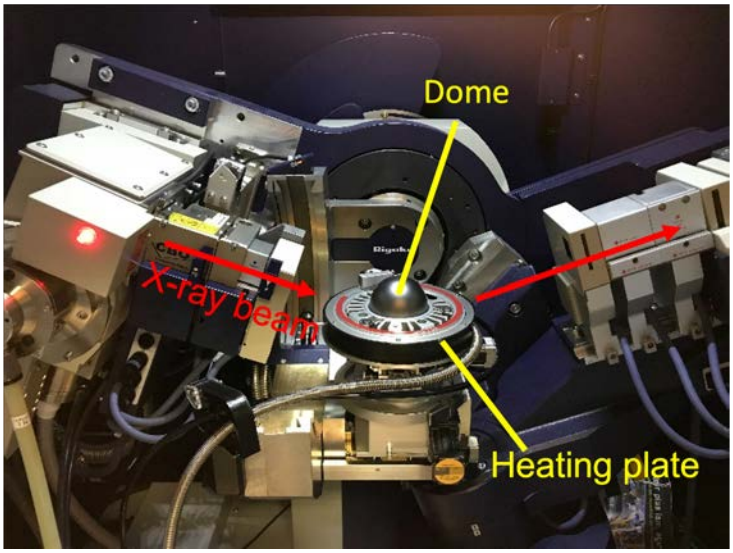

Figure 2.4.5: Setup of temperature-dependent XRD, out-of-plane configuration plus a heating plate (of 2 cm diameter) made of Al_2O_3 at the center of an hemisphere graphite dome.

Data analysis

From the diffraction peaks, it is possible to determine the position (2θ) and therefore the lattice parameter using the Bragg's law. But also the shape of the peak is related to the crystalline quality and structure. The shape of the diffraction peaks represents the crystalline quality and the crystalline structure. For example, powder diffraction peaks are usually broad and those of an epitaxial thin film are thin. The fundamental factors leading to the broadening of the peak include the size of the crystallite [156], non-uniform strain [159], non-uniform composition [22], etc. The FWHM of a Bragg peak is also related to the mosaicity of the thin film and to the crystals size when dealing with grains. The mosaicity represents the crystalline quality of a film, i.e. the alignment of the crystalline planes (as seen in Figure 2.4.6). According to the type of experiment done (out-of-plane or in-plane), we will be sensitive to the information along the growth direction or in the plane of the film.

The Voigt function results from the convolution of Gaussian and Lorentzian functions and is used in studying the broadening of diffraction peaks [229]. The Pseudo-Voigt function is the simplified Voigt function, which is more practical in data fitting. We use the pseudo-Voigt equation to evaluate the diffraction position and FWHM of diffraction peaks. Then, these peak information can be used in the Scherrer equation that gives the film thickness in the case of out-of-plane and the grain size in the case of in-plane scans. A crystalline layers of well defined thickness deposited on a substrate can cause interference of the diffracted X-ray beams, which

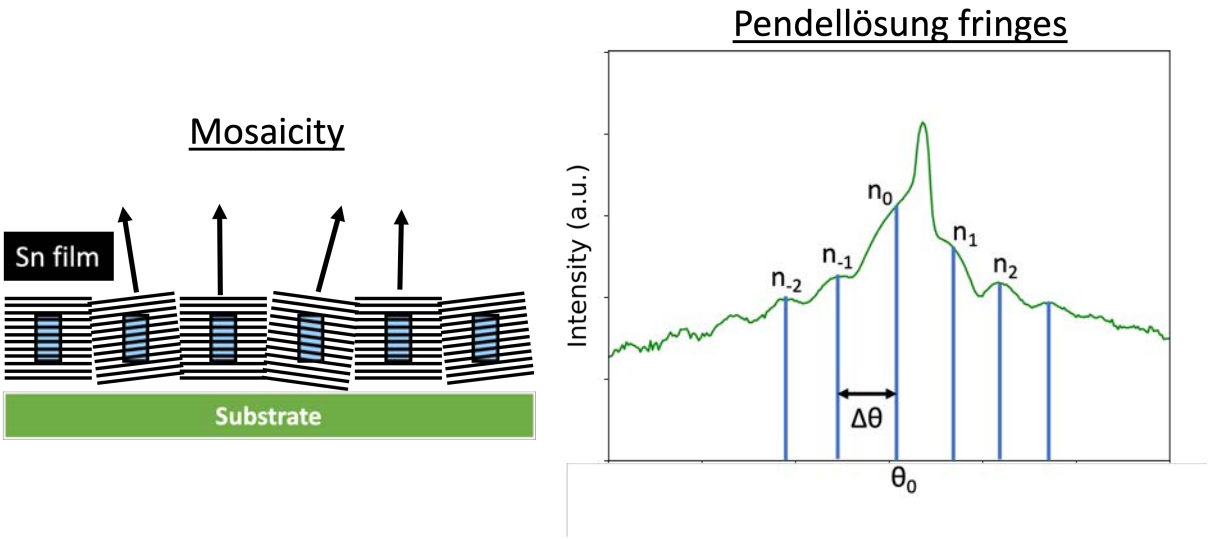

Figure 2.4.6: Schematic of the mosaicity of a film and the Pendellösung fringes. In Pendellösung fringes, n_0 is the zero-order peak positioned at θ_0, and $\Delta\theta$ is the distance of θ between the n-order peak and zero-order peak.

is the so-called Pendellösung phenomenon. In the XRD profile, the period of Pendellösung fringes is sensitive and related to the thickness of epitaxial layer. We use it to estimate the real thickness of α-Sn thin film on InSb based on the period of fringes (Figure 2.4.6).

Pseudo-Voigt function The pseudo-Voigt equation is shown as Eq.2.3, consisting of Lorentzian L(x) and Gaussian G(x) functions. The factor $\eta \leq 1$ can balance the proportion of two functions in order to maximally fit the peak shape [187]. In L(2θ) and G(2θ), $2\theta_0$ is the diffraction angle and $\mathcal{W}$ is the FWHM of the reflection peak.

$$\begin{aligned} &\mathrm{pV}(2\theta) = \mathrm{I}_0[\eta \mathrm{L}(2\theta) + (1-\eta)\mathrm{G}(2\theta)] \\ &\text{where} \\ &\mathrm{L}(2\theta) = [1 + (2\theta - 2\theta_0)^2/\mathcal{W}^2]^{-1} \\ &\text{and} \\ &\mathrm{G}(2\theta) = \exp[-(\ln 2)(2\theta - 2\theta_0)^2/\mathcal{W}^2] \end{aligned} \tag{2.3}$$

Scherrer equation The Scherrer equation is expressed as Eq.2.4 [167]. D is the average grain size (nm), K is the Scherrer constant related to crystal structure [103], λ is the X-ray wavelength (0.154 05 nm for our laboratory XRD, 0.1033 nm for our ESRF experiment), $\mathcal{W}$ is the FWHM of the peak (degree), and θ_0 is half of the diffraction angle $2\theta_0$ (degree).

$$\mathrm{D} = \frac{\mathrm{K}\lambda}{\mathcal{W}\cos(\theta_0)} \tag{2.4}$$

Pendellösung fringes for thickness measurement The thickness calculation based on Pendellösung fringes is shown in Eq.2.5, where e is the thickness of the thin film, n is the numbering

order of the interfering fringes, and θ_0 is the zero-oder peak which gives the average lattice constant. $\Delta\theta$ is the angle distance from the zero order peak and λ is the X-ray wavelength in our laboratory setups, Cu $\kappa_{\alpha 1}$ = 0.154 05 nm.

$$e = \frac{\pm n\lambda}{2\Delta\theta\cos\theta_0}$$
$$\lambda = 0.154\,05\ \text{nm} \tag{2.5}$$

2.4.3 ESRF setups

We want to have an *in situ* analysis of the Sn deposition and of the stability of the α and β phase when depositing Sn on the sidewalls of InSb nanowires. An ultra high vacuum and cryogenic environment are required to have a smooth and defect-free Sn deposition. GIXRD provides a diffraction measurements sensitive to the nanostructures on the surface. The European synchrotron radiation facility (ESRF) has one of the most intense synchrotron X-ray beams and higher brilliance than the laboratory XRD. Higher brilliance means higher precision in crystal diffraction, which gives more crystal details [4].

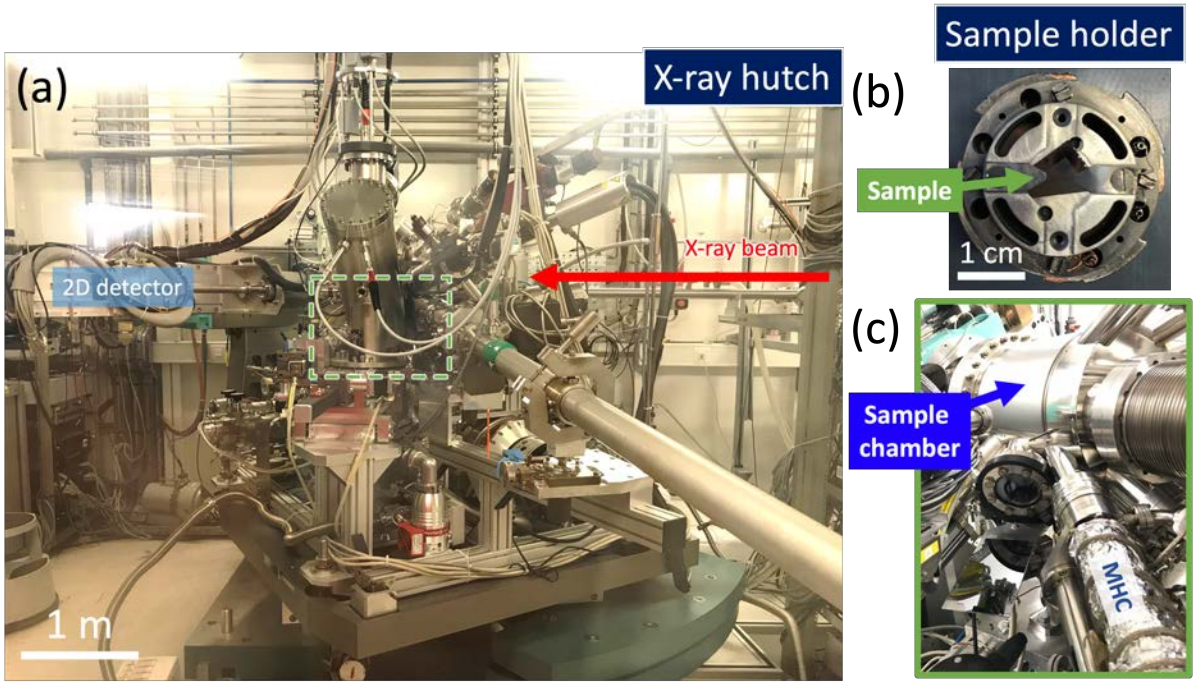

Figure 2.4.7: GIXRD setup in ESRF BM25. (a) The entire setup of GIXRD (b) An InSb nanowires sample mounted on a molybdenum sample holder fixed with tungsten clamps. (c) The sample is placed in a sample chamber equipped with an H_2 atomic source. It is the part marked with a green dashed square in (a).

The Spanish collaborative research group beam line 25 (BM25) in ESRF provides a multipurpose GIXRD dedicated to structural investigations. The main elements include an ultra-high

vacuum (UHV) MBE chamber, cryostats, a diffractometer with six-degree-of-freedom, a MAXIPIX detector for XPS analysis and a CCD type of 2D detector for X-ray. The Sn effusion cell and the cryostats are installed in UHV chamber for Sn deposition at low temperature, as well as an H_2 source for atomic hydrogen cleaning procedure. Figure 2.4.7 shows the whole setup of GIXRD hutch in BM25. The X-ray beam comes from the right-hand side of the chamber, and the 2D detector receives the signal from the left-hand side. The sample is fixed on a molybdenum sample holder with tungsten clamps, and placed in UHV chamber at the center of GIXRD machine as shown.

The synchrotron X-ray source is based on accelerated electrons, and the X-ray wavelength is related to the electron energy. We use 12 keV as the incident beam energy to avoid the X-ray absorption edges of In, Sn, and Sb [152]. Figure 2.4.8 shows the high-degree controlling system of GIXRD, including: (1) the diffractometer, (2) the incident beam, (3) the MAXIPIX detector and (4) the 2D detector.

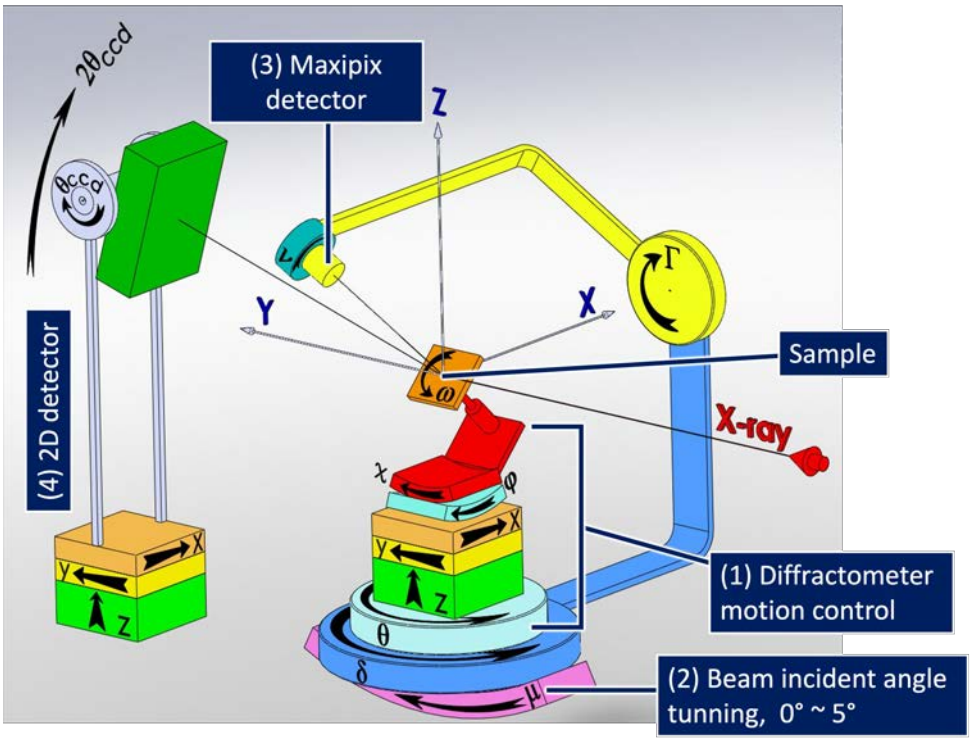

Figure 2.4.8: Illustration of diffractometer movement control system, modified from ESRF BM25 website [3].

(1) The diffractometer has a high degree of freedom of control with 6 control directions. In order to align the sample surface and the lattice planes with the X-ray beam, translation movements (X, Y, Z) and circular movements (χ, ϕ, θ) are used. The sample is mounted on the diffractometer and can rotate around ω direction used in H_2 cleaning and Sn deposition. (2) The grazing angle of the X-ray beam is controlled by μ by moving the entire experimental stage. (3) The MAXIPIX detector, which is controlled by δ, γ and ν, is served as XPS photoelectron detector. We used it in the calibration of H_2 cleaning. (4) The 2D detector has its own isolated

motion control stage, which includes X, Y, Z for translation displacements and θ_{CCD} for circular movement. It is used in collecting the reflected X-ray beam. The active area of the 2D detector is 250 mm $\times$ 125 mm and provides a high resolution image of 7651 pixels $\times$ 3825 pixels with 32.8 μm $\times$ 32.8 μm per pixel size [3].

We have to align the crystallographic axis of the samples in the referential experimental setup prior any diffraction measurement. For that we use three non colinear reflections and we determine for each of them the orientation matrix. Working in such manner allows to easily orient any crystallographic plane of the sample. In our case, we perform this alignment at low temperatures and adjust it at room temperature. Then we measure the crystalline planes along InSb[$1\bar{1}0$] and InSb[$11\bar{2}$], which correspond to two zinc-blende facets of InSb(111) nanowire. The grazing incident angle is controlled in the surface sensitive range between ALPHA = 0.15 and ALPHA = -0.25.

X-ray reflectivity

X-ray reflectivity (XRR) is a surface sensitive technique based on the total reflection of X-ray beam happening at the interface between layers [228]. It is frequently used in the thin film analysis to determine interface quality, layer thickness, thin film density, etc [179]. Both amorphous or crystalline films can be analyzed by XRR. The basic principle of XRR bases on the interference of the reflected beam at each interface, i.e. the constructive and destructive interference create an oscillation pattern. Therefore, the thin film thickness can be measured based on the period of oscillation fringes.

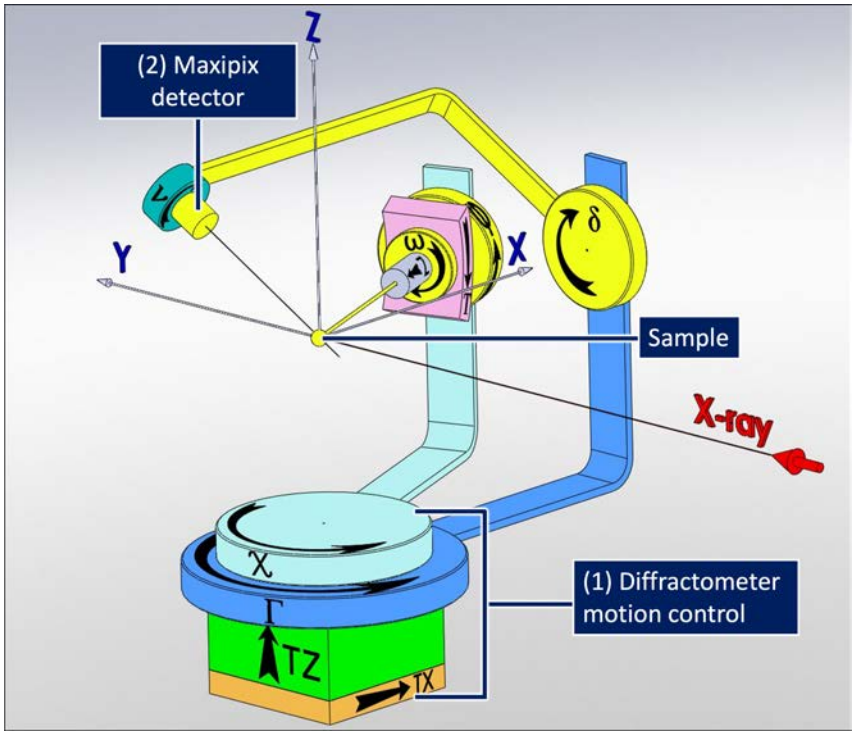

Figure 2.4.9: Illustration of XRR setup, modified from ESRF BM25 website [25].

We used XRR for calibrating the Sn deposition rate on 2D surface in ESRF BM25. The sample is placed at the sample chamber and the setup of their XRR includes: (1) diffractometer motion control system and (2) Maxipix detector. In the motion control system, χ and Γ (light and dark blue) are the angular rotations for the XRR measurements; TX and TZ (green and orange) are the translation movements for the sample alignment.

2.4.4 Transmission electronic microscopy

Transmission electron microscopy (TEM) is used to study the crystalline quality, the crystal phase, and the crystal structure. It is a microscopy technique based on an electron beam (e-beam) penetrating through an ultra thin specimen and forming high resolution images. It has high enough resolution for analyzing the structure at a nano or atomic scale. While a high energy e-beam passes through a specimen not more than 100 nm thick, the amplitude and the phase of electron waves have changed due to the absorption or the scattering. These cause the contrast of the image. There are two fundamental modes of imaging: one is conventional imaging and the other is diffraction imaging. In conventional imaging mode, an objective aperture is placed in the back focal plane of the objective aperture; in diffraction imaging mode, a selected area aperture is inserted in the image plane of the objective lens. These apertures can filter and select certain regions of the transmitted e-beam in order to obtain specific information about the sample. The conventional TEM image shows the structure of the sample as either crystalline or amorphous. Its image contrast is based on the energy lost by the e-beam after interacting with the specimen. The diffraction image shows the crystalline information for the samples, such as lattice constant, crystalline orientation, crystalline defects. It is the same principle as XRD, but the observation region is more local and limited.

The focused ion beam (FIB) is one method for preparing the lamella (specimen of TEM). It provides a precise and accurate milling region at a few nanometers thick. An energetic gallium ion beam is usually employed in the ion milling process, but the implantation of Ga needs to be considered. We used it for the cross-section observation of MoGe/InAs nanowires.

For nanowire observations other than cross section, the nanowire specimen preparation is only harvesting nanowires by sweeping a copper grid on the substrate. This is sufficient for observing the crystalline quality of semiconductor nanowires and superconductor shells, as well as semiconductor-superconductor interface. We use it for the side-view observation of the hybrid interface quality and the crystalline quality of InAs nanowires. We do not see atom but crystalline planes.

2.4.5 SEM and EDS

Scanning electron microscopy (SEM) is a common technique to observe the sample morphology from a micro to nano scale. An e-beam is injected into the sample and the scattered electrons are gathered to construct the image. There are several electron-matter interactions ongoing in the

sample, and by choosing the type of detector, we select the kind of signal to generate different contrasts in images. A classical SEM consists of an electron beam ranging from 3 – 40 keV, a backscattered electron (BSE) detector, a secondary electron (SE) detector, a CCD camera, an X-ray detector, and optical lens. BSE results from an elastic scattering which depends on the Z-value of the detected element. Therefore, it is sensitive to the elemental composition of the sample. SE results from inelastic interaction, which has a lower energy than BSE and originates from a near-surface region, so it is sensitive to the topography of the sample. By playing with these different modes, we can obtain a good contrast on the objects we're interested in from the SEM image.

There is also an X-ray detector in SEM setup for energy-dispersive X-ray spectroscopy (EDS) analysis. It is a technique used for analyzing the elemental composition and the chemical characterization of the sample [200]. We use EDS analysis for analyzing the droplets emerging on Sn thin films. The e-beam possesses enough energy to knock out an electron in the inner shell of an atom and create an electron hole. Then an electron in the outer shell bounces towards and fills up the electron hole in the inner shell, where X-ray is emitted from the energy difference between the shells. Each element has its own unique atomic structure, composing its own emission energy. Also, X-ray emission is different for electron migrating from different shells. For example, M to L emits L_α, L to K emits K_α and M to K emits K_β. The EDS spectra is recorded over all the energies lower than the incoming beam, and for the quantitative analysis only a few lines are analyzed after background subtraction. We use L_α to differentiate the element composition in our Sn films.

2.4.6 AFM

Atomic force microscopy (AFM) is a non-optical imaging technique that shows the morphology and the topography of a surface. It is an accurate, non-intrusive and non-destructive analysis to obtain 3D morphological information, such as root-mean-square (RMS) roughness, grain height, etc. AFM can be used for surface imaging in air, liquid, or vacuum. It is based on an atomic-scale tip approaching a sample surface and deflected by the height variation of the surface. A typical configuration of AFM in air contains a cantilever with its support, an atomic-scale tip mounted on the cantilever, piezoelectric elements, a laser beam reflecting the deflection of the cantilever, and a photodiode capturing the reflected laser beam. There are several scanning modes of AFM, namely tapping mode, contact mode and non-contact mode. Tapping mode is one of the most used methods and its dominated forces between tip and surface are repulsive, i.e. tips won't stick to the surface and remain intact while measuring. For imaging thin film topography, we use the standard tapping mode in air with an antimony doped Si tip with an Al-coated cantilever at the back side. The scanning range can vary from $1 \times 1\ \mu m^2$ to $30 \times 30\ \mu m^2$. The AFM software Gwyddion is used for data treatment.

2.5 Transport characterization techniques

Transport measurement is one of the approaches to measure the electrical properties of a material. We use low temperature transport measurements to study the electrical properties of Sn thin films grown on InSb substrates, Sn/InSb hybrid nanowires, and MoGe/InAs hybrid nanowires. For Sn/InSb systems, α-Sn is an insulator which is not conducting and β-Sn is a superconductor which is conducting at low temperatures. The fabrication of superconductor MoGe deposited on InAs nanowires is still developing, and the transport measurements on hybrid MoGe/InAs hybrid nanowires will be performed as perspectives.

The low temperature transport measurement can be carried out in a dilution refrigerator whose measuring temperature ranges from 4 K to as low as 2 mK. In this section, we introduce the dilution refrigerator and the nanofabrication process of nanowire devices.

2.5.1 Nanofabrication of nanowire devices

To know the electrical properties of a single nanowire, it is necessary to contact the nanowire; thus, nanowire devices are fabricated through nanofabrication. We use a 4-probes configuration (Figure 2.5.1) to get an accurate resistance value, which avoids measuring the resistance from setups. This configuration contains two probes for applying the current, and two others for measuring the voltage. The probes on one device are parallel and equadistance, ranging from 200 nm to 500 nm, to avoid unwanted resistance change from contacts.

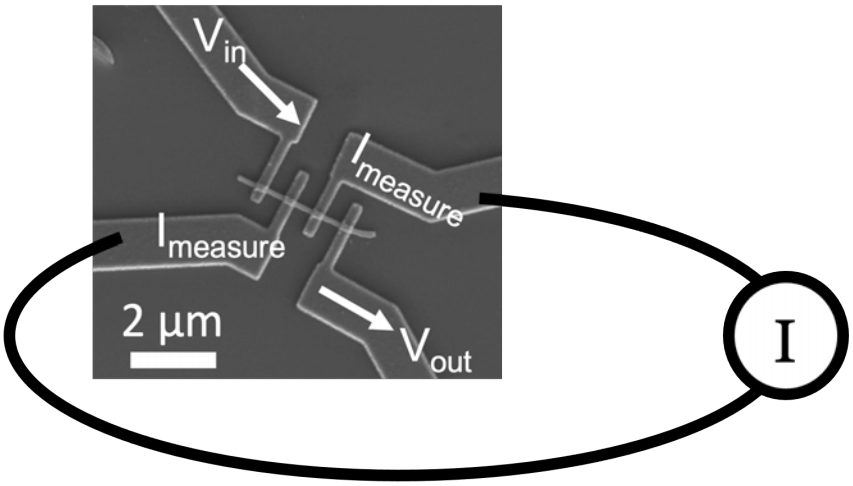

Figure 2.5.1: Plan-view SEM image of a single nanowire device with 4-probes configuration, two probes for applying voltage and the other two for measuring current.

The fabrication steps of single nanowire device are listed below:

1. Harvesting nanowire from substrate to Si/SiO_2 patterned chip by micromanipulator.
2. Imaging the position of nanowires by SEM for designing the ohmic contacts.

3. Inserting images in KLayout and designing the ohmic contacts on nanowire.

4. Depositing resist on the chip with poly(methyl methacrylate) (PMMA) 3% as first layer and then PMMA 4% as second layer by spin coater.

5. Baking each PMMA resist layer in vacuum $< 1 \times 10^{-7}$ torr for 2-3 days.

6. Exposuring the chip by e-beam lithography then developing the exposed area.

7. Depositing 50 nm-thick Ti and then 100 nm-thick Al by sputtering.

8. Lift-off in acetone then measuring the resistance of nanowire devices in prob station at room temperature.

After resistance measurement, we wirebond the functional nanowire devices to the sample holder of the dilution refrigerator with electrical conductive Al wire. Then the sample holder is loaded into a loading stick and inserted into the refrigerator. Prior to cooling down to 4 K, the air in the loading can need to be pumped out and reach a good vacuum in order to avoid the contaminations condensing on the sample.

The measurement temperature in dilution refridgerator ranges from 4 K to 50 mK. The resistance can be calculated using Ohm's law: V=IR, where I is the measured current and V is the applied voltage, which is fixed at 1 V.

2.5.2 Dilution refrigerator

A dilution refrigerator is a cryogenic device that uses an isotopes mixture of ^{3}He and ^{4}He as cooling power and can reach a cryogenic temperature below 4 K. The endothermic dilution process of ^{3}He is a powerful cooling engine, and the temperature of the mixing chamber cools down with more cycles of ^{3}He dilution process. The temperature range of the dilution refridgerator is appropriate for superconductivity measurements in our material of study, T_c = 3.7 K of bulk β-Sn. The structure of the dilution refrigerator is illustrated in Figure 2.5.2 (b). ^{3}He is circulated in a closed loop: (1) ^{3}He enters the cryostats and then gets precooled and purified in a liquid nitrogen bath at 77 K and then a ^{4}He bath at 4.2 K. (2) Then, ^{3}He gets further cooled and liquefied by another 1 K ^{4}He bath. (3) At 500 – 700 mK, the pure liquid ^{3}He enters the mixing chamber and dissolves into a superfluid ^{4}He. (4) In the mixing chamber, there are two separated phases: one is a concentrated phase with 100% liquid ^{3}He and the other is a dilute phase with < 7% of ^{3}He. (5) ^{3}He is removed from the diluted phase in a still and goes back to the pump for feeding back. The sample is sticking to the mixing chamber and reaches the thermal equivalent in the dilution refrigerator, as seen in Figure 2.5.2 (c).

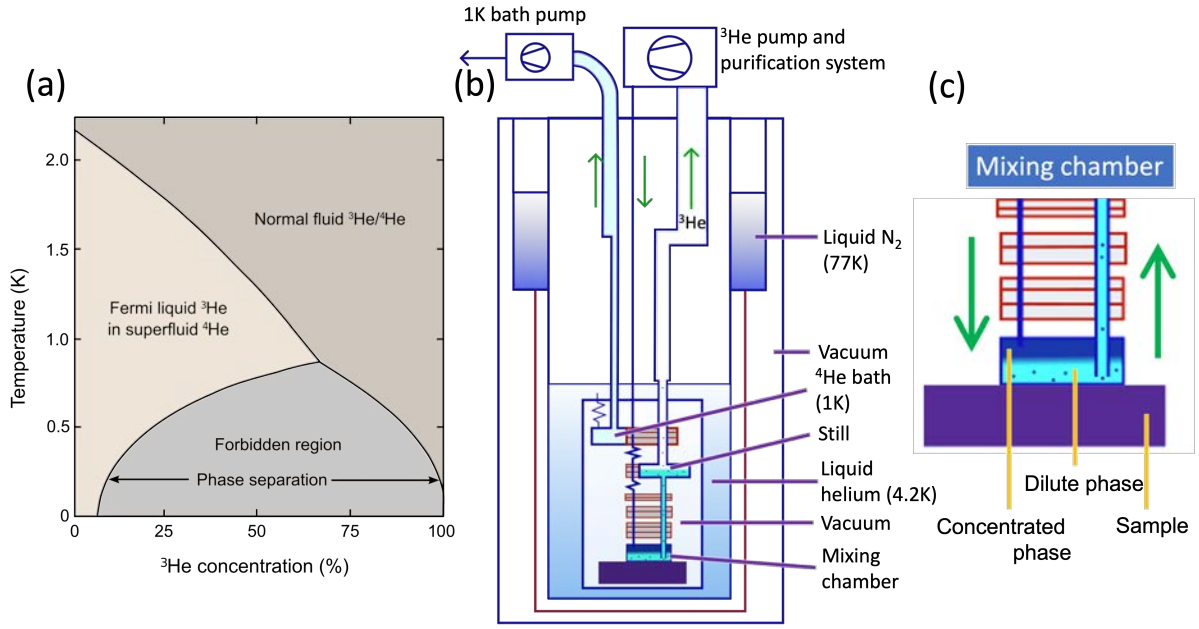

Figure 2.5.2: Concept of the dilution refrigerator based on liquid mixture of ^{3}He/^{4}He. (a) The phase diagram of ^{3}He/^{4}He [173]. (b)(c) The cooling system of whole dilution refrigerator. The schematic is inspired by [204].

2.6 DFT calculation

Density-functional theory (DFT) is a numerical method for calculating material's electronic properties which can aid the interpretation of the electronic effect at interfaces of hybrid heterostructures, for example the interface of a semiconductor and a superconductor [169]. We are interested in electronic properties and proximity effects of the lattice matched Sn/InSb system, with the electronic properties of the band structure and density of states (DOS) of particular interest. The Vienna Ab initio Simulation Package (VASP) [110] is one of the most utilized computer programs used in DFT calculation for such atomic scale material modeling. This tool is able to solve the Kohn-Sham equations in DFT calculations, using functionals such as Perdew-Burke-Ernzerhof (PBE) and Heyd-Scuseria-Ernzerhof (HSE). Additionally, VASP utilizes the projector augmented wave method (PAW) to describe the interactions between electrons and ions which gives the accuracy of calculation and avoids heavy computational cost [6].

The functionals used in this manuscript include HSE and PBE [68]. The generalized gradient approximation (GGA) of Perdew, Burke, and Ernzerhof (PBE) is a semi-local exchange-correlation functional, however it is known to miscalculate some system parameters such as underestimating band gaps. The hybrid HSE functional takes into account the exchange-correlations between electrons by containing a fraction of the exact, short-range, non-local Fock exchange, which leads to a correct physical description of spin-orbit coupling (SOC). This provides greater accuracy over PBE functionals, particularly for strong SOC semiconductor and metallic systems, but has a high computational cost. To provide a compromise, the PBE+U method was

employed which includes the extra term of a Hubbard U parameter that is added to an orbital on each atomic species that can correct the underestimated band gaps in PBE. To obtain the Hubbard U values, a machine learned Bayesian optimization approach was used which uses the HSE result as the reference [234]. The PBE+U method's computational cost is comparable to PBE and can give qualitatively correct results, so we mainly use PBE+U functional for calculations.

In order to build a correct model of Sn thin film on InSb, I start by calculating bulk InSb, bulk α-Sn, bulk β-Sn using PBE+U and HSE the reference. After establishing bulk materials, I converge the electronic properties of a slab of each material in order to mimic the thin film properties. The slab calculation is performed as a function of layer number and eventually can converge to the bulk properties with the required number of layers. To verify the slab properties, we can compare the band gap with the bulk calculation, the DOS profile (for metals), and compare the slab band structure to the bulk and also experimental results from angle-resolved photoemission spectroscopy (ARPES). ARPES is a technique that can map the electronic band structure below the Fermi level, based on measuring the emitted photoelectrons from materials [2]. Following this we can construct the interface, such as α-Sn(110)/InSb(110), to understand electronic properties of the heterostructure system.

Part I

Development of inclined hybrid InAs nanowires

The *in-situ* superconductor deposition on tilted semiconductor nanowire networks is an optimal method to create advanced quantum devices, such as gate-tunable superconductor-normal metal-superconductor (SNS) junctions. The development of those junctions is critically dependent on the quality of the interfaces formed at the junctions. The hybrid interfaces created *in-situ* are of better quality: lower contamination and disorder have been observed [118, 170]. The surface of semiconductors, in particular, oxidizes rapidly in the ambient environment. However, it becomes delicate when native oxides are removed by chemical etching or when a metal shell is selectively removed from top of it. SNS junctions based on nanowires have been fabricated entirely *in-situ* [118, 24, 171]. It involves the fabrication of nanowire networks, in which two adjacent nanowires cross, the front one shadowing the back one. During superconductor deposition, a superconductor-free segment is formed along the nanowire situated behind. The crossed nanowires are fabricated via the growth of tilted nanowires on (001) substrates. They can also be prepared following the controlled kinking of nanowires on (111)B substrates.

During my thesis, I first developed inclined InAs nanowires on InAs(001) substrates (Chapter 3). Then I studied the deposition of various superconductors (Chapter 4). My first objective was to control the morphology of the InAs nanowires grown on the InAs(001) substrate. For the device integration, the properties of the nanowires have to fulfill the following requirements: (1) proper dimensions in terms of long length for easy contact and large diameter for better conductance; (2) homogeneity in diameter over length for constant conductivity; and (3) high crystalline quality for a better conductivity. For example, the nanowire should be at least 3 μm in length, 50 nm in diameter with pure wurtzite crystalline structure for high electron mobility up to 3000 cm^2/Vs [213]. Then, my second objective was to study the deposition of several superconductors on the InAs nanowires both in the reactors of Institut Néel and in the cluster of C. Palmstrøm at UCSB. I evaluated the quality of the superconductor thin films in terms of thickness uniformity, crystalline structure, composition, and interface abruptness. These studies are a prerequisite for further device fabrication and electronic transport characterization of the interfaces and junctions.

CHAPTER 3

Growth of inclined InAs nanowires

In this chapter, I studied how each growth parameter affect inclined InAs nanowires grown on InAs(001) substrates. I optimized those parameters to achieve InAs nanowires with the desired length, diameter and density. In this regard, the chapter is organized as follow: after presenting the state-of-the-art, I outline how I prepared the samples to prevent contamination and achieve reproducible nanowires. Then, I explain the experimental steps involved in the nanowire growth. Then, I discuss the impact of the annealing temperature, an unexpected but crucial parameter. It's followed by a study of the growth temperature and V/III beam equivalent pressure (BEP) ratio, which impact the nanowires dimensions and length distribution. I finally study the initial growth stage on InAs(001) to better understand the nucleation and growth mechanism of inclined nanowires.

The TEM analysis was done by M. Hocevar. The EDS-TEM analysis was done by S. Tan at the University of Pittsburgh.

3.1 State-of-the-art

InAs nanowires grow via different techniques such as metal organic vapor phase epitaxy (MOVPE), chemical beam epitaxy (CBE), or molecular beam epitaxy (MBE). During my thesis, I used the VLS assisted by a metallic catalyst to grow InAs nanowires in a MBE reactor [94, 207, 58, 106]. A detailed description of the VLS mechanism can be found in Section 2.1.

According to the Wulff theory, a crystal favors certain crystalline planes to minimize its surface energy at a fixed volume. The 111 planes in III-V and group IV semiconductors have the lowest surface energy, so 111 planes form preferably during growth [239, 145]. This is the reason why nanowires grow along the [111] direction. Accordingly, the use of substrates having different orientations than the [111] results in nanowires oriented differently than normal to the surface. For example, InAs nanowires grow normal to the surface on a (111)B substrate.

As the (001) and (111)B planes are at 35.3° in the ZB crystalline phase, the nanowires grow with the same inclination on InAs(001) substrates. Therefore, InAs(111) nanowires grow tilted on InAs(001) substrates. This feature has been used for already 8 years to fabricate nanowire networks dedicated to superconductor junction devices [168, 40].

The growth conditions for InAs nanowires grown on InAs(111)B have been largely reported [115, 16, 126, 94, 64]. Yet, the parameters required to grow InAs nanowires on InAs(001) are not well known. For example, it is not clear what are the parameters influencing the nucleation of the nanowires on (001). Also, due to their inclination, all the facets of the nanowires are not exposed equally to the incoming beams of precursors, which may affect the growth conditions and therefore the morphology of the nanowires.

In 2020, H. Zeng et al. reported that GaAs nanowires grow obliquely on Si(001), which follows the lowest surface free energy [239]. Au-catalyzed inclined germanium nanowires were grown on Ge(001) to study the growth kinetic of merging nanowires [222]. In 2014, D. Car et al. developed single crystalline nanowire junctions by merging two tilted InSb nanowires grown on InP(001), showing the great control of the Au droplet positioning for engineering complex nanowire-based structures [39].

In 2018, Kang et al. reported that InAs nanowires grow tilted on InAs(001) substrates via the formation of faceted craters [113]. The growth processus is divided in two stages: firstly, Au nanoparticles assist in nucleating craters with large {111}B facets. Then, Au nanoparticles residing on the {111}B facets of the craters are in the optimal conditions to initiate growth of InAs nanowires. In 2020, inclined InAs nanowire networks were used as an *in situ* superconductor deposition platform for SNS junctions [118]. The predefined Au droplet positions by electron beam lithography on trenched InAs(001) substrates result in highly reproducible crossed nanowires. A smaller distance between nanowires leads to sharper junctions. Besides, kinked nanowires grown on (111)B substrates have been proposed for networks of crossed nanowires. Yet, the formation of defects at the position of the kink and the change in crystalline structure into cubic along the kinked segment make the fabrication of the crossed nanowires more challenging [124].

3.2 Sample preparation

I grow my nanowires from gold particles deposited on a substrates via drop casting of a colloidal solution. It is necessary to prepare an oxide-free InAs substrate prior to the deposition of the particles. A 50% solution of NH_4OH removes efficiently the native oxides of InAs [119]. Gold nanoparticles of different diameters (BBI solution) are then dispersed on the clean substrate. I use particles with diameters ranging from 20 to 60 nm. The density of the particles was evaluated by SEM : I find that the initial density of the nanoparticles on the InAs substrate decreases from 27 μm^{-2} to 0.3 μm^{-2} for diameters increasing from 20 to 60 nm. The initial density of Au colloids is listed in Table 3.2.1. This sample preparation provides reliable and

reproducible results for InAs nanowire growth and was used on all substrate orientations. The expected diameter of nanowires is the diameter of a gold hemisphere, whose volume is equal to the initial Au droplet plus an additional volume of 30% [60] due to the incorporation of In: $(1 + 30\%) \times (\frac{4}{3}\pi R^3) = 0.5 \times (\frac{4}{3}\pi R'^3)$, $R' = 1.38R$, where R is the radius of Au droplets, and R' is the radius of In-Au hemisphere. The expected diameter 2R' of all sizes of Au colloids can be found in Table 3.2.1.

Experimental protocol

1. Cleave a 2" InAs wafer (one side polished) into 1 cm $\times$ 1 cm pieces.
2. **[Chemical deoxidation]** Dip pieces into $NH_4OH : H_2O = 1 : 1$ solution for 10 minutes.
3. Rinse with DI water for 5 minutes and blow-dry by N_2 gun.
4. **[Seeding Au nanoparticles]** Fully cover the polished side of the piece with Au colloids solution of different diameters for 5 minutes in air.
5. Remove the colloids solution by blow-drying with an N_2 gun.
6. Glue seeded pieces onto the Si-wafer with pure indium balls on a heat plate (265 °C). The 30 nm Au seeded sample is always fixed in the center of the wafer.
7. Place the Si-wafer on an indium-free molyblock and insert it into the MBE intro chamber. The time between the chemical deoxidation and the insertion into an ultra-high vacuum (UHV) chamber is around 15 to 30 minutes.
8. Transfer and place the sample on the oven in the degassing chamber.
9. **[Degassing]** Degas the sample at 250 °C for at least 30 minutes to reach a base pressure of 10^{-9} torr.
10. Transfer the degassed sample to the growth chamber to proceed with nanowire growth.

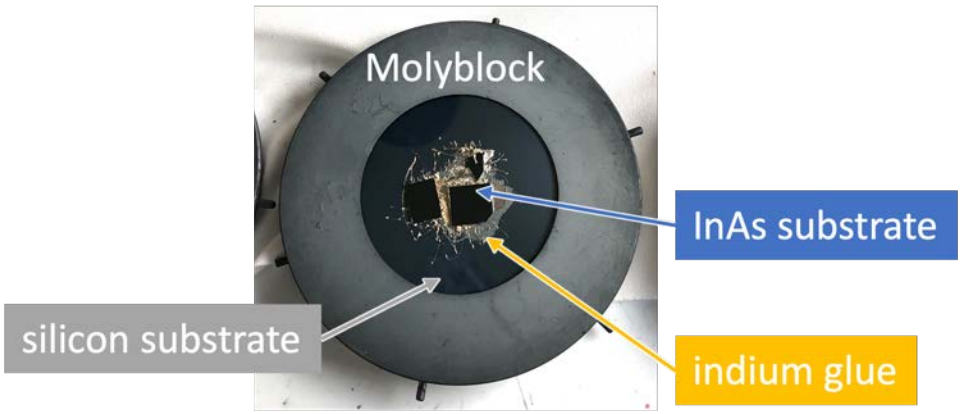

Figure 3.2.1: Sample preparation before insertion into the MBE intro chamber.

Au nanoparticles size (nm)	20	30	50	60
Deposited density (μm^{-2})	27 ± 4	1.9 ± 0.3	0.9 ± 0.3	0.3 ± 0.1
Expected diameter of nanowires (nm)	27.5	41.3	68.8	82.5

Table 3.2.1: Density of Au nanoparticles on InAs substrates following our procedure.

3.3 Temperature calibration

It is known that the real substrate temperature is crucial for semiconductor growth, but challenging in MBE. The filament is positioned at the back of the sample holder, often without touching it, while the substrate is glued on the front side of the sample holder. Therefore, the temperature difference between the filament and the substrate is hard to estimate. Indeed, the temperature gap depends on the morphology of the molybdenum sample holder (molyblock) in terms of thickness, plain or indium free, the distance between the thermocouple, and the back surface of the molyblock. Luckily, there exists phase diagrams describing the surface reconstruction of InAs(001) with respect to the As flux and the temperature [31]. The transition between the two reconstructions is related to the rearrangement of atoms at the surface and is visible using RHEED.

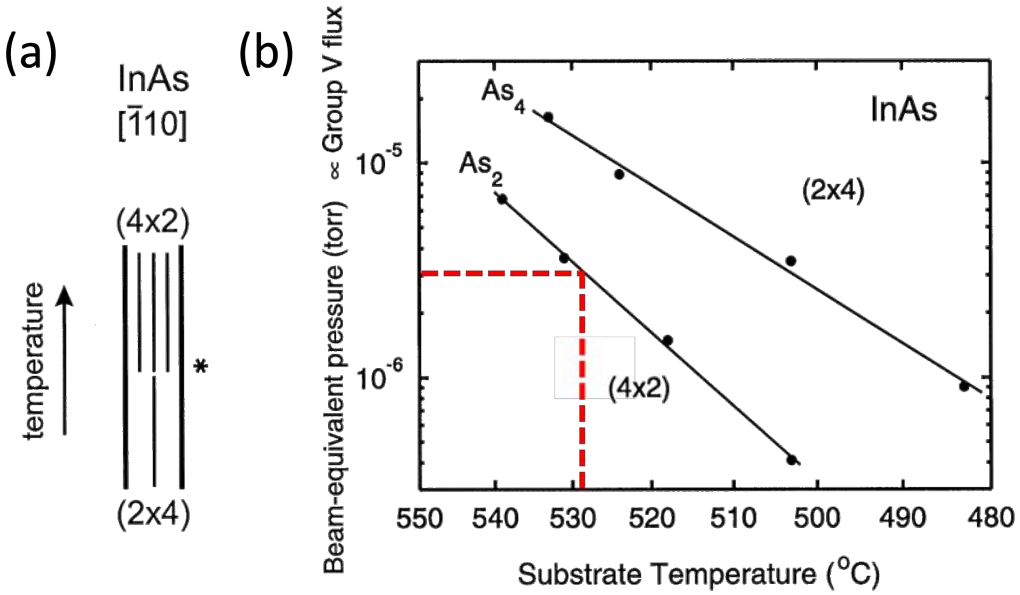

Figure 3.3.1: Temperature and flux dependent surface reconstruction observed by RHEED, modified from [31]. (a) (2×4) surface reconstruction at low temperature and (4×2) at high temperature. (b) Phase diagram of surface reconstruction as function of substrate temperature and As BEP. The red dashed lines indicate the As_2 pressure used during our temperature calibration.

Figure 3.3.1 (a) shows the evolution of the transition revealed via the RHEED pattern along the $[\bar{1}10]$ direction, as function of the temperature and the arsenic pressure [31]. In Figure 3.3.1 (b), both solid lines correspond to $[(2 \times 4) \leftrightarrow (4 \times 2)]$ reconstruction transitions when the surface is exposed to As_2 or As_4 respectively. This transition corresponds to the surface reconstructing from an As-rich to an In-rich region. We see that with increasing substrate temperature, the transition happens at higher arsenic pressure. Hence, I use the transition temperature at this fixed beam equivalent pressure (BEP) as a reference to calibrate the temperature read on the thermocouple.

In our MBE system, I evaluated the temperature transition between the (4×2) and (2×4) reconstructions during cooling down under a constant As_2 flux of 3.0×10^{-6} torr. Figure 3.3.2 shows the evolution of our RHEED patterns below the transition (520 °C) and above the transition (550 °C). All our molyblocks show the same transition temperature at around 540 °C, which gives a temperature difference between the thermocouple and the sample ΔT of 10 °C. In this chapter, I use the value read on the thermocouple when referring to the temperature.

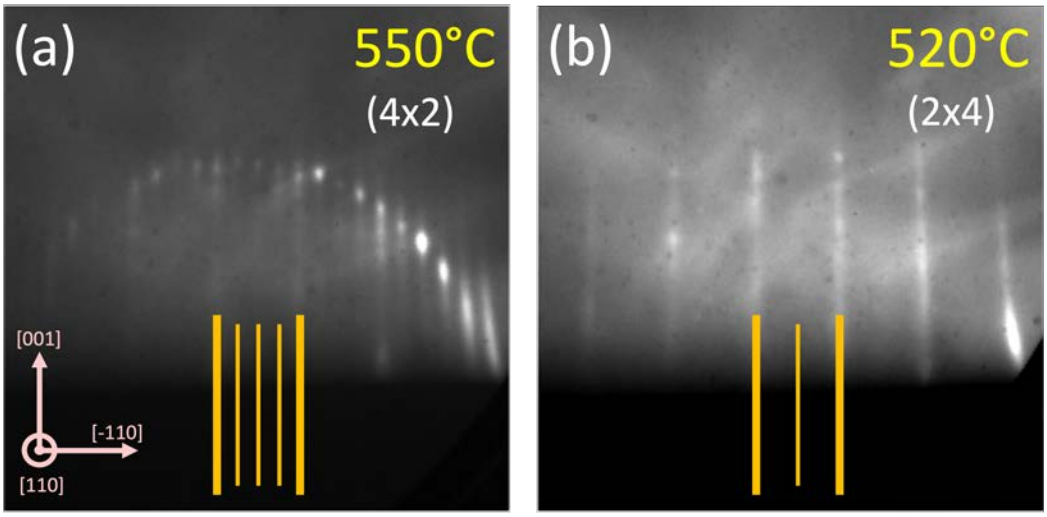

Figure 3.3.2: Surface reconstruction of the InAs(001) surface observed by RHEED along the [$\bar{1}$10] axis. (a) (4 × 2) high temperature pattern (550 °C) and (b) (2 × 4) low temperature pattern (520 °C). The orange vertical lines indicate the diffraction pattern: (4 × 2) and (2 × 4).

3.4 Optimization of the nanowires growth parameters on InAs(001)

Here I study the role of each growth parameter on the morphology of our InAs nanowires on InAs(001). I focus on the following parameters: the annealing temperature (T_a), the growth temperature (T_g), the V/III BEP ratio, and the growth time. A temperature-time profile, as seen in Figure 3.4.1, shows each growth step once a sample is loaded into the MBE growth chamber. It is first heated from room temperature to T_a. The primary purpose of the annealing step is the alloying of the gold catalyst with indium (In) originating from the substrate. During the heating of the sample, the As flux is introduced into the reactor as soon as the substrate temperature reaches 450 °C. This is done to prevent sublimation of As from the surface of the substrate, which roughens the surface. After the annealing step, the substrate temperature decreases to T_g and the As flux is adjusted to the desired value. After 5 minutes of T_g, open the In cell shutter to start InAs nanowire growth. I close the In shutter after a certain growth time. Finally, the substrate temperature decreases under As to 300 °C before removing the substrate from the growth chamber. The manipulator rotation is applied since the annealing step till the end of experiment for the flux homogeneity on the sample surface.

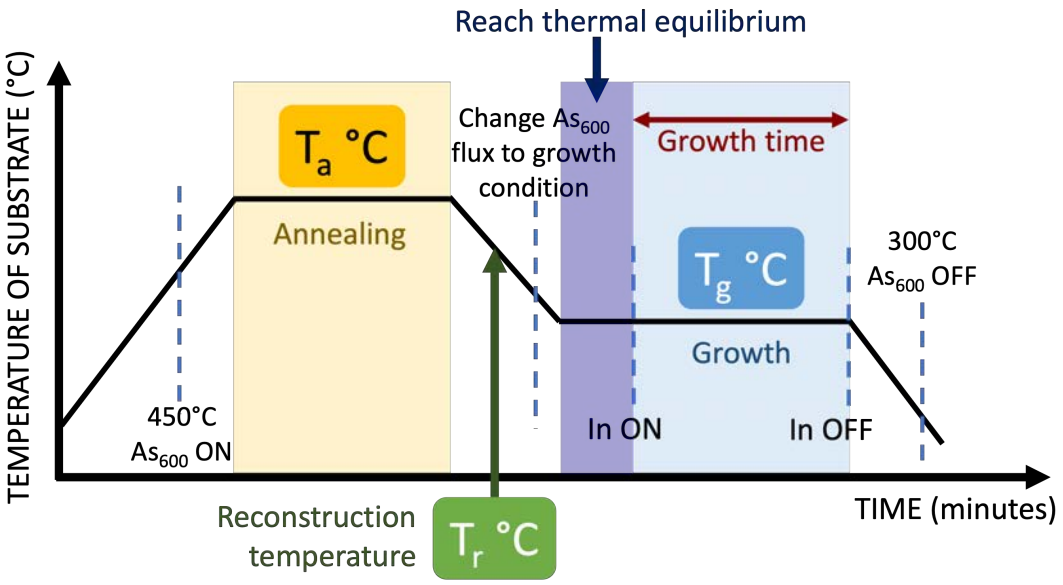

Figure 3.4.1: Schematic of the different steps used for the growth of our InAs nanowires. T_a is the annealing temperature. T_g is the growth temperature. T_r is the transition temperature of the surface reconstruction. "As_{600}" stands for the cracker temperature 600 °C of the As cell.

3.4.1 Annealing temperature

For this study, I used catalysts with diameters ranging from 20 to 60 nm. Before starting nanowire growth, InAs(001) substrates were annealed at T_a for 1 min under an As flux of 1.0×10^{-5} torr. I study T_a between 420 and 560 °C (see Table 3.4.1). After the annealing step, the sample temperature decreased to T_g = 420 °C. After a stabilization step of 5 minutes, the In shutter was opened and InAs nanowires grew for 40 minutes with a beam equivalent pressure V/III BEP ratio of 30. The In flux was 2.5×10^{-6} torr, which gave the growth rate 0.45 ML/sec (see the growth rate versus the In flux in Figure 2.2.4). The different samples were then imaged by SEM in plan view and side view to determine the density and dimensions of the nanowires as well as to characterize the sample surface. For clarity, I chose to present the influence of T_a:

- on the nanowire dimensions
- on the surface morphology for catalyst 30 nm
- on the nanowire density

Sample	T_a (°C)	T_g (°C)	**Growth time (minute)**	**V/III BEP ratio**	**Catalyst diameter (nm)**
NW871	420	420	40	30	20, 30, 50, 60
NW870	460	420	40	30	20, 30, 50, 60
NW869	480	420	40	30	20, 30, 50, 60
NW868	500	420	40	30	30, 50, 60
NW867	560	420	40	30	20, 30, 50, 60
NW893	560	420	1	30	20, 30, 50
NW894	500	420	1	30	20, 30, 50
NW895	480	420	1	30	20, 30, 50
NW896	460	420	1	30	20, 30, 50
NW897	420	420	1	30	20, 30, 50

Table 3.4.1: List of samples fabricated for the T_a study.

On the nanowire dimensions

First of all, we observe nanowires on all samples, regardless of T_a (Figure 3.4.2). In addition, all sample surfaces feature hexagonal craters (see insets). When looking closely at the sample surface, I observe the presence of nanoparticles in addition to the craters and nanowires. The main difference between samples lies in the nanowire, crater, and nanoparticle density. Finally, we observe that the nanowires are oriented in plan along $[\bar{1}10]$ directions.

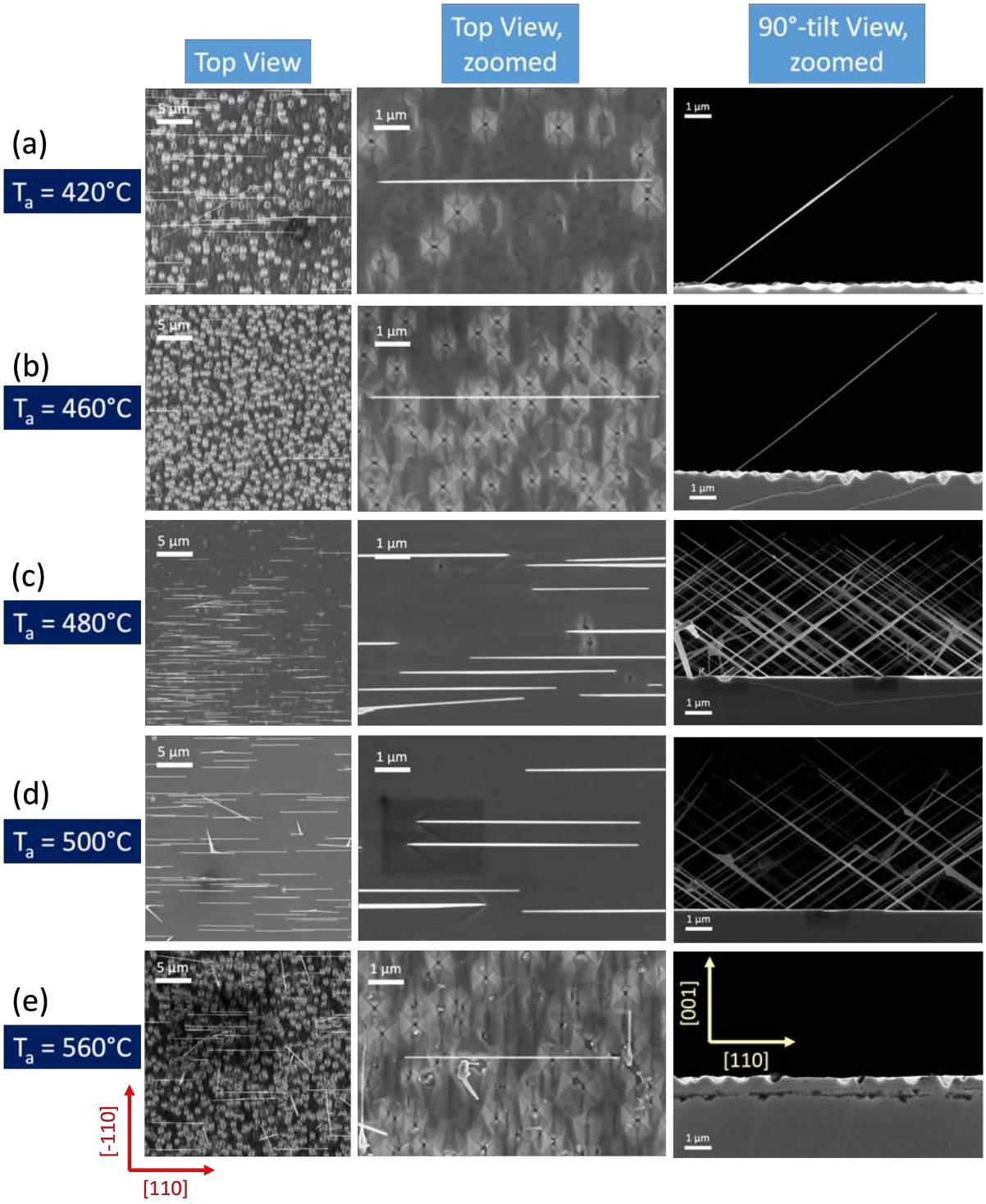

Figure 3.4.2: Plan-view SEM images of InAs nanowire grown on InAs(001) after different substrate T_a: (a)(c)(e)(g)(i) overviews of nanowire ensembles; (b)(d)(f)(h)(j) zoomed view in nanowires.

Next, I evaluate how the morphology of the InAs nanowires is affected by the annealing temperature. We measure the length and diameter of at least 10 nanowires for each sample out of plan-view SEM images. As nanowires grow in the ⟨111⟩B direction and that they form an angle of 35.26° with the surface of the substrate, the measured length from plan-view images

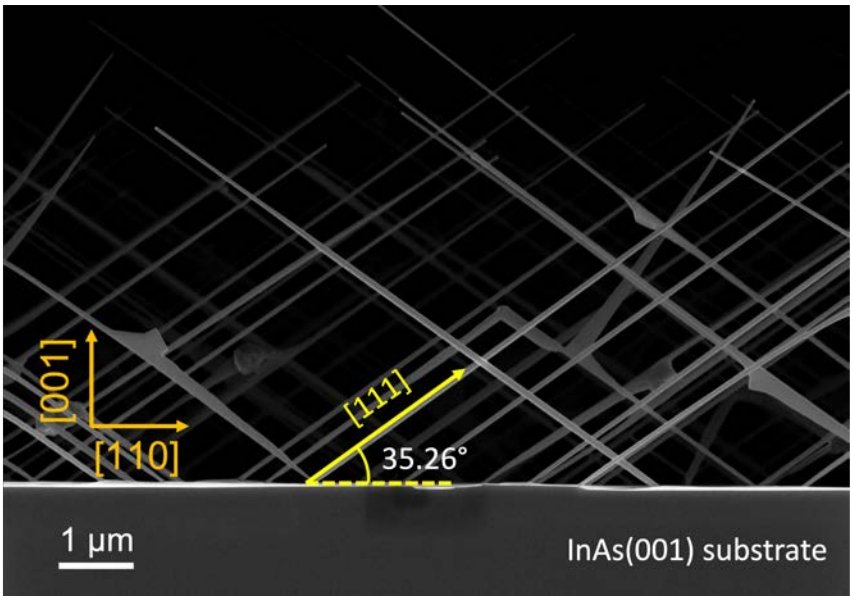

Figure 3.4.3: Side-view SEM image of inclined InAs nanowires grown on an InAs(001) substrate. The orientations are indicated.

is a projection of the nanowire length. This is confirmed by the side-view SEM, as seen in Figure 3.4.3. The real length is calculated using the following equation:

$$\text{Real length} = \frac{\text{Measured length}}{\cos(35.26°)} \tag{3.1}$$

Figure 3.4.4 shows the distribution of the InAs nanowires' diameter versus length for various T_a. First of all, we observed that all the nanowires have a larger diameter than expected by our calculations (see Table 3.2.1 in the sample preparation). We observed a dispersion in length for all T_a. The spread is minimal for growth performed after T_a = 500 °C. Above T_a = 500 °C, the dispersion in length is large for nanowires grown from 50 nm-diameter colloids. Their length ranges from 0.5 μm to 6 μm. In contrast, below 500 °C, the dispersion in length increases with decreasing temperature. While it is only of 2 – 4 μm for nanowires grown from 50 nm diameter colloids at 480 °C, it increases up to 2 to 10 μm at 420 °C.

Similarly, nanowires grown from 30 nm diameter colloids show an increase in the length dispersion with decreasing annealing temperatures. The minimum dispersion for nanowires grown from 30 nm diameter colloids is of 6 – 10 μm at 500 °C. We suspect that the nanowires dispersion in size is linked to the morphology of the InAs substrate surface. We study therefore carefully (1) the origin of the craters, (2) their density and size distribution, and (3) compare them to the nanowires density and size distribution at different T_a.

I would like to understand if the craters appear during annealing at T_a or if they form during the nanowire growth at T_g. I thus study the morphology of the samples shortly after growth started for different T_a.

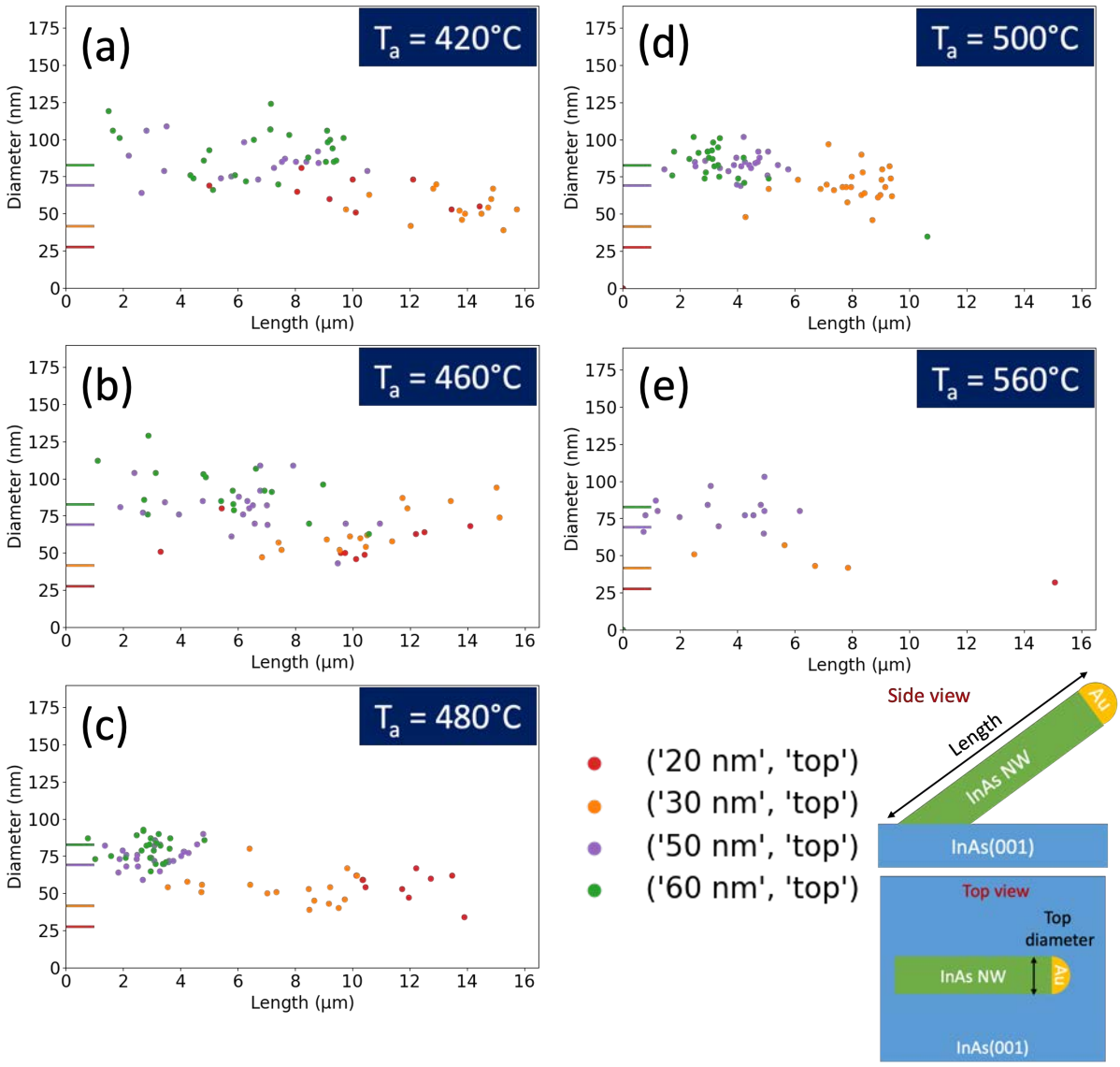

Figure 3.4.4: Distribution of the nanowires dimensions for samples grown after different annealing temperatures T_a. (a)-(e) Plot of nanowire diameter versus length. 'top' refers to the nanowire diameter at its tip. Schematics of the nanowire length and diameter extracted from SEM images. The number of data points depends unfortunately on the nanowire density. The expected diameter of each size of Au particles are indicated by colors on the y-axis.

I investigate the morphology of the samples at the initial growth stage for different T_a. Figure 3.4.5 shows the plan-view and side-view SEM images of samples after 1 minute growth for each T_a. First of all, there are no craters on the samples surface after 1 min growth at T_g = 420 °C for any of the studied T_a. Nevertheless, we observe interesting features on those samples and they are detailed below.

For T_a > 500 °C, we observe that after 1 min growth, droplets did not supersaturate: only few of them catalyzed into nanowires. This is also confirmed by the absence of a collecting area surrounding the droplets. Depleted regions are sometimes visible around droplets. Moreover, the surface is flat showing an incomplete but continuous thin film.

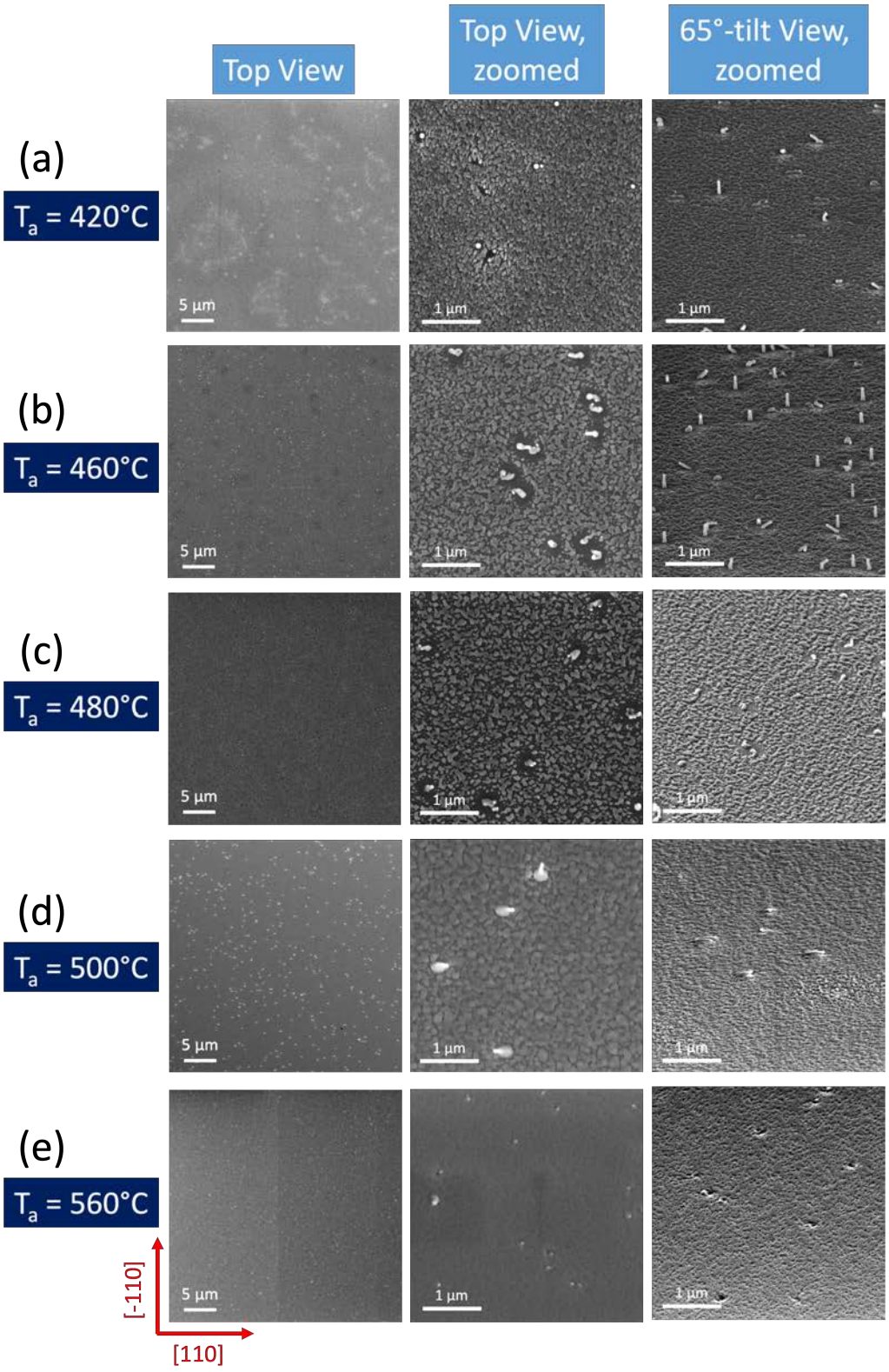

Figure 3.4.5: Plan-view and 65°-tilt-view SEM images of InAs nanowires after 1 minute growth for each T_a. The white bright spots in images correspond to Au-In alloy droplets. Growth parameters are listed in Table 3.4.1.

For $T_a \leq 500\,°C$, after 1 min growth the surface is granular: a discontinuous film has grown. The droplets catalyzed nanowires by direct impingement and adatoms surface diffusion (diffusion length measured of about 200 nm at $T_g = 420\,°C$). For the lowest T_a, we observe different types of nanowires ((001), (111) kinked, worms-like), while towards higher T_a, most nanowires grow tilted in the (111) crystalline direction from an elongated tail oriented along the (110) direction on the surface. Interestingly, most nanowires grown after $T_a = 460\,°C$ grow out-of-plane in the (001) crystalline direction.

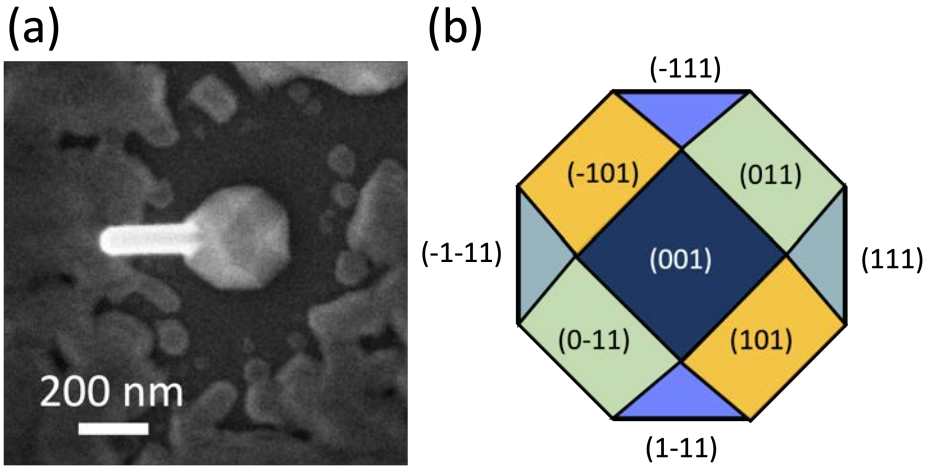

Figure 3.4.6: Faceted mound is formed after 5 minutes growth time with 50 nm Au droplet. (a) Zoomed plan-view SEM. (b) Schematic of the facets of pyramid with corresponding crystalline planes label.

Figure 3.4.6 shows the facets analysis of pyramid identified by geometrical coordination. We see that InAs nanowires grow from a equivalent (111)B facet, $(\bar{1}\,\bar{1}1)$.

There is already a large discrepancy in the samples after 1 min growth: in particular, the most homogeneous behavior for the droplets is after $T_a = 500\,°C$, as they seem to all procedure in-plane features along the same crystalline direction. In contrast, at low T_a, a large zoology of features is present at high T_a, the nanowire growth hasn't started yet.

We conclude from this set of samples that craters did not form during annealing but that they appear later during nanowire growth. In the next part, we investigate the dimension and density of the hexagonal craters to further understand why they appear.

On the surface morphology for catalyst 30 nm

As mentioned earlier, we observe that hexagonal craters appeared after 40 minutes on almost all surfaces for all T_a (Figure 3.4.2).

Figure 3.4.7 (a)-(e) shows the evolution of the craters size versus T_a. All craters have the same shape and orientation. Some of them feature a nanoscale object at their center. In ref [232], craters form around defects or contamination present on the surface. In our study, we find

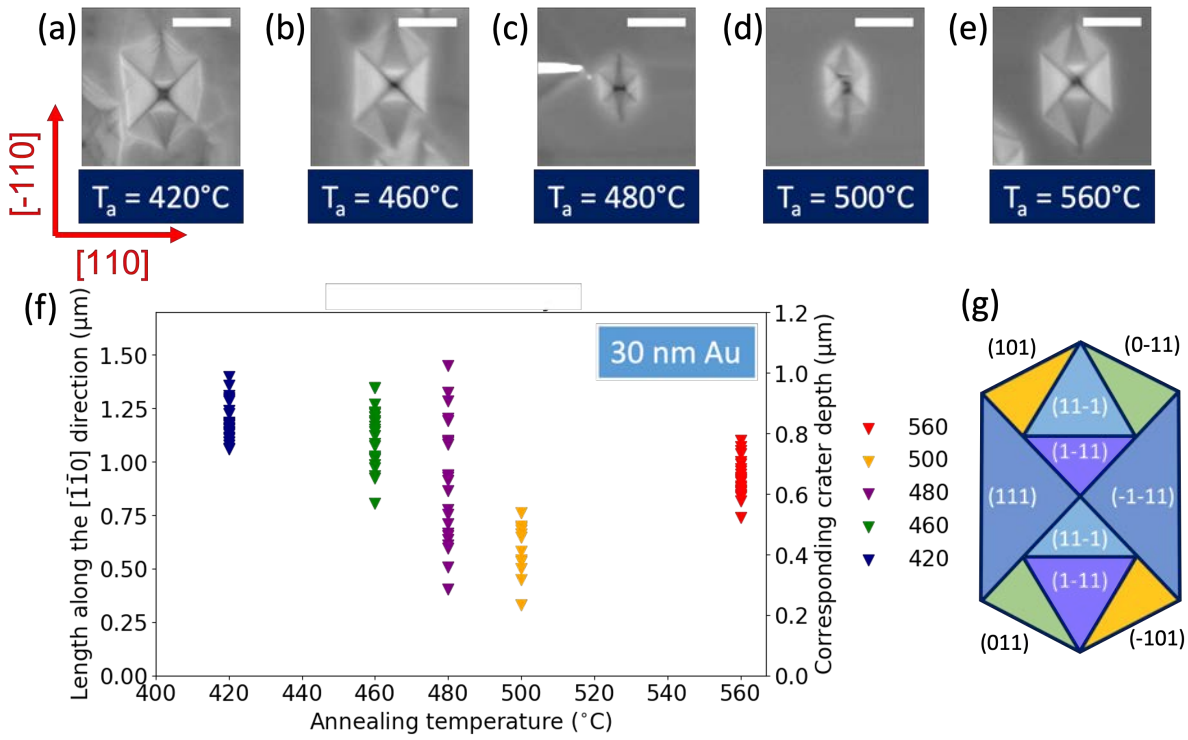

Figure 3.4.7: Evolution of the craters dimension with T_a. (a)-(e) Plan-view SEM images of single craters for samples grown after different T_a. The scale bar is 500 nm. (f) Plot of the crater length along $[\bar{1}\,\bar{1}0]$ as function of T_a. (g) Schematic of the facets forming the crater (adapted from Ref.[113]).

that the craters nucleate around short/defective nanowires. The shape of the craters have be explained by anisotropic surface diffusion of In on (001) InAs surfaces [113]. In adatoms have larger diffusion coefficient along $[\bar{1}10]$ direction than [110] on a (2×4) reconstructed surface [185]. On the surface, the low potential channels extending along the $[\bar{1}00]$ direction favors the In adatom diffusion.

Next, we see that the size of the craters after 40 minutes growth depends on the initial annealing temperatures T_a (Figure 3.4.7 (f)). The optimal temperature at which the craters size is minimum is around 480 – 500 °C. Bigger craters have more defined facets than smaller ones. We can determine the different facets of the craters, which are very similar to the oval defects observed in GaAs(001) [205] and InAs(001) [232, 113]. A well defined crater consists of two (111)B facets, (111) and $(\bar{1}\bar{1}0)$, where the nanowires may grow. Given our observations, it is very rare that nanowires grow from the (111)B facets forming the craters. We are doing more experiments for T_a = 520 and 520 °C to complete the data set.

We then study the evolution of the crater dimension with T_a. Figure 3.4.7 (g) is a schematic of the crystalline planes forming the facets of the crater. For that, we plot the $[\bar{1}\bar{1}0]$ length versus T_a (Figure 3.4.7 (f)). For T_a < 500 °C, the length decreases from 1.2 μm at 420 °C to 0.6 μm at 500 °C. While T_a > 500 °C, the length increases again up to 0.9 μm at T_a = 560 °C. The craters are perfectly faceted.

Conclusion for presence of craters As the crater is fully faceted, there is a geometrical relation between the length and the depth of each crater (see SupplementaryA.2.5). If we assume that the depth of the craters corresponds to the substrate surface prior to growth, we can then calculate the corresponding thickness of the 2D layer. We find that the deepest craters are around 1 μm. Despite careful analysis by cross section SEM, it has been difficult to verify this hypothesis. In conclusion, we may perform more analysis on the craters depth and the thickness of the 2D thin film using alternative techniques such as cross section TEM for example.

The presence of craters can be the nucleation from defects, which can be AsO_x, straight nanowires, or In clusters [232, 123]. In the next paragraph, we analyze the density of nanowires, craters and droplets versus T_a.

On the nanowire density

Finally, we analyzed the density of the different elements present at the surface of the samples: craters, nanowires, and nanoparticles. We observed that the samples lack homogeneity, which is probably due to ageing of the colloids solution. We therefore developed the following methodology to determine the density of the different features. We calculate the density of nanowires, particles, and craters on different images taken for a same sample. Each data point corresponds to the density of one element calculated after its counting on one SEM image larger than $3 \times 3\ \mu m^2$. The total area studied for each sample exceeds $600\ \mu m^2$.

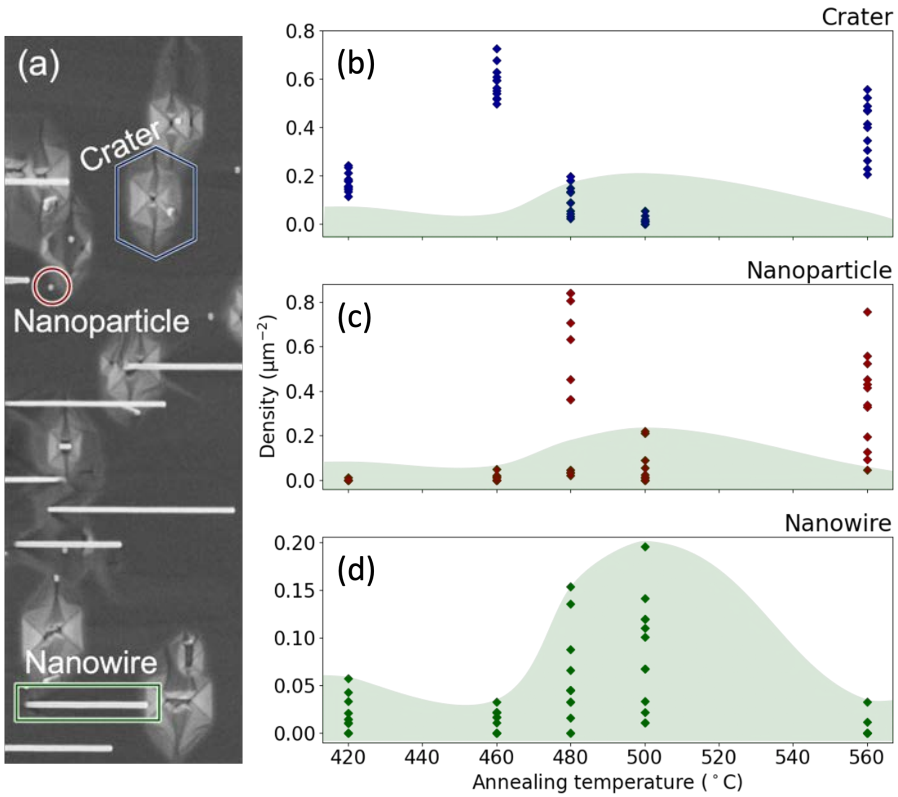

Figure 3.4.8: Analysis of the density of different features present on the sample (craters, nanoparticles, and nanowires) for different T_a (gold droplets 30 nm). On (a), a crater, a nanoparticle and a nanowire are highlighted in blue, red, and green, respectively. The initial density of catalyst particles is 1.9 μm^2. One data point of each item represents the density of one SEM image > 10 μm^2. Density of nanowire is indicated as green shadow in crater and nanoparticle plots. The deoxidation temperature of InAs(001) around 540 °C is indicated as red shadow. See the Supplementary for the complete study of the influence of T_a on the nanowire density.

Figure 3.4.8 (b)-(d) shows the evolution of the density of craters, nanoparticles, and nanowires with T_a. We see that the minimal density of craters at T_a = 500 °C corresponds to the maximal density of nanowires. We analyze separately two regions, below and above T_a = 500 °C (temperature of deoxidation of InAs). The maximal density of craters appears at T_a = 460 °C, of nanoparticles at T_a = 480 °C and of nanowires at T_a = 500 °C. Above T_a = 540 °C, density of craters and nanoparticles is high while nanowires is low. We observe the InAs nanowires density is maximum (0.2 μm^2) at the T_a for which craters' density is the minimum (0.02 μm^2). The maximum densities of craters and nanoparticles are $\sim$ 0.8 μm^2 while the maximum density of nanowires is only 0.2 μm^2. The values of density can be found in Table A.2.3.

Discussion of annealing temperature We observed that the dispersion in size of the nanowires is related to T_a. Yet, because nanowire growth takes place after annealing, T_a influence is indirect. T_a affects both the chemistry of the surface and the catalyst. We therefore need to understand first the effect of T_a on the surface and on the droplet composition. Then, the influ-

ence of those two parameters on the morphology of the samples (nanowire and surface) can be clarified.

We know from literature that InAs oxides desorb above 500 °C under As flux. We thus face two situations, $T_a > T_{deox}$ and $T_a < T_{deox}$. For $T_a > T_{deox}$, the surface prepared prior to growth is an As-rich surface with (2×4) reconstruction. It is also expected to be flat [192]. No crater formed after 1 min growth. Yet, scanning transmission microscope experiments showed that In clusters form when deoxidation temperature is too high [57, 232]. Concerning the catalyst, it is undoubtedly rich in indium (see phase diagram of Au-In and TEM-EDS analysis of Au-In droplet in Supplementary A.1).

In contrast, at $T_a < T_{deox}$, the surface is covered with a thin oxide (see dots on the RHEED). The higher T_a approaches 500 °C, the more As-oxide is removed, leaving behind In-oxide films. In parallel, after 1 minute growth we observe short InAs(001) nanowires.

For both cases, $T_a < T_{deox}$ and $T_a > T_{deox}$, the InAs surface presents defects after T_a: InAs(001) nanowires, AsO_x patches [192] and In droplets [57], respectively. Those lead to the formation of craters during nanowire growth. Craters are responsible for an overall increase in the surface roughness. Such roughness reduces In adatoms mobility on the surface of the substrate and to an increase in size dispersion. Nanowire density decreases because nanowires are partly covered (low T_a) or did not grow (high T_a).

In conclusion, I found that annealing the samples at 500 °C prior to growth leads to the smoothest surface, with a reduced dimensions and density of craters, to the largest nanowire density and lowest dispersion in size. In the following paragraphs, the annealing step will thus take place at 500 °C during 1 minute. I next study the influence of the growth temperature, the V/III BEP ratio, and the growth time on the inclined nanowires dimensions and density.

3.4.2 Growth temperature

I study the role of the growth temperature T_g between 380 °C and 440 °C on the InAs nanowire dimensions and density. The nanowire samples used for the T_g study are listed in Table 3.4.2. It includes the value of the V/III BEP ratio, the growth time and the colloids size.

Sample	T_a (°C)	T_g (°C)	**Growth time (min)**	**V/III BEP ratio**	**Catalyst diameter (nm)**
NW892	500	380	20	15	30, 50
NW889	500	400	20	15	30, 50
NW879	500	420	20	15	20, 30, 50
NW890	500	440	20	15	30, 50

Table 3.4.2: Sample list for the T_g study.

Figure 3.4.9 shows plan-view SEM images of nanowire growth at different T_g. All the surfaces emerge non-tapered nanowires. Craters and nanoparticles are visible on the images.

We observe that the surface of the samples is optimal at T_g = 420 °C: it is corrugated but no craters are visible. In contrast, craters are present below 420 °C, while above 420 °C the corrugated surface shows breaks.

I next analyze the influence of T_g on the nanowires dimensions. For that, I measure length, top diameter, and bottom diameter for each single nanowire. More than 15 nanowires are measured for each sample.

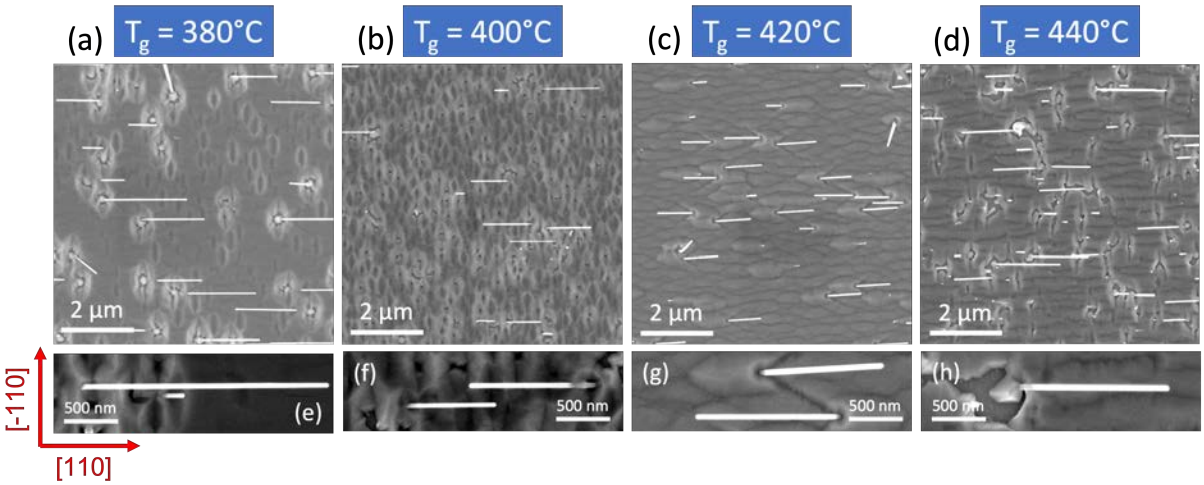

Figure 3.4.9: Plan-view SEM images of InAs nanowire grown from 30 nm colloids at different T_g. (a)-(d) Sample overview and (e)-(h) Single InAs nanowire.

Figure 3.4.10 and Figure 3.4.11 summarize the analysis of the InAs nanowire dimensions at each T_g. In the case of nanowires grown from 30 nm Au droplets, the optimal growth temperature is at 420 °C which results in a lower dispersion in length. For above or below 420 °C, the nanowire dimension is more dispersed. The length of nanowires are of the same level for 400 – 440 °C. Yet, a low growth temperature 380 °C leads to a longer nanowires length.

For nanowires grown from 50 nm Au droplets, the plan-view SEM images can be found in the Supplementary. All the samples present the growth of homogenous nanowires. Craters are visible on the images but not nanoparticles. We observe that at T_g = 380 °C the surface has only craters, while T_g increases, the surface becomes more corrugated and mixed with breaks and craters.

From the nanowire dimension measurements shown in Figure 3.4.10 and Figure 3.4.11, we observe that the optimal growth temperature is at 400 – 420 °C, which has low dispersion. For a low T_g = 380 °C, the length of nanowire is disperse but longer. For a higher T_g = 440 °C, the presence of nanowire is rare on the surface that only two nanowires are measured. All the data are summarized in Table A.2.4 in Supplementary.

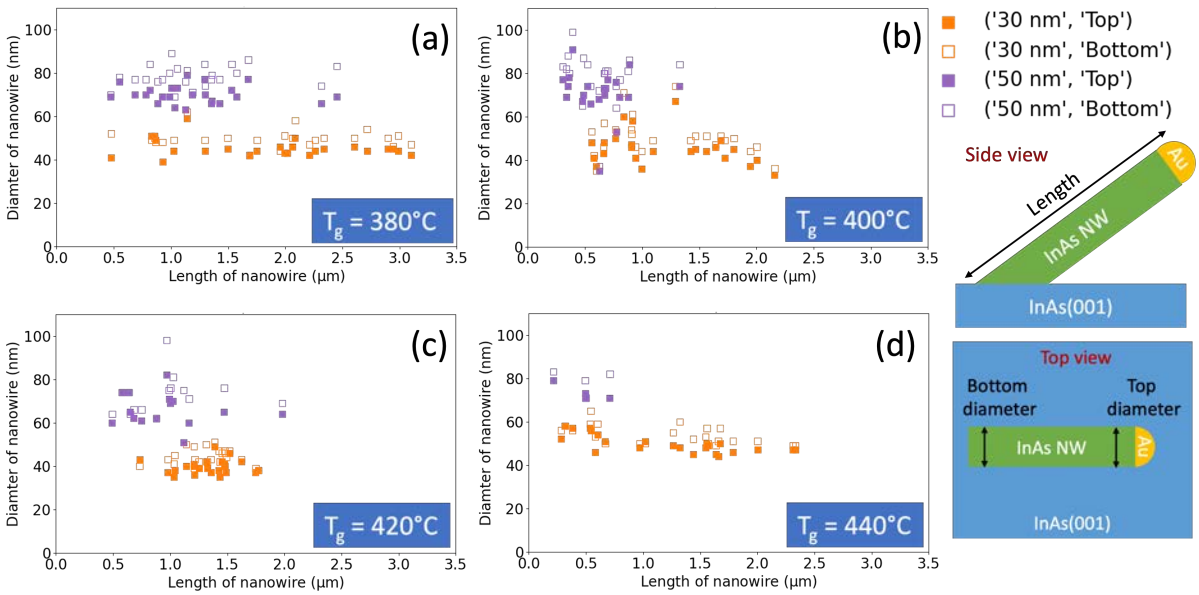

Figure 3.4.10: InAs nanowire dimensions as function of T_g measured from plan-view SEM images. 'Top' corresponds to 'the top diameter' and 'Bottom' to 'the bottom diameter'. Schematic of the nanowire. In (d), we found only four nanowires for the 50 nm sample grown at 440 °C. Therefore the data are not representative.

Finally, I evaluated the tapering angle α of the nanowires ($\sin\alpha = \frac{D_2 - D_1}{2L}$), where D_2 is the bottom diameter, D_1 is the top diameter, and L is the length of nanowires. Figure 3.4.11 (b) shows the tapering angle of nanowires versus growth temperatures. In the case of nanowires grown from 30 nm Au droplets, the diameters are of the same order of magnitude for all growth temperatures T_g. In contrast, the tapering is more pronounced in 50 nm Au case.

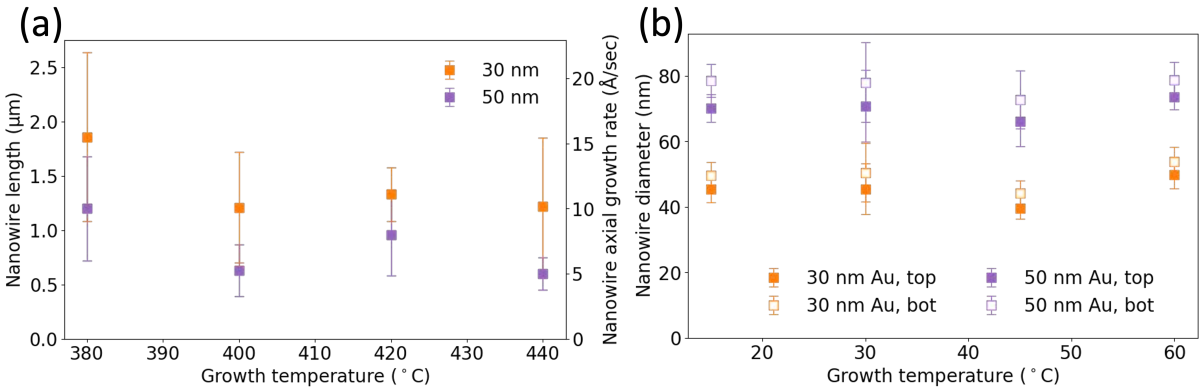

Figure 3.4.11: Summary of (a) length/axial growth rate and (b) diameters of nanowires affected by the growth temperature T_g. 'top' corresponds to the top and 'bot' corresponds to the bottom diameter of nanowire.

I then analyze the density of nanowires versus growth temperature. Figure 3.4.12 shows the evolution of the craters, nanoparticles, and nanowires density with respect to T_g for 30 nm droplets. The density of nanowires is constant around 0.4 μm^{-2} at all T_g. This represents 20%

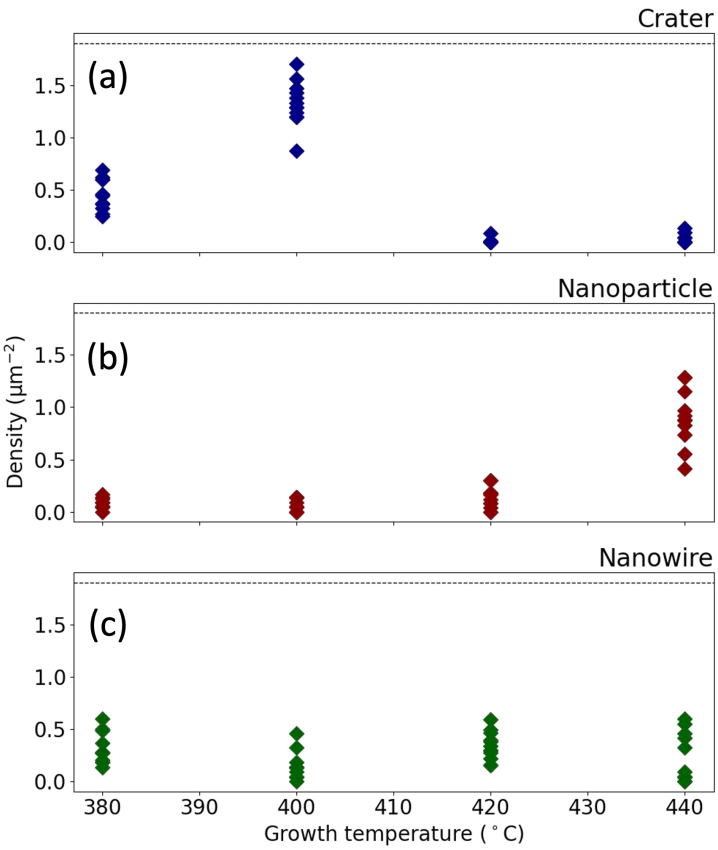

Figure 3.4.12: Density analysis as function of T_g for 30 nm Au catalysts. The black dashed line corresponds to the initial density of deposited 30 nm colloids 1.9 μm^{-2}. Each point corresponds to data extracted from one SEM image larger than 21 μm^2.

of the initial deposited 30 nm Au droplets grown into nanowire. The best morphology is resulted at T_g = 420 °C, which has the lowest density of craters. At lower growth temperature, there are more craters appearing. I also analyzed the 50 nm Au nanowires samples. The lowest crater density appears at T_g = 380 °C.

In conclusion, I found that the optimum growth temperature (in terms of size dispersion, tapering and density) for 30 nm diameter droplets is 420 °C while it is 400 °C for 50 nm diameter droplets. I achieve lengths of 1.3 μm and density of 0.3 μm^{-2} at 420 °C for 30 nm catalysts, 0.6 μm and 0.06 μm^{-2} at 400 °C for 50 nm catalysts.

3.4.3 V/III beam equivalent pressure ratio

Here, I study how the V/III beam equivalent pressure ratio (V/III BEP ratio) influences InAs nanowire growth on InAs(001) after having optimized T_a and T_g. The V/III BEP ratio is defined by V-group Beam equivalent pressure (As flux) divided by the III-group Beam equivalent pressure (In flux). Under our growth conditions, (T_g = 420 °C and large As flux), the 2D equivalent growth rate is controlled in principle by the In flux. I therefore fix the In flux and vary the As flux to study its influence on the nanowire morphology. The annealing process at 500 °C for 1 minute is applied and the nanowires are grown at T_g = 420 °C for 20 °C from 20 nm, 30 nm, or 50 nm Au catalysts. The In flux is fixed at 2.5 × 10^{-7} torr and the V/III BEP ratios varied between 15 (As flux = 3.75 × 10^{-6} torr) and 60 (As flux = 1.5 × 10^{-5} torr). The growth

parameters of the samples studied in this section are listed in Table 3.4.3.

Sample	T_a (°C)	T_g (°C)	**Growth time (minute)**	**V/III BEP ratio**	**Catalyst diameter (nm)**
NW879	500	420	20	15	20, 30, 50
NW880	500	420	20	30	20, 30, 50
NW883	500	420	20	45	20, 30, 50
NW882	500	420	20	60	20, 30, 50

Table 3.4.3: Sample list for the V/III BEP ratio.

Figure 3.4.13 shows SEM images of InAs nanowires grown with different V/III BEP ratios. We see that high density, non-tapered nanowires grow for any V/III BEP ratio between 15 and 60 and that the axial growth rate depends on the As flux. The surface is corrugated for all V/III BEP ratios, with a decrease in homogeneity when V/III BEP ratio increases.

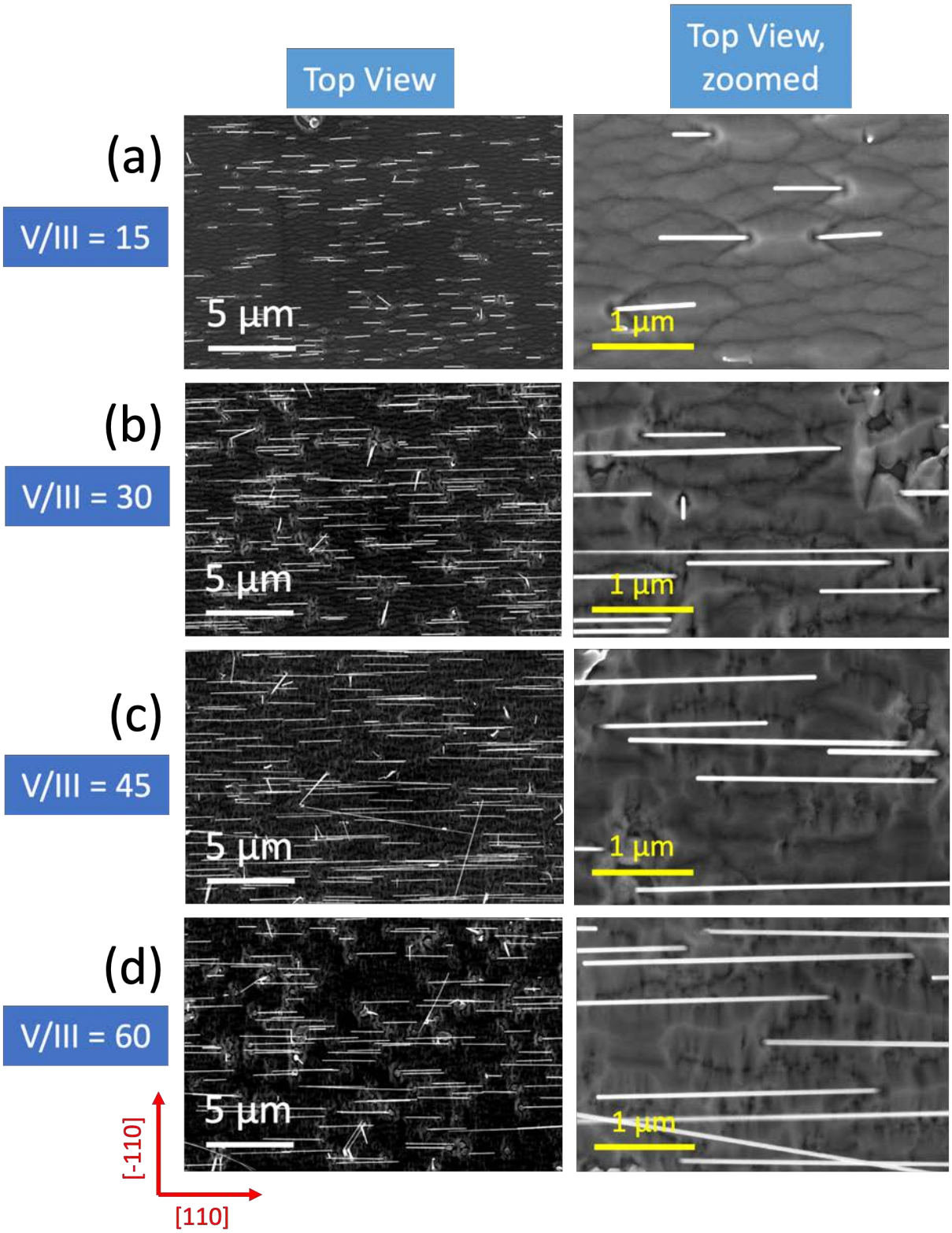

Figure 3.4.13: Plan-view SEM images of InAs nanowires grown from 30 nm colloids with different V/III BEP ratio.

Figure 3.4.14 shows the evolution of the diameter versus length for different catalyst sizes and V/III BEP ratios. We observe that the dispersion in length for a given initial colloid diameter

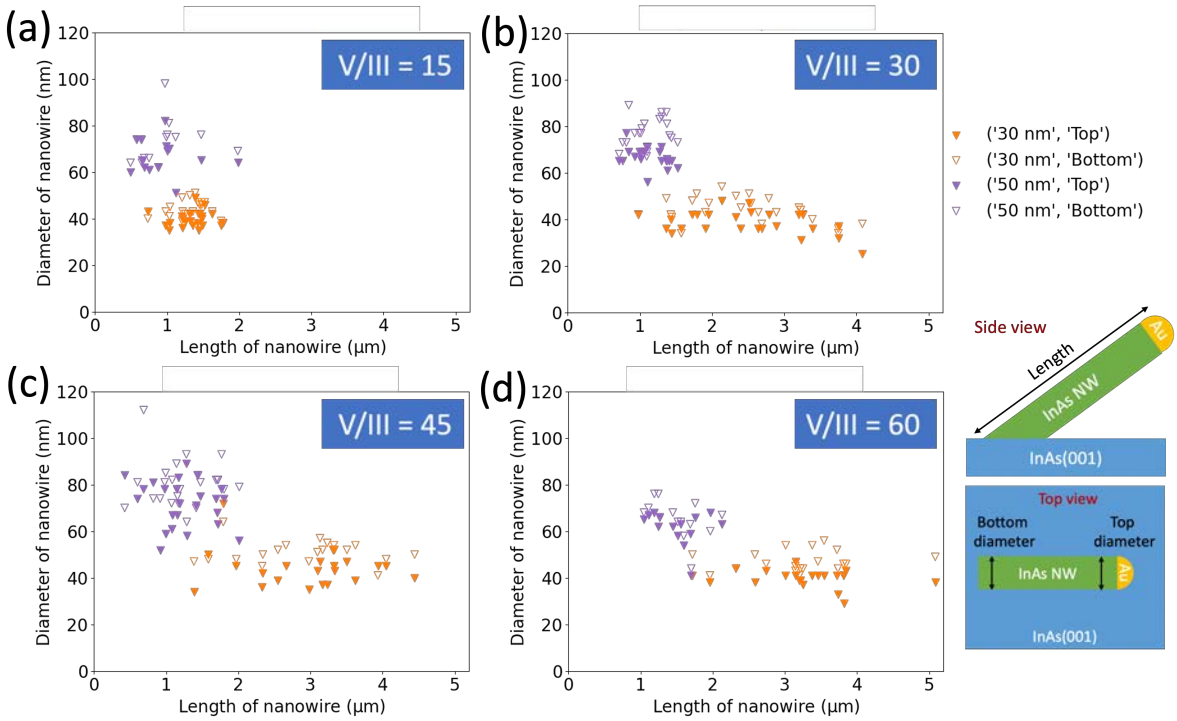

Figure 3.4.14: Measurements of InAs nanowire dimensions in V/III BEP ratio study. The illustrations of InAs nanowire dimensions are aside.

is dependent on the V/III BEP ratio. For example, nanowires grown from 30 nm Au droplets have the best homogeneity in length (lowest length dispersion) at V/III = 15. Above V/III = 15, the dispersion in length increases. For the case of nanowires grown from 50 nm Au droplets, the dispersion is low in the whole range compared to 30 nm case.

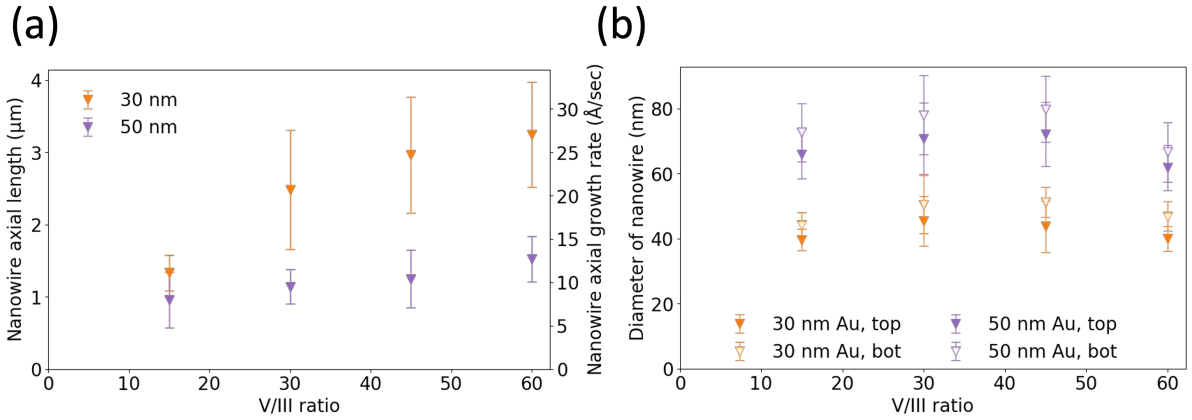

Figure 3.4.15: Influence of V/III BEP ratio on the axial length/growth rate and diameters of nanowires grown from 30 and 50 nm Au droplets. 'Top' corresponds to the top diameter and 'bot' corresponds to the bottom diameter of nanowire.

Figur 3.4.15 (a) shows that the axial growth rate of nanowires increases while V/III BEP ratio increases. We find as a general trend that nanowires grown with lower V/III BEP ratio

have the most homogeneous dimensions [145]. Lower V/III BEP ratio leads to more uniform but shorter nanowire in length, and it does not change the diameters.

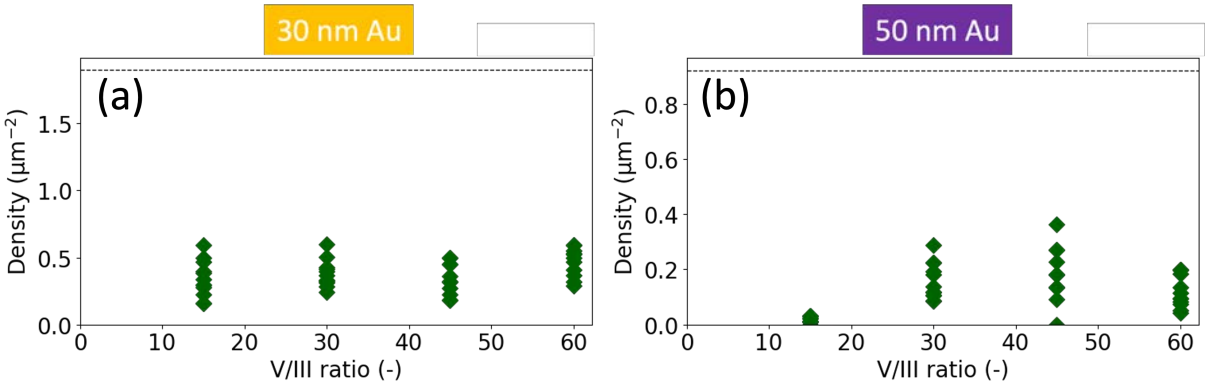

Figure 3.4.16: Evolution of the nanowire density with V/III BEP ratio. The initial density of deposited 30 nm Au droplet is 1.9 μm^{-2} and of 50 nm is 0.9 μm^{-2} marked as black dashed line.

Figure 3.4.16 shows the density analysis of nanowire grown with different V/III BEP ratios. For nanowires grown from 30 nm Au colloids, we see that the nanowire density is constant regardless of the V/III BEP ratio. In contrast, for nanowires grown from 50 nm Au colloids, the best density is around V/III = 30-45. The densities of nanowires grown at above or below V/III BEP ratios are lower. All the values are listed in Table A.2.7 in Supplementary.

I have studied the influence of V/III BEP ratio on InAs nanowire growth from 15 to 60 with fixed In flux. I find that the nanowire growth rate increases with V/III BEP ratio (which is typically explained by the reduction of the adatom diffusion on the substrates at high As flux [180]). I also found that the dispersion in length is lower at low V/III BEP ratio. In the next paragraph, I study the influence of the growth time on the nanowires morphology at the optimized V/III ratio = 15.

3.4.4 Growth time

I optimized step by step the different growth parameters, and now I study if the growth time influences the morphology of the nanowires. The growth conditions are the following: T_a = 500 °C for 1 minute with As flux= 1.0×10^{-5} torr, T_g = 420 °C, and V/III ratio = 15 where In flux 2.5×10^{-7} torr. The data are summarized in Table 3.4.4.

Sample	T_a (°C)	T_g (°C)	**Growth time (minute)**	**V/III BEP ratio**	**Catalyst diameter (nm)**
NW894	500	420	1	30	20, 30, 50
NW886	500	420	2	30	20, 30, 50
NW885	500	420	5	30	20, 30, 50
NW884	500	420	10	30	20, 30, 50
NW880	500	420	20	30	20, 30, 50
NW868	500	420	40	30	30, 50

Table 3.4.4: List of samples prepared for the growth time study.

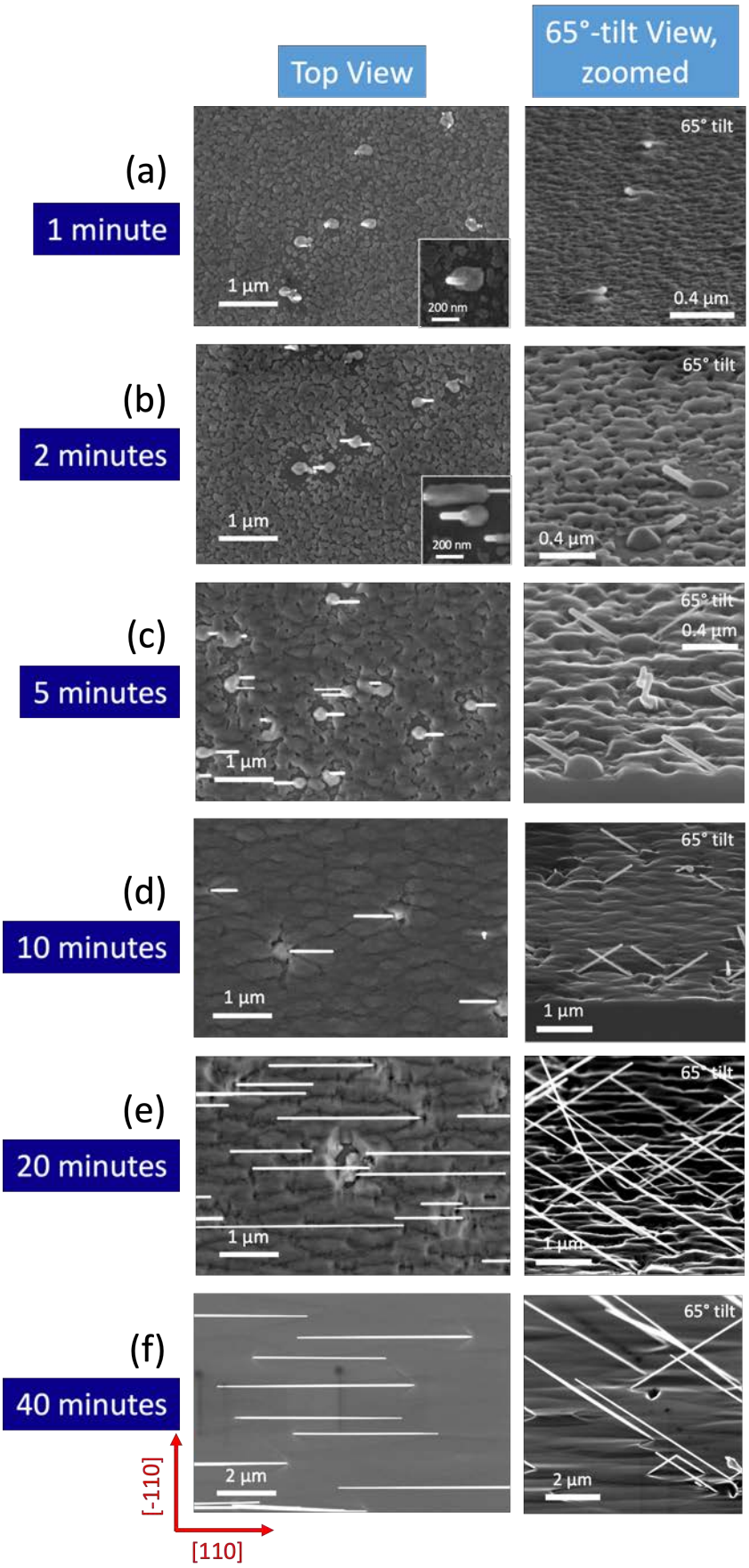

Figure 3.4.17: Plan-view and 65°-tilt-view SEM images of InAs nanowire grown from 30 nm Au colloids as function of the growth time. The insets in (a) and (b) are the magnified view focusing on mound.

Figure 3.4.17 shows plan-view and side-view SEM images of the nanowires grown from 30 nm diameter colloids for growth times ranging from 1 to 40 minutes. The evolution of the nanowire length is clear: the longer growth time, the longer the nanowires. Nevertheless, we observe a slight change in morphology of the nanowire and InAs surface that will be studied in details in the next paragraphs.

We observe that prior to effectively catalyze nanowires, the Au droplet is responsible for the formation of an oriented mound along the [110] direction. For an increase in the mound size, facets are better defined. Importantly, the mounds present two (111)B facets from which nanowires nucleate. Besides the mounds, the InAs surface is covered first by a granular film. With increasing growth times, the surface flattens until 10 minutes growth. Above 10 minutes, corrugations appear and their amplitude increases. Nonetheless, the surface flattens again after 40 minutes growth.

Now I analyze in details the dimensions of the nanowires and their dependence with growth time. Figure 3.4.18 shows the statistic analysis of the nanowire dimensions. We see that the length increases but is not linear with time for all diameters of Au colloids studied. This is confirmed by looking at the axial growth rate which increases with time. Also, the dispersion in length increases with time. For long growth times, the dispersion in diameter also increases. The broadening of length distribution is a feature of diffusion-induced growth [64].

We see that the shape of nanowires evolves with time. For nanowires from all sizes of Au colloids, the difference between top and bottom diameters is less than 10 nm during the first 10 minutes: the shape of the nanowires is cylindrical. For nanowires grown from 30 nm Au colloids, the bottom and middle diameters increase significantly which could be attributed from the vapor-solid growth mechanism on the side walls due to diffusion and impingement of adatoms on the nanowire facets [69]. For 50 nm Au catalyzed nanowires, the bottom diameter is constant over time. In contrast, the top and middle diameters increase with time and the nanowire shape becomes inverse conical. We do not understand yet the reasons for such a change in morphology. To go further, we need to develop a model taking into account the length and diameter dependence of the adatom diffusion, desorption and direct impingement.

After the analysis of nanowire growth evolution with time, 50 nm Au catalyzed nanowires have smaller axial growth rate (17 Å/sec) than 30 nm catalyzed ones (33 Å/sec). The axial growth of nanowires for the 50 nm colloids starts 10 minutes later than the 30 nm colloids. Under those growth conditions, the middle diameter of nanowire increases after 40 minutes growth.

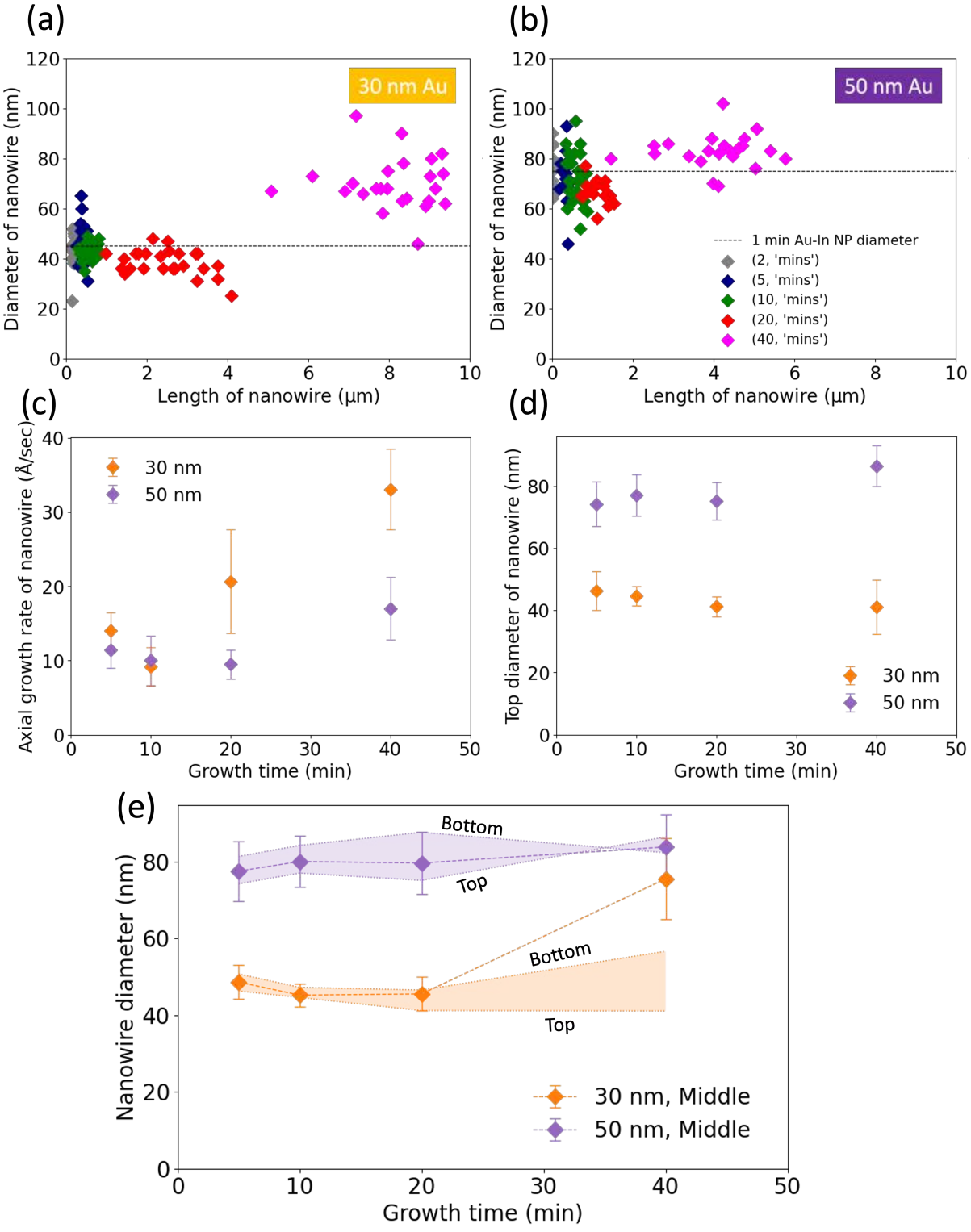

Figure 3.4.18: Evolution of the InAs nanowire dimensions as function of growth time. Nanowire top diameter versus nanowire length grown from (a) 30 nm and (b) 50 nm Au colloids. The diameter of Au-In alloy droplet after one minute growth is represented by the dashed line. (c) Axial growth rate and (d) top diameter of nanowires versus the growth time. (e) Nanowire diameter versus the growth time. The shadowing region is the diameter between top and bottom of nanowire. 'Middle' corresponds to the middle diameter of nanowire. Schematics of the shape of nanowire.

Finally, I analyze the evolution of the nanowires density. Figure 3.4.19 shows the density with respect to growth time. The maximum density of nanowires grown from 30 nm Au colloids appears after 10 minutes , and from 50 nm Au colloids appears after 20 minutes . After reaching the maximum, the density of nanowires decreases with time. At short growth times, not all nanowires have started nucleating yet, which is not usual in comparison with (111)B oriented nanowires. We do not fully understand yet the reasons for the non uniformity of the nanowire density with growth time. We propose the following hypothesis to explain the variation of nanowire density with growth time. Because annealing time is very short, not all Au particles have time to reach the ideal eutectic composition. Delay in nucleation between particles might occur and only a fraction of nanowires grow out [63]. After long growth times exceeding 40 min, branched, kinked, and merged nanowires appear. Those faulted nanowires are not taken into account in the calculation of the nanowire density. This might be the reason why the density decreases with long growth times. The use of Au-patterned substrates will bring additional inputs in this direction.

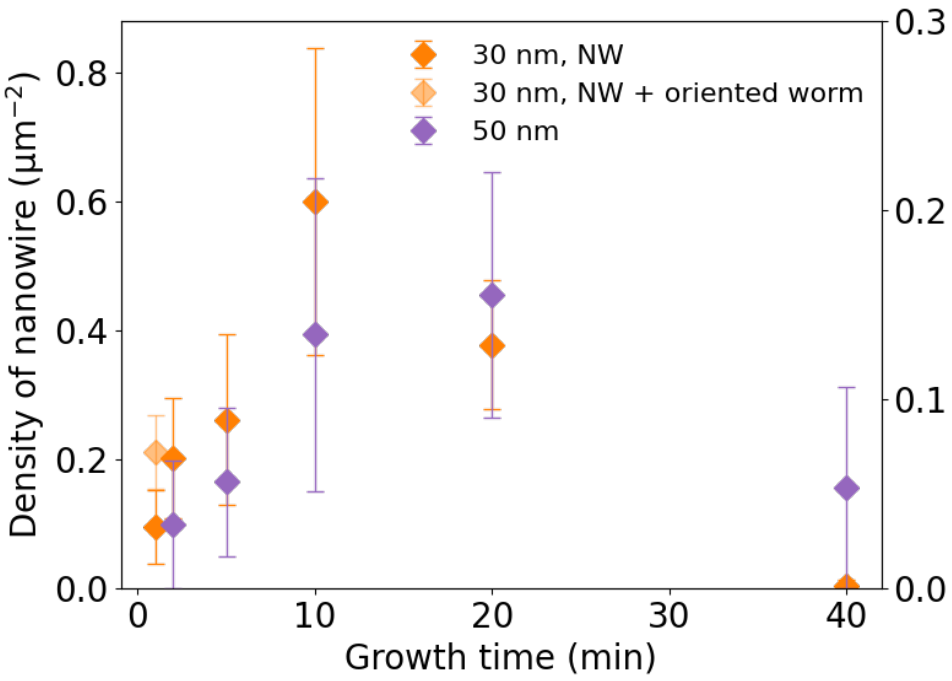

Figure 3.4.19: Nanowire density analysis for 30 and 50 nm Au colloids as function of growth time. 'NW' corresponds to tilt nanowires and 'oriented worm' corresponds to the mounds oriented in the [110] directions after one minute growth.

Similarly to T_a, I optimized the growth parameters to achieve the most homogenous nanowire. The optimal parameters depend on the catalyst diameter, nevertheless, there is a general trend:

- growth temperature: higher nanowire axial growth rate at 380 °C, no pronounced effect on nanowire diameters, no effect on density, lower dispersion in nanowire length at 420 °C.

- V/III BEP ratio: lower dispersion at 15, higher growth rate at higher V/III BEP ratios, no effect on nanowire density and diameters.

- growth time: the nanowire length increases with longer growth time, dispersion in length increases above 20 min.

In the next section, I discuss the effects of the different growth parameters on the growth of inclined InAs nanowires.

Discussion of the standard growth parameters The goal of this study was to find the growth conditions to achieve homogeneous nanowires. This translates into nanowires dimensions (diameter and length) having the lowest dispersion but also reduced tapering.

As a first step it has been necessary to adapt the annealing temperature prior to growth. While the annealing temperature exceeds usually the deoxidation temperature prior to nanowire growth on (111)B InAs surfaces, such high temperature is not optimal on (001) surfaces. Nanowires density drops drastically while craters form on the surface. I thus studied the effect of the annealing temperatures on InAs nanowires by analyzing both the nanowires and the substrate surface after 1 min and 40 min growth on (001) InAs substrates.

One important finding is the optimal annealing temperature of 500 °C at which nanowire size dispersion is the lowest and nanowire density is the highest. Below 500 °C, I find that vertical nanowires have nucleated after 1 min (with a peak of density at 460 °C) in addition to inclined nanowires. The presence of vertical nanowires is attributed to a reduced incorporation of In into the droplet during T_a [122]. Those vertical nanowires are no more visible after 40 min of growth. We suspect that the 2D thin film covers the vertical nanowires, which then act as a seed for the nucleation of the craters.

Above T_a = 500 °C, I found very little nanowires having nucleated after 1 min, but numerous droplets. After 40 min growth, almost no nanowires grew but the density of craters matches the density of droplets observed after 1 min. We propose that due to a high annealing temperature, In incorporation into Au catalysts exceeded the limit above which the wetting angle of the droplet is adequate to catalyze growth [148].

Thus, I found that the optimal annealing temperature is 500 °C. The subsequent growth shows an interesting behavior. After 1 min growth, InAs nanowire growth starts from oriented mounds along the [110] directions. For larger catalysts (50 nm), we even observe a faceted pyramid, exhibiting two (111)B facets from which the InAs nanowires grow inclined. This behavior is totally different from previous works on inclined InAs nanowires which nucleated from craters [113]. Our growth conditions show indeed that no craters form before 20 min of growth.

Once optimized the annealing temperature, I studied the influence of the growth parameters commonly available in the MBE chamber: T_g, V/III BEP ratio and growth time. Overall, the growth parameters that I use to grow Au-catalyzed VLS inclined InAs nanowires on InAs(001)

substrates do not differ drastically from vertical InAs nanowires grown from InAs(111)B substrates [207, 82, 242, 101, 121]. Nevertheless, there are slightly different behaviors.

For example, we observe that the main influence of T_g in the range studied (380 °C - 440 °C) is that the dispersion in size of the nanowires is lower at 420 °C, while a slightly lower growth rate (15 Å/sec at 380 °C and 12 Å/sec at 420 °C) is measured. In the work of M. Tchernycheva on InAs(111)B substrate, the growth rate achieved a maximum at 420 °C (17 Å/sec) with drastic reductions of growth rate at 380 °C and 440 °C. The reason for such difference lies in the excess of As [180]. We notice that the dispersion in size was dependent on the growth temperature: we have a lower dispersion for 30 nm at 420 °C, which also coincides with a smoother surface (less craters density) at this growth temperature.

The V/III BEP ratio showed a pronounced effect on the nanowire length which represents the growth condition is at In-rich regime that the growth rate is limited by As-flux [180]. Yet similarly to T_g, the lower dispersion was accompanied with a fully covered and continues surface.

Finally, some interesting features were observed with the increase in the growth time: (1) super linear growth rate (14 Å/sec for 5 min growth and 33 Å/sec for 40 min growth) and (2) higher dispersion. These two features are related the diffusion-induced growth model proposed by V. Dubrovskii [64]. (3) At very long growth times, tapering which remained very small for most of the growth parameters, which is minimal at 20 min growth but 40 min growth leads to double bottle shaped nanowires. One hypothesis we advance is that the top tapering is due to the In-diffusion length reaching its limit [207]. The reverse-tapering at the bottom of nanowire is maybe due to the shadowing effect from the vicinity of nanowires [180]. More investigations are needed to understand better.

The competition between crater and nanowire growth observed in Figure 3.4.8 is related to the ratio of "good" inclined nanowires nucleating versus "bad" or "not nucleating". If all nanowires nucleate well on the surface at the beginning of the growth, then there is barely any craters. In contrast, if nanowires nucleate mostly into vertical nanowires, worms, or droplets, the craters form around the "defects".

The nanowire density is always much lower than the initial deposited Au colloids for all experiments. This represents that not all the Au colloids nucleated successfully into nanowires. For the case of annealing at T_a = 560 °C, Au droplet dissolves too much indium according to the In-Au phase diagram, which does not favor the nucleation of nanowires [206]. For the case of annealing at and below T_a = 500 °C, the vertical nanowires grow slowly and become the center of craters [232]. In our optimal annealing condition at T_a = 500 °C, the nanowire density reaches a maximum of 10% of the initial deposited colloids.

3.5 Conclusion and perspective

In this chapter, I developed Au-assisted InAs nanowire on InAs(001) substrates by the VLS mechanism in a MBE reactor. The optimal growth parameters for 50 nm Au colloids are the following.

- anneal at T_a = 500 °C for 1 minute,
- grow at T_g = 400 – 420 °C,
- grow with V/III ratio = 60, and
- grow for 20 minutes.

Those growth parameters will soon been used for the fabrication of nanowires on Au-patterned substrates in my team. In the future, we will assess the crystalline structure and quality of our inclined nanowires by TEM (see Figure 3.5.1). Figure 3.5.1 show some stacking faults along axial direction of InAs nanowires. Indeed, the crystalline structure depends highly on the dimensions and growth parameters. One solution to prevent the formation of stacking faults or defects is to grow cubic InAs(001) nanowires. Early works by J. Wang et al demonstrated the growth of cubic InP(001) nanowires on (001)InP substrates [220]. Inclined cubic InAs nanowires grown on (111)GaAs were reported in 2015 by Z. Zhang et al.[243] This is an interesting new route to produce inclined cubic nanowires free of defects for crossed nanowire networks.

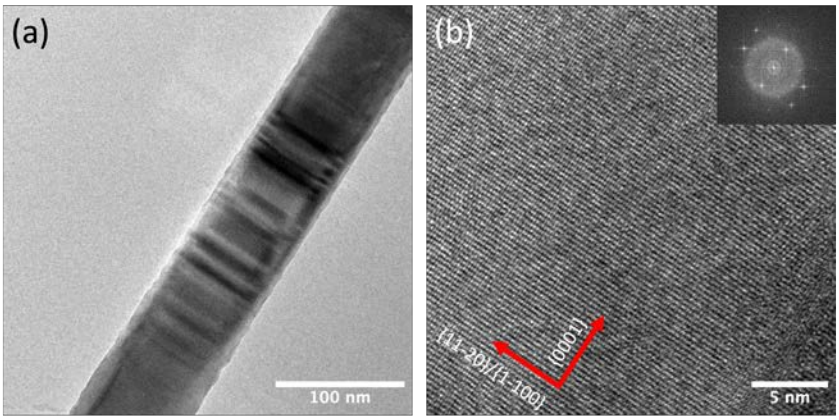

Figure 3.5.1: TEM analysis of WZ InAs nanowire grown from 30 nm Au droplet with V/III = 45. (a) Large view of a single nanowire with the defects. (b) Magnified TEM image labeled with the orientation and its FFT is shown as inset.

CHAPTER 4

Superconductor deposition on InAs nanowires

4.1 Introduction

In the context of tunable Josephson junctions for quantum computing, a perfect interface is required between the superconductor and the semiconductor. Indeed, defects such as contamination or dislocations may affect the electronic properties at the interface and thus disturb the proximity effect emerging in the semiconductor. One solution to prevent defects consists is *in situ* deposition the superconductor on the semiconductor but this can be technologically challenging. Importantly, we demonstrated proximity effect in devices made of Sn shells fabricated *ex situ* on atomic hydrogen cleaned (AHC) InSb nanowires. This is an indication that high quality interfaces can be fabricated *ex situ*. Hence, protecting the InAs nanowire surface is an interesting path prior to *ex situ* fabrication of the superconducting shell.

In this chapter, I present our efforts in developing an *in situ* method for the deposition of Al in the MBE reactor, and an *ex situ* method in which Sn or MoGe shells are deposited on the nanowires after the removal of a protective cap of amorphous As. For metallic superconductor depositions, I find that low deposition temperatures are required for obtaining smooth films on InAs nanowires, –50 °C for Al and –190 °C for Sn. The As capping can be effectively form at a low substrate temperature of 10 °C. The amorphous MoGe deposition on InAs nanowire side walls has the smoothest surface.

I presented the state-of-the-art about superconductor/semiconductor nanowires for topological superconductivity in Chapter 1.3, as well as the selected superconductors. This is an exploratory chapter in which I have been learning how to solve technological challenges to meet the needs of high quality materials from collaborators for further device fabrications.

The TEM analysis was done by M. Hocevar. The EDS-TEM analysis was done by S. Tan at the University of Pittsburgh.

Sample name [nanowire substrate]	Deposition time (minutes)	Deposition temperature (°C)	Al cell temperature (°C)
NW270 [InAs(111)B]	10	-19	-*
NW705 [InAs(111)B]	2	-30	1180
NW644 [InAs(001)]	10	-50	1100

Table 4.2.1: *In situ* Al deposition parameters in MBE. * states a missing data.

4.2 *In situ* deposition of Al

In this section, we show the effect of the deposition temperature (T_d) on the morphology of Al shells grown in our MBE system. After nanowire growth, the substrate's temperature decreases via the radiation of the MBE cryopanels in which flows liquid N_2. Cooling down to negative temperatures takes several hours. Yet, as mentioned earlier, it is mandatory to deposit Al at cryogenic temperatures to achieve thin and homogenous layers. In our system, negative celsius cannot be controlled: once the Al shutter is open, radiations from the Al cell reach the sample and heat it. Therefore, depositing Al *in situ* in the main chamber of the MBE reactor consists in carefully adjusting growth time and Al flux to keep the substrate temperature as low as possible during the entire process. The Al flux is controlled by the temperature of the Al cell: a higher cell temperature results in a higher Al flux and therefore a larger growth rate and therefore a larger growth rate. The deposition parameters used in this study are listed in Table 4.2.1. Al shells were deposited on vertical nanowires grown on InAs(111)B and inclined ones grown on InAs(001).

Figure 4.2.1 shows SEM observations of the deposited Al shells on InAs nanowires at different deposition temperature T_d from –19 °C to –50 °C. We see that the Al shell deposited at -19 and –30 °C dewet and become small droplets varying from a few nm to 20 nm. In contrast, the Al deposition at a lower deposition temperature –50 °C is continuous and smooth without dewetting. We direct the Al flux from a side of sample which results in a Al film covering two side walls of InAs nanowires grown on InAs(001) substrate.

In the case of Al, small adatom mobility and high Al flux favor smooth and continuous metal deposition on a surface [118]. At room temperature, the mobility of adatoms is enhanced and the nucleus density is low. When highly mobile adatoms reach a nucleation site and form a big metallic cluster. At negative celsius deposition temperature, Al atoms get absorbed on the surface and form high density nucleation sites. The suppressed diffusion of adatoms leads to the formation of small grains of large density and results in a smooth metallic deposition. In our system, we can achieve a smooth Al film at the lowest deposition temperature of –50 °C: at this temperature, the diffsion of adatom is sufficiently low.

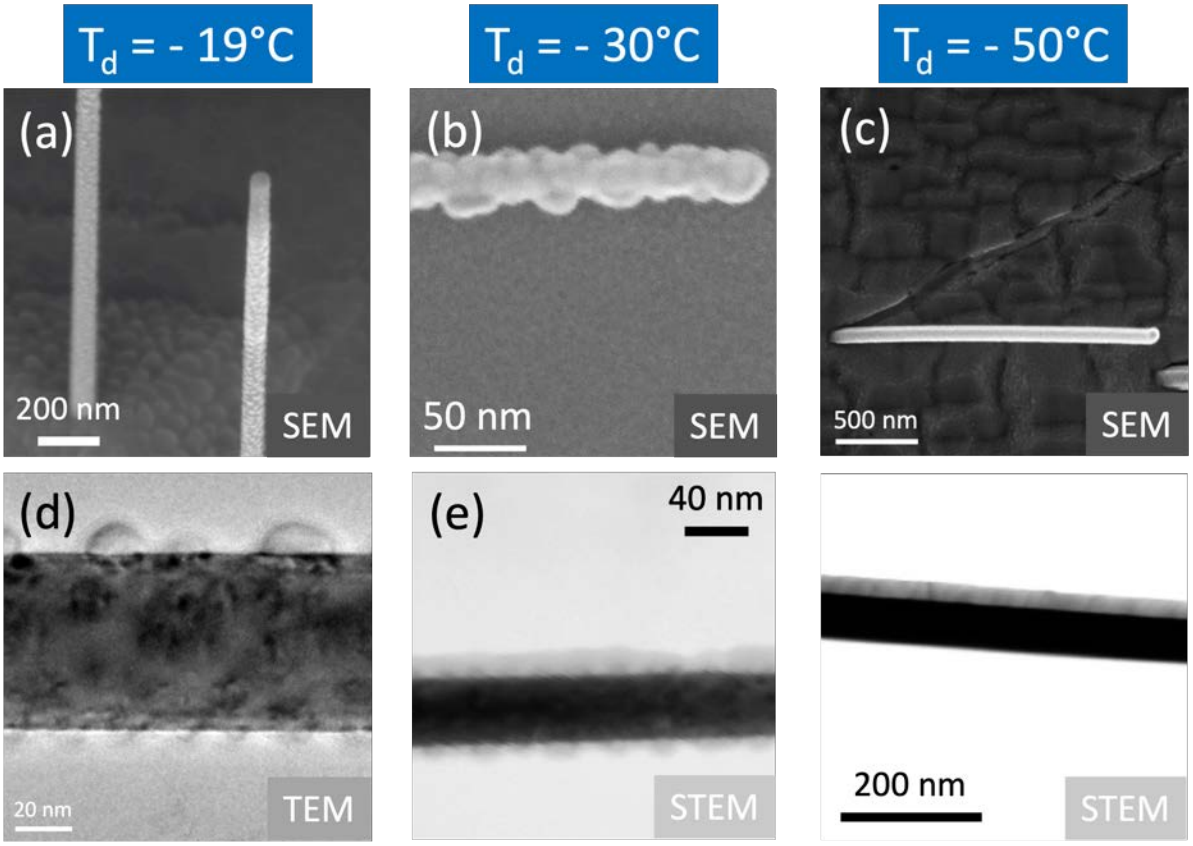

Figure 4.2.1: Al shells around InAs nanowires deposited at different T_d. (a) 30° tilted-view SEM image and (d) TEM image of the shell deposited at T_d = –19 °C. (b) SEM image (on TEM grid) and (e) STEM image of Al shell deposited at T_d = –30 °C. (c) Plan-view SEM image and (f) STEM image of the shell deposited at T_d = –50 °C.

4.3 *Ex situ* deposition of Sn

It is mandatory to deposit Sn thin films at cryogenic temperatures on nanowires to achieve smooth and continuous metallic shells. Here we discuss and show the morphology of Sn shells deposited on InAs nanowires at different temperatures, T_d = –70 °C, –120 °C, and –190 °C. Sn was deposited on InAs nanowires grown on InAs(110) and InAs(111)B substrates at UCSB. Prior to Sn deposition, the sample is cleaned by atomic hydrogen cleaning (AHC) for 45 minutes at 450 °C (filament value). The oxides are removed from the surface. The details of AHC can be found in Chapter 2.3.1. After Sn deposition, the sample which is still cold is transferred to a low vacuum loadlock chamber for 15 minutes to be oxidized and form a native Sn oxide as capping layer. This prevents the film from dewetting. We let finally the sample warm up naturally to room temperature . The Sn deposition parameters are listed in Table 4.3.1.

The SEM images of Sn/InAs core/shell nanowires with different deposition temperatures are shown in Figure 4.3.1. We see that at T_d = –70 °C, the Sn shell is rough and consists of grains. Those grains can be seen not only on the nanowires but also on the 2D surface. When decreasing the temperature to –120 °C, grains turn into a thin film which lacks of homogeneity.

Sample name	AHC T (°C) /time (min)	Sn cell temperature (°C)	Sn deposition time (min)	T_d (°C)	Oxidation time (min)
MP617-NW582 [InAs(110)]	450/45	1100	45	-70	15
MP637A-NW297 [InAs(111)]	450/45	1100	80	-120	15
MP636D-NW574 [InAs(110)]	450/45	1100	80	-190	15
MP615-NW582 [InAs(110)]	450/45	1100	45	-190	15

Table 4.3.1: *Ex situ* Sn deposition parameters in metal evaporator, including sample name [substrate where nanowire grown], AHC temperature and its duration, Sn cell temperature, substrate temperature during Sn deposition and its duration time, oxidation time in a low vacuum chamber before taking out from evaporator.

At T_d = –190 °C, the Sn film is smooth and homogeneous without any visible grain. As the wires are tilted with respect to the source, the region below the wires is not exposed to the Sn flux, therefore we observe shadowed regions (indicated in red arrows) under nanowires during the Sn deposition confirming the presence of the film.

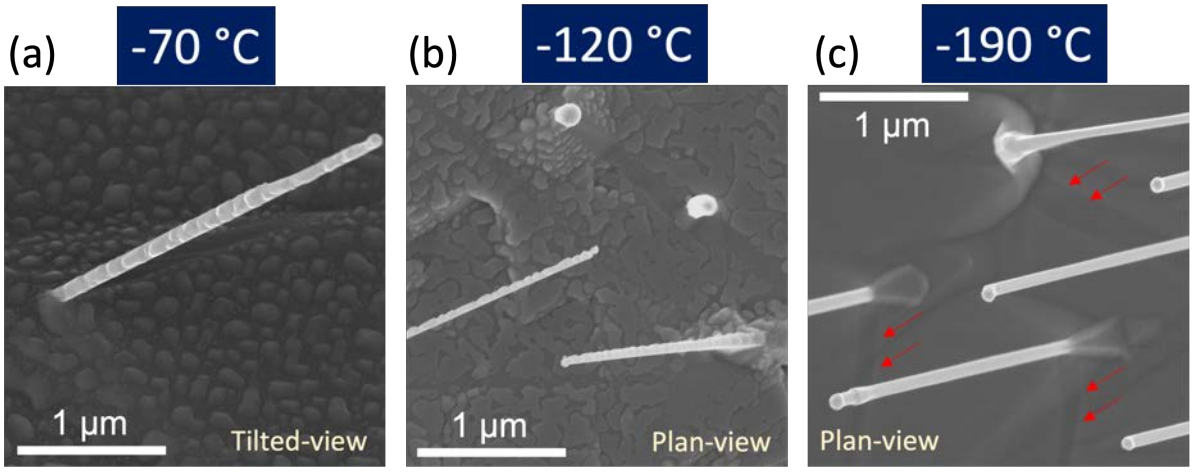

Figure 4.3.1: SEM images of Sn films deposited at different T_d. [MP617-NW582](a) Tilted view SEM image of Sn deposited at –70 °C. [MP637A-NW297](b) Plan-view SEM image of Sn deposited at –120 °C. [MP636D-NW574](c) Plan-view SEM image of Sn deposited at –190 °C. Red arrows indicate the shadowed regions without Sn deposition.

Figure 4.3.2 show a TEM image of nanowire sample with Sn shells deposited at –190 °C. We see that the half-covering Sn shell is continuous and smooth. TEM analysis show that the Sn shell is in the β-phase. In addition, the nanowire does not have a hexagonal cross section and it has defects. The nanowires are grown on InAs(110) substrate at 420 °C with V/III ratio = 65 and 50 nm Au colloids.

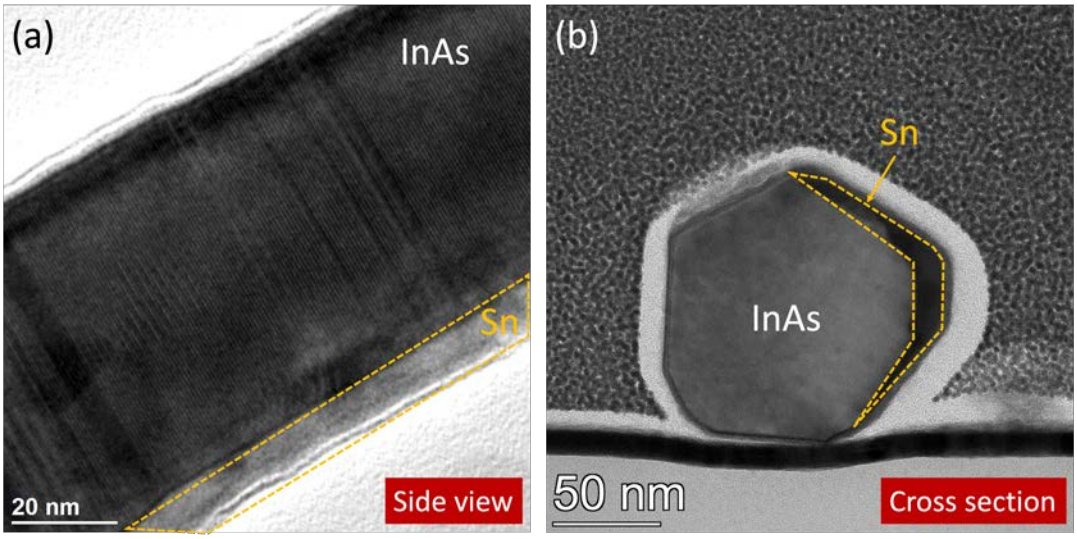

Figure 4.3.2: [MP615-NW582] TEM images of Sn deposited on tilted InAs nanowire at –190 °C. (a) Side view and (b) cross section of Sn/InAs nanowire.

4.4 Capping and decapping of amorphous As

We just observed that direct *in situ* shell deposition on nanowires and *ex situ* shell deposition on *in situ* AHC nanowires are optimal solutions to protect the InAs surface. Yet, other deposition tools such as sputtering not always incluse a cleaning system. Therefore, we developed a capping method adapted to our sputtering equipment at Institut Néel, in which the capping can be removed thermally. The aim of As capping after growth is to prevent InAs nanowire getting oxidized in air during the sample transfer for *ex situ* deposition. To effectively initiate the As capping, we cool down the InAs nanowire sample under As_2 flux of 1×10^{-5} torr for either 10 or 20 minutes. The As capping process is monitored by RHEED. The RHEED pattern becomes weak and even disappears when the wires are fully covered with the amorphous As cap.

Figure 4.4.1 shows the effect of the temperature during As capping. Two cappings (40 °C for 20 minutes and 5 °C for 10 minutes) are performed on different nanowires samples. Note that the nanowire growth parameters are different.

The SEM images do not reveal noticeable differences between the samples (before and after capping, compare with sample NW879 and NW867, respectively from Chapter 3). We then image single nanowires by STEM and TEM to observe the As shell surrounding the nanowires (Figure 4.4.1 (c)(d)). For an As capping temperature of 40 °C, we barely see a shell. In contrast, for an As capping temperature of 5 °C, the TEM image shows clearly that the InAs nanowire is covered by the As shell with a thickness ranging between 5 nm and 20 nm. The asymmetry of As cap is due to the orientation of the nanowire on the substrate. During the As capping, the exterior nanowire sidewalls receive more As flux than the sidewalls close to the substrate. We then conclude that this difference in thickness is responsible for a light bending of the wires due to strain observed in the SEM image. The As capping can form at lower substrate

temperature and cover nanowires entirely. The As shell thickness is thicker on one side of the nanowire than on the other side. As the InAs nanowires are tilted, they act as masks for the deposition of As. The hidden nanowire facets do not see as much As flux as the exposed nanowire facets. Moreover, the As shell is deposited at low temperature. When the sample comes back to room temperature, because of the slight asymmetry of the shell and possible thermal strain, the nanowires bend.

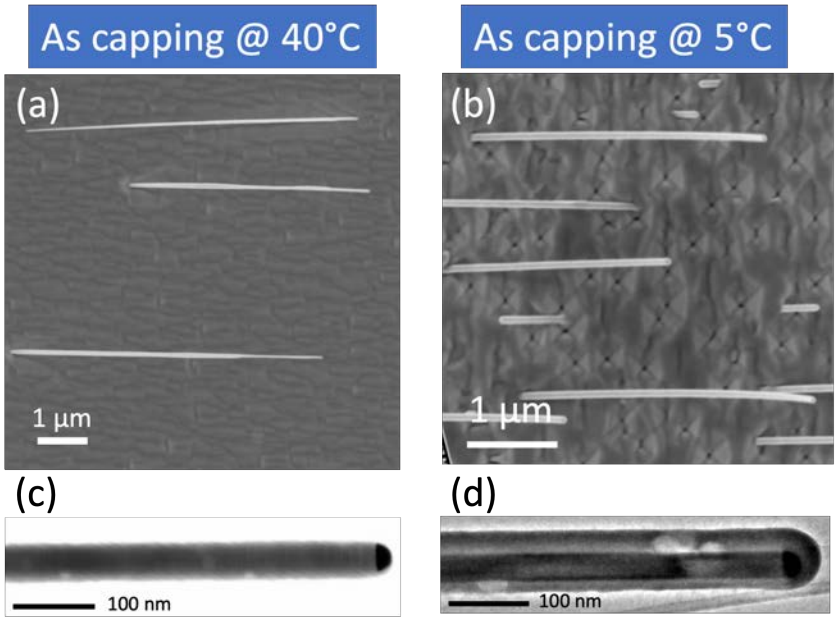

Figure 4.4.1: Effect of the temperature on the As capping. [NW722-30 nm] (a) Plan-view SEM image and (c) STEM image of InAs nanowires capped by As at 40 °C for 20 minutes. [NW790-10 nm](b) Plan-view SEM image and (d) TEM image of InAs nanowires capped by As at 5 °C for 10 minutes.

Prior to superconductor deposition, it is necessary to remove the As shell. As starts sublimating at 230 °C under high vacuum $\sim 1 \times 10^{-9}$ torr [49]. We optimize the As decapping procedure in our MBE system, fixing the decapping temperature at 250 °C and measuring the diameter evolution of nanowires by 30°-tilt SEM.

We used sample NW817-50 nm which has been previously covered with amorphous As. It is then divided into three small pieces to study the time necessary for As to evaporate from the sample without damaging the sample. The nanowires are grown on InP(111)B substrate and capped with an As flux 1×10^{-5} torr at a substrate temperature 10 °C for 20 minutes. The nanowire sample glued with indium ball is removed from molyblock at 260 °C in the air for a short heating time (less than 1 min), which is not sufficient to remove the As capping (Figure 4.4.1 (d)). The statistics of nanowires' diameter for each decapping time are based on the measurements of 10 nanowires for each sample.

Figure 4.4.2(b)-(d) shows 30°-tilt SEM images after each As decapping time. The morphology of the InAs nanowires shows that they were not damaged with thermal heating in UHV.

The diameters of the InAs nanowire is compared to a non-capped InAs nanowire sample (Figure 4.4.2 (a)). We observe that the diameters decrease with time. The dashed horizontal lines are the InAs nanowire diameters of the uncapped nanowire sample. After 60 minutes, the diameters of nanowire reach the uncapped nanowire dimensions. To completely remove the As capping, it is necessary to heat the nanowires up to 250 °C for 60 minutes.

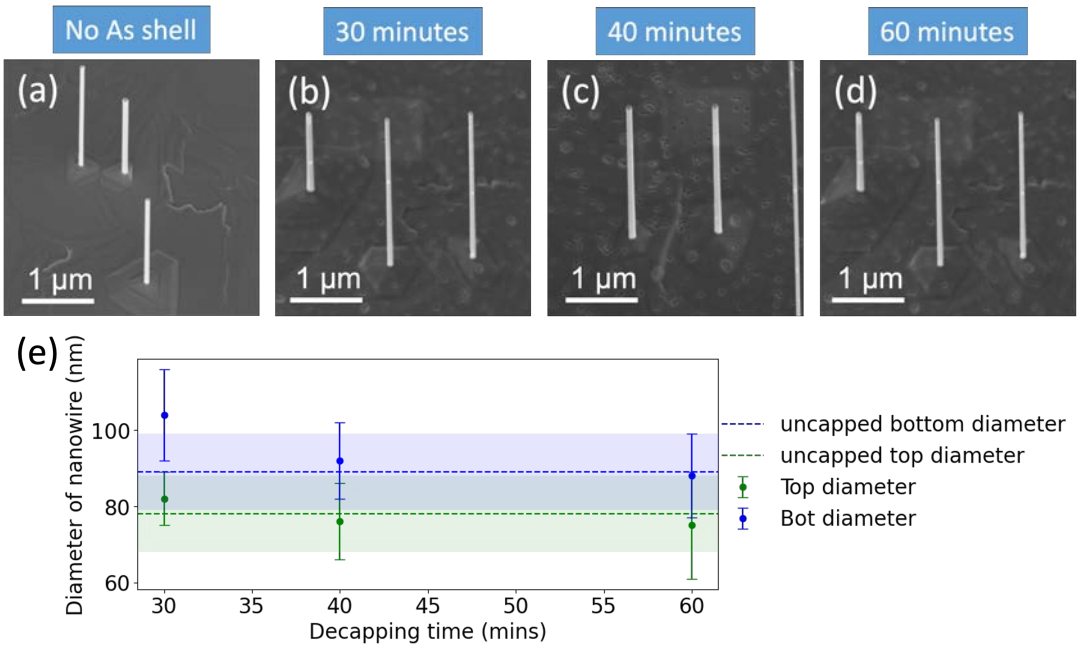

Figure 4.4.2: [NW816-50 nm, NW817-50 nm] 30°-tilted SEM images of InAs nanowires without As shell and decapped at after different decapping time, (b) 30 minutes, (c) 40 minutes and (d) 60 minutes. (e) Evolution of the measured diameter of InAs nanowire versus time. The green circle is the top diameter and the blue circle is the bottom diameter of the same InAs nanowire. The green and blue dashed line are the average top and bottom diameter of uncapped InAs nanowire individually (NW816). The light blue and green regions are the error bar of the diameters of uncapped nanowires.

4.5 *Ex situ* deposition of MoGe

MoGe deposition is performed in a sputtering reactor. Thus we tested the temperature and time of the decapping process in the sputtering chamber directly. First, we calibrated the sample holder temperature using a thermocouple. The sample is then glued in the center of the copper sample holder by thermally conductive indium balls. In is the optimal glue for an optimal thermal contact. All the temperatures shown in this section are the real temperatures. The As capping parameters are listed in Table 4.5.1 and the decapping parameters followed by MoGe deposition are listed in Table 4.5.2.

Sample name	Substrate nanowires grown	Substrate T (°C)	As capping time (min)	As flux (torr)
NW722	InAs(001)	32∼47	23	1×10^{-5}
NW727	InAs(001)	-8∼-4	60	1×10^{-5}
NW734	InAs(001)	3∼5	20	1×10^{-5}
NW759	InAs(001)	9∼12	20	1×10^{-5}
NW768	InAs(111)B	9∼12	20	1×10^{-5}

Table 4.5.1: As capping parameters of InAs nanowires used for MoGe deposition.

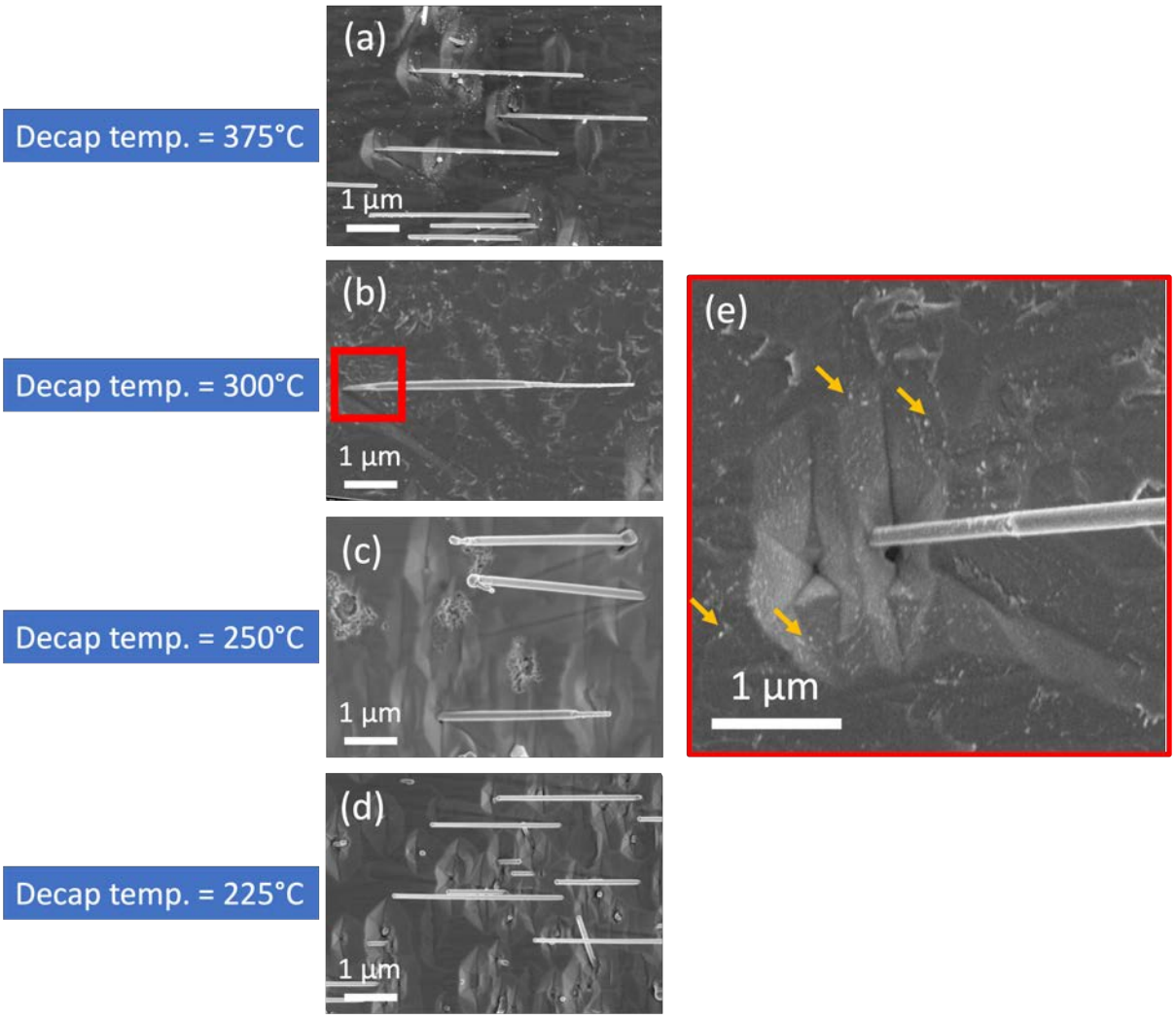

Figure 4.5.1: Plan-view SEM images of MoGe deposition on tilted InAs nanowires with different As decapping temperatures. The decapping temperature in [MoGe04-NW727](a) is 375 °C, in [MoGe06-NW734](b)(e) is 300 °C, in [MoGe07-NW734](c) is 250 °C, and in [MoGe08-NW759](d) is 225 °C. (e) Zoomed image of (b) indicated by the red square. The white particles are indicated by the yellow arrows.

Figure 4.5.1 shows plan-view SEM images of InAs nanowires decapped at different temperatures and then covered with MoGe shell. We see that the InAs nanowires are damaged when a too high decapping temperature 300 °C, and we see numerous bright particles (indicated by

yellow arrows) appearing and sticking on the surface. The surface is still rough after decapping at 250 °C. When decapping at 225 °C, the sample surface remains smooth. Yet, we cannot confirm the As capping is entirely removed by SEM images: TEM analysis is mandatory to observe the interface.

Sample name	**Decapping T (°C)**	**Decapping time (min)**	**MoGe deposition time (min)**	**Substrate temperature (°C)**
MoGe04-NW722 [InAs(001)]	375	20	2	25
MoGe04-NW727 [InAs(001)]	375	20	2	25
MoGe06-NW734 [InAs(001)]	300	20	2	25
MoGe07-NW734 [InAs(001)]	250	20	2	25
MoGe07-NW759 [InAs(001)]	225	20	2	25
MoGe09-NW768 [InAs(111)B]	225	20	1	25

Table 4.5.2: *Ex situ* MoGe deposition parameters in sputtering. All the MoGe depositions are performed on nanowires grown on InAs(001).

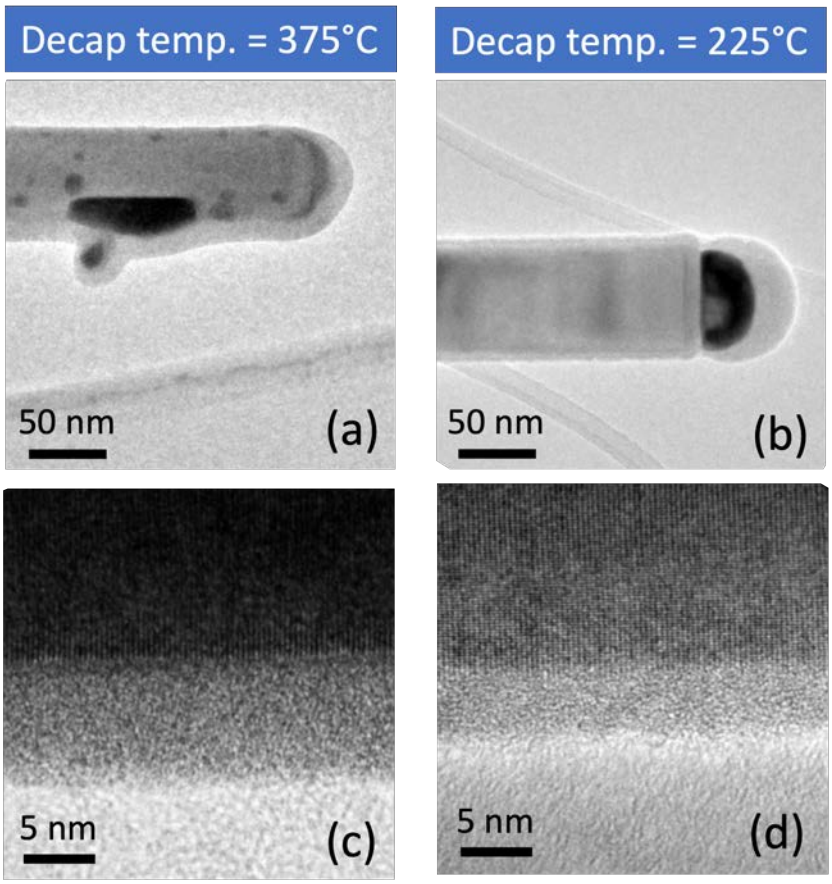

Figure 4.5.2: TEM images of the MoGe/InAs nanowires decapped at different temperatures. (a)(b) Low magnified TEM images showing the tip of the nanowires. (c)(d) High resolution TEM images focusing on the interface between the InAs nanowire and the MoGe shell.

From the TEM images in Figure 4.5.2, we notice that the Au droplet slides from the tip of the InAs nanowire and splits into smaller droplets (dark gray) at 375 °C. The 15 nm-thick MoGe shell half-covers the nanowire grown (as it grows tilted on InAs(001) substrate). At 225 °C, the Au droplet (dark gray) stays at the tip of the nanowire, and the MoGe shell (light gray) covers entirely the nanowire grown on a InAs(111)B substrate. The MoGe shell thickness is around 5 nm on both sides of the nanowire. The magnified TEM images in Figure 4.5.2 (c)(d) show a clean and abrupt interface between MoGe and InAs, indicating no residual As capping in between. So the optimized decapping temperature is 225 °C inside the sputtering machine since As capping can be successfully and completely removed without overheating the InAs nanowires.

We are interested in the composition of the white particles, thus we perform a chemical analysis of the shell and the particles on the nanowire sidewall. Figure 4.5.3 shows the TEM-EDS analysis performed by our collaborator S. Tan at the University of Pittsburgh. We observe that MoGe is deposited on one side of the InAs nanowire and the split-up Au droplet spreads and sticks on the nanowire side walls.

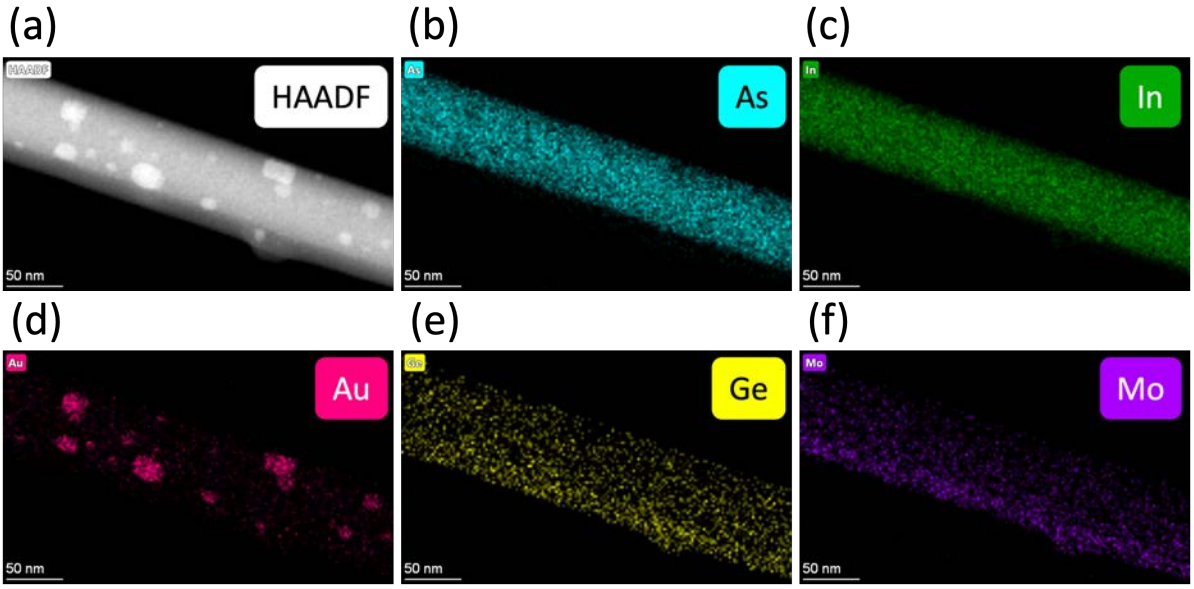

Figure 4.5.3: [MoGe04-NW727(001)] EDS-TEM composition analysis of half-shell MoGe/InAs hybrid nanowire. (a) High angle annular dark-field (HAADF) image of a single nanowire. (b)-(f) Mapping of each element.

To better understand the radial distribution of MoGe deposition on inclined InAs nanowires, cross-section TEM on these hybrid nanowires was performed by S. Tan. Two hybrid nanowires are analyzed and shown here, A1 for the cross-section TEM and B5 for the side-view TEM. The As capping, decapping, and MoGe deposition parameters are listed in Table 4.5.1 and Table 4.5.2 respectively.

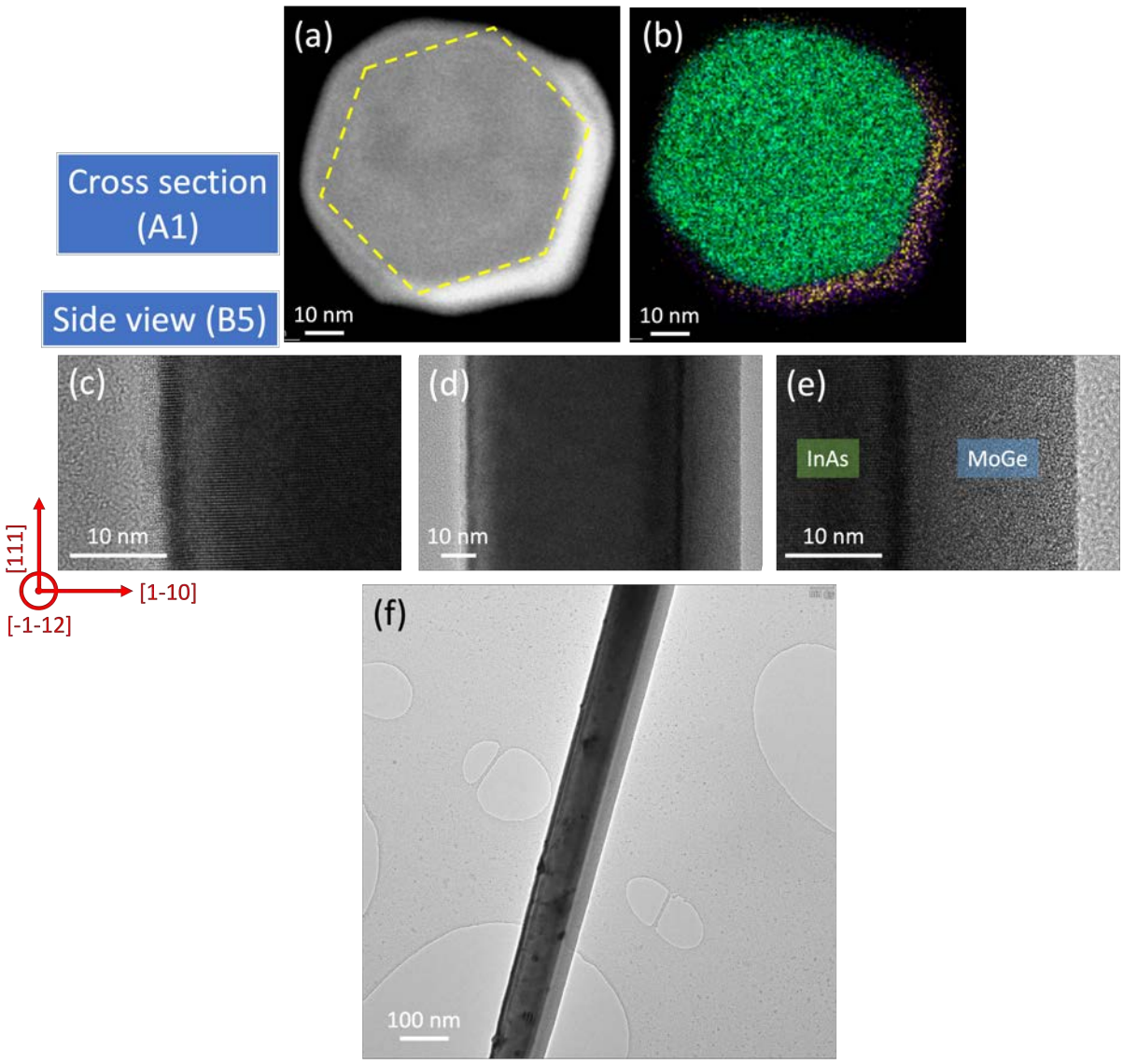

Figure 4.5.4: [MoGe04-NW722] TEM-EDS analysis and side-view TEM images. Two MoGe/InAs nanowires are observed numbered A1 and B5. (a) High resolution TEM image of MoGe/InAs nanowire cross-section and its composition analysis in (b). (d) TEM image of a section of nanowire, (c)(e) Zoom-in TEM images on both sides of nanowires, focusing on the InAs side wall and interface. The orientation of (c)(d)(e), x-axis is along $[1\bar{1}0]$ and y-axis is along [111]. (f) Low magnified TEM image of a long segment of MoGe/InAs nanowire.

Figure 4.5.4 (a)(b) shows the TEM-EDS images of the cross-section of A1 nanowire. We find that the continuous MoGe deposition covers two side walls of InAs nanowire. The InAs nanowire grown on InAs(001) substrate does not have the hexagonal cross section which can contribute to the different radial growth on both sides of the nanowire. The maximal thickness of MoGe from cross-section TEM is around 9.4 ± 0.6nm. In Figure 4.5.4 (d), the side view of MoGe/InAs nanowire (B5) in larger scale shows one side of nanowire having a layer of 17.6 ± 0.3nm-thick MoGe deposition while the other side of nanowire has no MoGe deposition. The MoGe shell thickness is different from A1 nanowire to B5 nanowire in TEM analysis.

The distribution of MoGe deposition thickness on a single nanowire is probably uneven along the nanowire axial length. From the zoomed TEM images in Figure 4.5.4 (c) and (e), the interface of InAs nanowire and MoGe shell is clear and abrupt, and the amorphous MoGe shell is continuous without crystalline structure. Thus, we successfully fabricate *ex situ* half-covering MoGe shell on InAs hybrid nanowire with a clear interface in the sputtering machine, which is a non-directional deposition technique.

4.6 Discussion

The deposition of metallic superconductor usually requires low temperature to have smooth shell deposition, which we observe from our results of depositing Sn and Al on InAs nanowires. The metallic adatoms migrate on the surface with high mobility and nucleate into metallic clusters. At lower deposition temperature, the nucleation spots are numerous and have small collecting area because of limited adatom mobility and follows Volmer-Weber mechanism. So the metallic clusters are small but dense, then coalesce into a continuous surface with tiny grains. However, at higher temperature, the nucleation spots are less but larger because the adatom has higher mobility to diffuse. Meanwhile, the Ostwald ripening makes the big cluster larger and the small cluster disappear. The big metallic clusters grow and coalesce into a rough film with big grains. To prevent the large clusters during metal deposition, lowering substrate temperature is necessary [70, 126, 118]. We observe our deposition results of Al and Sn: at higher deposition temperature, the surface is rough and covered with big metallic grains. While decreasing the deposition temperature, the grain size decreases and a smooth and continuous superconductor shell is formed.

4.7 Conclusion

The deposition temperature of metallic superconductor, Sn and Al, is discussed. We confirmed that low-temperature deposition favors a smooth and continuous shell thanks to reduced adatom mobility. The optimized deposition temperature of Al is –50 °C and Sn is –190 °C. We successfully developed amorphous As capping/decapping on InAs nanowires for *ex situ* superconductor deposition. The InAs nanowires are intact after the thermal As decapping procedure. The optimized decapping process in our MBE cluster is 250 °C for 60 minutes; in our sputtering reactor - 225 °C for 20 minutes. Superconducting amorphous MoGe is deposited at room temperature by sputtering and we successfully obtain MoGe half-shells on InAs nanowire by using inclined InAs nanowires. Based on our TEM observations, amorphous MoGe shells present the smoothest surfaces among the three superconductors I studied.

Part II

Decoding the properties of Sn thin films on InSb

We recently showed that Sn/InSb nanowire devices exhibit a superconducting hard gap albeit the Sn shell is polycrystalline and non-epitaxial with InSb nanowire. This motivated further investigations on the formation of Sn films on InSb with planar and nanowire geometries. In this second part of my manuscript, we used non-destructive X-ray diffraction (XRD) technique to study the crystalline properties of Sn/InSb system in 2D and 1D. In the framework of the ANR-NSF HYBRID project, we received samples from the group of C. Palmstrøm at UCSB. They consist in 2D Sn thin films on InSb substrate. Those samples were studied by *ex situ* XRD to understand the influence of the deposition parameters on the crystalline properties of Sn thin film. We also receive InSb nanowires from the group of E. Bakkers from Eindhoven University of Technology. Those samples were brought to the ESRF to perform *in situ* GIXRD and determine the crystal phase of Sn thin films deposited on InSb nanowire at cryogenic temperature of 80 K.

In chapter 5, we show that the epitaxial Sn thin film is stabilized in the cubic phase by compressive strain on InSb substrate at room temperature, which is above the phase transition temperature of Sn between the cubic low temperature phase and the tetragonal high temperature phase. The tetragonal phase of Sn appears as oriented grains in the cubic thin film. The gradual phase transformation from cubic to tetragonal phase appears due thermal effects during capping layers deposition. The presence of the tetragonal β-Sn is responsible for the superconducting behavior of the Sn films.

In chapter 6, we found that the tetragonal high temperature phase of Sn forms on InSb nanowire facets even at a deposition temperature of 80 K with no evidence of the presence of the cubic phase. This is in stark contrast with the 2D Sn/InSb. Moreover, the Sn shell is polycrystalline with grains of 67 nm average and superconducts with a critical temperature of 3.4 K.

Finally, the results of this second part of my manuscript present a deep understanding of the structural properties of Sn thin film deposited on InSb.

CHAPTER 5

Sn thin films on InSb substrate

All the Sn thin film samples were fabricated by C. Palmstrøm research group at the UCSB. XRD measurement was advised and assisted by E. Bellet-Amalric. The heat balance calculation was established by L. Bellon. EDS analysis was performed by E. Robin. The transport measurement of thin films was conducted by S. Frolov research group at the University of Pittsburgh. The DFT calculation was performed via the clusters of N. Marom group at the Carnegie Mellon University and S. Frolov group at the University of Pittsburgh with the VASP license of N. Marom's group.

Part of the results presented in the chapter can be found in an article in preparation [43].

5.1 Introduction

Back in 2019, the observation of the tetragonal β phase in the Sn shell surrounding an InSb nanowire attracted our curiosity [168]. Yet, the analysis of the Sn crystalline phase on a nanowire was rather challenging because of the fragility of the heterostructure during focus ion beam lamella preparation. We decided to analyze the influence of the processing parameters, such as deposition temperature and nature of the protective layer. We fabricated Sn thin films on InSb substrates to access their structural properties directly and non-destructively using X-ray diffraction.

Sn thin films deposited on InSb substrates have been studied in material science for decades. α-Sn and InSb have a very low lattice mismatch of only 0.14%, InSb is therefore a perfect substrate to grow epitaxial α-Sn layer. In 1981, R.F.C. Farrow reported that epitaxial α-Sn thin films grow on lattice-matched InSb or CdTe substrates up to 0.5 μm at 300 K under a high vacuum of 10^{-5} torr [72]. In 2018, C.-Z. Xu et al. showed that a strained monolayer α-Sn (stanene) grown on InSb has a direct band gap of 0.44 eV at the Γ point, larger than the theoretical freestanding stanene $\sim$ 0.1 eV [231]. Thanks to the strong spin-orbit coupling of stanene, it is considered an optimal platform to observe the quantum spin Hall effect at room temperature. In 2019, H. Song et al. showed that epitaxial α-Sn on InSb is thermally stable at

room temperature. α-Sn thermal stability depends on its thickness and it can be monitored by temperature X-ray diffraction and Raman spectrum. The α to β phase transition temperature in a 30 nm α-Sn film reached 373 K, which is significantly higher than the bulk value of 286 K [201]. In 2002, I. Didschuns studied the Sn thin films and showed that the critical temperature T_c decreased as a function of Sn layer thickness. The 190 nm-thick Sn layer became zero-resistant below 3.14 K, whereas 25 nm-thick Sn layer did not show any superconductivity [61].

In this chapter, I used XRD to investigate the crystal phase and crystalline quality of Sn thin films. The conventional TEM analysis was ineffective for observing the crystalline structure of Sn since the sample degrades during focus ion beam [131]. Compared to TEM, we can leave the samples intact during the XRD analysis. Besides XRD analysis, the morphology of Sn layers was studied using atomic force microscopy (AFM), the chemical composition was investigated using the energy-dispersive X-ray spectroscopy (EDS), and the electrical properties are studied by low temperature transport measurements in a dilution refrigerator. Heat balance calculations are performed to estimate the heating effect on Sn thin films during the AlO_x capping procedure. I also used density-functional theory (DFT) to calculate the band structure and density of states of α-Sn/InSb, with the aim of interpreting the transport properties of Sn/InSb heterostructures.

The Sn thin film samples are fabricated following two steps, (1) metal deposition at low temperature and (2) post-deposition capping. Sn was deposited at 80 K on oxide-free InSb substrate after an atomic hydrogen cleaning (AHC) procedure. The experimental details of the AHC procedure and the Sn deposition parameters are detailed in Chapter 2.3.1 and Chapter 2.3.2. Low deposition temperature ensures the nucleation of a high density of small grains and the growth of a smooth thin film. The capping layer stabilizes the morphology of the film while heating up to room temperature. We studied three capping strategies: AlO_x, Al followed by oxidation and Sn followed by oxidation. AlO_x is known to be thermally stable and have a low permeability to gas. It may therefore prevent the degradation of Sn films in the ambient environment [197, 163]. Native Sn oxide also showed a good thermal stability and is suitable as a capping layer [127, 13].

The standard capping layer recipe is 3 nm-thick AlO_x, used in the Sn thickness study samples. It is the deposition process applied "historically" to the nanowires studied in our group research [168]. For Sn capping layer study, there are three different cappings: (1) 3 nm-thick AlO_x, (2) deposited 1.5 nm-thick Al got oxidized, and (3) deposited Sn got oxidized in poor vacuum.

I aim to understand the growth process on nanowire facets. InSb nanowire has cubic crystalline structure and grows in the (111)B direction. The facets of the nanowire are thus (110). Therefore, my study is focused on the deposition of Sn on InSb(110) substrates. We follow the same growth condition as in [168]: Sn is deposited at 80 K and then capped with AlO_x.

First, I used XRD to study in depth a typical stack (AlO_x/Sn/InSb(110)) (**Subsection: Extended study of 40 nm-thick Sn on InSb**), and second, the influence of the Sn thickness on the crystalline properties (**Subsection: Thickness effect**). Besides, I evaluated the thermal stability

of α-Sn films (**Subsection: α and β-Sn thermal stability**). Finally, I studied the influence of the capping layer on the phase of Sn films (**Subsection: Influence of the capping layers**). To complete the study of Sn thin films, I used AFM and EDS for surface properties. Finally, I used the transport measurements and DFT calculations for studying electronic properties of Sn thin films.

5.2 Crystalline properties by XRD

The crystallographic structure and the crystalline quality of Sn thin film can be revealed by XRD analysis. As detailed in Chapter 2.4.2, we use two scanning modes. The standard out-of-plane mode measures lattice planes parallel to the surface. The in-plane scans measure diffraction in the plane of the sample surface: information on the lattice of ultra thin films and the orientation of grains are collected. In this section, we use XRD analysis to determine both in-plane and out-of-plane lattices of the Sn thin films deposited under different growth conditions.

A crystalline family of planes have an individual diffraction angle which is associated with the d-spacing of the corresponding crystalline planes. We present the diffraction position in Q = 1/d (nm^{-1}), where d is the d-spacing of crystal, also known as interplanar spacing. We present in Table 5.2.1 the diffraction positions using the wave vector values Q (1/d) instead of θ in order to compare data from experiments using different X-ray sources (see Chapter 6). The Q value of α-Sn and InSb are very similar while none of the β-Sn diffractions approach the Q values of InSb.

Crystalline plane	**Q (nm^{-1})**	**Crystalline plane**	**Q (nm^{-1})**	**Crystalline plane**	**Q (nm^{-1})**
β-Sn(200)	3.45	**InSb(220)**	**4.37**	SnO(101)	3.35
β-Sn(101)	3.60	**InSb(400)**	**6.18**	SnO(110)	3.73
β-Sn(220)	4.87	SbSn(101)	3.26	SnO(002)	4.13
β-Sn(400)	6.89	SbSn(012)	4.60	SnO(111)	4.26
α-Sn(220)	**4.36**	SbSn(110)	4.63	SnO(102)	4.90
α-Sn(400)	**6.17**	SbSn(202)	6.52	SnO(202)	6.70

Table 5.2.1: Q value list of relevant crystalline planes of different materials used, namely β-Sn, α-Sn, InSb, SbSn and SnO. The Q values are taken from ICDD database [102].

5.2.1 Extended study of a 40 nm-thick Sn film

First, we focus on one sample Tin4W-110 to understand first the crystalline relation between the Sn layer and InSb(110) substrate. It composes with a nominal 40 nm-thick Sn deposited on a InSb(110) substrate and capped with a 3-nm amorphous AlO_x layer. We determine the crystallographic orientation along the out-of-plane direction.

Figure 5.2.1 shows the crystalline planes of the 40 nm-Sn/InSb(110) sample along the growth direction, revealed by the out-of-plane scan. The intense and sharp peak at Q = 4.37 nm^{-1}, surrounded by periodic fringes, corresponds to InSb(220). The periodic fringes arise from a clean and abrupt interface, namely the interface formed between the α-Sn thin film and the InSb(110) substrate. They are known as "Pendellösung" fringes and correspond to the interference between two X-ray beams propagating in the same direction in a thin film [116]. As expected from Table 5.2.1, the reflections of α-Sn(220) and InSb(220) are almost at the same position due to their similar lattice constant. The magnified region around the InSb(220)/α-Sn(220) reflection shows the α-Sn(220) peak convoluted with InSb(220). Moreover, the InSb peak is asymmetric. From the periods of the fringes, we calculate a thickness of the α-Sn thin film of 38 $\pm$ 0.5 nm using Eq. 2.5, which is relatively close to the nominal thickness of 40 nm. Importantly, we do not observe a diffraction peak of β-Sn in the out-of-plane scan.

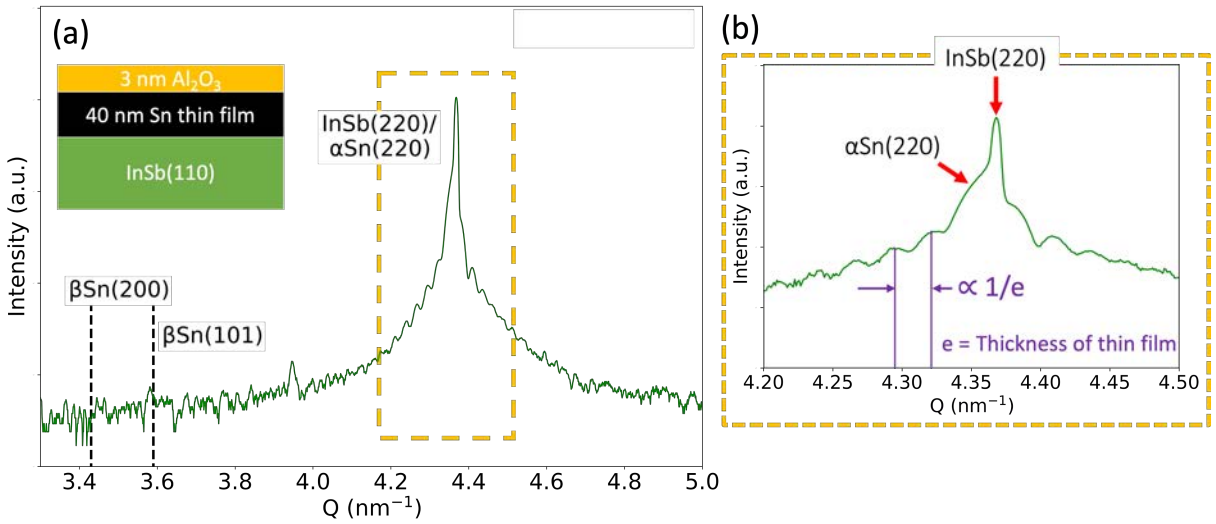

Figure 5.2.1: Out-of-plane XRD scan of sample Tin4W-110. (a) Full scale out-of-plane scan. (b) Magnified region centered around the InSb/Sn peak in (a). The expected β-Sn diffractions are indicated by black dashed lines.

We are interested in the crystalline quality of the α-Sn thin film, which can be evaluated through mosaicity (the definition of mosaicity can be found in chapter 2). Figure 5.2.2 (a) show the ω scans centered on the InSb(220) and α-Sn(220) diffraction individually. We observe that the peak corresponding to the α-Sn layer is broader than the substrate. It suggests that the crystalline quality of the α-Sn film is not as good as that of InSb substrate. We then extracted the peak's FWHM (see Table 5.2.2) from the fit by the Pseudo-Voigt equation. We find that the mosaicity of the α-Sn thin film is three times larger than that of the InSb substrate. This increase in the FWHM of the diffraction in ω-scans confirms that the crystalline quality of the thin film is lower than the InSb substrate.

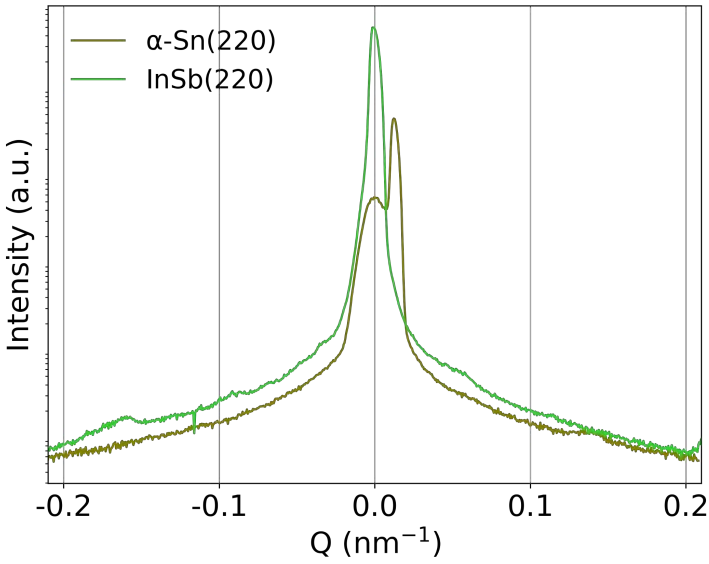

Figure 5.2.2: ω-scans of Tin4W-110 concentrated around α-Sn(220) and InSb(220).

Centered diffraction	**Q (nm^{-1})**	**FWHM (nm^{-1})**
α-Sn(220)	4.36	0.015
InSb(220)	4.37	0.0050

Table 5.2.2: Wave vector Q and FWHM obtained from the fit of the ω-scans of InSb(220) and α-Sn(220) diffractions.

As the difference in lattice parameter between InSb and α-Sn is very small, we expect that an epitaxial relationship between α-Sn layer and InSb substrate, i.e. the Sn thin film to be strained. The strain can be revealed in both in-plane directions, [1$\bar{1}$0] and [001] by a reciprocal space map (RSM) measurement. RSM consists in an in-plane and an out-of-plane component, giving crystalline information along the in-plane and out-of-plane directions, such as strain, mosaicity, and thickness.

We performed RSM measurements centered around the InSb diffractions on two different directions, the InSb(444) (Figure 5.2.3 (b)) and the InSb(800) (Figure 5.2.3 (c)). In the case of the (444) diffraction, the measurement we performed composes diffraction of both (440) and (004), while in the case of the (800) diffraction, it composes the diffraction of (440) and (4$\bar{4}$0).

In both RSM ((444) and (800)) cases, we observe a very thin and intense peak at Q = –0.618 and –0.873 nm^{-1} assigned to the InSb substrate and an extension of this peak towards smaller Q_z attributed to the α-Sn layer. The Sn peak extension has the same in-plane Q_x coordinate as the substrate. We can see that a_0 of Sn in the Q_z direction approaches the bulk value because of strain relaxation along the free direction. The α-Sn thin film is strained in both in-plane directions (Q_x//[001] and Q_y//[1$\bar{1}$0]) but is relaxed in the out-of-plane direction (Q_z//[110]), as illustrated in Figure 5.2.3 (e). The Q values extracted from the RSMs and corresponding to the InSb and Sn diffractions are listed in Table 5.2.3.

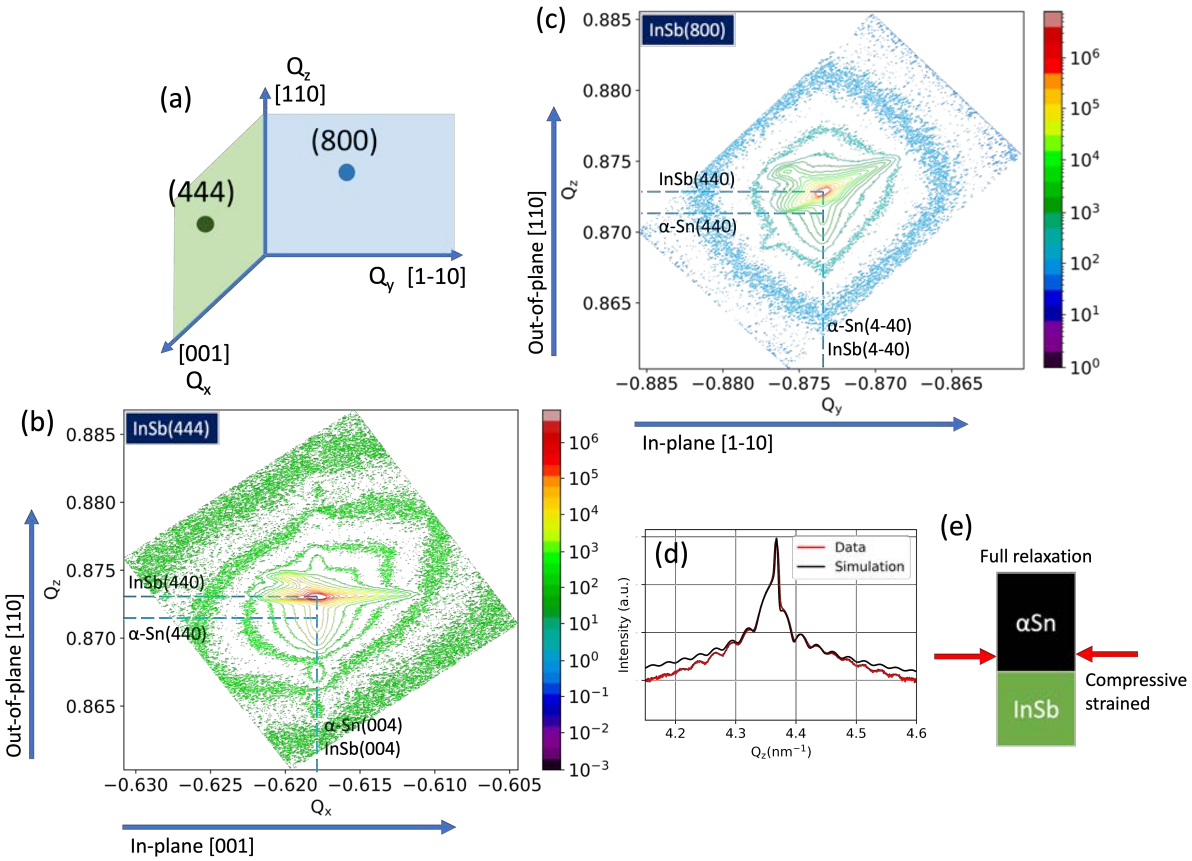

Figure 5.2.3: RSMs of InSb(444) and InSb(800) of Tin4W-110 sample. (a) The positions of chosen diffractions in RSM measurements. RSM measurements on (b) InSb(444) and (c) InSb(800). (d) The simulation of out-of-plane scan and measurement data extracted from (b) along Q_X = –0.618 nm^{-1} (red) plotted with the simulation of α-Sn film of 38 nm fully strained on InSb. (e) Schematic of epitaxial α-Sn thin film on InSb undergoing compressive strain.

We extracted a line scan for Q_X = –0.618 nm^{-1} from RSM InSb(444) (see Figure 5.2.3 (c)). We observe Pendellösung fringes as seen in Figure 5.2.1. We then simulate α-Sn layer of thickness 38 nm fully strained on InSb using the software Smart Studio provided by Rigaku. The result of the simulation is plotted together with the experimental data. We observe that the two curves matched, confirming that the α-Sn layer is fully strained on InSb substrate.

In conclusion, our RSM measurements show that the 40 nm Sn thin film is fully strained in the in-plane direction. The measurements were performed with an out-of-plane component, and we would like to see now only in-plane measurement to have a comprehensive assessment of the crystalline properties of thin film along the in-plane direction.

Direction	Crystalline plane	Measured Q (nm^{-1})	Measured a_0 (nm)	ICDD a_0 (nm)
Q_x	α-Sn(004)	0.618	6.472	6.489
	InSb(004)	0.618	6.472	6.478
Q_y	α-Sn(4$\bar{4}$0)	0.874	6.472	6.489
	InSb(4$\bar{4}$0)	0.874	6.472	6.478
Q_z	α-Sn(440)	0.872	6.487	6.489
	InSb(440)	0.874	6.472	6.478

Table 5.2.3: Q values and lattice parameters a_0 along Q_x, Q_y, and Q_z for α-Sn and InSb.

We expect the in-plane XRD analysis to show overlapping diffraction peaks of α-Sn and InSb. The two in-plane directions, [001] and [$\bar{1}$10], are studied. Surprisingly, several β-Sn peaks are visible along those directions. We indexed three diffractions: β-Sn(200), β-Sn(101), and β-Sn(400), as seen in Figure 5.2.4 (b). In addition, SnO peaks are visible at Q = 3.35 and 6.68 nm^{-1} and correspond to the SnO(101) and SnO(202) diffractions respectively. The presence of these SnO peaks indicates the existence of Sn oxide grains in/on the Sn thin film. Finally, we observe a peak at Q = 4.62 nm^{-1} which corresponds to the SbSn(110) diffraction. We next determined the possible β-Sn orientation with respect to the InSb substrate.

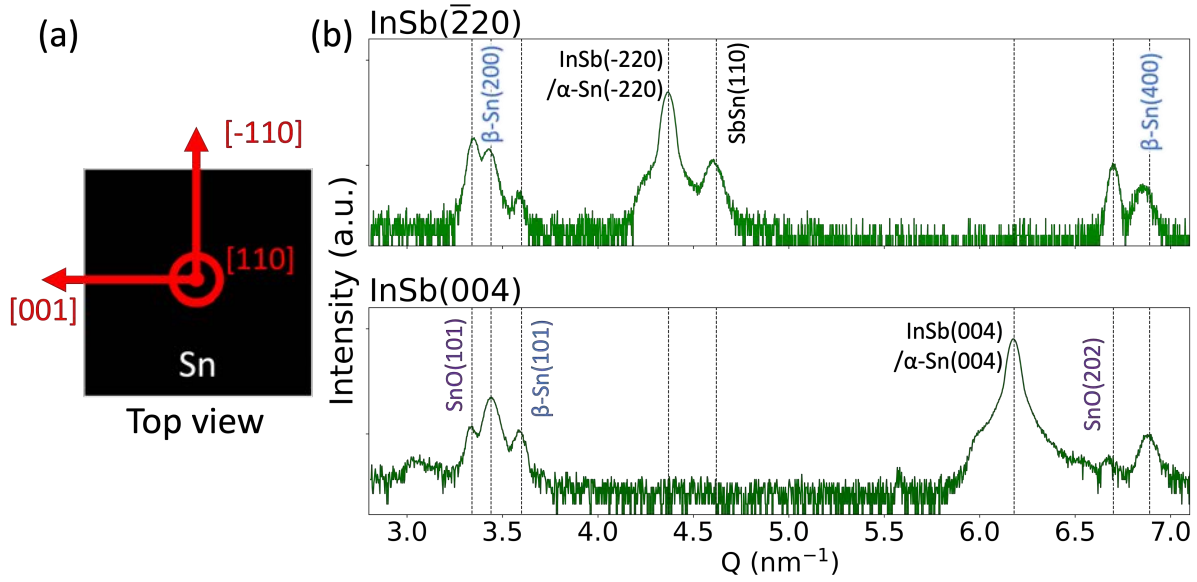

Figure 5.2.4: In-plane XRD measurements along [001] and [$\bar{1}$10] directions. (a) Schematic of the two measurement directions. (b) In-plane XRD scans along InSb(2̄20) and InSb(004). The diffraction peaks are marked as black dashed lines.

The crystalline orientation of the β-Sn grains is analyzed with ϕ scans. While rotating the sample in the ϕ direction, the $2\theta_\chi$ diffraction angle is fixed to certain value, probing the corresponding crystalline plane in all directions in the plane of the sample (see Figure 5.2.5 (a)).

Figure 5.2.5 (b)-(d) shows the ϕ scans performed on the sample with a 200° scanning range for three different diffractions: β-Sn(200), β-Sn(101), and InSb(2̄20). We observe that β-Sn

crystalline grains are not randomly orientated in the α-Sn layer, i.e. they show 90° periodicity. Also, β-Sn(200) and β-Sn(101) planes align with InSb($\bar{2}$20) at ϕ = 0°. Therefore, β-Sn grains have two preferable orientations in Sn thin film.

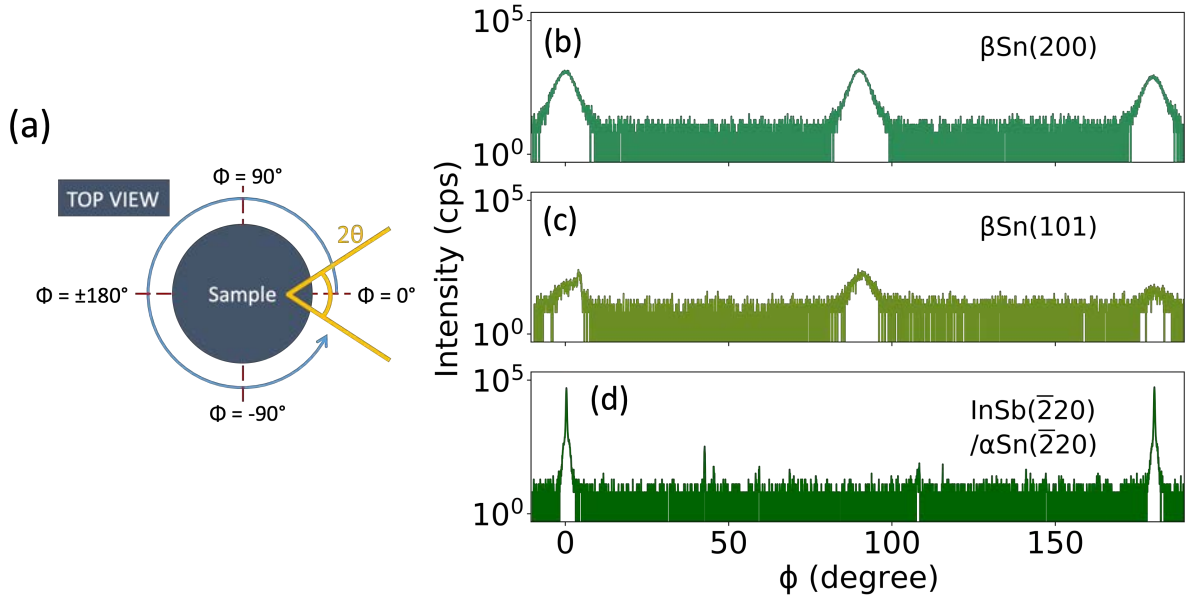

Figure 5.2.5: ϕ scans. (a) Schematic of the ϕ direction from the top of the sample. (b)(c)(d) ϕ scans of individual crystalline plane aligned with InSb($\bar{2}$20) at ϕ = 0°.

Using the ϕ scans from Figure 5.2.5, we can then construct the orientation of the β-Sn grains with respect to the α-Sn layer. Figure 5.2.6 shows how both β-Sn(200) and β-Sn(101) grains align with α-Sn($\bar{2}$20).

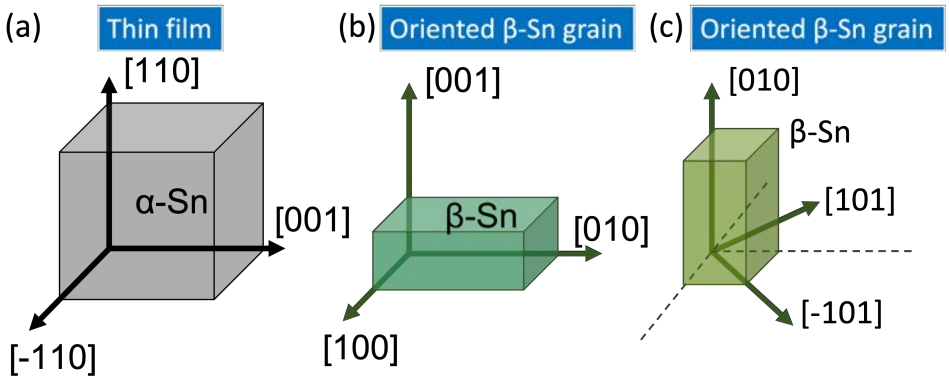

Figure 5.2.6: Illustration of β-Sn grain orientations in α-Sn thin film revealed by the ϕ scans.

To verify the hypothesis that the most abundant β-Sn has its [001] plane oriented parallel to the [110] plane of the substrate, we looked for the presence of a diffraction equivalent to the β-Sn(001) planes along the out-of-plane direction. Based on the calculation and the simulation of Smart Studio (provided by Rigaku), the only possible diffraction along β-Sn[001] is β-Sn(004), which is a weak diffraction peak at a high wave vector Q = 12.57 nm^{-1}. It can thus be seen only

for a large amount of β-Sn. In one of the Sn/InSb(110) samples, CPD156-110, the β-Sn(004) is visible in the out-of-plane XRD scan. The sample stacking consists in a 40 nm-thick Sn thin film grown on an InSb(110) substrate and capped with 10 nm thick AlO_x.

Figure 5.2.7 shows the out-of-plane scan on CPD156-110. We observe an intense InSb(220) peak surrounded by fringes caused by the presence of the α-Sn film. A second weak peak is visible at Q = 12.57 nm^{-1} and we assign it to β-Sn(004). The β-Sn(200) and β-Sn(101) diffractions are not visible similarly to the out-of-plane XRD scan of Tin4W-110. This observation supports our previous hypothesis that part of the β-Sn grains are aligned in-plane along β-Sn[100]//InSb[$\bar{1}$10] and β-Sn[010]//InSb[001], and out-of β-Sn[001]//InSb[110] direction. Thus, we confirm that the major orientation of β-Sn in the epitaxial α-Sn layer corresponds to the drawing of Figure 5.2.6 (b).

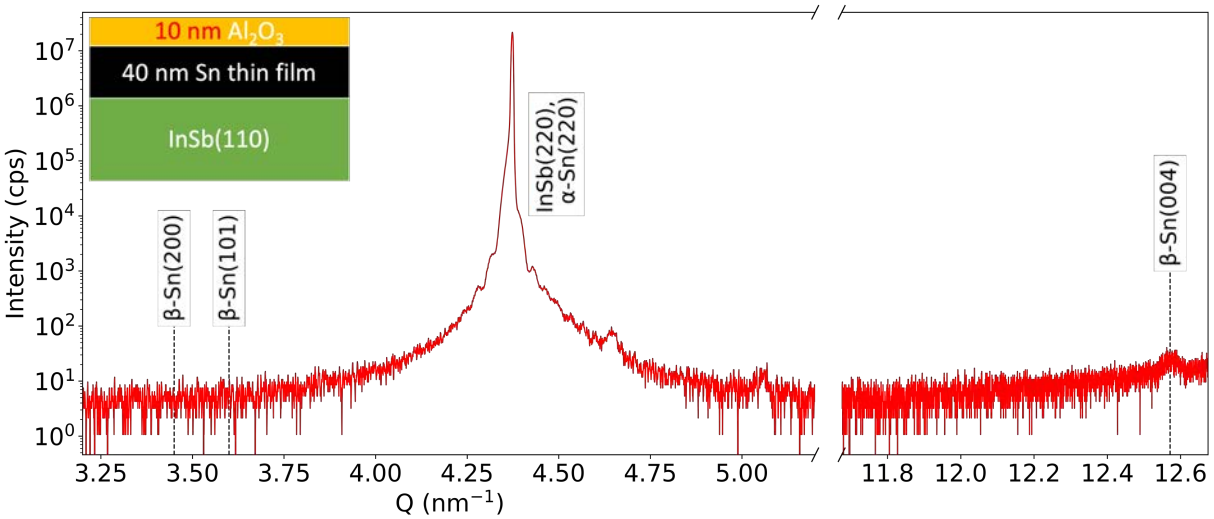

Figure 5.2.7: [CPD156-110] Out-of-plane XRD measurement of a 40 nm-thick Sn thin film grown on InSb(110) with a 10 nm AlO_x capping layer. The sample stacking is shown on the top left. Black vertical dashed lines with label correspond to expected β-Sn diffractions.

5.2.2 Influence of the thin film thickness

We are interested in the evolution of the crystalline structure and quality of Sn thin films for increasing thicknesses. We studied: 6, 10, 15, and 40 nm thick Sn layers grown on InSb(110) and InSb(100) substrates. On the top of the Sn layer, a 3 nm AlO_x capping layer is deposited to protect the thin film from oxidation and de-wetting (see paragraph on Sn films fabrication description in chapter 2). The samples are listed in Table 5.2.4.

Substrate	Sample name	Nominal Sn thickness (nm)	Measured Sn thickness (nm)	Capping
InSb(110)	Tin1W-110	6	7.2 ± 0.5	3 nm AlO_x
	Tin2W-110	10	10.2 ± 0.5	
	Tin3W-110	15	14.2 ± 0.5	
	Tin4W-110	40	38.1 ± 0.5	
InSb(100)	Tin1W-100	6	4.7 ± 0.5	3 nm AlO_x
	Tin2W-100	10	6.7 ± 0.5	
	Tin3W-100	15	10.6 ± 0.5	
	Tin4W-100	40	27.5 ± 0.5	

Table 5.2.4: Sample list of Sn thickness study with the used substrate, the sample name, their nominal thickness, measured thickness from out-of-plane XRD measurement and capping material.

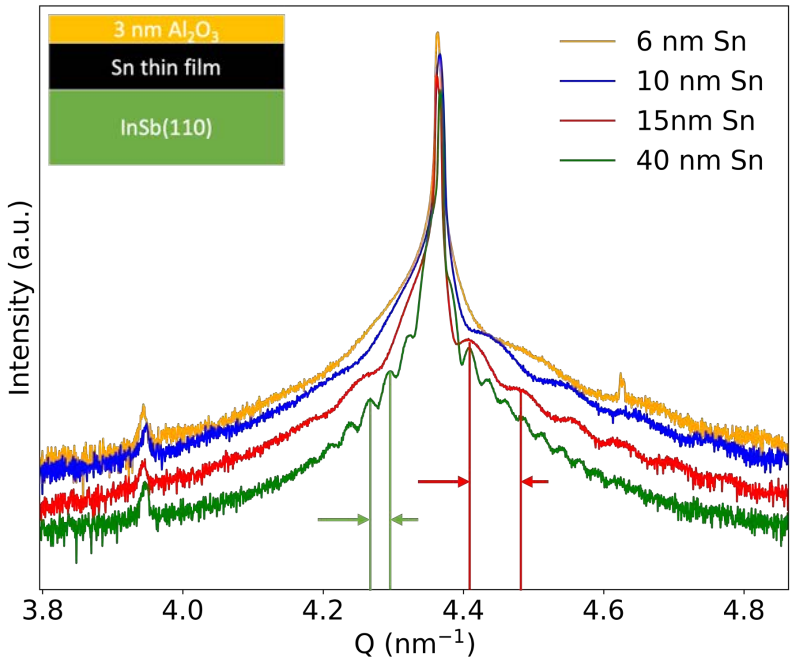

Figure 5.2.8: [Tin1W-110, Tin2W-110, Tin3W-110, Tin4W-110] Out-of-plane XRD measurements of Sn thin films grown on InSb(110) with different thickness. The solid vertical lines highlight one period of a Pendellösung fringe for two different Sn thicknesses.

Figure 5.2.8 shows out-of-plane XRD measurements of Sn thin films with different thicknesses grown on InSb(110) substrates. We observe that the period of the fringes surrounding the InSb(220) diffraction varies as function of Sn thickness, i.e. for the thinnest Sn layers, the fringe period is longer, whereas for the thickest Sn thin films, the fringe period is shorter. α-Sn layer thickness calculated from the period of fringes is listed in Table 5.2.8 for each sample: we observe that the calculated thickness approaches its nominal value. We also notice that Sn

layers are thicker on InSb(110) samples than on InSb(100) samples. We need to verify if the reason for that is technical (the (001) sample was placed in the center where flux is maximum) or structural, as growth rates may be sensitive to substrate orientation [42]. The out-of-plane measurements on Sn/InSb(100) samples can be found in the Supplementary.

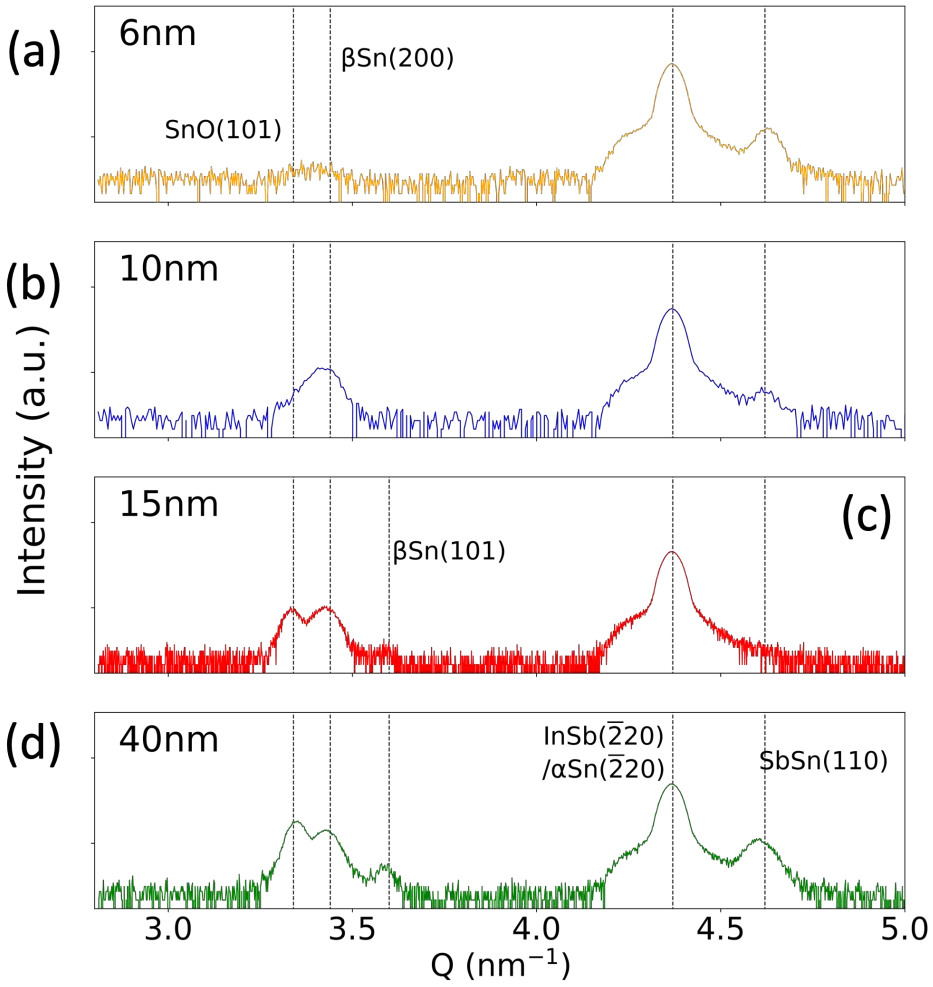

Figure 5.2.9: [Tin1W-110, Tin2W-110, Tin3W-110, Tin4W-110] In-plane XRD measurements along the InSb($\bar{2}$20) direction for different Sn thicknesses. The dotted vertical lines indicated the diffractions.

After studying the consequence of an increase in the Sn film thickness in the out-of-plane direction, we study the same films using in-plane XRD. Figure 5.2.9 shows the in-plane XRD measurements realized on Sn thin films for different thicknesses. We find that all the Sn/InSb(110) samples show the substrate diffraction at Q = 4.37 nm^{-1} assigned to InSb($\bar{2}$20). α-Sn is fully strained in the in-plane directions, so we cannot resolve the diffractions of α-Sn($\bar{2}$20) and InSb($\bar{2}$20) via the in-plane measurements. β-Sn diffractions becomes more visible at Q = 3.45 and 3.60 nm^{-1} with increasing Sn thickness. Also, the SnO(101) diffraction at Q = 3.35 nm^{-1} is visible, indicating that the Sn layer got oxidized even with the AlO_x capping layer. The presence of SbSn(110) at Q = 4.63 nm^{-1} indicates that the Sn layer and the InSb substrate intermixed [164]. But the reason for the formation of this phase is not yet clear to us. SbSn

appeared in all the Sn/InSb(110) samples except the 15 nm thick Sn film. Understanding such behavior requires additional analysis focusing on SbSn diffractions, yet it is not the goal of this manuscript.

5.2.3 α and β-Sn thermal stability

We are interested in studying the thermal stability of α-Sn thin films using temperature-dependent XRD. Previous researches showed that the transition temperature of 20 nm-thick epitaxial α-Sn film on InSb substrate is 440 K, which is much higher than the transition value of Sn in bulk (286 K) [201]. The α-Sn thin film is indeed stabilized by the strain induced by epitaxy on the InSb substrate. This strain prevents phase transition from α to β [201, 98]. Thus, we studied 15 and 40 nm Sn films to evaluate the effect of the thickness on the transition temperature. The details of the temperature-dependent XRD technique can be found in the Methodology.

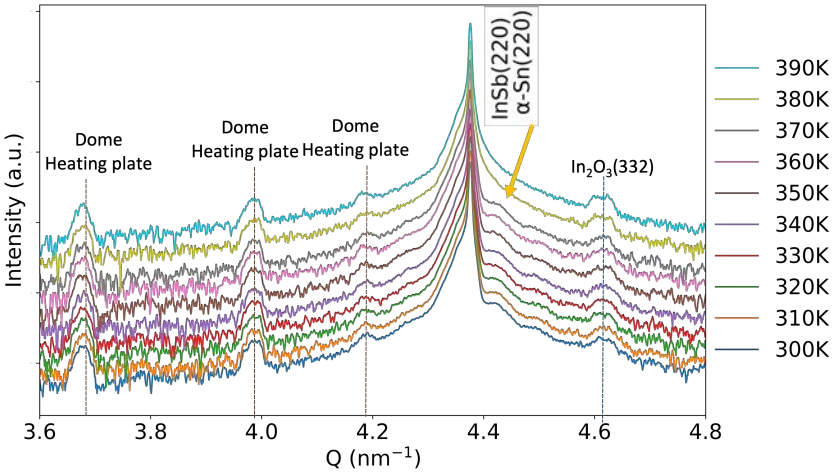

Figure 5.2.10: [Tin3W-110] Out-of-plane XRD scans performed on the 15 nm-thick Sn film. The yellow arrow indicates the temperature at which the Pendellösung fringes disappear. The peaks originating from the setup are indicated by labeled vertical lines.

Figure 5.2.10 shows the temperature-dependent XRD measurements on the 15 nm-thick Sn film grown on an InSb(110) from 30 to 390 K. We observe that the Pendellösung fringes of the epitaxial α-Sn disappear at 380 K.

Figure 5.2.11 shows the temperature-dependent XRD measurements on the 40 nm-thick Sn thin film. We observe that the periodic fringes disappear at around 340 K, and meanwhile β-Sn peaks appear. This evolution suggests that α-Sn transitions into β-Sn at this temperature. The phase transition temperature of the 40 nm-Sn film on InSb is around 330 K to 340 K, which is lower than that of 15 nm-thick Sn film. From these two temperature-dependent XRD measurements, we conclude that thicker α-Sn epitaxial films are thermally less stable. The transition from the α- to β-phase of Sn is irreversible in our temperature range.

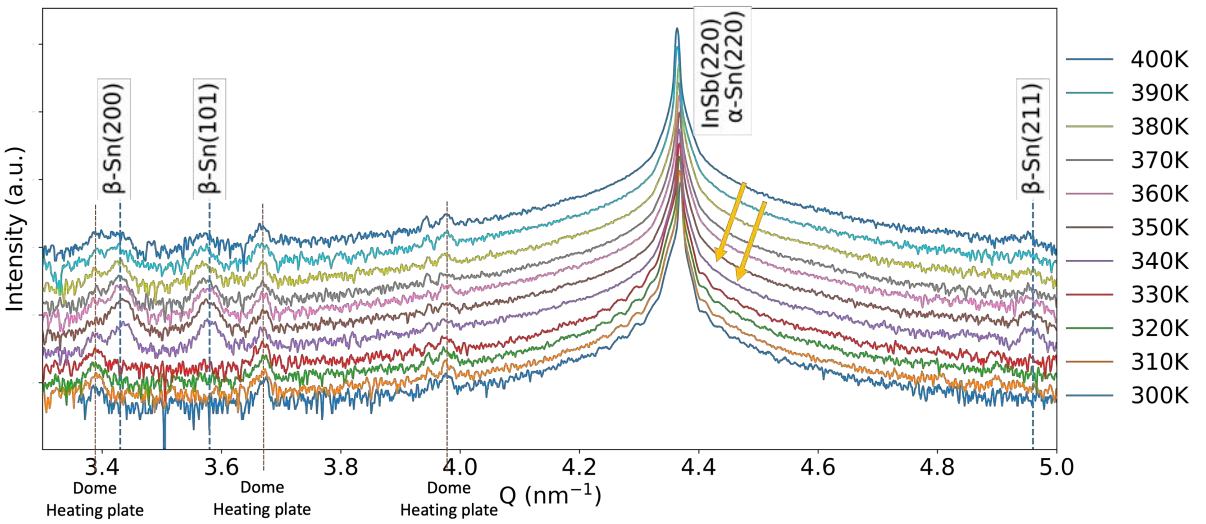

Figure 5.2.11: [Tin4W-110] Out-of-plane XRD scans performed on the 40 nm-thick Sn thin film. The yellow arrows indicate the temperature at which the Pendellösung fringes disappear. The β-Sn diffractions are indicated by the blue dashed lines. The peaks originating from the setup are indicated by labeled vertical lines.

5.2.4 Influence of a capping layer

The function of the capping layer is to firstly prevent Sn films from de-wetting and then prevent it from oxidation in the ambient environment. Thus, we studied three capping methods: (1) AlO_x, (2) a 1.5 nm-thick Al layer followed by oxidation at poor vacuum to form an AlOx cap (deposited Al oxidized), and (3) the surface of Sn is oxidized to form an native Sn oxides cap (deposited Sn oxidized). We are curious if the different capping methods can affect the crystalline properties of Sn thin films. Sn thin films of 16 nm are deposited on InSb(110) and InSb(100) substrates under the same conditions yet capped differently (see Table 5.2.5). For clarity, only the measurements of Sn/InSb(110) are presented in the main text, while the measurements of Sn/InSb(100) can be found in the Supplementary.

First, we studied the influence of capping on the crystalline structure of the thin film along the growth direction. Figure 5.2.12 shows out-of-plane XRD measurements of three capped samples. The intense and sharp InSb(220) diffraction is present at Q = 4.37 nm^{-1} in all samples. It is surrounded by the fringes caused by the presence of an epitaxial α-Sn layer. The fringe period of the Sn oxidized sample is slightly longer than that of the others, meaning that the effective thickness of the Sn thin film stabilized by oxidation is smaller. We expected that Sn is consumed via the formation of an oxide, reducing effectively the thickness of the Sn film. The measured thicknesses are in Table 5.2.5. We do not observe any β-Sn peak along the growth [110] direction, yet a SbSn(110) diffraction is present in all samples with a higher intensity for the AlO_x capped Sn thin film.

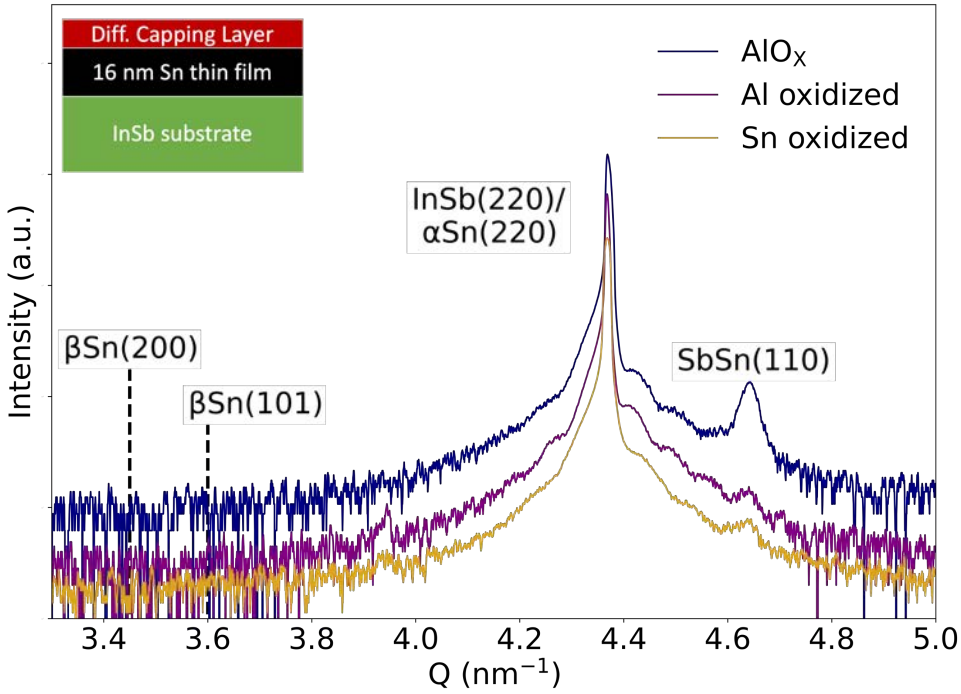

Figure 5.2.12: [CPD166-110, CPD167-110, CPD168-110] Out-of-plane XRD measurements on the capping study samples. The expected β-Sn diffractions are indicated with the black dashed lines with the labels. The sample stacking is illustrated at upper left.

Substrate	Sample name	Nominal Sn thickness (nm)	Measured Sn thickness (nm)	Capping layer
InSb(110)	CPD166-110	16.3	12.3 ± 0.5	3 nm AlO_x
	CPD167-110	16.3	13.5 ± 0.5	deposited 1.5 nm Al oxidized
	CPD168-110	16.3	10.1 ± 0.5	deposited Sn oxidized
InSb(100)	CPD166-100	16.3	11.0 ± 0.5	3 nm AlO_x
	CPD167-100	16.3	10.5 ± 0.5	deposited 1.5 nm Al oxidized
	CPD168-100	16.3	8.4 ± 0.5	deposited Sn oxidized

Table 5.2.5: List of samples analyzed to study the influence of the nature of the capping.

We then studied the structural properties of the differently capped thin films along the in-plane direction of the sample. Figure 5.2.13 shows the in-plane XRD measurements along the InSb($\bar{2}$20) direction. InSb($\bar{2}$20)/α-Sn($\bar{2}$20) and SbSn(110) diffractions are present for all samples and do not differ from a capping method to another one. The β-Sn(200) diffraction appears only in the AlO_x capped Sn thin film, and not in the Al oxidized or the Sn oxidized ones. Besides, the SnO(101) diffraction is visible for all the samples, with higher intensity for the AlO_x capped sample. From those measurements, we learn that the AlO_x capping is responsible for the presence of the β-Sn phase in Sn thin film.

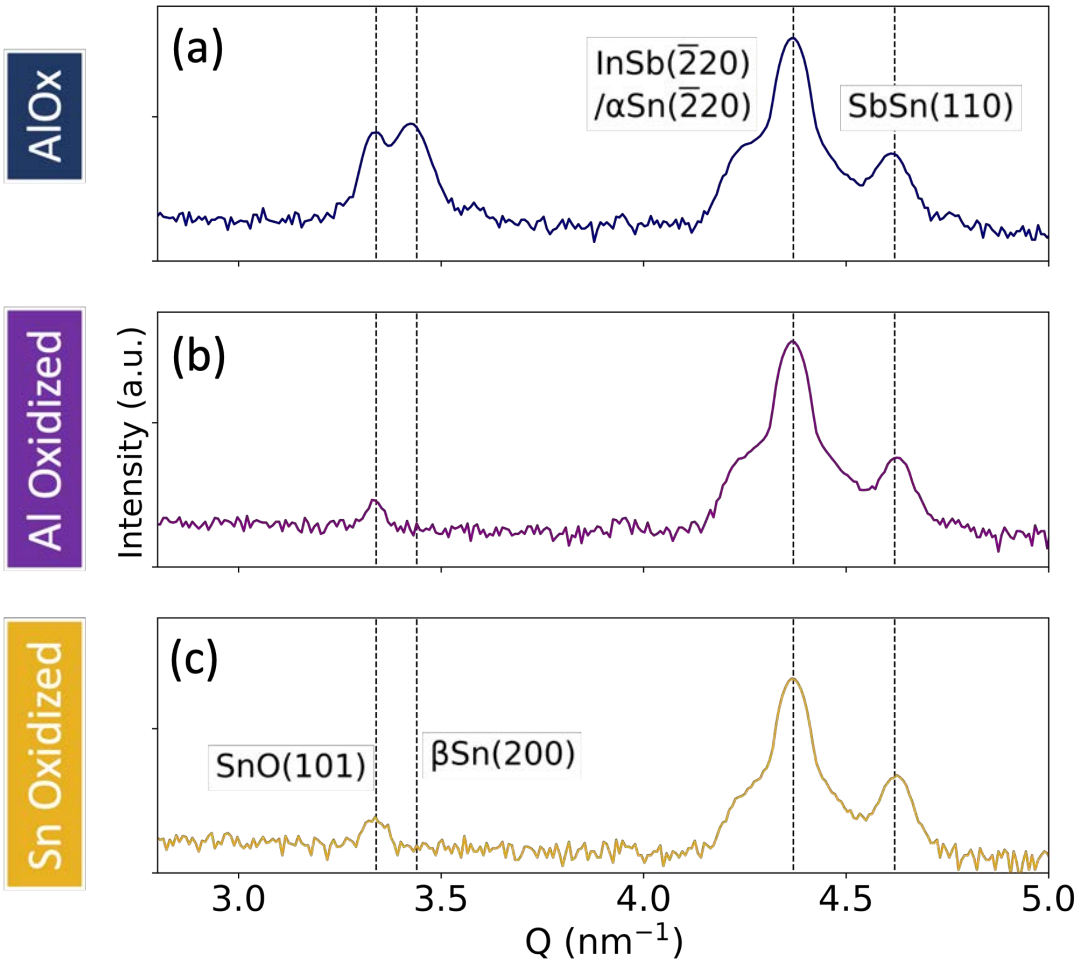

Figure 5.2.13: [CPD166-110, CPD167-110, CPD168-110] In-plane XRD measurements along the InSb($\bar{2}$20) direction. The black dashed lines indicat the diffractions of interest, including SnO(101), β-Sn(200), InSb($\bar{2}$20)/α-Sn($\bar{2}$20) and SbSn(110).

We wanted to understand which parameter in the AlO_x deposition triggers the formation of β-Sn. The β-phase of Sn is favored at higher temperature, and appears upon heating of the α-Sn phase [201]. Remember that the Sn films are deposited at 80 K. They are then transferred *in situ* to a different chamber for AlO_x deposition (in this chamber there is no possibility to control the temperature). AlO_x is deposited by evaporation from an electron beam source. In the following, we thus try to estimate the temperature of the sample surface during deposition.

The Sn/InSb sample is fixed on a 3-inch molybdenum sample holder with a 2 mm-thick of indium, which has good thermal conductance. The size of the sample is around 1 inch in diameter and 0.5 mm-thick. Its total volume is negligible in comparison with the sample holder. We therefore consider that the temperature of the sample holder will determine the temperature of the sample surface.

In order to calculate the heat balance of the system comprising the holder and the sample, we consider three heating sources: (1) the absorbed radiations from the AlO_x source P_a, (2) the absorbed radiations from the walls of the vacuum chamber (considered to be at 300 K) P_b

and (3) the emission of the sample holder (considered to be at 80 K prior to deposition) P_c. We neglected the absorbed heat converted from the kinetic energy of AlO_x molecules reaching the sample surface, and consider the sample holder isolated from its support.

We consider that during the deposition process, the energy due to the variation of temperature of the sample holder equals to the sum of the heat absorbed and emitted by the sample holder. This translate into the following question:

$$C(T)\frac{dT}{dt} = P_a + P_b - P_c(T) \tag{5.1}$$

C(T) is the heat capacity of the sample holder and t is the time at which the deposition of AlO_x starts. To eventually integrate Eq.5.1, we need to estimate the powers, P_a, P_b and P_c individually using the black body approximation described by the Stephan-Boltzmann law $j^* = \sigma T^4$. j^* is the total radiated energy per unit surface area of a black body per unit time, σ is the Stefan-Boltzmann constant ($5.6 \times 10^{-8}\,Wm^{-2}K^{-4}$), and T is the thermodynamic temperature of the black body. Then, the estimation of the emissivity of the materials is difficult because the emissivity depends practically on the temperature, the range of wavelength, and the surface coating, for example. In our experimental condition, the steel evaporate chamber and the molybdenum sample holder are oxidized, rough and covered with the deposited materials. Hence we make the approximation that the AlO_x source, the steel chamber and the sample holder are ideal black bodies with an emissivity of 1. The equation is solved using Matlab software by our colleague L. Bellon from ENS Lyon. The details of the computation can be found in [43].

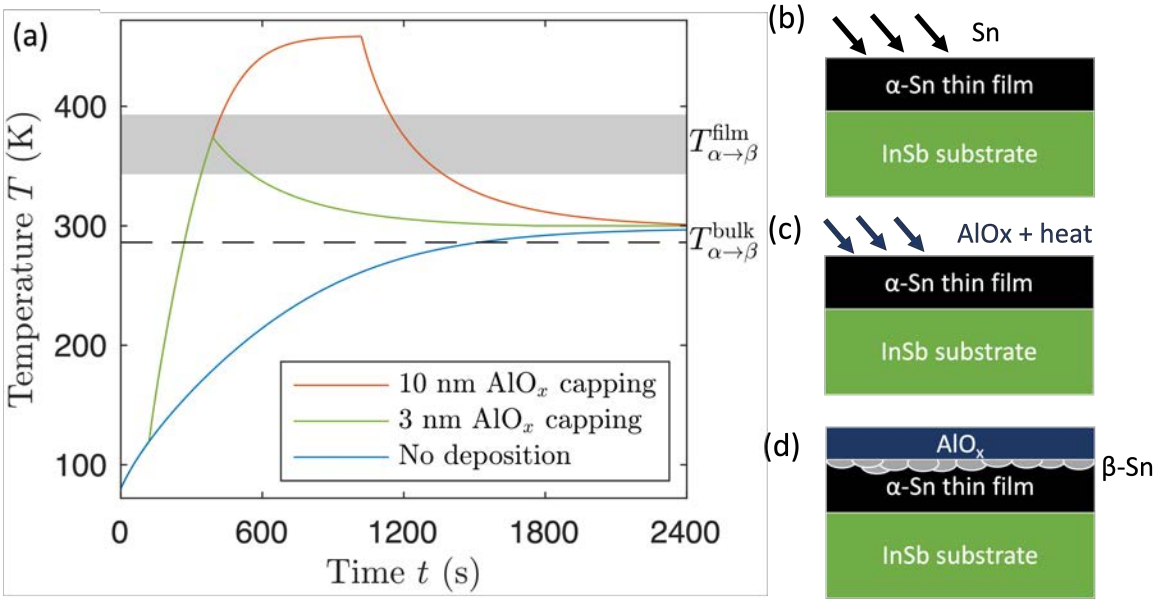

Figure 5.2.14: (a) Substrate temperature evolution during AlO_x capping process as function of time. The black dashed line at 286 K indicates the phase transformation temperature of bulk Sn and the gray region represents the phase transformation temperature range of α-Sn epitaxial thin films. (b)-(d) Schematics illustrate our theory on the formation of β-Sn grain based on the experimental conditions and calculations [43].

Based on those assumptions, we solved Eq.5.1 and plot the evolution of the sample holder temperature with the time in Figure 5.2.14 (a). We observe that if no AlO_x deposition occurs, the sample holder reaches room temperature after 30 minutes. If we consider that there is a slight delay between the end of Sn deposition and the beginning of AlO_x deposition due to transfer (around 2 minutes), then the sample temperature reaches 370 K after 4 minutes 30 seconds (3 nm AlO_x) and 450 K after 15 minutes (10 nm AlO_x). We observe that the sample temperature attains a critical region of phase transformation, which ranged from 343 K to 393 K depending on the thickness. We see that 10 nm-thick AlO_x capping leads to a temperature exceeding the phase transformation region. Figure 5.2.14 (b)-(d) illustrates how epitaxial α-Sn thin film is transformed partially into β-Sn grains as a result of the AlO_x capping procedure.

5.3 Surface properties by AFM and EDS

5.3.1 Effect of substrate and layer thickness

We used the AFM tapping mode to profile the the sample surface and measure its root-mean-square (RMS) roughness. At least three images 10 μm $\times$ 10 μm large are measured per Sn/InSb sample to avoid measurement bias. The RMS roughness of the surface is measured on the surface outside the grains if any appeared. The AFM analysis of Sn thin films grown on InSb(110) and on InSb(001) can be found below.

First, we observe that (110) and (001) do not have the same morphology, as seen in Figure 5.3.1). On Sn/InSb(110) sample, we observe the presence of grains; in contrast, there is no grains observed on the surfaces of Sn/InSb(001) samples. The RMS roughness slightly increased with increasing Sn thicknesses, i.e. root-mean-square (RMS) roughness = 0.49 nm for 6 nm Sn layer and 0.61 nm for 40 nm.

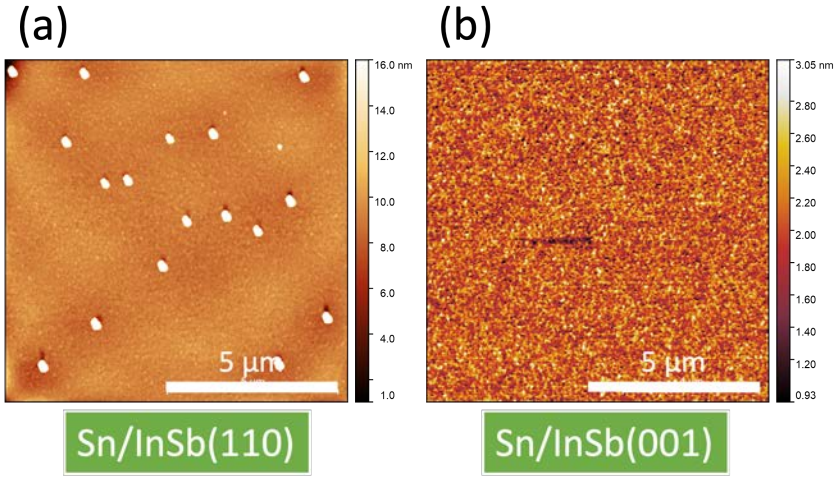

Figure 5.3.1: [CPD166-110, CPD167-100] AFM images of Sn thin films grown on InSb(110) and InSb(001) substrates.

Second, we discussed the morphology of Sn thin films as a function of thickness, as seen in Figure 5.3.2. We observe that the grains are present in all the samples. Besides, the surface area outside the grains becomes rougher when the Sn thickness increases, i.e. RMS roughness = 0.35 nm for 6 nm Sn layer and 1.28 nm for 40 nm. The RMS roughness is listed in Table 5.3.1 for each sample. The grains grow bigger in thicker Sn thin films in terms of height and radius. The 6 nm Sn layer has grains of 39 nm in height and 57 nm in radius; in contrast, the 40 nm Sn layer had grains of 70 nm in height and 158 nm in radius. The density of grains does not change as a function of Sn thickness, which suggests that the grains are already present on the substrate prior to the deposition of the Sn film.

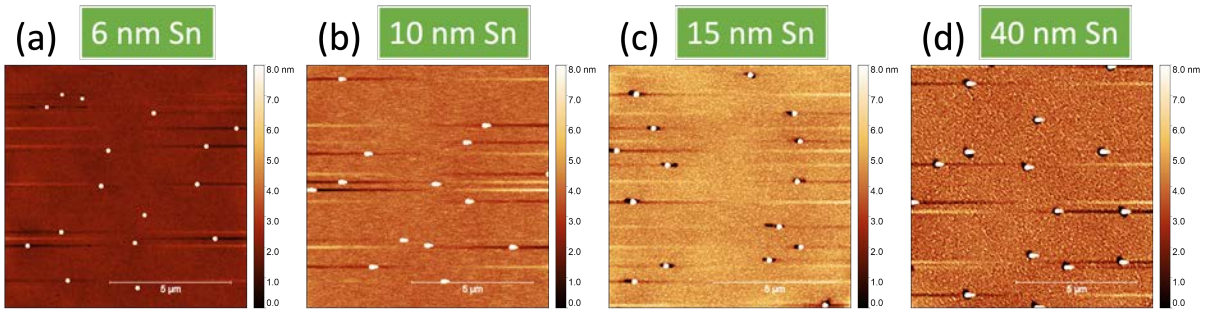

Figure 5.3.2: [Tin1W-110, Tin2W-110, Tin3W-110, Tin4W-110] AFM images of Sn thin films in the Sn thickness study. The scanning area is 10 μm $\times$ 10 μm for each.

Sample	**Capping**	**RMS roughness (nm)**	**Grain height (nm)**	**Grain radius (nm)**	**Grain density (μm^{-2})**
Tin1W-110	AlO_x	0.35 ± 0.11	39 ± 6	57 ± 10	0.19 ± 0.01
Tin2W-110	AlO_x	0.60 ± 0.07	52 ± 6	77 ± 15	0.14 ± 0.01
Tin3W-110	AlO_x	0.64 ± 0.11	66 ± 8	82 ± 14	0.14 ± 0.01
Tin4W-110	AlO_x	1.28 ± 0.20	70 ± 5	158 ± 17	0.13 ± 0.01
CPD166-110	AlO_x	0.45 ± 0.09	49 ± 3	111 ± 5	0.20 ± 0.02
CPD167-110	Al oxidized	0.73 ± 0.34	72 ± 5	152 ± 10	0.15 ± 0.01
CPD168-110	Sn oxidized	0.89 ± 0.34	96 ± 3	159 ± 3	0.10 ± 0.01

Table 5.3.1: List of AFM analysis on the Sn/InSb(110) samples, including the RMS roughness the grains' dimensions, and the grains' density.

From these AFM analysis, we conclude that the presence of the grains is irrelevant to the emergence of β-Sn. The three reasons are: (1) No grains observed on Sn/InSb(001) substrates while they show β-Sn by XRD. (2) Grain density remains constant with thicker Sn films. (3) No change in density for different capping. Yet only AlO_x capping leads to β-Sn. Now we want to analyze the chemical composition of those grains.

5.3.2 Surface grains: composition analysis

The composition of the grains cannot be determined by XRD as they seem to not diffract the X-rays. Therefore, we used energy dispersive X-ray spectroscopy (EDS) installed in the SEM to analyze the chemical composition of the grains. A 6 keV electron beam is used based on the energy of L_α emission of Sn, In, and Sb. We analyzed 7 grains on the 16 nm Sn film grown on the InSb(110) substrate and capped with a 3 nm AlO_x layer (CPD166-110).

Figure 5.3.3 shows the elemental analysis on a surface comprising grain. We find that the grain is Sn-rich and surrounded by an In-rich region. The elemental spectrum confirmed that the center of grain is Sn-rich compared to the substrate region, the same as the observation in the element mappings. The reasons for the grain formation are still unknown and require more analysis.

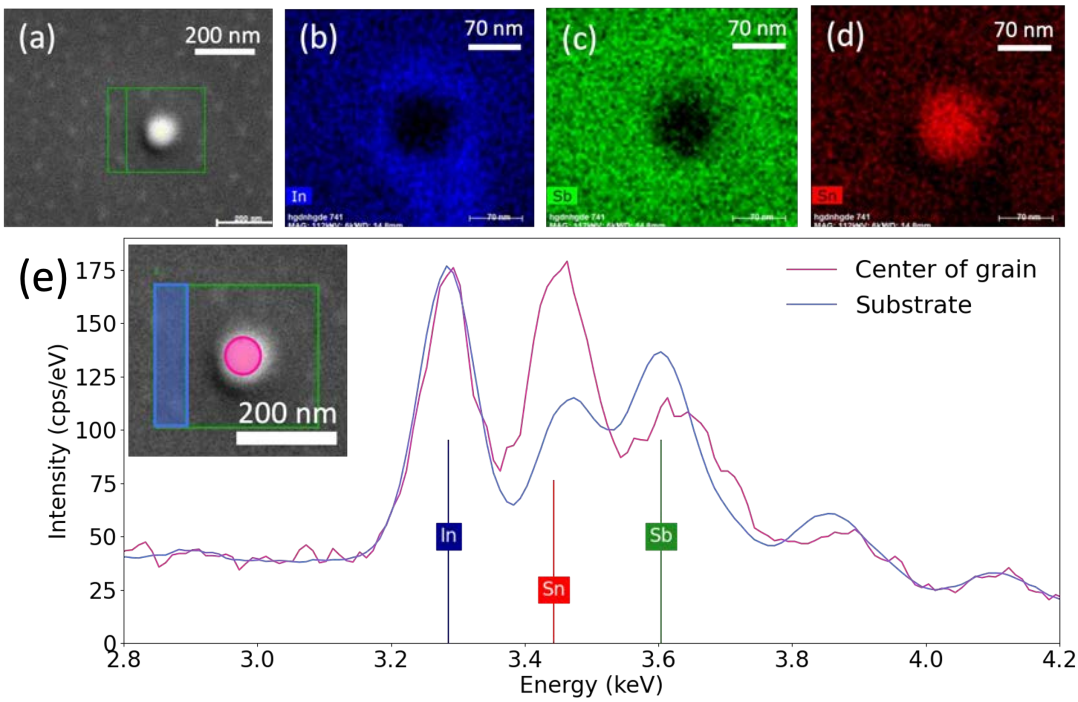

Figure 5.3.3: [CPD166-110] Composition analysis of grains on the Sn/InSb(110) surface in the SEM-EDS system. (a) Plan-view SEM image of the surface containing a grain. The green rectangle region indicates the region probed by EDS. EDS maps for (a) In, (b) Sb, and (c) Sn. (e) EDS spectrum of elemental analysis performed on the grain (in pink) and the substrate (in blue).

In conclusion, the grains observed by AFM are Sn-rich and are mostly present on the (110) surfaces. Their density does not depend on the Sn thickness, yet their size does. Importantly, they are not related to the formation of β-Sn grains.

We have the hypothesis that the grains are linked to the surface preparation prior to Sn deposition. As mentioned earlier, we use the atomic hydrogen cleaning (AHC) technique to remove oxide from the substrate. Yet, the cleaning was optimized for InSb(001) substrates which has no visible grains. One detrimental effect known from AHC studies is that if too

strong, AHC can also damage the surface of III-V substrate [208] by creating shortage of group V, In droplets, and/or removing crystallites [209]. Thus, it results in a rougher surface or even the formation of clusters (grains) [28, 12]. The cleaning conditions need to be optimized to prevent subsequent formation of those Sn-rich grains on InSb(110) surfaces.

5.4 Electronic properties

5.4.1 Transport measurements

Influence of the Sn thickness

We are interested in the electrical properties of our Sn films and in particular, we wanted to determine whether they were superconducting or not. We then studied: the 6 nm-thick and 15 nm-thick Sn films grown on InSb(001). The transport measurements at a low temperature are performed in a dilution fridge at the University of Pittsburgh in the group of S. Frolov, our collaborator in the ANR-NSF HYBRID project. A 4-probes configuration is used: two probes used to apply voltage and the two others are used to measure current.

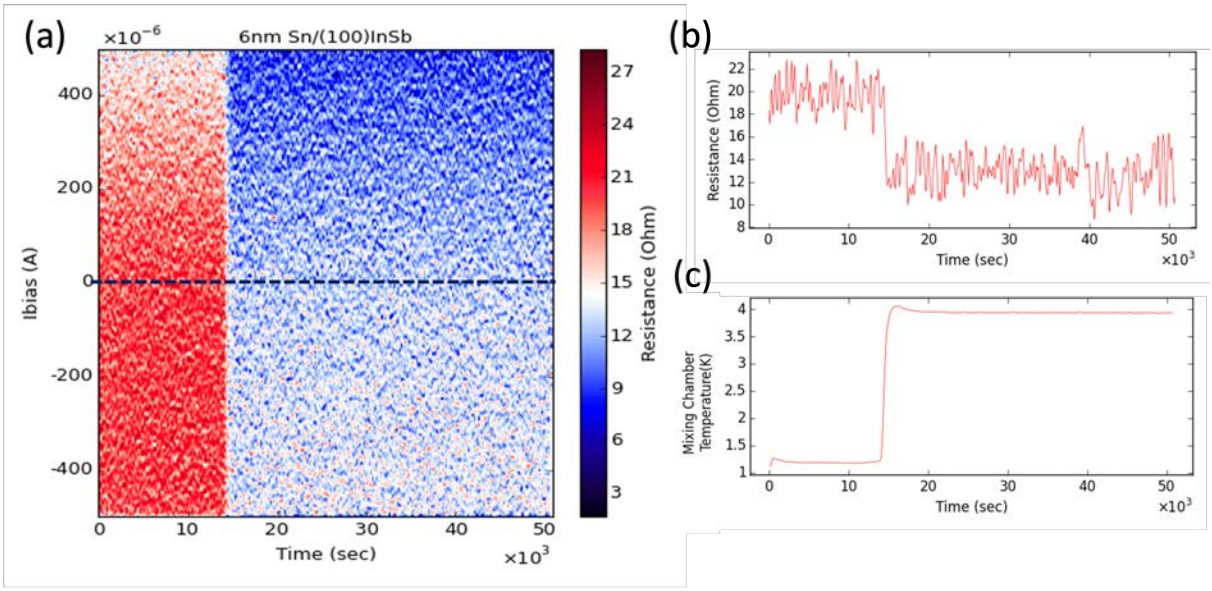

Figure 5.4.1: [Tin1W-100] Low temperature transport measurement of a 6 nm Sn film grown on InSb(100) done. (a) 2D resistivity map as a function of I_{bias} and time. (b) Resistance of the 6 nm Sn film versus time, extracted from (a), indicated with the black horizontal dashed line. (c) The temperature of mixing chamber (considered equivalent to the sample temperature) versus time.

Figure 5.4.1 shows the transport measurement in the 6 nm Sn layer. Note that the temperature cooling rate is not well controlled due to the malfunction of the heater in the dilution fridge. We find that 6 nm-thick Sn thin film is more resistant (20 Ω) at 1.3 K than (12 Ω) at 4 K. It did not show any superconductivity but insulator-like behavior.

Figure 5.4.2 shows the low temperature electronic transport measurement performed on the Sn thin film of 15 nm grown on InSb(001). We see that a switching current appears between I_{bias} = 200 μA and –200 μA while the temperature decreases below 2 K. Between the switching currents, we observe a relatively low-resistance region surrounding I_{bias} = 0 μA: it is the superconducting gap. We find that the superconducting gap closes up while the temperature increases. The non-zero resistance in the superconducting gap is attributed to the insulating α-Sn layer.

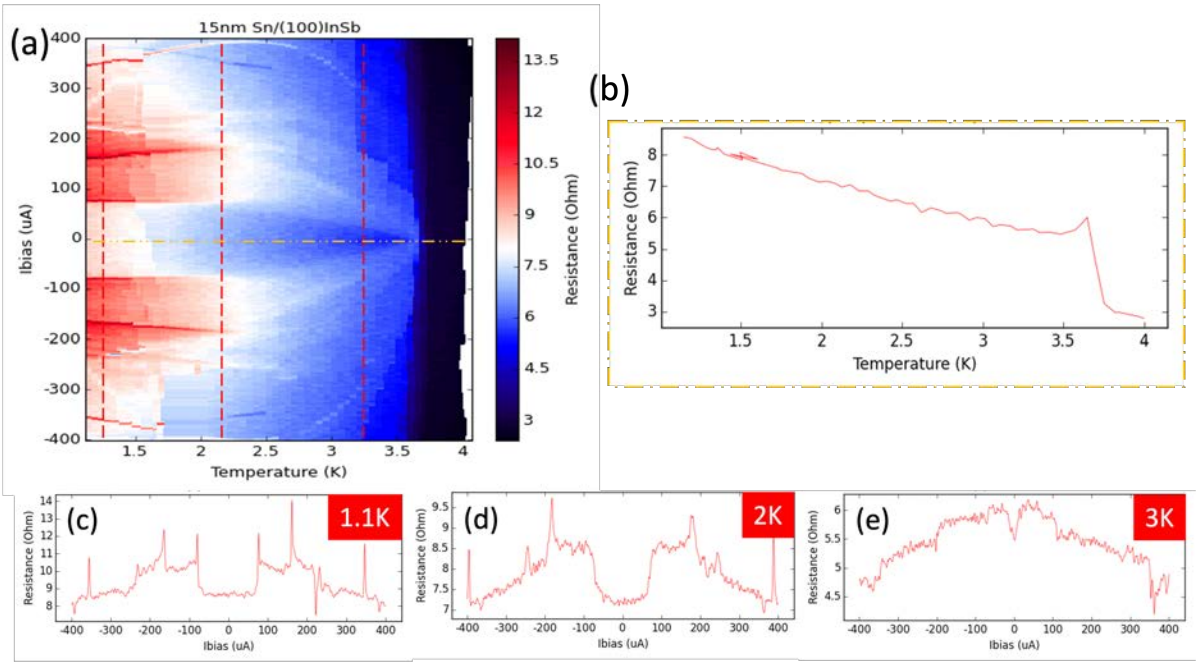

Figure 5.4.2: [Tin3W-100] Low temperature transport measurement of the 15 nm Sn thin film grown on an InSb(100) substrate. (a) 2D resistivity map as a function of I_{bias} and temperature. (b) R-T line scan at I_{bias} = 0 μA extracted from (a) (indicated by a yellow horizontal dashed line). (c)-(e) Resistance versus I_{bias} at different temperatures extracted from (a).

In conclusion, we find that the thicker Sn film shows superconductivity whereas the thinner Sn film shows the insulator-like resistance. Our in-plane XRD measurements revealed that the amount of β-Sn is larger for thicker Sn thin films. Therefore, the superconductivity in the 15 nm Sn film is attributed to the presence of β-Sn grains in the α-Sn films.

Influence of the capping layer

Next, we want to know if the electrical properties of the Sn thin films are affected by the nature of the capping layer. The superconductivity measurements are done in the dilution fridge. A 3-probes configuration is used. The difference with the 4-probes measurement resides in the fact that an additional resistance of 2.1 kΩ is present in series with the thin film due to a RC filter cable.

Figure 5.4.3 shows the superconductivity measurements at 20 mK for 16 nm Sn films covered with different capping layers. We see that a resistance drop around I_{bias} = 0 μA appears

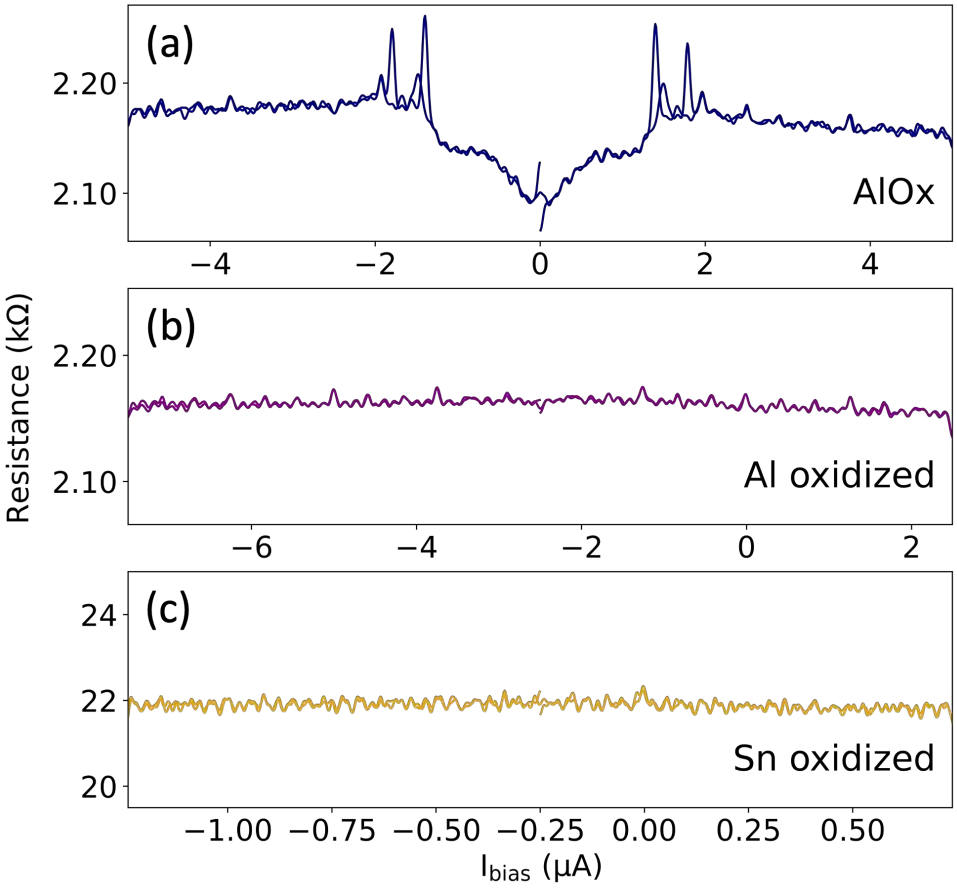

Figure 5.4.3: [CPD166-110, CPD167-110, CPD168-110] Evolution of the resistivity of the Sn film versus I_{bias} for (a) AlO_x capping, (b) Al oxidized capping, and (c) Sn oxidized capping.

in the AlO_x capped Sn film, while the resistance remained constant in both the Al oxidized and the Sn oxidized Sn films. This resistance drop is considered a feature of superconductivity. This measurement confirms that the AlO_x capping is responsible for the superconducting nature of the thin film electronic transport. As observed in 5.2.4, AlO_x capped Sn thin films host β-Sn grains. In conclusion, we have superconductivity in AlO_x capped α-Sn films with thicknesses > 15 nm because sufficient β grains were formed and contribute to the transport of Cooper pairs.

5.4.2 DFT calculations

During the pandemic, N. Marom from Carnegie Mellon University proposed to the students experimentalists from the HYBRID project to join her group to perform a theoretical project. We were interested in understanding the difference in electronic properties of α-Sn/InSb and β-Sn/InSb interfaces.

This section is the theoretical investigation of the electronic effects of interfacing Sn and InSb by first principles simulation based on density functional theory (DFT). In our DFT calculations, we mainly used the PBE+U (Perdew-Burke-Ernzerhof with the Hubbard U parameter) approach, which balances between accuracy and computational cost. PBE+U is a functional in

DFT calculations and the details can be found in Chapter 2.6. The more accurate but computational demanding Heyd-Scuseria-Ernzerhof (HSE) approach is used for verifying the results from PBE+U (see Chapter 2.6). We considered the electronic properties of three materials that appear in our Sn/InSb system: α-Sn, β-Sn and InSb. The calculation of bulk systems is first performed to have an overview of their electronic properties, such as band structure and density of states (DOS). Then, we built up the slab, the unit building block of repeating crystalline structure. With increasing number of slabs, we can eventually reach bulk material properties. Moreover, the slab band structure result can be compared to the experimental band structure obtained from angle-resolved photoemission (ARPES) measurements.

We present the band structure and the DOS of each material, namely InSb, α-Sn and β-Sn, in bulk and for the slab. The orientation of the slab is decided accordingly by the results of XRD analysis (Chapter 5.2.1), i.e. InSb(110), α-Sn(110) and β-Sn(001) are considered along the growth direction. Eventually, we built the interface between InSb(110) and α-Sn(110) and evaluated the electronic development at the interface.

While the β-Sn(001) slab is built, the combination with InSb is computationally challenging in our approach due to the large lattice constant mismatch between these materials. This made the interface slab models construction and simulation difficult. The combination of InSb and β-Sn, such as bi-layer β-Sn/InSb or even tri-layer β-Sn/α-Sn/InSb, will be the perspectives in the future, with a proper solution expected.

InSb

We started by calculating the band structure of the InSb(110) substrate. Figure 5.4.4 (a) show bulk band structures from HSE and PBE+U approaches. Spin-orbit coupling (SOC) is considered in all calculations due to InSb possessing strong SOC. We see that the band structure calculated from the PBE+U approach is comparable to that from the HSE approach. This signified the used U correction values are sufficient to simulate InSb (U values = –0.2 eV for In and –6.1 eV for Sb on p-orbitals). The direct band gap at the Γ-point of the Brillouin zone (BZ) is reported at 0.12 eV, with a 30% error comparing to the experimental value (0.17 eV).

Following this, we built up InSb(110) slabs to see the development of the band gap from a small number of layers until the required number for satisfactory convergence. The InSb(110) slab is constructed with pseudo-H passivation at both ends to eliminate the extra charges left by dangling bonds at the cleaved surfaces. Structural relaxation on the two last atomic layers of both sides is applied since they are the free surfaces in the real world. In Figure 5.4.4 (b), the band gap of the InSb(110) slab decreased with the increasing number of layers towards the bulk band gap value. The slab is considered as convergent above 30 layers based on the reasonable value of band gap while using an affordable calculation cost. After successfully constructing the InSb substrate, we are going to calculate the α-Sn thin film in the next section.

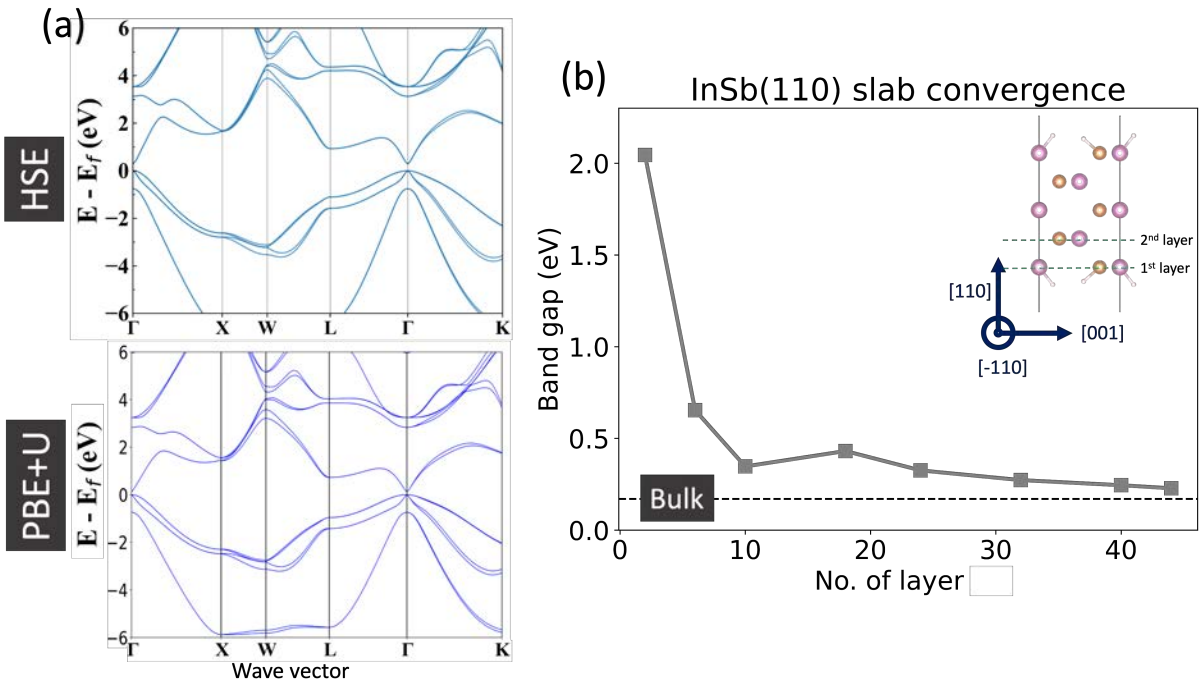

Figure 5.4.4: Band structure and slab convergence of InSb(110) from DFT calculation by VASP. (a) Band structure of bulk InSb. (b) Band gap evolution with the number of slabs. The bulk band gap is indicated with the black dashed line. Schematic at the corner is a 5-layer InSb(110) slab as an example.

α-Sn

We are interested in the electronic properties of α-Sn, which grows epitaxially on InSb. According to the results from XRD measurements, the α-Sn is strained in an in-plane direction on an InSb substrate, i.e. the lattice parameters of InSb and α-Sn are the same. Therefore, we use the InSb lattice constant in the α-Sn calculation, 6.479 Å.

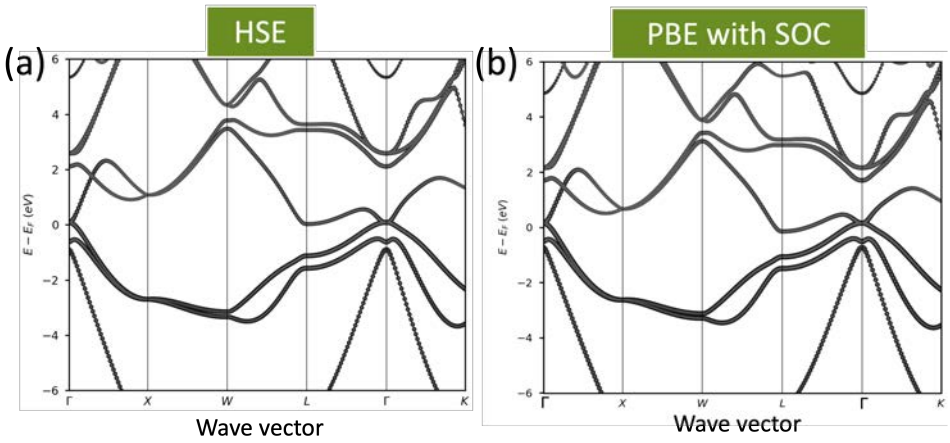

Figure 5.4.5: Full range band structure of bulk α-Sn from DFT calculation using (a) HSE and (b) PBE with SOC approximation.

Figure 5.4.5, shows the band structure of bulk α-Sn calculated by PBE with SOC, which is similar to that calculated by HSE at Γ point near the Fermi level. Notably, the band gap at Γ point is zero, which agrees with the literature that states that α-Sn is a zero-gap semimetal [14, 144].

We then constructed an α-Sn(110) slab and tried to converge to the bulk properties. Structural relaxation is also applied on the slab calculation, indicated in red dashed squares in Figure 5.4.6 (a). We prepared two different α-Sn(110) slabs: one with only structure relaxation and the other passivated by the pseudo-H and relaxed.

The DOS profile of the α-Sn slab without passivation shows extra states compared to the bulk DOS profile at the Fermi level ($E - E_F = 0$ eV). However, the α-Sn(110) slab with pseudo-H has no spurious states and matches better to the bulk DOS. This suggests that passivation of pseudo-H is required. The convergence with slab layer number shows that the calculated band gap value is near zero above 30 layers, which is considered convergent. We believe it will reach zero with more layers but we are limited by the power and the consummation of the calculation.

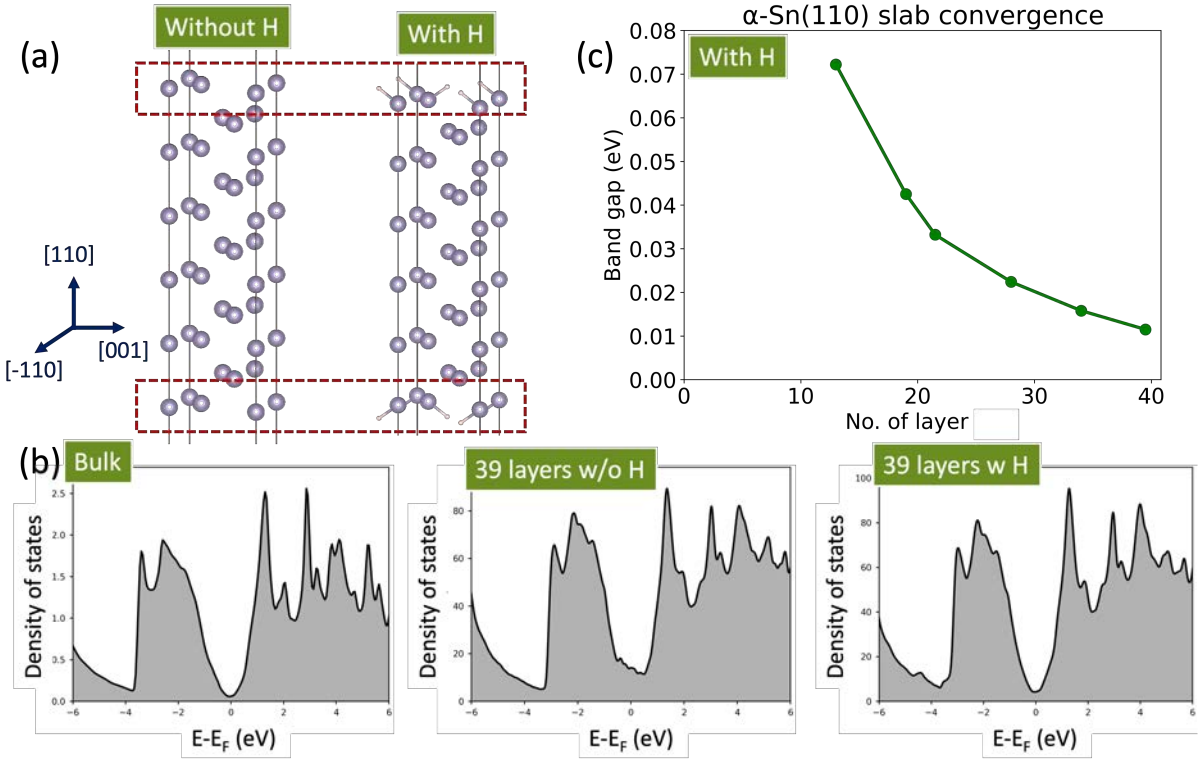

Figure 5.4.6: Convergence of the α-Sn(110) slab. (a) 11 layers of the α-Sn(110) slab, with and without pseudo-H at the ends of the structure. (b) DOS calculation of α-Sn from bulk, 39-layer slab with and without pseudo-H. (c) Band gap evolution with the number of α-Sn(110) slabs with pseudo-H passivation.

We wanted to verify the reliability of our DFT simulations by comparing the band structure of the convergent α-Sn(110) slab to an ARPES measurement, shown in Figure 5.4.7. The

chosen band path of the 39-layer slab, X – Γ – X, is the same path as the shown ARPES measurement, from -0.4 (1/Å) to 0.4 (1/Å) in k_x. Note that to be able to be compared with the experimental result, the calculated band structure is unfolded [188]. There is a good agreement in band structure between the experimental and simulated results, suggesting our α-Sn(110) slab with pseudo-H represents correctly α-Sn. With both slabs of InSb(110) and α-Sn(110), the interface of Sn/InSb hereostructure can be constructed and discussed in the next section.

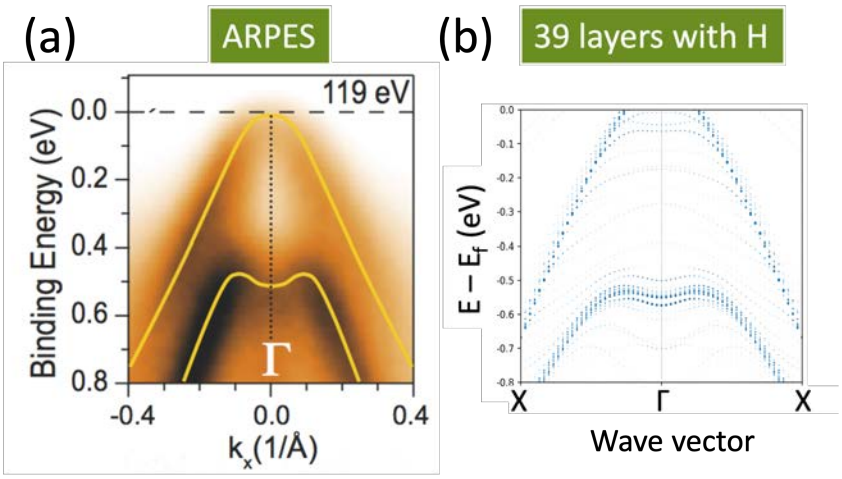

Figure 5.4.7: Band structure comparison of ARPES measurements and DFT calculation of α-Sn(110). (a) The ARPES measurement of bulk α-Sn band structure at Γ point of the Brillouin zone, taken from [15]. (b) The band structure of a 39-layers slab of α-Sn(110) with pseudo-H.

Interface between InSb and α-Sn

Here we constructed the interface of InSb and α-Sn and evaluated their electronic properties. The relaxation and pseudo-H are applied at both ends of the interface slab. There is no structural relaxation required at the interface due to no surface states appearing with no relaxation. An ideal interface is simulated with no intermixing.

Figure 5.4.8 shows the interface slab composed of 40 layers of InSb(110) and 39 layers of α-Sn(110). We see that the wavefunction of the states at the zero-gap point of α-Sn penetrates the interface and tails off into InSb, seen via the finite density of states that occupy the band gap of InSb near the interface. This is a phenomenon called "metal-induced gap states", which occurs at a metal/semiconductor interface [155, 154].

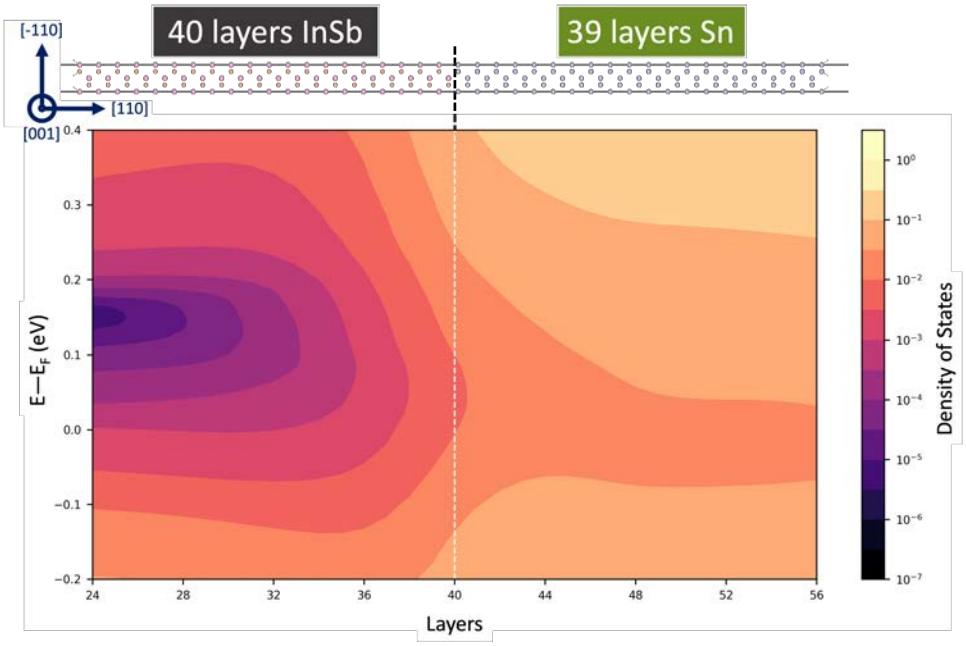

Figure 5.4.8: DOS calculation of the heterostructure slab of 40-layer InSb(110) and 39-layer α-Sn(110). The white dashed vertical line indicates the interface.

β-Sn

We are interested to calculate the electronic properties of β-Sn independently in order to possibly construct a tri-layer structure in the future. These bulk calculations are performed with the HSE functional. We estimate its electronic properties at the beginning and introduced the deformation (strain) into the calculation. The difference in lattice constant between β-Sn (5.81 Å) and InSb (6.48 Å) is approximately 10%.

To build an atomic structure interfacing β-Sn/InSb in DFT, the first option is to find the lowest common multiple number for unit cells to reduce the strain of one material, which would be a costly calculation due to the use of a larger supercell. Another option is to deform the β-Sn unit cell to match the lattice constant of InSb in a (1×1) supercell, however this strain could seriously affect the electronic properties of the β-Sn from the deformation. Therefore, we estimate the evolution of electronic properties by introducing strain to the β-Sn. The deformation changes in-plane and out-of-plane lattice constants while keeping the unit cell volume constant.

In Figure 5.4.9 (b), the band structure of bulk β-Sn seems intact from the deformation. Figure 5.4.10 shows the DOS of β-Sn in bulk. We note that the states near the Fermi level changed by a small amount.

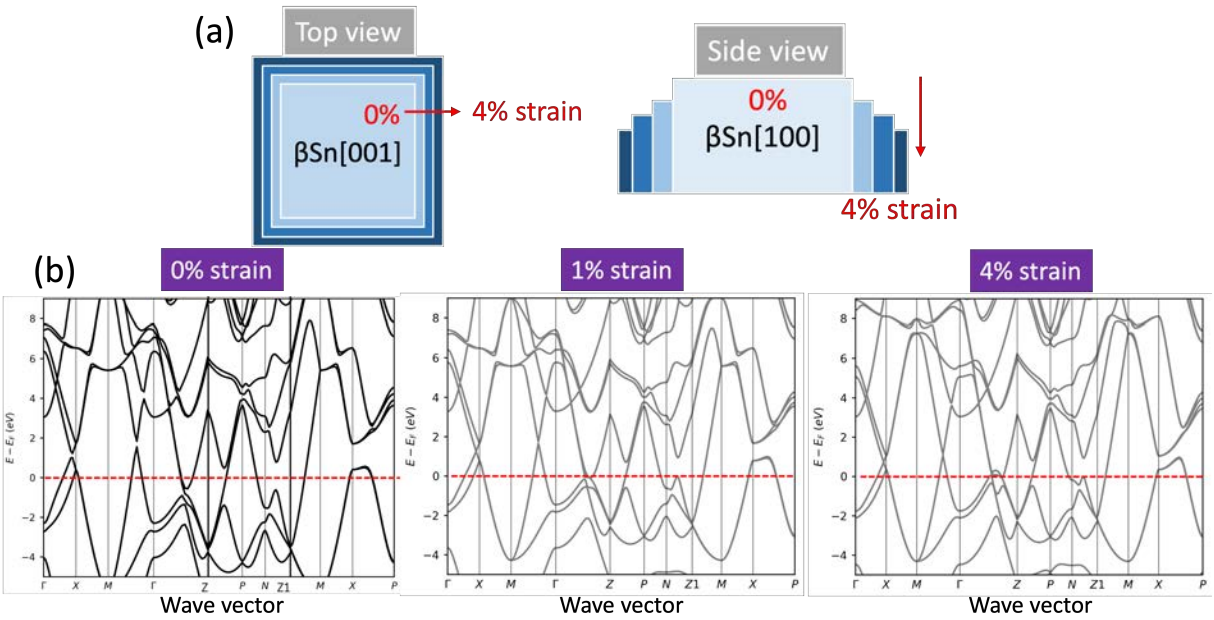

Figure 5.4.9: Band structure of bulk β-Sn with strain effect in (b). (a) Illustration of the deformation of the Sn film with constant volume. (b) Evolution of the band structure with increasing strain. The red horizontal dashed lines indicate the position of fermi level.

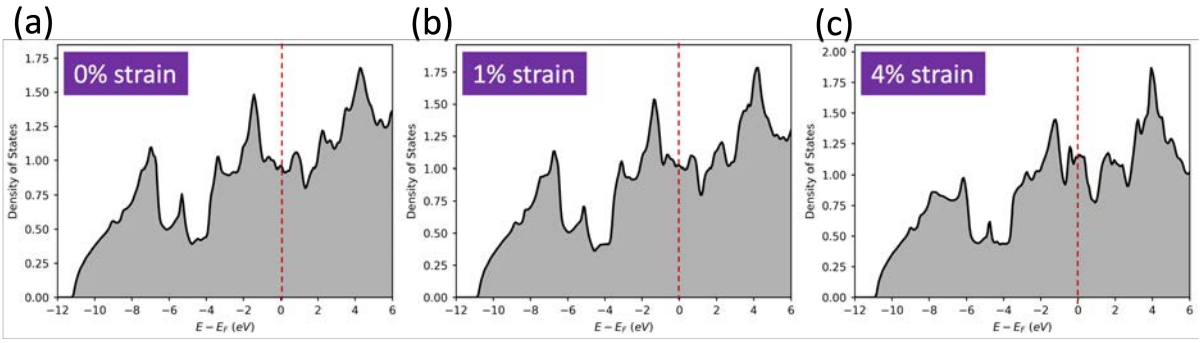

Figure 5.4.10: Evolution of the DOS of β-Sn with strain influence. The red vertical dashed line indicates the position of the Fermi level.

We also construct the β-Sn slab without strain, as seen in Figure 5.4.11. We apply a structural relaxation to the last two atomic layers. We see that by increasing the number of layer, the band structure of the β-Sn(001) slab evolves towards the bulk band structure. We then consider the 58-layers β-Sn(001) slab to be convergent.

As experimental work resumed at the end of the pandemic, this DFT study is not finished. However, these slabs and results are the base for further works by our collaborators, such as the tri-layer structure of CdTe/α-Sn/InSb for tunnel barriers study [105].

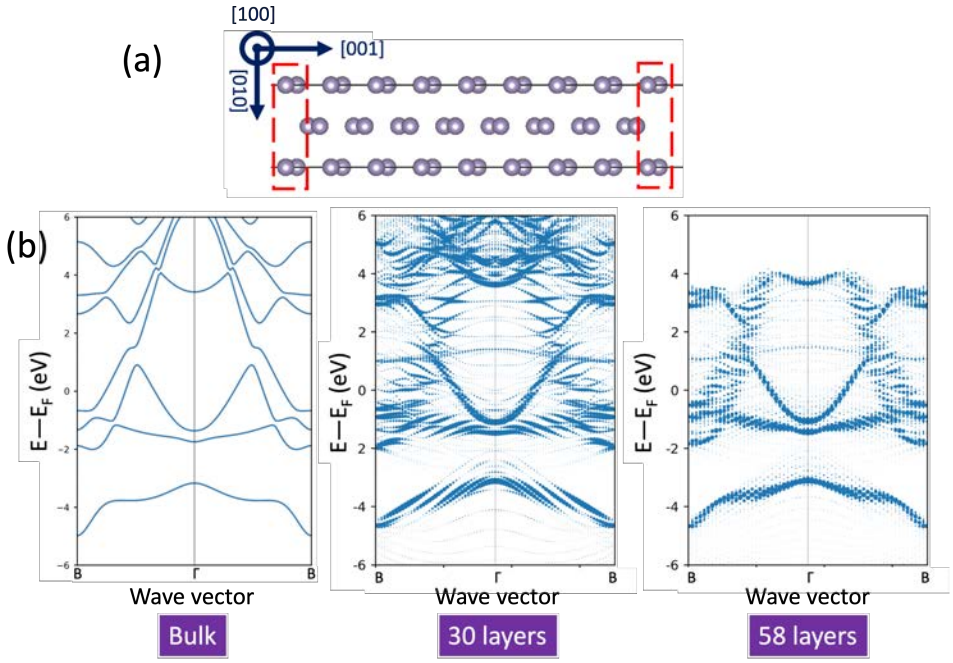

Figure 5.4.11: Convergence of β-Sn(001) slab by PBE approximation. (a) The 34-layers β-Sn(001) slab structure is shown as example and the red dashed squares indicate two atomic relaxation layers at both ends. (b) The band structures at Γ point for bulk Sn, 30-layers slab and 58-layers slab.

5.5 Discussion on the formation of β-Sn in α-Sn thin films

We studied the crystalline properties of Sn thin films grown on InSb substrates with different fabrication parameters, such as the Sn thickness and the capping methods. Our main finding is that β-Sn grain formed in the Sn thin films which are capped with electron-beam evaporated AlO_x. The radiations from the AlO_x source received by the sample are in the order of 11 mW to 20 mW, which is sufficient to increase the temperature of sample. Thicker AlO_x deposition leads to longer exposing time of the sample under the radiations. Therefore, more β-Sn is formed in the Sn film capped with 10 nm AlO_x in which we observe a β-Sn(004) diffraction in the out-of-plane XRD measurement. Sn films are a mixture of α and β-Sn: they superconduct but an additional resistive channel is present. One way to prevent β-Sn forming in epitaxial α-Sn films is to not use AlO_x capping layer. In contrast, to have pure β-Sn films: capped with thicker AlO_x layer or heat at temperature around 370 K. But a Sn deposition at room temperature would result in granular films.

Interestingly, the films stay smooth (RMS roughness = 0.35 nm to 1.28 nm) despite the formation of β-Sn in the film and the large volume difference between α and β-phase. We know that α-Sn is strained but its mosaicity is larger than bulk InSb (FWHM = 0.015 nm^{-1} for 40 nm-thick Sn). This is a sign that the film presents structural defects, for example dislocations.

On one side, the strain prevents full transformation. To totally transform the α-Sn film into β-Sn, it still requires an external heating to overcome the strain in the thin film, as seen in the temperature-dependent XRD. On the other side, the phase transformation starts at those weak point. The phase transition from α to β is martensitic and diffusionless via dislocations or defects [10, 35]. The martensitic mechanism usually results in a polycrystalline structure, which explain the appearance of two orientations of β-Sn grains. The β-Sn appeared in the thicker Sn film because the strain is relaxed in the thicker film. Thus, the thicker film with larger Sn deposition volume has more dislocations, which are reflected by more intense β-Sn diffractions. Finally, we could not conclude on the size of the β- grains and their distribution within the α-Sn film: one possibility is to use either in-plane TEM.

Furthermore, the emerging superconductivity in the thicker Sn film supports the abundance of superconducting β-Sn grains, whereas the thinner Sn film lacks it and exhibits insulator behavior. The established superconductivity of thin films is related to the phase-coupling between grains [104]. The higher resistance of the Sn oxidized sample can be due to the thinner Sn film than the other capping samples [203].

5.6 Conclusion

We successfully assessed the deposition parameters responsible for the appearance of β-Sn in Sn thin films. The strain from the InSb substrate stabilizes the α-Sn epitaxial film. While the film thickness increases, the latent heat of forming defects and dislocations decreases. The martensitic phase transition takes place locally via defects in Sn film, that is capped with AlO_x. The β-Sn grains have specific orientation in epitaxial α-Sn films and the coupling between grains makes the film superconducting. This chapter manifests the conditions to achieve a superconducting film with a smooth morphology on a semiconductor substrate, which could eventually serve as a quantum computing platform.

We found that Sn film is in α-phase on InSb(110) substrate. The epitaxial α-Sn film is strained in the in-plane directions. We observe that β-Sn diffractions are visible in the in-plane directions and more Sn deposition leads to more intense β-Sn peaks. The reason for β-Sn formation is related to AlO_x capping procedure. During AlO_x deposition, the radiations of AlO_x source can heat up the sample surface and trigger the phase transformation from α to β-Sn. Finally, we found that not only a way to produce smooth but also superconducting Sn films which comprises a mixture of α and β-Sn.

CHAPTER 6

Sn shell on InSb nanowire

In the previous chapter, we studied the role of the deposition parameters for Sn thin film on the InSb substrate. It appeared that low deposition temperature of Sn leads to an epitaxial thin film in the α phase. It showed that the Al_2O_3 capping process triggers the formation of β-Sn grains by heating. Above a given thickness the Sn thin film superconducts due to the presence of β-Sn. In this chapter, I investigate the crystalline structure and crystalline phase of Sn on nanowires using *in situ* XRD.

M. Pendharkar et al showed that the polycrystalline Sn shell fabricated on InSb nanowires at UCSB consists almost exclusively of β-Sn grains. The samples were analyzed by *ex situ* TEM analysis [168]. Note that these hybrid nanowires were fabricated at 80 K and are covered with an 3 nm Al_2O_3 capping layer to prevent de-wetting of Sn.

We want to know the reason for the formation of β-Sn on the nanowires and we have 3 hypothesis: (1) the Al_2O_3 capping heats the Sn shell similarly to the Sn thin films Sn on InSb results; (2) the *ex situ* TEM analysis is performed at room temperature, therefore Sn transformed already from the α- to the β-phase; or (3) β-Sn forms directly on the InSb nanowire at cryogenic temperatures.

An *in situ* study has advantage over an *ex situ* one in providing an experimental condition that excludes the disturbance from the environment, such as sample oxidation, contamination, and in our case ambient temperature. Several studies on *in situ* characterization techniques have been reported. In 2020, Y. Wang et al. showed the nanowires merging process during the growth of Ge nanowires by a real-time *in situ* SEM, in the interest of forming nanowire junctions [222]. In 2014, F. Lenrick et al. showed the growth mechanism of InAs nanowires by a real-time *in situ* TEM with the aim of understanding the formation of kinked nanowires [130]. In 2022, E. Bellet-Amalric showed the two-monolayer-steps growth modes of ZnTe nanowires in Au-assist MBE by *in situ* TEM [18].

The crystalline nanostructures can be investigated by *in situ* XRD. In 2015, V. Cantelli et al. showed an *in situ* GIXRD study of the Si nanowires on Si(111) or Ge(111) by Au-assisted MBE growth [37]. At the beginning of the growth stage, the Si is strained on the Ge(111) sub-

strate due to the 4% lattice mismatch between Ge and Si. By increasing growth time, Si started relaxing. For Si nanowires grown on Si(111) substrates, the broad Si($\bar{4}22$) diffraction peak appeared additionally to the narrow Bragg peak of the Si substrate as soon as the nanowire growth started. In 2021, S. Mostafavi Kashani et al. reported the growth stages of self-catalyzed GaAs nanowires grown on Si(111) in MBE monitored by *in situ* μXRD [157]. The axial growth of nanowire is more pronounced in the first stage, and the radial growth is enhanced in the second stage, suppressing axial growth. In 2019, K. Meng et al. used *in situ* GIXRD to investigate the formation of perovskite films, which are used in highly efficient solar cells [151]. The additive ions, such as Br^+ and Cl^-, accelerate the crystallization speed and regulate the orientation of crystal grains, which improves the film quality.

In this chapter, we studied *in situ* the crystalline properties of the Sn shell on the InSb nanowire at cryogenic temperature on BM25 at ESRF. Compared to laboratory XRD, GIXRD is a more surface-sensitive technique that is powerful for observing nanostructures on a surface. Here, we detail all the steps of the *in situ* GIXRD experiment leading to the analysis of the Sn deposition on InSb nanowires. Deposition was performed in an ultra-high vacuum (UHV) chamber after deoxidation by atomic hydrogen cleaning . We investigated the crystalline properties of Sn, influenced by the cryogenic deposition temperature and deposition thickness. This study was completed by *ex situ* analysis, such as XRD, TEM, SEM, and low temperature electronic transport measurement to evaluate the morphology and the electrical properties of the Sn shells.

The in situ GIXRD experiment in ESRF BM25 involved myself, E. Bellet-Amalric, J. Eymery, and M. Hocevar. We were assisted by J. Rubio-Zuazo and G. Castro. The ex situ *XRD measurement was advised by E. Bellet-Amalric. The TEM analysis was performed by M. A. Verheijen from TU Eindhoven and M. Hocevar. The transport measurement in a dilution refrigerator was assisted by B. Sacépé, B. Kousar, F. Gay and M. Hocevar from Institut Néel. The InSb nanowires were provided by M. Rossi, T. van Schijndel, E. P. A. M. Bakkers from TU Eindhoven.*

6.1 Description of the InSb nanowire samples

Figure 6.1.1 shows SEM images of the InSb nanowire samples. The vertical InSb nanowires are grown by the selective-area method using Au-catalysts by MOCVD on an InP(111)B substrate. There is a 22 nm-thick Si_3N_4 mask on the InP substrate. Arsenic flux is applied prior to InSb nanowire growth to facilitate the nucleation of the InSb nanowires on InP substrates [172]. The sample stacking from bottom to top is InP(111) substrate, Si_3N_4 amorphous mask, a short stem of InAs(Sb), and InSb nanowire. A 1 cm $\times$ 1 cm array of InSb nanowires, whose dimensions are 4.0 ± 0.1 μm in length and 88 ± 4 nm in diameter, are obtained. The nanowires density is around 0.66 μm^{-2} that makes InSb diffraction peak visible under GIXRD.

After loading the sample in the UHV chamber, the InSb nanowires undergo the atomic hydrogen cleaning process at 300 °C for oxide removal (see Section 2.3.1 for more details). In

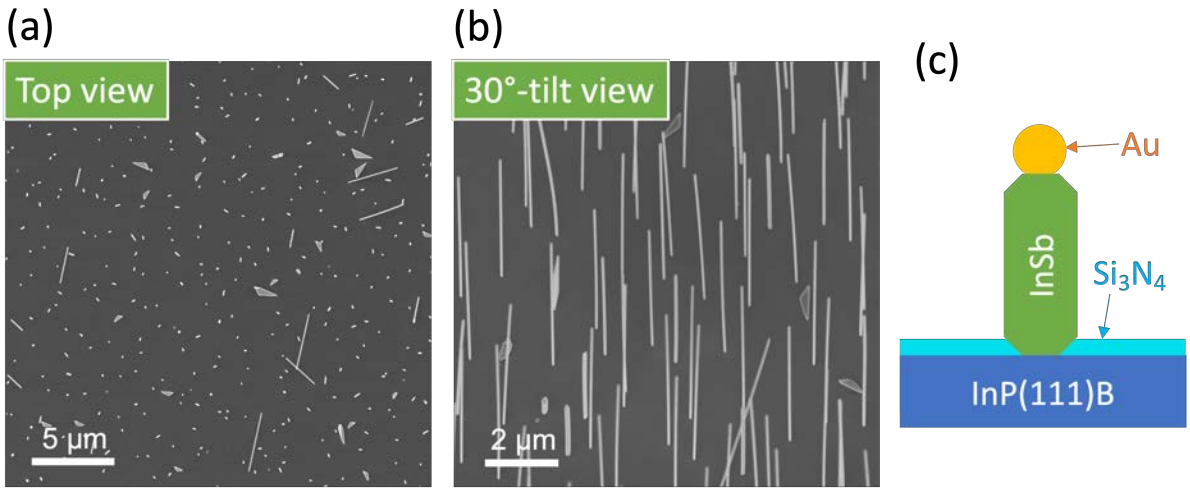

Figure 6.1.1: SEM images of as-received InSb nanowires from TU/e. (a) Top view and (b) 30°-tilt view. InSb nanowires length 4.0 ± 0.1 μm and diameter 88 ± 4 nm. (c) Schematic of InSb nanowire sample stacking.

this work, Sn is deposited on one side of the nanowires to obtain the same half-covering Sn shell on InSb nanowires as in our previous research. To estimate the Sn deposition rate, we first deposit Sn on an InSb(110) substrate for 30 minutes, which is monitored by a quartz installed in the chamber. Then, we perform X-ray reflectivity measurement (XRR) and obtain a 2D Sn deposition thickness (Figure 6.1.2). The value read on the quartz balance is then used for calibration. Thus, the thickness of the next films is directly read on the quartz.

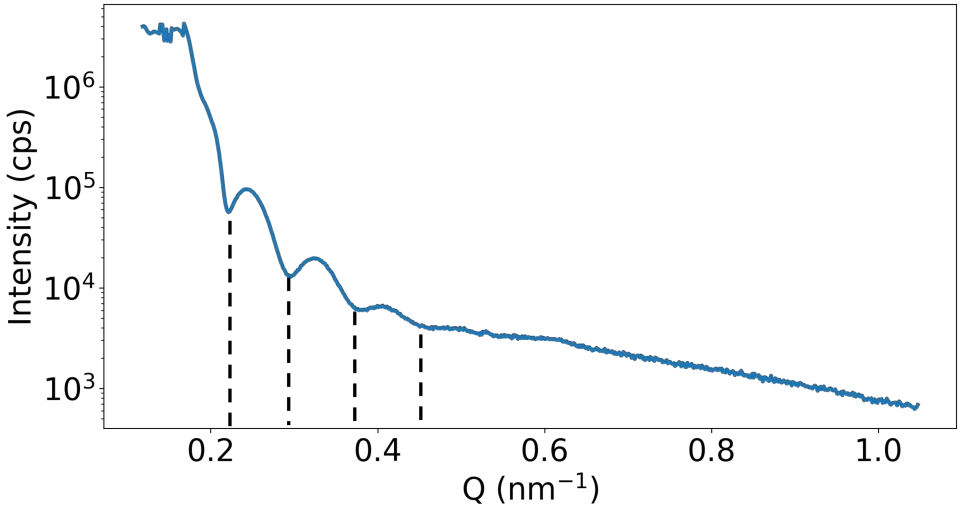

Figure 6.1.2: X-ray reflectivity of 2D Sn layer deposited on a InSb(110) substrate. The deposited Sn thickness is 13.45 nm. Black dashed lines indicate the period of fringes.

In this study, we have successfully deposited Sn on the side of two nanowires samples of InSb, which are listed in Table 6.1.1.

Sample name	Estimated 2D Sn deposition thickness (nm)	Sn deposition temperature (K)
ESRF2	9	80
ESRF4	20/25/46	80

Table 6.1.1: List of *in situ* Sn deposition samples studied at BM25 in ESRF, including sample name, estimated 2D Sn deposition thickness, and Sn deposition temperature. Sn was deposited three times on ESRF4.

6.1.1 In situ GIXRD

InSb nanowires

First of all, we determine the 2D diffraction map corresponding to the InSb nanowire sample before Sn deposition, as seen in Figure 6.1.3 (a). A low incident angle ALPHA = 0.010 is used. We measured InSb[$1\bar{1}0$] and InSb[$11\bar{2}$] corresponding to the two different facets of nanowires. For clarity, we demonstrate the measurements along InSb[$1\bar{1}0$] in this manuscript, and the ones along InSb[$11\bar{2}$] are given in the Supplementary.

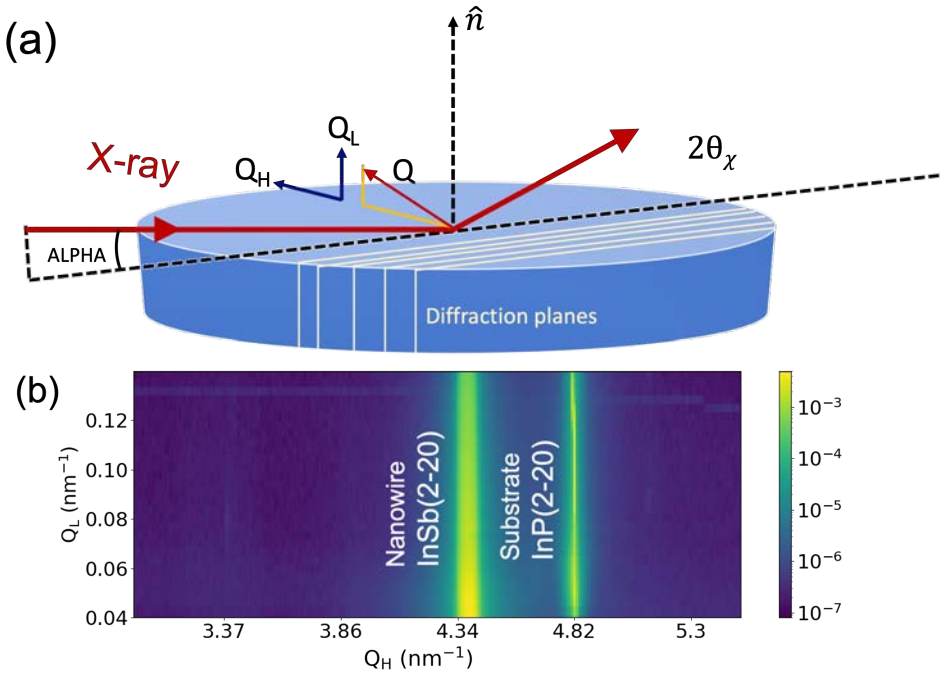

Figure 6.1.3: Demonstration of GIXRD measurements. (a) Diffraction direction Q consists of Q_L along the out-of-plane direction and Q_H along the in-plane direction. The grazing incident angle is indicated as ALPHA. (b) 2D diffraction map of InSb nanowire sample.

Figure 6.1.3 (b) shows two vertical diffractions streaks. The first one at 4.35 nm^{-1} is identified as InSb($2\bar{2}0$), and the other one at 4.82 nm^{-1} is identified as InP($2\bar{2}0$). The broadening of the XRD diffraction streaks results from the small crystallite size, such as the nanowire cross section [224]. A crystallite is an individual perfect crystal who has a coherent crystalline structure. Therefore, the limited coherent length in the nanowire's diameter causes the line to

broaden in the lateral Q_H direction. In contrast, the high crystalline quality of the InP substrate with a very long in-plane coherent length, leads to a narrow diffraction streak limited by the experimental resolution. The intensity of the diffraction is normalized by the intensity of the incident X-ray beam, i.e. the intensity of reflected beam I divided by the one of the incident beam I_0.

After understanding the 2D diffraction maps of the InSb nanowires sample, we then deposit Sn at a cryogenic temperature of 80 K and observe the evolution of the diffraction pattern.

Sn deposition at 80 K

We then deposit Sn with an equivalent 2D thickness of 9 nm on one side of the sample. Figure 6.1.4 shows 2D diffraction maps of InSb nanowires sample before and after the Sn deposition.

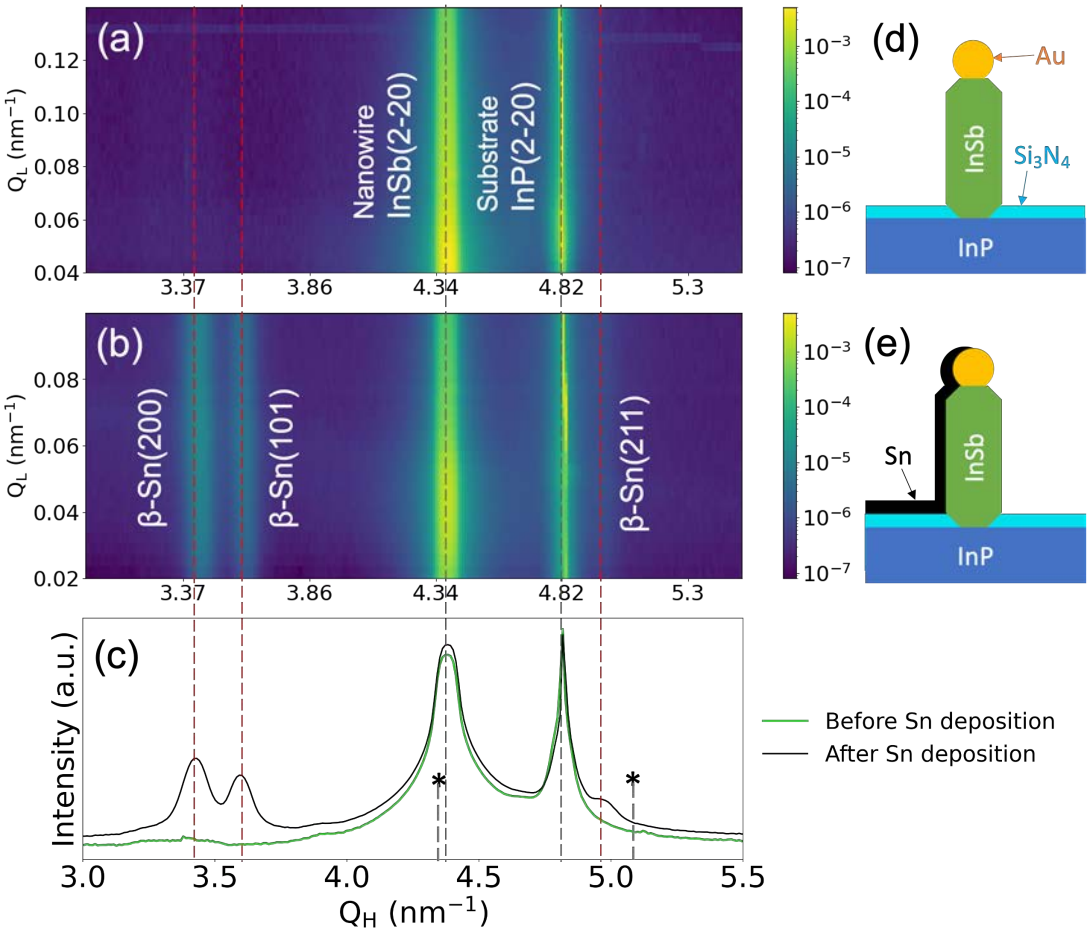

Figure 6.1.4: [ESRF2] In-plane diffraction 2D map at 80 K (a) before and (b) after Sn deposition. The scan direction is along InSb[1$\bar{1}$0] direction. (c) Plot of the integrated intensity versus Q_H from (a) and (b). The β-Sn diffractions are represented by red dashed lines at Q = 3.38, 3.54 and 4.90 nm^{-1}. The InSb nanowire is represented by gray dashed line 4.35 nm^{-1}, and the InP substrate is represented by 4.82 nm^{-1}. Based on ICDD database, the dashed lines with aster at 4.36 and 5.11 nm^{-1} are for α-Sn(220) and α-Sn(311), respectively. (d)(e) Schematics of a sample's status.

We observe two additional streaks, corresponding to β-Sn(200) at $Q_H = 3.38\,nm^{-1}$ and β-Sn(101) at $Q_H = 3.54\,nm^{-1}$, respectively, that appear after Sn deposition at 80 K. Moreover, the integrated 1D curves reveal a third β-Sn peak, β-Sn(211) at $4.90\,nm^{-1}$. The appearance of these three peaks reveals the presence of polycrystalline and non-oriented β-Sn at 80 K. The different intensity level of background can be due to the different scanning condition, in terms of scanning speed or surface scattering (i.e. a surface with or without Sn deposition). The α-Sn diffractions are invisible at the expected Q values.

We find that the high-temperature phase (β-phase) of Sn can form at 80 K, yet the low-temperature phase (α-phase) of Sn is invisible. The β-Sn diffraction can include 1D shell on InSb nanowires as well as 2D surface on InP substrate. In the next paragraph, we are going to separate the Sn signal from the 1D nanowires and the 2D substrate by tuning the grazing incident angle ALPHA.

Grazing incidence angle ALPHA

We found that β-Sn forms on the nanowires sample regardless of the cryogenic temperature 80 K. Sn is deposited not only on the InSb nanowires side walls but also on the substrate. We made the hypothesis that α-Sn could form on InSb nanowires given our 2D Sn/InSb results, and that β-Sn would form on non-lattice matched (or amorphous) substrates like the SiN layer. Thus, we use different critical grazing angle ALPHA to distinguish between the different contributions of the Sn diffractions coming from the nanowire facets and the substrate by optimizing the diffraction of the nanowires. A lower grazing incident angle ALPHA means more surface sensitivity and less diffraction from the substrate. Ideally, we expect the X-ray beam to pass above the substrate and through nanowires only, observing only the contribution of Sn deposited on the free-standing nanowires. The ALPHA study shown here is performed on ESRF4 after the 1st Sn deposition with an estimated 2D Sn thickness of 20 nm.

Figure 6.1.5 shows the diffraction maps with different ALPHAs, -0.25 and 0.15. There is no significant change in terms of diffraction pattern. Based on the integrated 1D curve, the InSb nanowires peak InSb($2\bar{2}0$) become relatively more intense with the lower ALPHA, but the substrate peak InP($2\bar{2}0$) remains the same. Meanwhile, the peaks of β-Sn remain the same in terms of their peak shape and intensity. We used the pseudo-Voigt model to fit the InSb ($2\bar{2}0$) peak and found that its FWHM is slightly smaller at lower ALPHA, 0.059 ± 0.001 at ALPHA = –0.25 and 0.062 ± 0.001 at ALPHA = 0.15. Yet, the difference is too small and near the range of error bars, which is hard to interpret physically.

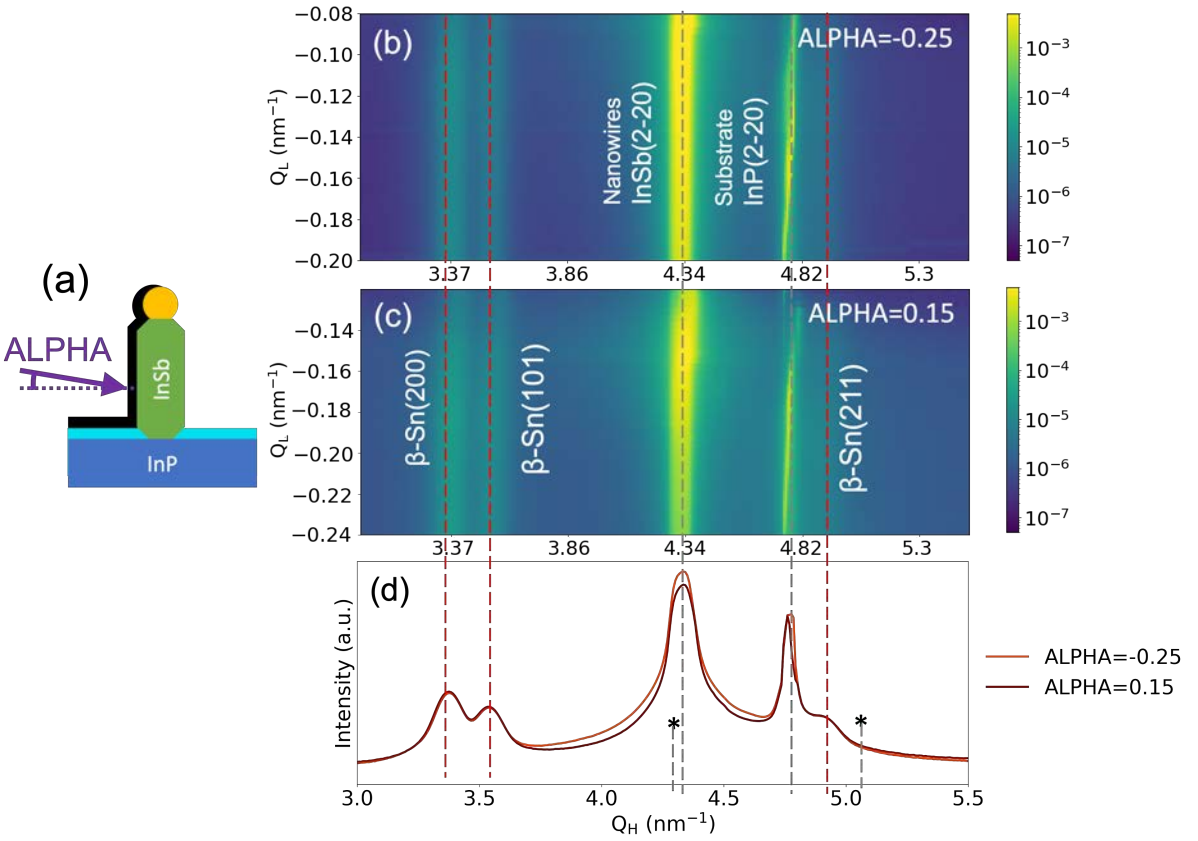

Figure 6.1.5: [ESRF4] GIXRD measurements of the Sn/InSb nanowire sample at 80 K with different ALPHAs, -0.25 and 0.15. (a) Schematic of ALPHA. (b)(c) 2D diffraction maps of InSb nanowires with Sn deposition. (d) Plot of integrated intensity versus Q_H at the different ALPHAs.

We studied the influence of the grazing incidence angle ALPHA on the diffraction of nanowires. The diffraction is enhanced at a smaller angle, ALPHA = –0.25. We cannot determine the phase of Sn on InSb nanowires because we did not observe a relevant evolution of the Sn diffractions and did not eliminate the contribution of the diffraction from Sn deposited on the substrate. We use ALPHA = –0.25 as the optimized grazing angle for the next measurements. In the next paragraph, we are going to study the effect of the deposited Sn thickness in terms of crystalline quality and crystalline phase.

Sn thickness

We want to know if the crystalline quality and the crystalline phase of Sn evolves with the deposited thickness. We perform three consecutive Sn depositions on the same side of the sample, and perform identical scans after each deposition. Figure 6.1.6 (a)-(c) show the 2D diffraction maps for increasing thicknesses of Sn . We observe that with increasing Sn deposition, the intensity of the substrate diffraction InP($2\bar{2}0$) and the nanowires diffraction InSb($2\bar{2}0$) decrease. By contrast, the diffractions of the β-Sn phase become more defined and intense with increasing Sn deposition.

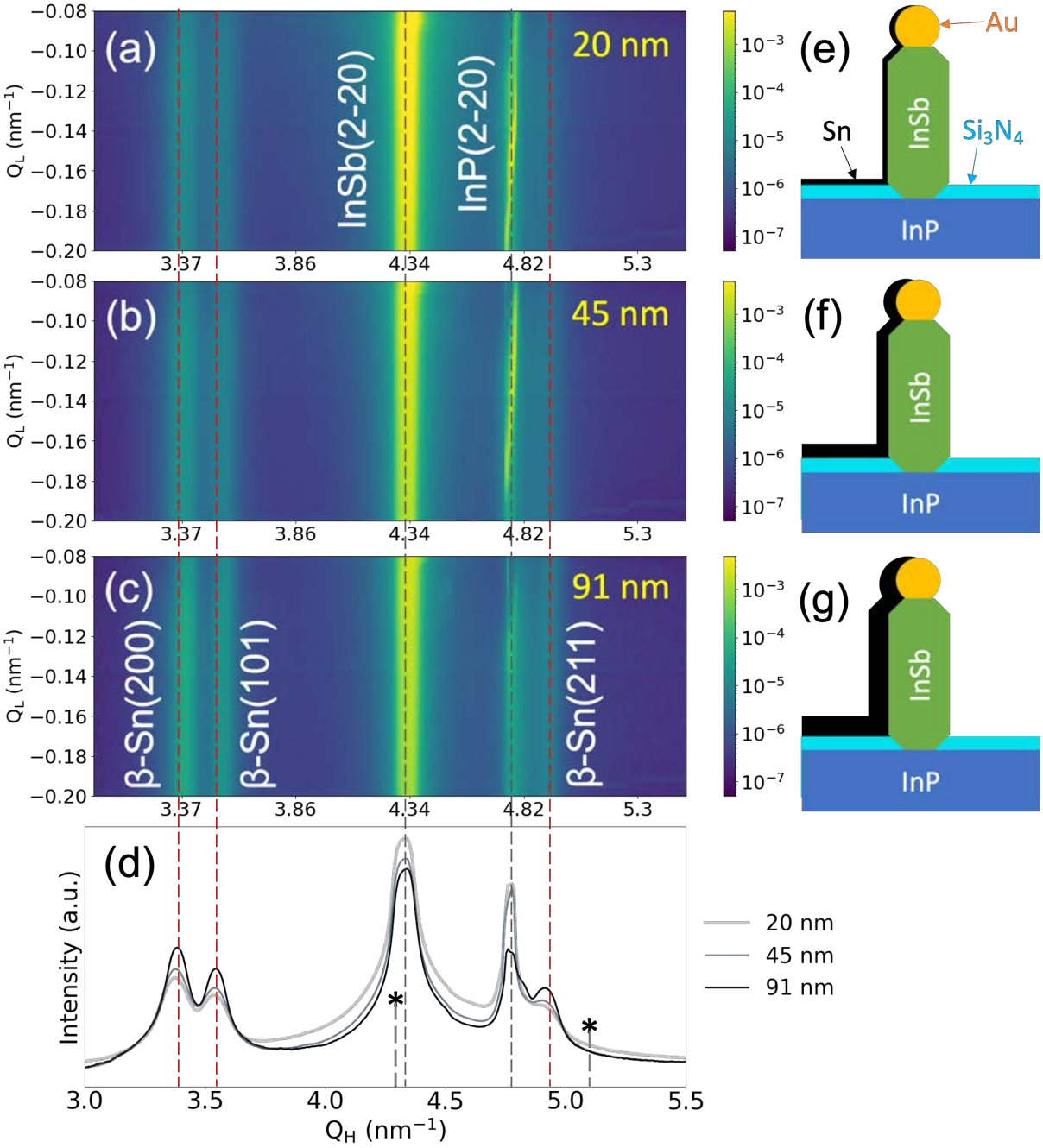

Figure 6.1.6: [ESRF4] In-plane 2D diffraction maps for different Sn deposition thickness (a) 20 nm, (b) 45 nm and (c) 91 nm. The measurements are done with a grazing incident angle ALPHA = -0.25. (d) Plot of integrated intensity versus Q_H from the 2D maps (a)-(c). The β-Sn diffractions are represented by red dashed lines at Q = 3.38, 3.54 and 4.90 nm^{-1}. The InSb nanowire is represented by gray dashed line 4.35 nm^{-1}, and the InP substrate is represented by 4.82 nm^{-1}. The dashed lines with aster at Q = 4.36 nm^{-1} and 5.11 nm^{-1} are the expected positions of α-Sn. (e)(f)(g) Schematics of sample stacking.

Figure 6.1.6 (d) shows the 1D curves integrated from 2D diffraction maps. We fitted these β-Sn peaks using the pseudo-Voigt equation in order to evaluate more accurately how peak shape evolves. The FWHM of the β-Sn(200) peak for the first deposition is 0.09 nm^{-1} and decreases

to 0.06 nm^{-1} for the third deposition. All the observed β-Sn peaks have the same trend as seen in Table 6.1.2.

Meanwhile, InSb($2\bar{2}0$) nanowire diffraction decreases in intensity. We suspect that it is due to nanowires bending, which can cause a misalignment of the diffracted planes. The nanowire bending happens easily when deposition is inhomogeneous, in particular when it covers only one side of the wires. This is confirmed by post-experiment SEM images and *ex situ* XRD, which will be shown in the next section. The diffraction signal of α-Sn (expected atQ_H = 4.36 and 5.11 nm^{-1}) is still invisible.

Which Sn deposition / deposited 2D thickness (nm)	**Diffraction**	**Q** (nm^{-1})	**FWHM** (nm^{-1})
1^{st} deposition / 20	β-Sn(200)	3.38	0.09 ± 0.01
	β-Sn(101)	3.53	0.12 ± 0.01
	β-Sn(211)	4.87	0.20 ± 0.01
2^{nd} deposition / 45	β-Sn(200)	3.38	0.08 ± 0.01
	β-Sn(101)	3.53	0.10 ± 0.01
	β-Sn(211)	4.87	0.15 ± 0.07
3^{rd} deposition / 91	β-Sn(200)	3.38	0.06 ± 0.01
	β-Sn(101)	3.53	0.07 ± 0.01
	β-Sn(211)	4.87	0.11 ± 0.05

Table 6.1.2: [ESRF4] Table of the pseudo-Voigt model fitting parameters for β-Sn diffraction peaks for Sn thickness study, including deposited 2D Sn thickness, diffraction, Q, and FWHM.

Based on the peak's shape, one can estimate the β-Sn grain size using the Scherrer equation, Eq. 2.4. In Figure 6.1.7, we observe that increasing Sn deposition results in larger β-Sn crystalline grains. For example, the grain size of β-Sn(200) grows from 14 to 21 nm.

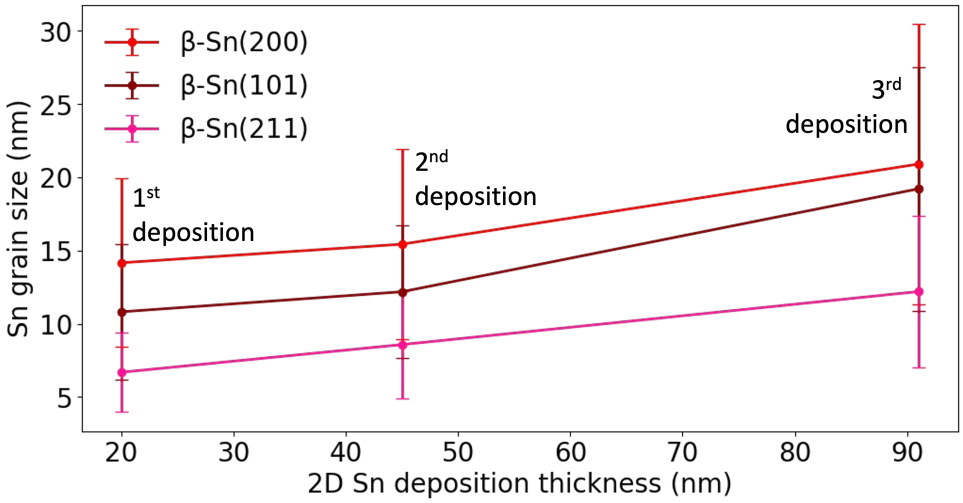

Figure 6.1.7: Plot of the estimated Sn grain size versus the 2D thickness of deposited Sn.

The diffraction of α-Sn is still invisible. In the next paragraph, we are going to search for the α-Sn existence and its contribution to the diffraction pattern by changing the temperature.

Sn phase at 300 K

We want to know if the Sn crystalline phase evolve the temperature increases to room temperature. We warm up ESRF4 gently from 80 to 300 K and perform the scan once the sample has reached thermal equilibrium. Sample realignment is necessary prior to the diffraction measurement to overcome misalignment from thermal expansion. Figure 6.1.8 (a)-(b) shows the 2D diffraction maps, Q_L versus Q_H, 80 K and 300 K. Figure 6.1.8 (c) shows the integrated intensity of 2D diffraction maps on Q_H.

We observe no significant evolution after warming up, i.e. no extra diffraction appearing or disappearing. We fit the integrated curves to be more accurate, and the fitting parameters are listed in Table 6.1.3. The shape of β-Sn peaks changes slightly in terms of FWHM. For example, the β-Sn(200) peak shrinks from 0.060 to 0.051 nm^{-1}.

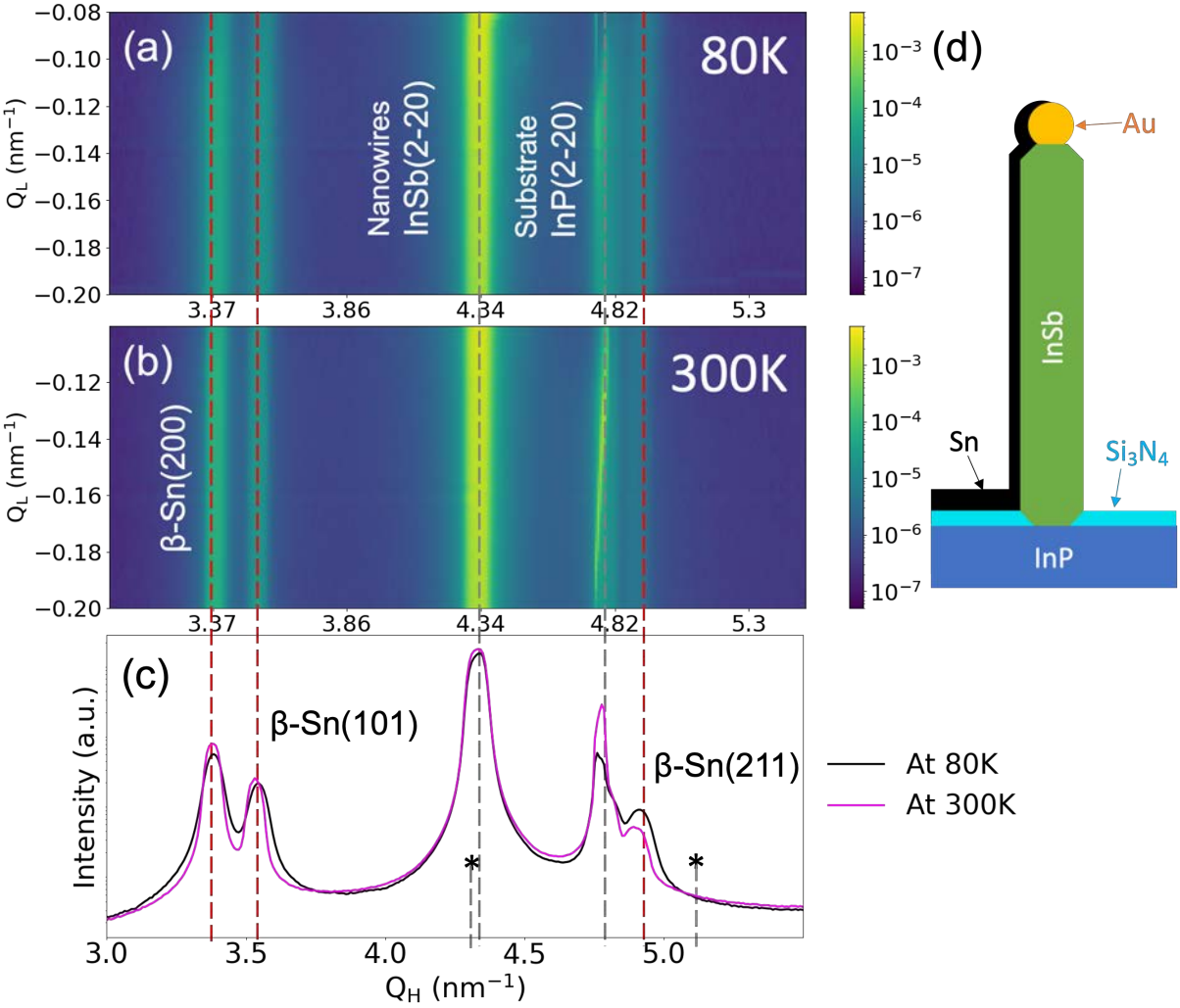

Figure 6.1.8: [ESRF4] In-plane diffraction 2D maps of Sn deposition at (a) 80 K and at (b) 300 K. (c) Plot of the integrated intensity versus Q_H from the 2D diffraction maps (a)(b). The β-Sn diffractions are represented by red dashed lines at Q = 3.38, 3.54 and 4.90 nm^{-1}. The InSb nanowire is represented by gray dashed line 4.35 nm^{-1}, and the InP substrate is represented by 4.82 nm^{-1}. (d) Schematic of 30 nm-Sn deposition on InSb nanowire.

Temperature (K)	Diffraction	Q (nm^{-1})	FWHM (nm^{-1})
80	β-Sn(200)	3.38	0.060 ± 0.001
	β-Sn(101)	3.54	0.065 ± 0.003
	β-Sn(211)	4.91	0.11 ± 0.005
300	β-Sn(200)	3.38	0.051 ± 0.001
	β-Sn(101)	3.53	0.052 ± 0.002
	β-Sn(211)	4.89	0.10 ± 0.006

Table 6.1.3: [ESRF4] Table of the pseudo-Voigt model fitting parameters for β-Sn diffraction peaks for temperature study, including temperature, diffraction, Q, and FWHM.

We conclude that temperature does not affect the crystalline properties of the deposited Sn shells. After studying *in situ* Sn deposition by GIXRD, we know that β-Sn forms at a cryogenic temperature 80 K, yet the question comes up of whether β-Sn is on InSb nanowire. As mentioned earlier, there are two types surfaces on which Sn was deposited on the sample: the amorphous Si_3N_4 mask and the InSb nanowires. To distinguish between them, we use the laboratory XRD setup and transport measurement after the ESRF experiment.

6.1.2 Ex situ XRD

Due to the limited time of the *in situ* experiments in ESRF, we used the *ex situ* laboratory XRD setup to complete the crystalline study of 1D Sn/InSb nanowires.

Incident angle optimization

Here, we aim to observe the Sn signal only from the 1D nanowires, i.e. ideally eliminate the diffraction from the substrate. We did not manage to do so during the experiments at ESRF, as seen in Figure 6.1.5. Thus, we redo the incident angle study in our laboratory setup on ESRF4, which has no crystalline change after warming up according to the temperature study by *in situ* GIXRD.

Figure 6.1.9 show the in-plane XRD measurements of ESRF4 with different incident angles ω, 0.15° and 0.28°. We observe that the InP($2\bar{2}0$) substrate diffraction decreases significantly at a lower ω = 0.15°, in comparison to the one at a higher ω = 0.28. Meanwhile, the InSb($2\bar{2}0$) nanowire diffraction increases slightly at a lower incident angle ω = 0.15. The β-Sn(200) and β-Sn(101) diffractions keep at similar intensity, and do not decrease as much as the InP($2\bar{2}0$) diffraction. This evidence supports that the β-phase of Sn is present on the InSb nanowire side walls.

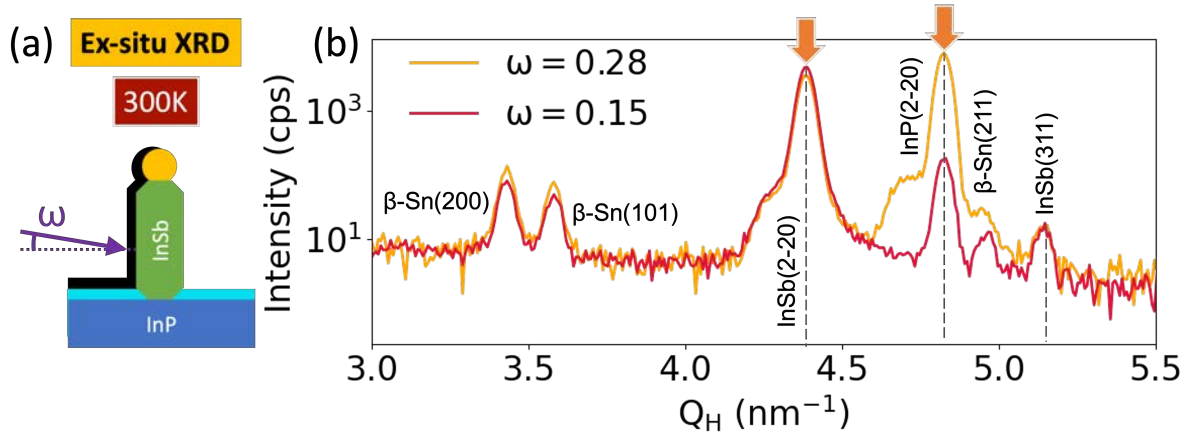

Figure 6.1.9: [ESRF4] In-plane *ex situ* XRD scans of ESRF4 with different incident angles. (a) Schematic of the incident angle ω in the laboratory XRD setup. (b) Plot of in-plane XRD measurements at 300 K along the InSb($2\bar{2}0$) direction with ω = 0.28° and 0.15°. The orange arrows highlight the diffractions of InSb($2\bar{2}0$) and InP($2\bar{2}0$). β-Sn diffractions are indicated with labels at 3.38, 3.54 and 4.90 nm^{-1}. The dashed vertical lines correspond to InSb($2\bar{2}0$) at 4.34nm^{-1}, InP($2\bar{2}0$) at 4.80 nm^{-1}, and InSb(311) at 5.12 nm^{-1}.

Crystalline quality of β-Sn

We want to know the orientation and the distribution of the β-Sn grains and if β-Sn has a preferable orientation. We use the ϕ-scan mode at 2θ angle corresponding to certain diffraction peaks in the structure. We study whether the β-Sn grains' and InSb nanowires' orientations can be related to the InP substrate orientation.

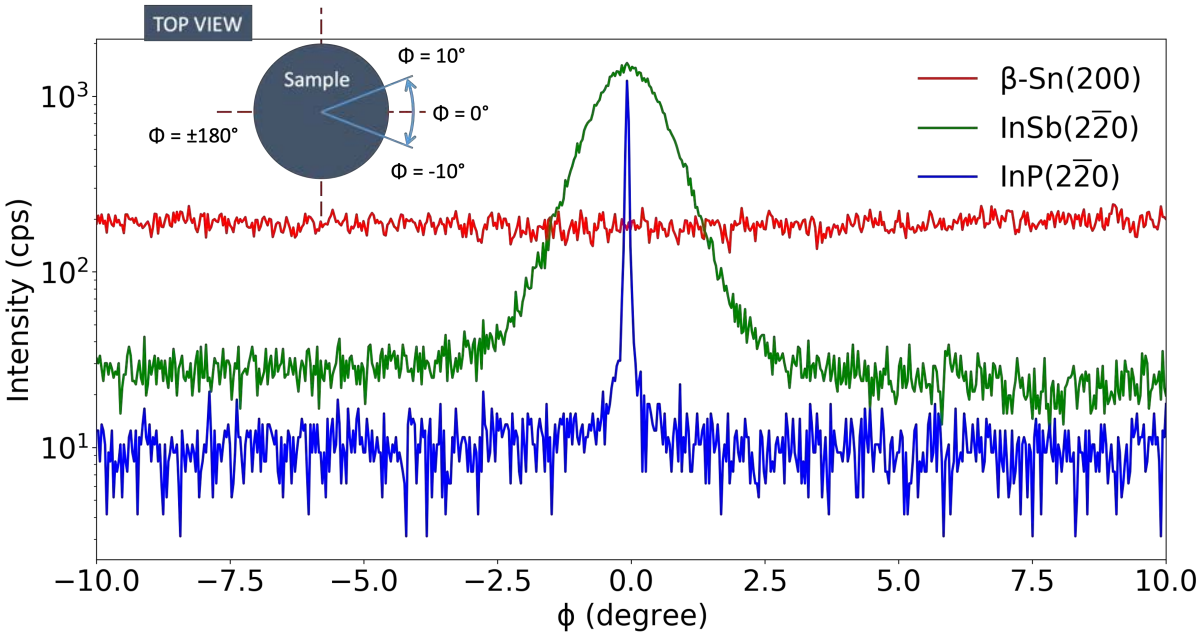

Figure 6.1.10: [ESRF4] ϕ-scans for different 2θ values that corresponded to the diffractions of β-Sn(200) from Sn deposition, InSb($2\bar{2}0$) from nanowires and InP($2\bar{2}0$) from substrate. Schematic ϕ angle from the top view of sample is illustrated at upper left.

Figure 6.1.10 shows the ϕ-scans of major diffraction peaks: β-Sn(200), InSb($2\bar{2}0$) and InP($2\bar{2}0$). We observe that the FWHM of InSb($2\bar{2}0$) is much wider (FWHM $\sim 4^\circ$) than that of InP($2\bar{2}0$) (FWHM << 1°). Their peaks are aligned at $\phi = 0^\circ$. Moreover, we optimize the signal from InSb nanowires, so the base line of InSb($2\bar{2}0$) is higher than that of InP($2\bar{2}0$). Nevertheless, β-Sn(200) diffraction shows featureless intensity along the ϕ angle. Note that the incident angle ω isn't low enough to eliminate the signal from the InP substrate, so the β-Sn intensity includes the 2D Sn film on the substrate surface. We conclude that the β-Sn(200) grains are not oriented with the substrate, confirming the polycrystalline nature of the Sn film.

Nanowire bending and shape effect

The half-covering shell usually induces strain in nanowires, which in result bend on one side [23]. We observe by SEM that the InSb nanowire are bent (Figure 6.1.11 (b)) and we want to know how this bending affects the XRD intensity.

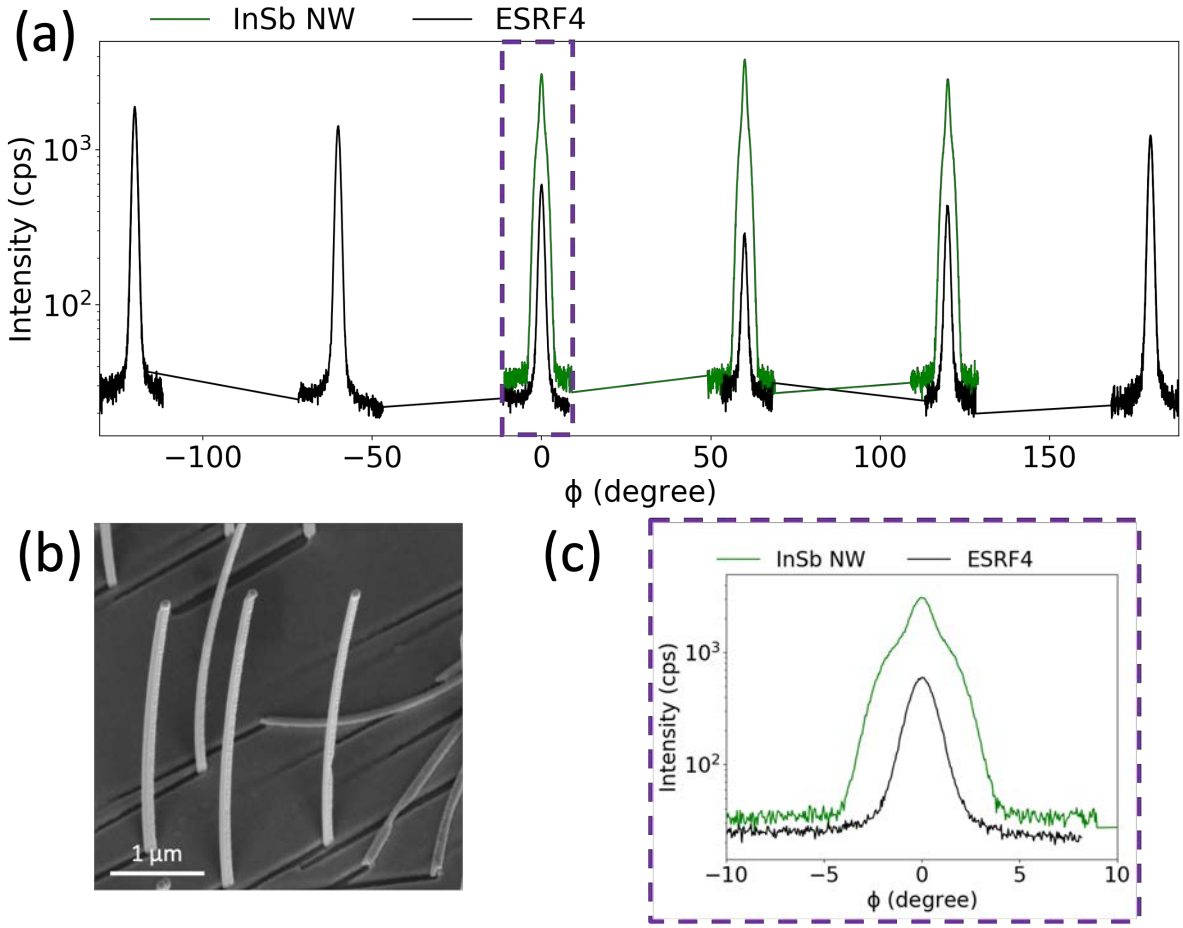

Figure 6.1.11: 360° ϕ-scan on InSb nanowires with (ESRF4 sample) and without Sn deposition (InSb NW from another sample) are measured by the *ex situ* laboratory XRD setup. (a) Full range ϕ-scans of InSb nanowires with and without Sn shell. (b) 30°-tilt view SEM image of ESRF4. (c) A zoomed-in view of the purple dashed square in (a) at $\phi = 0^\circ$.

Figure 6.1.11 (a) shows the ϕ-scans on InSb($2\bar{2}0$) diffraction peak over 360°. InSb NW represents a bare InSb nanowires sample and it is compared to sample ESRF4. The InSb($2\bar{2}0$) diffractions have a 60° period, which represents the 6-fold symmetry of the InSb nanowire grown on an InP substrate.

The intensity of the peaks of bare InSb nanowires is constant and intense, and the SEM image show that the nanowires are vertical and straight (Figure 6.1.1 (b)). In contrast, the diffraction intensity of ESRF4 varies with different ϕ angles. Therefore, this intensity evolution is due to bending and results in the misalignment of InSb($2\bar{2}0$) along certain directions. We also observe that the shape of the nanowires change with the Sn shell (Figure 6.1.11 (c)), but we do not have an explanation yet.

6.2 Morphology and transport measurements

To allow a better understanding of the material properties of the Sn/InSb nanowires grown at ESRF, we investigate their morphology and transport property.

6.2.1 Morphology of Sn

To see the morphology of the deposited Sn, we use SEM and TEM on samples ESRF2 and ESRF4. The thickness of Sn is different in these two samples: 9 nm for ESRF2 and 91 nm for ESRF4.

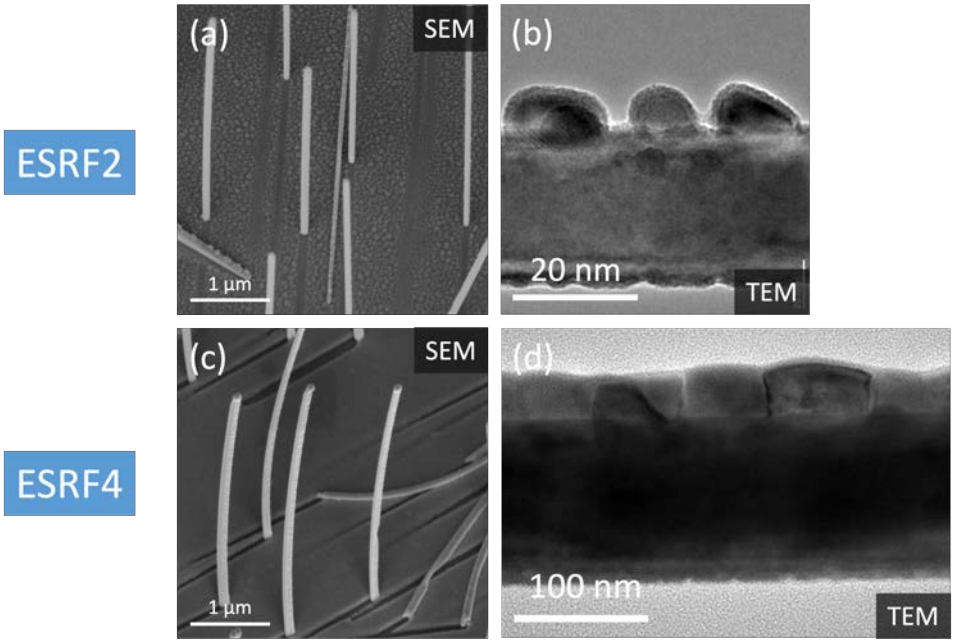

Figure 6.2.1: [ESRF2, ESRF4] SEM and TEM images of ESRF2 and ESRF4. (a)(c) 30°-tilt SEM images, (b)(d) TEM images of Sn/InSb nanowire from side view.

Figure 6.2.1 shows the corresponding SEM images. The Sn shell of ESRF2 does not affect the rectitude of the nanowires but the film de-wets into droplets. In contrast, the Sn shell of ESRF4 produces a curvature of the wire but the film remains continuous. The lateral size of the Sn droplets on ESRF2 nanowires range from 8 to 15 nm. The nanowires of ESRF4 show a stable and polycrystalline Sn shell around 38 ± 8 nm thick, and the lateral size of the Sn grains ranges from 25 to 120 nm. We discover that thicker metal deposition does not de-wet.

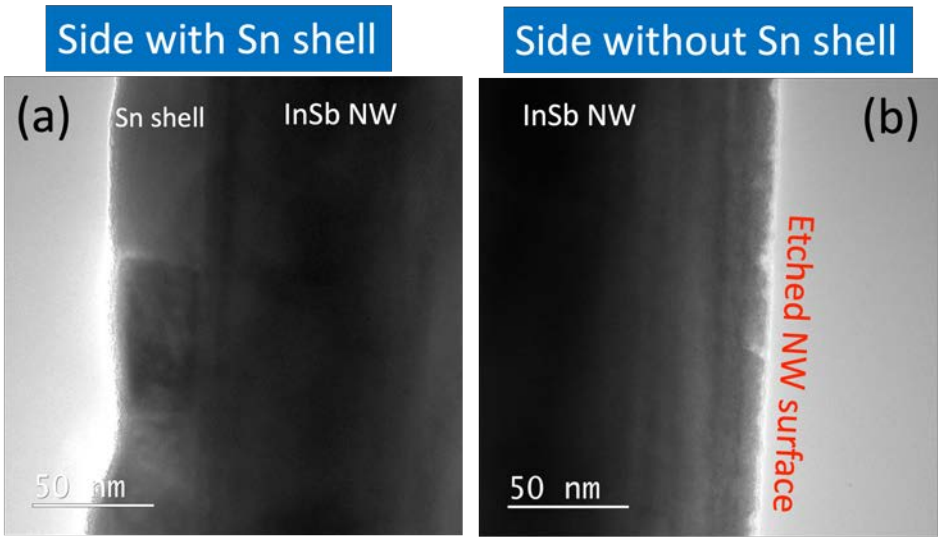

Figure 6.2.2: [ESRF4] TEM images of ESRF4 on both sides. (a) Side covered with a Sn shell, (b) side without a Sn shell.

Figure 6.2.2 is a closer view of TEM images on both sides of the ESRF4 nanowire. The surface is rough on the uncovered side, which may be the consequence of AHC "over-etching" prior to Sn deposition. For interface quality, we miss a high-resolution TEM image to determine the quality of the interface, such as Sn and InSb intermixing. The crystalline analysis of these Sn grains requires more time and will be completed in a future work.

6.2.2 Superconductivity measurement at low temperature

We are interested in the electrical properties of the Sn shells. From previous XRD results, we do not have critical evidence to confirm the Sn phase on the nanowires because of the mixed β-Sn signals from the surface and the nanowires, the invisible diffraction of the α-Sn. Our only hint is the presence of a polycrystalline shell (TEM) and that the only polycrystalline phase is β-Sn (GIXRD). Measuring superconductivity in the shell by resistance-temperature (R-T) measurements may therefore confirm the nature of the Sn phase, i.e. β-Sn.

Figure 6.2.3 shows the R-T measurements of an ESRF4 nanowire device at low temperature, where the R of the shell is plotted versus the T. Vacuum baking to prevent heating the shell during processing. Details can be found in Chapter 2: Methodology.

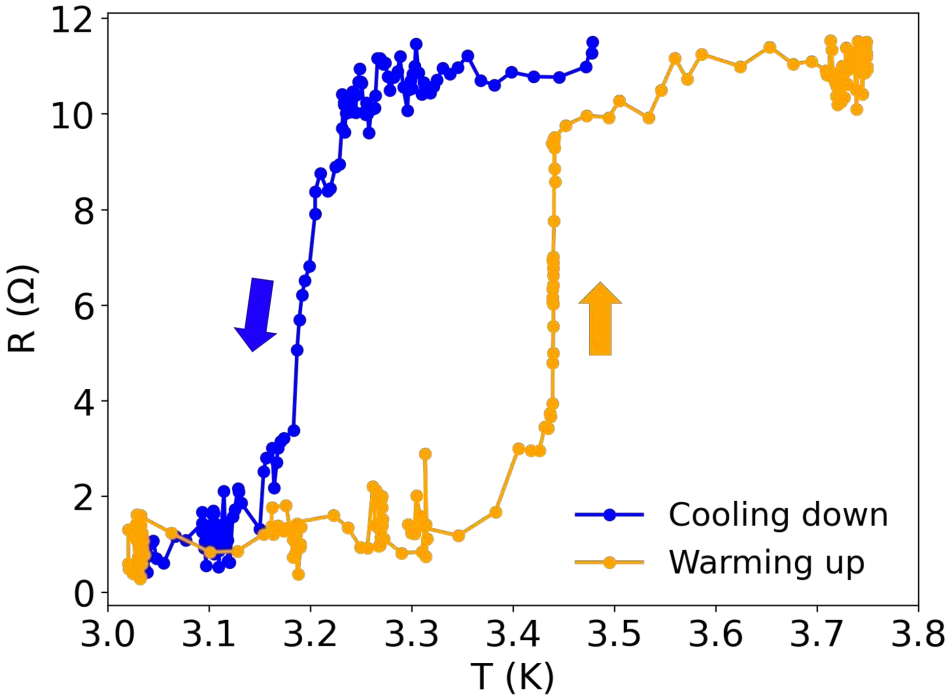

Figure 6.2.3: [ESRF4-Chip09] Plot of the resistance *R* of an ESRF4 nanowire device versus the temperature *T*. There are two sweeping directions: cooling down marked with a blue arrow and warming up marked with an orange arrow.

We observe that the *R* drops at 3.2 K from 11 Ω to near-zero resistivity during cooling down; when warming up, the *R* rises at around 3.45 K. In our measurement range, the superconducting process is reversible. The hysteresis is caused by a fast cooling and heating rates. The resistance *R* evolution demonstrates the presence of a superconducting shell of Sn (the bulk Sn critical temperature is 3.4 K [97]) with no resistive path. It confirms that the Sn shell is in the β-phase and that there is no α-Sn in the shell (in contrast to the Sn thin films studied in Chapter 4).

6.3 Discussion on the Sn phase on InSb nanowires

We observed by *in situ* GIXRD the β-Sn forming at a cryogenic temperature of 80 K, which is far below the bulk Sn transformation temperature 286 K. We did not see any α-Sn diffraction from our measurements, which is different from what we observed in 2D Sn thin films on InSb. Previous reports showed that an epitaxial α-Sn thin film can grow on an InSb substrate at room temperature [72]. Based on our *in situ* GIXRD data, we found that α-Sn does not form on the amorphous Si_3N_4 mask and neither on the InSb nanowires, regardless of the cryogenic temperature of deposition. The reasons for the absence of the α-Sn signal by GIXRD could be: (1) α-Sn does not grow on InSb nanowires, which differs from what we observe in 2D Sn/InSb; or (2) α-Sn is fully strained on InSb nanowires. The resolution of the experiment is not sufficient and the InSb nanowire diffraction totally covers that of α-Sn.

Most of the signal of β-Sn comes from the 2D surface, i.e. on the Si_3N_4 mask. In the incident angle study in *ex situ* XRD (Figure 6.1.9), the evolution of the β-Sn peaks suggests that it is also present on the InSb nanowires side walls. Yet, we couldn't eliminate the diffraction from the InP substrate, meaning that the β-Sn on the 2D surface is still taken into account in the β-Sn diffraction intensity. Finally, we found that the shell in sample ESRF4 superconducts, which confirms the presence of β-Sn on InSb nanowires.

Based on the results, we believe that the Sn forms in β phase on the InSb nanowires even at a cryogenic temperatures. Due to the small cross section of the nanowire, The strain provided by the InSb nanowire side walls is probably not enough to stabilize α-Sn. Another hypothesis is that the rough surface of the InSb nanowire, caused by an over-etching by AHC, favors the formation of β-Sn. The epitaxial relationship between the β-Sn grain and the InSb nanowire side walls would need further investigations, such as HRTEM analysis and XRD measurements of Sn/InSb nanowires transferred to another foreign substrate.

6.4 Conclusion

We are interested in the presence of β-phase in Sn shells on InSb nanowires, which is puzzling from a material science perspective. We used *in situ* GIXRD at BM25 in the ESRF to investigate the crystalline properties of as-deposited Sn on InSb nanowires sample. We find that the poly-crystalline β-Sn shell forms on the InSb nanowires at cryogenic temperatures, which is different from the Sn/InSb thin films. Grazing incident X-ray beams at ESRF are more surface-sensitive, which can enhance the intensity of InSb nanowires. The capping layer is not needed to prevent de-wetting while the Sn shell thickness exceeds its transition thickness.

CHAPTER 7

Conclusions and perspectives

In this thesis, I have developed superconductor-semiconductor materials for gate tunable Josephson junctions. In the first part of my thesis, I looked after the growth of inclined InAs nanowires on InAs(001) substrates to create inclined crossed nanowires. I then studied different superconductor deposition processes on the nanowires. In a second part of the thesis, I have focused on the Sn-InSb system. I evaluated the influence of the deposition conditions on the structure of the Sn thin films. Then, I performed an in situ experiment at the European Synchrotron Research Facility to study the structural properties of Sn thin films grown at cryogenic temperatures. The findings of my thesis are summarized below and are followed by an outlook on this exciting field of research.

Part I: Development of inclined hybrid InAs nanowires

The first finding of my thesis is that the annealing temperature T_a, the temperature at which the sample is brought prior to reaching the growth temperature T_a is the most important parameter for the growth of inclined InAs nanowires on InAs(001) substrates. I demonstrated that the optimal $T_a = 500\,^{\circ}C$ results in InAs nanowires with high density and reduced dispersion in length. Meanwhile, the sample surface is smooth and has a low density of craters. By using $T_a \neq 500\,^{\circ}C$, the density of nanowires decreased and the surface of the sample roughens due to the presence of a large number of craters. The craters formation is related to the presence of defects on the surface (non nucleated particles, kinked wires, Those results suggest that T_a determines the initial composition in In of the Au droplet, which in turn dictates the first stages of growth.

After optimizing T_a, I evaluated the influence of the growth temperature T_g, V/III BEP ratio, and growth time. I wanted to achieve long nanowires with the lowest dispersion in size but also with a cylindrical shape. For that I had to understand how inclined nanowires grow in our MBE. It appears that T_g, BEP V/III ratio and the growth time influence the growth of inclined nanowires in a similar way as the usual vertical nanowires. The optimal growth temperature

is around 420 °C as reported in 2007 by M. Tchernycheva [207]. Moreover, an increase in the BEP V/III ratio leads to the increase in the growth rate and the reduction of tapering. This is typical from the reduction of In adatom diffusion at the expense of direct impingement on the droplet when As flux increases [21]. Finally, long growth times lead to super linear growth rates but also inverse tapering. I thus conclude that the best nanowire growth parameters grown from 50 nm Au colloids in our MBE reactor are the following:

1. annealing at T_a = 500 °C for 1 minute,
2. growth at T_g = 400 °C – 420 °C
3. with V/III ratio = 60, and
4. for 20 minutes.

I explored *in situ* and *ex situ* processes for superconductor shells on InAs nanowires. I achieved high structural quality hybrid interfaces with smooth superconductor shell. I confirmed that the deposition temperature at cryogenic temperatures is important for metallic superconductors, such as Al and Sn. I developed a As capping procedure to protect InAs nanowire from oxidation once the sample is in air. An effective capping consists in decreasing the nanowire temperature to 10 °C for 10 minutes under a flux of As to fully cover the nanowires. In order to decap the sample, it is necessary to increase the temperature up to 250 °C for 60 minutes in our MBE growth chamber and at 225 °C for 20 minutes in our sputtering chamber. Finally, this technique was applied to MoGe, an amorphous superconductor. We found that the produced MoGe shell is smooth, homogeneous and superconducts.

Part II: Decoding the properties of Sn thin films on InSb

In this second part, I got inspired by the exciting results on Sn/InSb nanowires obtained by our collaborators in the USA and the Netherlands and in which I took part [168]. Yet despite having observed hard superconducting gaps, we could not understand the reason for the presence of β-Sn in the nanowire shells. This is the reason why I started studying thin films of Sn deposited on InSb substrates under the same conditions as on the initial InSb nanowires.

In the second part of my thesis, I reported on the structural properties of epitaxial Sn on InSb substrates by XRD. My main finding is that the films, despite being in the α-phase, contain β-Sn grains. The α-Sn layers are epitaxial and strained on InSb substrates. They also present a mosaicity three times higher than InSb substrates. The amount of β-Sn depends on the thickness of the film but also on the thickness of the AlO_x capping layer. Thus, by a thorough study of different capping procedures, I figured out that only the AlO_x-capped Sn films contain β-phase. We then calculated the heat balance of the sample during AlOx deposition. Our results suggest that the radiation of the AlO_x source during capping is responsible for the heating of the Sn film above the phase transition temperature, leading to the formation of β-Sn.

Next, we thought that the hypothesis of the AlO_x capping being responsible for the formation of β-Sn grains on InSb substrates may not be valid for nanowires. The surface area of nanowire sidewalls is smaller than a substrate and facilitates strain relaxation. Moreover, the shape of nanowire can influence the crystalline structure of the shell [112]. I then explored how Sn grows on InSb nanowire by *in situ* GIXRD using the synchrotron radiation source at ESRF. During this experiment, the nanowire sample was cooled down to cryogenic temperature. Then GIXRD was performed on the sample prior and after Sn deposition at 80K.

My main finding is that β-Sn forms immediately on InSb nanowires at cryogenic temperatures as low as 80 K. Increasing the temperature from 80 K to 300 K does not change the diffraction pattern of Sn/InSb nanowires, meaning that no phase transformation is noticed by GIXRD while the sample is heated to room temperature. I found that the thickest deposited Sn films do not de-wet after warming up. Moreover, they are stable at room temperature. The ex situ characterizations confirmed that the β-Sn shell is polycrystalline (TEM), superconducts with a slightly lower T_c than that of the bulk or single-crystalline β-Sn (low temperature transport measurement). This experiment showed that the structural properties of thin film are highly dependent on the growth conditions.

Outlook

Shadow junctions using patterned nanowires is the Holy Grail to produce reproducible devices. Our plan is to transfer the knowledge gained by the optimization of inclined InAs nanowires to patterned substrates. The InAs nanowires were grown with randomly dispersed Au colloids, which means that crossing of nanowires takes place randomly. Now, InAs nanowires will grow on a patterned substrate with predefined locations of Au droplets. We will thus have a better control and higher yield of crossed nanowires to create shadowing superconductor junction.

Besides, the electronic properties of the nanowires depend highly on the presence of defects and stacking faults. We will improve the quality of the wires by a fine tuning of the growth parameters to reach pure crystalline phases. We will adapt the V/III ratios to reduce the stacking faults density, and use TEM systematically to evaluate the density of defects. Another path will be to either grow ultrathin nanowires which are known to have less defects or to change the growth axis to [001] as in this crystalline direction the nanowires form in the cubic phase, which is known to be defect free.

Finally, a cooling stage will be installed in the evaporating chamber of our MBE cluster in a near future. In this chamber, multiple superconductors will be deposited *in situ* and analyzed by different means. Among them, our favorite superconductor has been Sn and we plan to continue working with this superconductor.

Sn thin films are now being deposited on InAs nanowires at UCSB and devices measured at the University of Pittsburgh. We have seen in preliminary XRD studies that Sn films deposited on InAs substrates are in the β phase and do not contain any α phase (see Figure 7.0.1 (a)). The

sample stacking is a 15 nm Sn film grown on InAs(001) substrate and capped with a 3 nm AlO_x capping. β-Sn diffraction clearly visible at $2\theta/\omega = 44.1^\circ$ (equivalent to $Q = 4.87\,nm^{-1}$). The Pendellösung fringes surrounding β-Sn(220) show a clean and abrupt interface.

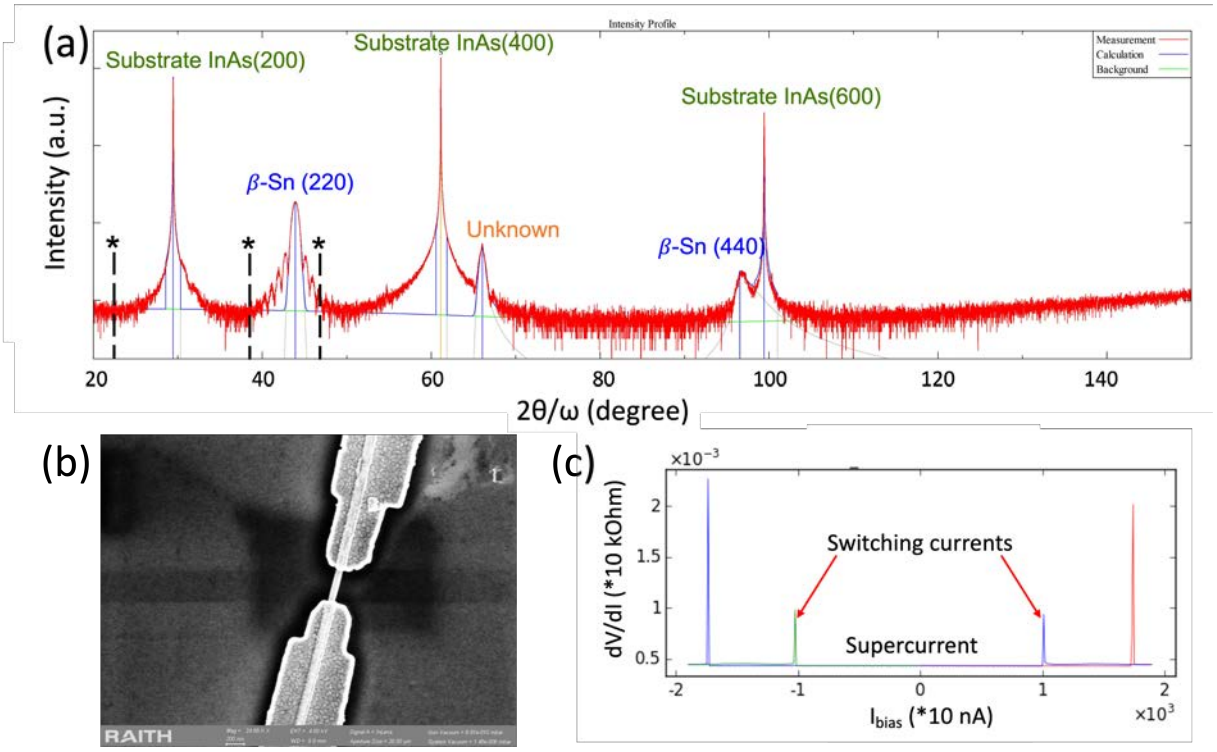

Figure 7.0.1: Preliminary studies of Sn/InAs heterostructures. (a) Out-of-plane XRD measurements of Sn film deposited on InAs(001) substrate. The black lines with aster correspond to expected diffractions of α-Sn. (b) SEM image of a nanowires device based on Sn/InAs. (c) Derivative voltage versus I_{bias}.

The electrical properties of Sn/InAs nanowires have been recently assessed in the group of S. Frolov at the University of Pittsburgh. Figure 7.0.1 (c) preliminary transport measurements on a Sn/InAs nanowire device in which we observe supercurrent. Those data show that the Sn/InAs system has high potential for the development of tunable Josephson junctions.

Bibliography

[1] Aluminium — Wikipedia, the free encyclopedia, 2022. [Online; accessed 21-August-2022].

[2] Angle-resolved photoemission spectroscopy, 2022. [Online; accessed 5-September-2022].

[3] Eh2 - grazing incidence x-ray diffraction (gixrd), 2022. [Online; accessed 6-July-2022].

[4] Questions and answers, 2022. [Online; accessed 4-September-2022].

[5] Tin, 2022. [Online; accessed 6-September-2022].

[6] The vasp manual, 2022. [Online; accessed 5-September-2022].

[7] S. M. Albrecht, A. P. Higginbotham, M. Madsen, F. Kuemmeth, T. S. Jespersen, J. Nygård, P. Krogstrup, and C. M. Marcus. Exponential protection of zero modes in Majorana islands. *Nature*, 531(7593):206–209, 2016.

[8] J. Arbiol and Q. Xiong. *Semiconductor nanowires: materials, synthesis, characterization and applications*. Woodhead Publishing, 2015.

[9] K. Y. Arutyunov, J. S. Lehtinen, A. Radkevich, A. G. Semenov, and A. D. Zaikin. Superconducting insulators and localization of cooper pairs. *Communications Physics*, 4(1):1–7, 2021.

[10] M. T. Asom, A. R. Kortan, L. C. Kimerling, and R. C. Farrow. Structure and stability of metastable α-Sn. *Applied Physics Letters*, 55(14):1439–1441, 1989.

[11] A. Association et al. *Aluminum: properties and physical metallurgy*. ASM international, 1984.

[12] P. Bai, J. F. McDonald, T. Lu, and M. J. Costa. Effect of substrate surface roughness on the columnar growth of Cu films. *Journal of Vacuum Science & Technology A: Vacuum, Surfaces, and Films*, 9(4):2113–2117, 1991.

[13] N. S. Baik, G. Sakai, K. Shimanoe, N. Miura, and N. Yamazoe. Hydrothermal treatment of tin oxide sol solution for preparation of thin-film sensor with enhanced thermal stability and gas sensitivity. *Sensors and Actuators, B: Chemical*, 65(1):97–100, 2000.

[14] Q. Barbedienne, J. Varignon, N. Reyren, A. Marty, C. Vergnaud, M. Jamet, C. Gomez-Carbonell, A. Lemaître, P. Le Fèvre, F. Bertran, A. Taleb-Ibrahimi, H. Jaffrès, J. M. George, and A. Fert. Angular-resolved photoemission electron spectroscopy and transport studies of the elemental topological insulator α -Sn. *Physical Review B*, 98(19):16–19, 2018.

[15] A. Barfuss, L. Dudy, M. R. Scholz, H. Roth, P. Höpfner, C. Blumenstein, G. Landolt, J. H. Dil, N. C. Plumb, M. Radovic, A. Bostwick, E. Rotenberg, A. Fleszar, G. Bihlmayer, D. Wortmann, G. Li, W. Hanke, R. Claessen, and J. Schäfer. Elemental topological insulator with tunable fermi level: Strained α-sn on insb(001). *Physical Review Letters*, 111(15):1–5, 2013.

[16] J. Becker, S. Morkötter, J. Treu, M. Sonner, M. Speckbacher, M. Döblinger, G. Abstreiter, J. J. Finley, and G. Koblmüller. Carrier trapping and activation at short-period wurtzite/zinc-blende stacking sequences in polytypic InAs nanowires. *Physical Review B*, 97(11):1–13, 2018.

[17] C. Beenakker and L. Kouwenhoven. A road to reality with topological superconductors. *Nature Physics*, 12(7):618–621, 2016.

[18] E. Bellet-Amalric, F. Panciera, G. Patriarche, L. Travers, M. Den Hertog, J. C. Harmand, F. Glas, and J. Cibert. Regulated Dynamics with Two Monolayer Steps in Vapor-Solid-Solid Growth of Nanowires. *ACS Nano*, 16(3):4397–4407, 2022.

[19] A. Bett, F. Dimroth, G. Stollwerck, and O. Sulima. Iii-v compounds for solar cell applications. *Applied Physics A*, 69(2):119–129, 1999.

[20] D. V. Beznasyuk. *Axial GaAs / InAs nanowire heterostructures for photonic applications on Si To cite this version : HAL Id : tel-01970033 Nanofils à hétérostructures axiales GaAs / InAs pour applications photoniques sur Si Axial GaAs / InAs nanowire heterostructures for p*. PhD thesis, 2019.

[21] D. V. Beznasyuk, E. Robin, M. D. Hertog, J. Claudon, and M. Hocevar. Dislocation-free axial InAs-on-GaAs nanowires on silicon. *Nanotechnology*, 28(36), 2017.

[22] A. Biswas, I. S. Bayer, A. S. Biris, T. Wang, E. Dervishi, and F. Faupel. Advances in top-down and bottom-up surface nanofabrication: Techniques, applications & future prospects. *Advances in Colloid and Interface Science*, 170(1-2):2–27, 2012.

[23] M. Bjergfelt, D. J. Carrad, T. Kanne, M. Aagesen, E. M. Fiordaliso, and E. Johnson. Superconducting vanadium / indium-arsenide hybrid nanowires. 2019.

[24] M. S. Bjergfelt, D. J. Carrad, T. Kanne, E. Johnson, E. M. Fiordaliso, T. S. Jespersen, and J. Nygård. Superconductivity and Parity Preservation in As-Grown in Islands on InAs Nanowires. *Nano Letters*, 21(23):9875–9881, 2021.

[25] E. BM25. Eh2 - surface x-ray diffraction and hard x-ray photoelectron spectroscopy (sxd+haxpes), 2022. [Online; accessed 11-September-2022].

[26] J. L. Boland, A. Casadei, G. Tutuncuoglu, F. Matteini, C. L. Davies, F. Jabeen, H. J. Joyce, L. M. Herz, A. Fontcuberta i Morral, and M. B. Johnston. Increased photoconductivity lifetime in gaas nanowires by controlled n-type and p-type doping. *ACS Nano*, 10(4):4219–4227, 2016.

[27] J. B. Boos, W. Kruppa, B. R. Bennett, D. Park, S. W. Kirchoefer, R. Bass, and H. B. Dietrich. Alsb/inas hemt's for low-voltage, high-speed applications. *IEEE Transactions on electron devices*, 45(9):1869–1875, 1998.

[28] K. Bordo and H. G. Rubahn. Effect of deposition rate on structure and surface morphology of thin evaporated al films on Dielectrics and Semiconductors. *Medziagotyra*, 18(4):313–317, 2012.

[29] F. Borsoi, G. P. Mazur, N. van Loo, M. P. Nowak, L. Bourdet, K. Li, S. Korneychuk, A. Fursina, J. Y. Wang, V. Levajac, E. Memisevic, G. Badawy, S. Gazibegovic, K. van Hoogdalem, E. P. Bakkers, L. P. Kouwenhoven, S. Heedt, and M. Quintero-Pérez. Single-Shot Fabrication of Semiconducting-Superconducting Nanowire Devices. *Advanced Functional Materials*, 31(34), 2021.

[30] J. Boulanger and R. Lapierre. Patterned gold-assisted growth of gap nanowires on si. *Semiconductor Science and Technology*, 27(3):035002, 2012.

[31] A. S. Bracker, M. J. Yang, B. R. Bennett, J. C. Culbertson, and W. J. Moore. Surface reconstruction phase diagrams for InAs, AlSb, and GaSb. *Journal of Crystal Growth*, 220(4):384–392, 2000.

[32] M. Brahlek, J. Lapano, and J. S. Lee. Topological materials by molecular beam epitaxy. *Journal of Applied Physics*, 128(21), 2020.

[33] W. Braun. *Applied RHEED: reflection high-energy electron diffraction during crystal growth*, volume 154. Springer Science & Business Media, 1999.

[34] P. W. Brouwer, M. Duckheim, A. Romito, and F. Von Oppen. Topological superconducting phases in disordered quantum wires with strong spin-orbit coupling. *Physical Review B - Condensed Matter and Materials Physics*, 84(14):1–6, 2011.

[35] R. Bruinsma and A. Zangwill. Structural Transitions in Epitaxial Overlayers. *Journal de physique Paris*, 47(12):2055–2073, 1986.

[36] G. Bruno, M. Losurdo, and P. Capezzuto. On the Use of H 2 Plasma for the Cleaning and Passivation of InP Substrates . *Le Journal de Physique IV*, 05(C5):C5–663–C5–670, 1995.

[37] V. Cantelli, O. Geaymond, O. Ulrich, T. Zhou, N. Blanc, and G. Renaud. The in situ growth of Nanostructures on Surfaces (INS) endstation of the ESRF BM32 beamline: A combined UHV-CVD and MBE reactor for in situ X-ray scattering investigations of growing nanoparticles and semiconductor nanowires. *Journal of Synchrotron Radiation*, 22:688–700, 2015.

[38] D. Car, J. Wang, M. A. Verheijen, E. P. Bakkers, and S. R. Plissard. Rationally designed single-crystalline nanowire networks. *Advanced Materials*, 26(28):4875–4879, 2014.

[39] D. Car, J. Wang, M. A. Verheijen, E. P. Bakkers, and S. R. Plissard. Rationally designed single-crystalline nanowire networks. *Advanced Materials*, 26(28):4875–4879, 2014.

[40] D. J. Carrad, M. Bjergfelt, T. Kanne, M. Aagesen, F. Krizek, E. M. Fiordaliso, E. Johnson, J. Nygård, and T. S. Jespersen. Shadow Epitaxy for In Situ Growth of Generic Semiconductor/Superconductor Hybrids. *Advanced Materials*, 32(23):1–9, 2020.

[41] W. Chang, S. M. Albrecht, T. S. Jespersen, F. Kuemmeth, P. Krogstrup, J. Nygård, and C. M. Marcus. Hard gap in epitaxial semiconductor-superconductor nanowires. *Nature Nanotechnology*, 10(3):232–236, 2015.

[42] D. Chatain, B. Courtois, I. Ozerov, N. Bozzolo, M. Kelly, G. S. Rohrer, and P. Wynblatt. Growth and orientation relationships of Ni and Cu films annealed on slightly miscut (11ŕ02) r-sapphire substrates. *Journal of Crystal Growth*, 508:24–33, 2019.

[43] A.-H. Chen, C. Dempsey, M. Pendharkar, S. Tan, A. Sharma, B. Zhang, S. Frolov, C. Palmstrom, L. Bellon, E. Bellet-Amalric, and M. Hocevar. Role of a capping layer on the crystalline structure of Sn thin films grown at cryogenic temperatures on InSb substrates. 2022.

[44] H. Chen, X. Sun, K. W. Lai, M. Meyyappan, and N. Xi. Infrared detection using an insb nanowire. In *2009 IEEE Nanotechnology Materials and Devices Conference*, pages 212–216. IEEE, 2009.

[45] J. Chen, B. D. Woods, P. Yu, M. Hocevar, D. Car, S. R. Plissard, E. P. Bakkers, T. D. Stanescu, and S. M. Frolov. Ubiquitous non-Majorana zero-bias conductance peaks in nanowire devices. *Physical Review Letters*, 123(10):1–14, 2019.

[46] J. Chen, P. Yu, J. Stenger, M. Hocevar, D. Car, S. R. Plissard, E. P. Bakkers, T. D. Stanescu, and S. M. Frolov. Experimental phase diagram of zero-bias conductance peaks in superconductor/semiconductor nanowire devices. *Science Advances*, 3(9):1–6, 2017.

[47] K. H. M. Chen, K. Y. Lin, S. W. Lien, S. W. Huang, C. K. Cheng, H. Y. Lin, C.-H. Hsu, T.-R. Chang, C.-M. Cheng, M. Hong, and J. Kwo. Thickness-dependent topological phase transition and Rashba-like preformed topological surface states of α-Sn(001) thin films on InSb(001). *Physical Review B*, 105(7):1–8, 2022.

[48] Y. Chen, X. Cui, K. Zhang, D. Pan, S. Zhang, B. Wang, and J. Hou. Bulk-quantity synthesis and self-catalytic vls growth of sno2 nanowires by lower-temperature evaporation. *Chemical Physics Letters*, 369(1-2):16–20, 2003.

[49] V. A. Chikichev S.I. CONDENSATION AND SUBLIMATION OF THIN AMORPHOUS ARSENIC FILMS STUDIED BY ELLIPSOMETRY. pages 285–291.

[50] L. Chirolli, N. Y. Yao, and J. E. Moore. Swap gate between a majorana qubit and a parity-protected superconducting qubit. *Phys. Rev. Lett.*, 129:177701, Oct 2022.

[51] D. Chow, R. Miles, T. Hasenberg, A. Kost, Y.-H. Zhang, H. Dunlap, and L. West. Mid-wave infrared diode lasers based on gainsb/inas and inas/alsb superlattices. *Applied Physics Letters*, 67(25):3700–3702, 1995.

[52] S. Chuang, Q. Gao, R. Kapadia, A. C. Ford, J. Guo, and A. Javey. Ballistic inas nanowire transistors. *Nano Letters*, 13(2):555–558, 2013.

[53] R. Citro, P. Marra, and F. Romeo. Topological states of matter: theory and applications. *European Physical Journal: Special Topics*, 227(12):1291–1294, 2018.

[54] J. F. Cochran and D. E. Mapother. Superconducting Transition in Aluminum. *Physical Review*, 111(1):132–142, 1958.

[55] W. S. Cole, S. Das Sarma, and T. D. Stanescu. Effects of large induced superconducting gap on semiconductor Majorana nanowires. *Physical Review B - Condensed Matter and Materials Physics*, 92(17):1–8, 2015.

[56] B. D. Cullity. *Elements of X-ray Diffraction*. Addison-Wesley Publishing, 1956.

[57] M. Dąbrowski, Y. Dai, M. Hocevar, S. Frolov, and H. Petek. Nanoscale guiding and shaping of indium droplets. *Applied Physics Letters*, 109(26), 2016.

[58] S. A. Dayeh, E. T. Yu, and D. Wang. Surface diffusion and substrate- nanowire adatom exchange in inas nanowire growth. *Nano Letters*, 9(5):1967–1972, 2009.

[59] M. T. Deng, S. Vaitiekenas, E. B. Hansen, J. Danon, M. Leijnse, K. Flensberg, J. Nygård, P. Krogstrup, and C. M. Marcus. Majorana bound state in a coupled quantum-dot hybrid-nanowire system. *Science*, 354(6319):1557–1562, 2016.

[60] K. A. Dick, K. Deppert, T. Mårtensson, B. Mandl, L. Samuelson, and W. Seifert. Failure of the vapor-liquid-solid mechanism in au-assisted MOVPE growth of InAs nanowires. *Nano Letters*, 5(4):761–764, 2005.

[61] I. Didschuns, K. Fleischer, P. Schilbe, N. Esser, W. Richter, and K. Lüders. Superconductivity in Sn films on InSb(1 1 0) taking account of the film morphology and structure. *Physica C: Superconductivity and its Applications*, 377(1-2):89–95, 2002.

[62] F. Domínguez-Adame, M. Martín-González, D. Sánchez, and A. Cantarero. Nanowires: A route to efficient thermoelectric devices. *Physica E: Low-Dimensional Systems and Nanostructures*, 113:213–225, 2019.

[63] V. G. Dubrovskii. *Nucleation Theory and Growth of Nanostructures*. 2014.

[64] V. G. Dubrovskii, Y. Berdnikov, J. Schmidtbauer, M. Borg, K. Storm, K. Deppert, and J. Johansson. Length Distributions of Nanowires Growing by Surface Diffusion. *Crystal Growth and Design*, 16(4):2167–2172, 2016.

[65] V. G. Dubrovskii, N. V. Sibirev, G. E. Cirlin, J. C. Harmand, and V. M. Ustinov. Theoretical analysis of the vapor-liquid-solid mechanism of nanowire growth during molecular beam epitaxy. *Physical Review E - Statistical, Nonlinear, and Soft Matter Physics*, 73(2):1–10, 2006.

[66] V. G. Dubrovskii, N. V. Sibirev, G. E. Cirlin, M. Tchernycheva, J. C. Harmand, and V. M. Ustinov. Shape modification of III-V nanowires: The role of nucleation on sidewalls. *Physical Review E - Statistical, Nonlinear, and Soft Matter Physics*, 77(3):1–7, 2008.

[67] V. G. Dubrovskii, N. V. Sibirev, R. A. Suris, G. E. Cirlin, J. C. Harmand, and V. M. Ustinov. Diffusion-controlled growth of semiconductor nanowires: Vapor pressure versus high vacuum deposition. *Surface Science*, 601(18):4395–4401, 2007.

[68] S. L. Dudarev, G. A. Botton, S. Y. Savrasov, C. J. Humphreys, and A. P. Sutton. Electron-energy-loss spectra and the structural stability of nickel oxide: An lsda+u study. *Phys. Rev. B*, 57:1505–1509, Jan 1998.

[69] J. Dufouleur, C. Colombo, T. Garma, B. Ketterer, E. Uccelli, M. Nicotra, and A. Fontcuberta I Morral. P-Doping mechanisms in catalyst-free gallium arsenide nanowires. *Nano Letters*, 10(5):1734–1740, 2010.

[70] J. W. Evans, D. E. Sanders, P. A. Thiel, and A. E. Depristo. Low-temperature epitaxial growth of thin metal films. *Physical Review B*, 41(8):5410–5413, 1990.

[71] E. M. Fadaly, H. Zhang, S. Conesa-Boj, D. Car, O. Gul, S. R. Plissard, R. L. Op het Veld, S. Kolling, L. P. Kouwenhoven, and E. P. Bakkers. Observation of conductance quantization in insb nanowire networks. *Nano Letters*, 17(11):6511–6515, 2017.

[72] R. F. Farrow, D. S. Robertson, G. M. Williams, A. G. Cullis, G. R. Jones, I. M. Young, and P. N. Dennis. The growth of metastable, heteroepitaxial films of α-Sn by metal beam epitaxy. *Journal of Crystal Growth*, 54(3):507–518, 1981.

[73] A. Fluri, C. Schneider, and D. Pergolesi. In situ stress measurements of metal oxide thin films. In *Metal Oxide-Based Thin Film Structures*, pages 109–132. Elsevier, 2018.

[74] S. A. Fortuna and X. Li. Metal-catalyzed semiconductor nanowires: a review on the control of growth directions. *Semiconductor Science and Technology*, 25(2):024005, 2010.

[75] S. Frolov, M. Manfra, and J. Sau. Topological superconductivity in hybrid devices. *Nature Physics*, 16(7):718–724, 2020.

[76] L. Fu and C. L. Kane. Superconducting proximity effect and majorana fermions at the surface of a topological insulator. *Physical Review Letters*, 100(9):1–4, 2008.

[77] C. Garcia Nunez, A. F. Braña, N. López, and B. J. García. A novel growth method to improve the quality of gaas nanowires grown by ga-assisted chemical beam epitaxy. *Nano Letters*, 18(6):3608–3615, 2018.

[78] C. B. Geller, W. Wolf, S. Picozzi, A. Continenza, R. Asahi, W. Mannstadt, A. J. Freeman, and E. Wimmer. Computational band-structure engineering of III-V semiconductor alloys. *Applied Physics Letters*, 79(3):368–370, 2001.

[79] S. G. Ghalamestani, M. Berg, K. A. Dick, and L.-E. Wernersson. High quality inas and gasb thin layers grown on si (1 1 1). *Journal of Crystal Growth*, 332(1):12–16, 2011.

[80] F. Glas, J. C. Harmand, and G. Patriarche. Why does wurtzite form in nanowires of III-V zinc blende semiconductors? *Physical Review Letters*, 99(14):3–6, 2007.

[81] N. Goel, J. Graham, J. Keay, K. Suzuki, S. Miyashita, M. Santos, and Y. Hirayama. Ballistic transport in insb mesoscopic structures. *Physica E: Low-dimensional Systems and Nanostructures*, 26(1-4):455–459, 2005.

[82] U. P. Gomes, D. Ercolani, V. Zannier, F. Beltram, and L. Sorba. Controlling the diameter distribution and density of InAs nanowires grown by Au-assisted methods. *Semiconductor Science and Technology*, 30(11):115012, 2015.

[83] T. Grap, T. Rieger, C. Blömers, T. Schäpers, D. Grützmacher, and M. Lepsa. Self-catalyzed vls grown inas nanowires with twinning superlattices. *Nanotechnology*, 24(33):335601, 2013.

[84] J. M. Graybeal. Competition between superconductivity and localization in two-dimensional ultrathin a-MoGe films. *Physica B+C*, 135(1-3):113–119, 1985.

[85] P. Gu, M. Tani, S. Kono, K. Sakai, and X.-C. Zhang. Study of terahertz radiation from inas and insb. *Journal of Applied Physics*, 91(9):5533–5537, 2002.

[86] Ö. Gül, H. Zhang, J. D. Bommer, M. W. De Moor, D. Car, S. R. Plissard, E. P. Bakkers, A. Geresdi, K. Watanabe, T. Taniguchi, and L. P. Kouwenhoven. Ballistic Majorana nanowire devices. *Nature Nanotechnology*, 13(3):192–197, 2018.

[87] L. Güniat, P. Caroff, and A. Fontcuberta I Morral. Vapor Phase Growth of Semiconductor Nanowires: Key Developments and Open Questions. *Chemical Reviews*, 119(15):8958–8971, 2019.

[88] N. A. Güsken, T. Rieger, P. Zellekens, B. Bennemann, E. Neumann, M. I. Lepsa, T. Schäpers, and D. Grützmacher. MBE growth of Al/InAs and Nb/InAs superconducting hybrid nanowire structures. *Nanoscale*, 9(43):16735–16741, 2017.

[89] N. N. Halder, A. Kelrich, Y. Kauffmann, S. Cohen, and D. Ritter. Growth of wurtzite inp/gap core-shell nanowires by metal-organic molecular beam epitaxy. *Journal of Crystal Growth*, 463:10–13, 2017.

[90] J. C. Harmand, G. Patriarche, F. Glas, F. Panciera, I. Florea, J. L. Maurice, L. Travers, and Y. Ollivier. Atomic Step Flow on a Nanofacet. *Physical Review Letters*, 121(16):166101, 2018.

[91] M. Z. Hasan and C. L. Kane. Colloquium: topological insulators. *Reviews of modern physics*, 82(4):3045, 2010.

[92] O. Hayden, R. Agarwal, and W. Lu. Semiconductor nanowire devices. *Nano Today*, 3(5-6):12–22, 2008.

[93] S. Hikami, A. I. Larkin, and Y. Nagaoka. Spin-orbit interaction and magnetoresistance in the two dimensional random system. *Progress of Theoretical Physics*, 63(2):707–710, 1980.

[94] K. Hiruma, M. Yazawa, T. Katsuyama, K. Ogawa, K. Haraguchi, M. Koguchi, and H. Kakibayashi. Growth and optical properties of nanometer-scale GaAs and InAs whiskers. *Journal of Applied Physics*, 77(2):447–462, 1995.

[95] R. G. Hobbs, N. Petkov, and J. D. Holmes. Semiconductor nanowire fabrication by bottom-up and top-down paradigms. *Chemistry of Materials*, 24(11):1975–1991, 2012.

[96] Y. Horio. Reflection High-Energy Electron Diffraction. *Compendium of Surface and Interface Analysis*, pages 527–530, 2018.

[97] K. Houben, J. K. Jochum, S. Couet, E. Menéndez, T. Picot, M. Y. Hu, J. Y. Zhao, E. E. Alp, A. Vantomme, K. Temst, et al. The influence of phonon softening on the superconducting critical temperature of sn nanostructures. *Scientific reports*, 10(1):1–9, 2020.

[98] K. Houben, J. K. Jochum, D. P. Lozano, M. Bisht, E. Menéndez, D. G. Merkel, R. Rüffer, A. I. Chumakov, S. Roelants, B. Partoens, M. V. Milošević, F. M. Peeters, S. Couet, A. Vantomme, K. Temst, and M. J. Van Bael. In situ study of the α -Sn to β -Sn phase transition in low-dimensional systems: Phonon behavior and thermodynamic properties. *Physical Review B*, 100(7):1–9, 2019.

[99] S. Y. Hsu and J. M. Valles. Magnetic-field-induced pair-breaking effects in granular Pb films near the superconductor-to-insulator transition. *Physical Review B*, 48(6):4164–4167, 1993.

[100] Y. J. Hsu and S. Y. Lu. Vapor-solid growth of Sn nanowires: Growth mechanism and superconductivity. *Journal of Physical Chemistry B*, 109(10):4398–4403, 2005.

[101] H. Huang, X. Ren, X. Ye, J. Guo, Q. Wang, X. Zhang, S. Cai, and Y. Huang. Control of the crystal structure of InAs nanowires by tuning contributions of adatom diffusion. *Nanotechnology*, 21(47), 2010.

[102] ICDD. Icdd database - pdf-4+ 2023, 2022. [Online; accessed 21-October-2022].

[103] J. I. LANGFORD and A. J. C. WILSON. Seherrer after Sixty Years: A Survey and Some New Results in the Determination of Crystallite Size. *Journal of Applied crystal*, pages 1536–1545, 1978.

[104] H. M. Jaeger, D. B. Haviland, B. G. Orr, and A. M. Goldman. Onset of superconductivity in ultrathin granular metal films. *Physical Review B*, 40(1):182–196, 1989.

[105] M. J. A. Jardine, D. Dardzinski, M. Yu, A. Purkayastha, A. Chen, S. M. Frolov, and N. Marom. First Principles Assessment of CdTe as a Tunnel Barrier at the α-Sn / InSb Interface.

[106] L. E. Jensen, M. T. Björk, S. Jeppesen, A. I. Persson, B. J. Ohlsson, and L. Samuelson. Role of surface diffusion in chemical beam epitaxy of inas nanowires. *Nano Letters*, 4(10):1961–1964, 2004.

[107] T. Jiang, Q. Guo, R.-Y. Zhang, Z.-Q. Zhang, B. Yang, and C. T. Chan. Four-band non-abelian topological insulator and its experimental realization. *Nature communications*, 12(1):1–9, 2021.

[108] J. Johansson, K. A. Dick, P. Caroff, M. E. Messing, J. Bolinsson, K. Deppert, and L. Samuelson. Diameter dependence of the wurtzite-zinc blende transition in inas nanowires. *Journal of Physical Chemistry C*, 114(9):3837–3842, 2010.

[109] H. J. Joyce, J. L. Boland, C. L. Davies, S. A. Baig, and M. B. Johnston. A review of the electrical properties of semiconductor nanowires: Insights gained from terahertz conductivity spectroscopy. *Semiconductor Science and Technology*, 31(10), 2016.

[110] JÜRGEN HAFNER. Ab-Initio Simulations of Materials Using VASP: Density-Functional Theory and Beyond. *Journal of computational chemistry*, 32:174–182, 2008.

[111] I. L. Kalnin and J. Rosenstock. Vapor Deposition of Germanium on Molybdenum. *Journal of The Electrochemical Society*, 112(3):329, 1965.

[112] J. H. Kang, A. Grivnin, E. Bor, J. Reiner, N. Avraham, Y. Ronen, Y. Cohen, P. Kacman, H. Shtrikman, and H. Beidenkopf. Robust Epitaxial Al Coating of Reclined InAs Nanowires. *Nano Letters*, 17(12):7520–7527, 2017.

[113] J. H. Kang, F. Krizek, M. Zaluska-Kotur, P. Krogstrup, P. Kacman, H. Beidenkopf, and H. Shtrikman. Au-Assisted Substrate-Faceting for Inclined Nanowire Growth. *Nano Letters*, 18(7):4115–4122, 2018.

[114] Y. Kang, H.-D. Liu, M. Morse, M. J. Paniccia, M. Zadka, S. Litski, G. Sarid, A. Pauchard, Y.-H. Kuo, H.-W. Chen, et al. Monolithic germanium/silicon avalanche photodiodes with 340 ghz gain–bandwidth product. *Nature Photonics*, 3(1):59–63, 2009.

[115] T. Kanne, M. Marnauza, D. Olsteins, D. J. Carrad, J. E. Sestoft, J. de Bruijckere, L. Zeng, E. Johnson, E. Olsson, K. Grove-Rasmussen, et al. Epitaxial pb on inas nanowires for quantum devices. *Nature Nanotechnology*, 16(7):776–781, 2021.

[116] N. Kato and A. Lang. A study of pendellösung fringes in x-ray diffraction. *Acta Crystallographica*, 12(10):787–794, 1959.

[117] M. D. Kelzenberg, S. W. Boettcher, J. A. Petykiewicz, D. B. Turner-Evans, M. C. Putnam, E. L. Warren, J. M. Spurgeon, R. M. Briggs, N. S. Lewis, and H. A. Atwater. Enhanced absorption and carrier collection in si wire arrays for photovoltaic applications. *Nature materials*, 9(3):239–244, 2010.

[118] S. A. Khan. *Epitaxy of Hybrid Nanowires , Shadow Junctions and Networks*. PhD thesis, 2020.

[119] A. Kirk, M. Milojevic, J. Kim, and R. Wallace. An in situ examination of atomic layer deposited alumina/inas (100) interfaces. *Applied Physics Letters*, 96(20):202905, 2010.

[120] C. Kloeffel, M. Trif, P. Stano, and D. Loss. Circuit qed with hole-spin qubits in ge/si nanowire quantum dots. *Physical Review B*, 88(24):241405, 2013.

[121] A. A. Koryakin, S. A. Kukushkin, K. P. Kotlyar, E. D. Ubyivovk, R. R. Reznik, and G. E. Cirlin. A new insight into the mechanism of low-temperature Au-assisted growth of InAs nanowires. *CrystEngComm*, 21(32):4707–4717, 2019.

[122] U. Krishnamachari, M. Borgstrom, B. J. Ohlsson, N. Panev, L. Samuelson, W. Seifert, M. W. Larsson, and L. R. Wallenberg. Defect-free InP nanowires grown in [001] direction on InP (001). *Applied Physics Letters*, 85(11):2077–2079, 2004.

[123] F. Krizek. *Semiconductor Nanowire Networks Grown By Molecular Beam Epitaxy Vapor-Liquid-Solid*. PhD thesis, 2018.

[124] F. Krizek, T. Kanne, D. Razmadze, E. Johnson, J. Nygård, C. M. Marcus, and P. Krogstrup. Growth of InAs Wurtzite Nanocrosses from Hexagonal and Cubic Basis. *Nano Letters*, 17(10):6090–6096, 2017.

[125] P. Krogstrup, S. Curiotto, E. Johnson, M. Aagesen, J. Nygård, and D. Chatain. Impact of the liquid phase shape on the structure of iii-v nanowires. *Physical Review Letters*, 106(12):125505, 2011.

[126] P. Krogstrup, N. L. Ziino, W. Chang, S. M. Albrecht, M. H. Madsen, E. Johnson, J. Nygård, C. M. Marcus, and T. S. Jespersen. Epitaxy of semiconductor-superconductor nanowires. *Nature Materials*, 14(4):400–406, 2015.

[127] A. F. Lee and R. M. Lambert. Oxidation of Sn overlayers and the structure and stability of Sn oxide films on Pd(111). *Physical Review B - Condensed Matter and Materials Physics*, 58(7):4156–4165, 1998.

[128] S.-K. Lee, H.-J. Choi, P. Pauzauskie, P. Yang, N.-K. Cho, H.-D. Park, E.-K. Suh, K.-Y. Lim, and H.-J. Lee. Gallium nitride nanowires with a metal initiated metal-organic chemical vapor deposition (mocvd) approach. *physica status solidi (b)*, 241(12):2775–2778, 2004.

[129] M. Leijnse and K. Flensberg. Quantum information transfer between topological and spin qubit systems. *Physical Review Letters*, 107(21):210502, 2011.

[130] F. Lenrick, M. Ek, K. Deppert, L. Samuelson, and L. Reine Wallenberg. Straight and kinked InAs nanowire growth observed in situ by transmission electron microscopy. *Nano Research*, 7(8):1188–1194, 2014.

[131] H. Li, Y. X. Cui, K. Y. Wu, W. K. Tseng, H. H. Cheng, and H. Chen. Strain relaxation and Sn segregation in GeSn epilayers under thermal treatment. *Applied Physics Letters*, 102(25), 2013.

[132] M. Li, R. B. Bhiladvala, T. J. Morrow, J. A. Sioss, K.-K. Lew, J. M. Redwing, C. D. Keating, and T. S. Mayer. Bottom-up assembly of large-area nanowire resonator arrays. *Nature nanotechnology*, 3(2):88–92, 2008.

[133] S. Li, Y. Chen, X. Shang, Y. Yu, J. Yang, J. Huang, X. Su, J. Shen, B. Sun, H. Ni, et al. Boost of single-photon emission by perfect coupling of inas/gaas quantum dot and micropillar cavity mode. *Nanoscale Research Letters*, 15(1):1–7, 2020.

[134] M. Liao, Y. Zang, Z. Guan, H. Li, Y. Gong, K. Zhu, X. P. Hu, D. Zhang, Y. Xu, Y. Y. Wang, K. He, X. C. Ma, S. C. Zhang, and Q. K. Xue. Superconductivity in few-layer stanene. *Nature Physics*, 14(4):344–348, 2018.

[135] C. M. Lieber. One-dimensional nanostructures: chemistry, physics & applications. *Solid state communications*, 107(11):607–616, 1998.

[136] C. Lindberg. *Growth of Ag-seeded III-V nanowires and TEM characterization*. PhD thesis, 2017.

[137] B. Liu, J. Wu, Y. Cui, H. Wang, Y. Liu, Z. Wang, Z. Ren, and G. Cao. Superconductivity in SnSb with a natural superlattice structure. *Superconductor Science and Technology*, 31(12), 2018.

[138] T. Liu and E. Peretti. Lattice parameter of insb. *JOM*, 3(9):791–791, 1951.

[139] T. D. Lowes, L. Schowalter, G. C. Weatherly, and J. M. Gibson. Observations on interactions between metal clusters and III-V semiconductor substrates. *Scanning Microscopy*, 8(4):773–780, 1994.

[140] D. Lozano, S. Couet, C. Petermann, G. Hamoir, J. Jochum, T. Picot, E. Menéndez, K. Houben, V. Joly, V. Antohe, et al. Experimental observation of electron-phonon coupling enhancement in sn nanowires caused by phonon confinement effects. *Physical Review B*, 99(6):064512, 2019.

[141] D. Lucot, F. Pierre, D. Mailly, K. Yu-Zhang, S. Michotte, F. De Menten De Horne, and L. Piraux. Multicontact measurements of a superconducting Sn nanowire. *Applied Physics Letters*, 91(4):2005–2008, 2007.

[142] R. M. Lutchyn, J. D. Sau, and S. D. Sarma. Majorana fermions and a topological phase transition in semiconductor-superconductor heterostructures. *Physical Review Letters*, 105(7):077001, 2010.

[143] F. Luthi, T. Stavenga, O. Enzing, A. Bruno, C. Dickel, N. Langford, M. A. Rol, T. S. Jespersen, J. Nygård, P. Krogstrup, et al. Evolution of nanowire transmon qubits and their coherence in a magnetic field. *Physical Review Letters*, 120(10):100502, 2018.

[144] I. Madarevic, U. Thupakula, G. Lippertz, N. Claessens, P. C. Lin, H. Bana, S. Gonzalez, G. Di Santo, L. Petaccia, M. N. Nair, L. M. Pereira, C. Van Haesendonck, and M. J. Van Bael. Structural and electronic properties of the pure and stable elemental 3D topological Dirac semimetal α -Sn. *APL Materials*, 8(3), 2020.

[145] M. H. Madsen. Indium Arsenide Nanowires. 2012.

[146] M. H. Madsen, P. Krogstrup, E. Johnson, S. Venkatesan, E. Mühlbauer, C. Scheu, C. B. Sørensen, and J. Nygård. Experimental determination of adatom diffusion lengths for growth of InAs nanowires. *Journal of Crystal Growth*, 364:16–22, 2013.

[147] S. Mandal, S. Dutta, S. Basistha, I. Roy, J. Jesudasan, V. Bagwe, L. Benfatto, A. Thamizhavel, and P. Raychaudhuri. Destruction of superconductivity through phase fluctuations in ultrathin a -MoGe films. *Physical Review B*, 102(6):1–8, 2020.

[148] F. Matteini, G. Tütüncüoglu, H. Potts, F. Jabeen, and A. Fontcuberta I Morral. Wetting of Ga on SiOx and Its Impact on GaAs Nanowire Growth. *Crystal Growth and Design*, 15(7):3105–3109, 2015.

[149] J. D. McBrayer, R. M. Swanson, and T. W. Sigmon. Diffusion of Metals in Silicon Dioxide. *Journal of The Electrochemical Society*, 133(6):1242–1246, 1986.

[150] P. C. McIntyre and A. Fontcuberta i Morral. Semiconductor nanowires: to grow or not to grow? *Materials Today Nano*, 9:100058, 2020.

[151] K. Meng, X. Wang, Q. Xu, Z. Li, Z. Liu, L. Wu, Y. Hu, N. Liu, and G. Chen. In situ observation of crystallization dynamics and grain orientation in sequential deposition of metal halide perovskites. *Advanced Functional Materials*, 29(35):1902319, 2019.

[152] E. A. Merritt. X-ray absorption edges, 2022. [Online; accessed 1-October-2022].

[153] T. Mitsunaga. II. Out-of-plane diffraction measurements. *The Rigaku Journal*, 25(1):7–12, 2009.

[154] W. Mönch. Role of virtual gap states and defects in metal-semiconductor contacts. *Physical Review Letters*, 58(12):1260–1263, 1987.

[155] W. Mönch. Barrier heights of real Schottky contacts explained by metal-induced gap states and lateral inhomogeneities. *Journal of Vacuum Science & Technology B: Microelectronics and Nanometer Structures*, 17(4):1867, 1999.

[156] A. Monshi, M. R. Foroughi, and M. R. Monshi. Modified Scherrer Equation to Estimate More Accurately Nano-Crystallite Size Using XRD. *World Journal of Nano Science and Engineering*, 02(03):154–160, 2012.

[157] S. M. Mostafavi Kashani, V. G. Dubrovskii, T. Baumbach, and U. Pietsch. In Situ Monitoring of MBE Growth of a Single Self-Catalyzed GaAs Nanowire by X-ray Diffraction. *Journal of Physical Chemistry C*, 125(41):22724–22732, 2021.

[158] V. Mourik, K. Zuo, S. M. Frolov, S. R. Plissard, E. P. Bakkers, and L. P. Kouwenhoven. Signatures of majorana fermions in hybrid superconductor-semiconductor nanowire devices. *Science*, 336(6084):1003–1007, 2012.

[159] B. Nasiri-Tabrizi. Thermal treatment effect on structural features of mechano-synthesized fluorapatite-titania nanocomposite: A comparative study. *Journal of Advanced Ceramics*, 3(1):31–42, 2014.

[160] C. Nayak, S. H. Simon, A. Stern, M. Freedman, and S. D. Sarma. Non-abelian anyons and topological quantum computation. *Reviews of Modern Physics*, 80(3):1083, 2008.

[161] I. P. Nevirkovets, M. A. Belogolovskii, and J. B. Ketterson. Josephson junctions based on amorphous MoGe: Prospects for use in superconducting electronics. *Superconductor Science and Technology*, 35(3), 2022.

[162] B. Nijholt and A. R. Akhmerov. Orbital effect of magnetic field on the majorana phase diagram. *Physical Review B*, 93(23):235434, 2016.

[163] Z. Ogorzalek, B. Seredynski, S. Kret, A. Kwiatkowski, K. P. Korona, M. Grzeszczyk, J. Mierzejewski, D. Wasik, W. Pacuski, J. Sadowski, and M. Gryglas-Borysiewicz. Charge transport in MBE-grown 2H-MoTe2bilayers with enhanced stability provided by an AlO: Xcapping layer. *Nanoscale*, 12(31):16535–16542, 2020.

[164] H. Omi, H. Saito, and T. Osaka. Polarity propagation in the InSb/α-Sn/InSb heterostructure. *Physical Review Letters*, 72(16):2596–2599, 1994.

[165] Y. Oreg, G. Refael, and F. Von Oppen. Helical liquids and majorana bound states in quantum wires. *Physical Review Letters*, 105(17):177002, 2010.

[166] M. Orrù, E. Robin, M. Den Hertog, K. Moratis, Y. Genuist, R. André, D. Ferrand, J. Cibert, and E. Bellet-Amalric. Nanowire growth and sublimation: Cdte quantum dots in znte nanowires. *Physical Review Materials*, 2(4):043404, 2018.

[167] A. Patterson. The scherrer formula for x-ray particle size determination. *Physical Review*, 56(10):978, 1939.

[168] M. Pendharkar, B. Zhang, H. Wu, A. Zarassi, P. Zhang, C. P. Dempsey, J. S. Lee, S. D. Harrington, G. Badawy, S. Gazibegovic, R. L. Op het Veld, M. Rossi, J. Jung, A. H. Chen, M. A. Verheijen, M. Hocevar, E. P. Bakkers, C. J. Palmstrøm, and S. M. Frolov. Parity-preserving and magnetic field-resilient superconductivity in InSb nanowires with Sn shells. *Science*, 372(6541):508–511, 2021.

[169] J. P. Perdew. Jacob's ladder of density functional approximations for the exchange-correlation energy. *American Institute of Physics*, 1(2001):1–20, 2001.

[170] P. Perla, H. A. Fonseka, P. Zellekens, R. Deacon, Y. Han, J. Kölzer, T. Mörstedt, B. Bennemann, A. Espiari, K. Ishibashi, et al. Fully in situ nb/inas-nanowire josephson junctions by selective-area growth and shadow evaporation. *Nanoscale Advances*, 3(5):1413–1421, 2021.

[171] P. Perla, H. A. Fonseka, P. Zellekens, R. Deacon, Y. Han, J. Kölzer, T. Mörstedt, B. Bennemann, A. Espiari, K. Ishibashi, D. Grützmacher, A. M. Sanchez, M. I. Lepsa, and T. Schäpers. Fullyin situNb/InAs-nanowire Josephson junctions by selective-area growth and shadow evaporation. *Nanoscale Advances*, 3(5):1413–1421, 2021.

[172] S. R. Plissard, D. R. Slapak, M. A. Verheijen, M. Hocevar, G. W. Immink, I. Van Weperen, S. Nadj-Perge, S. M. Frolov, L. P. Kouwenhoven, and E. P. Bakkers. From InSb nanowires to nanocubes: Looking for the sweet spot. *Nano Letters*, 12(4):1794–1798, 2012.

[173] F. Pobell. *Matter and methods at low temperatures*. Springer Science & Business Media, 2007.

[174] D. M. Poirier and J. H. Weaver. InSb(110) by XPS. *Surface Science Spectra*, 2(3):217–223, 1993.

[175] X. L. Qi and S. C. Zhang. Topological insulators and superconductors. *Reviews of Modern Physics*, 83(4), 2011.

[176] M. E. Reimer, G. Bulgarini, N. Akopian, M. Hocevar, M. B. Bavinck, M. A. Verheijen, E. P. Bakkers, L. P. Kouwenhoven, and V. Zwiller. Bright single-photon sources in bottom-up tailored nanowires. *Nature Communications*, 3, 2012.

[177] RIBER. Mbe sources, 2022. [Online; accessed 2-September-2022].

[178] T. Rieger, P. Zellekens, N. Demarina, A. A. Hassan, F. J. Hackemüller, H. Lüth, U. Pietsch, T. Schäpers, D. Grützmacher, and M. I. Lepsa. Strain relaxation and ambipolar electrical transport in GaAs/InSb core-shell nanowires. *Nanoscale*, 9(46):18392–18401, 2017.

[179] Rigaku. X-ray reflectometry (xrr), 2022. [Online; accessed 11-September-2022].

[180] M. T. Robson and R. R. Lapierre. InAs nanowire growth modes on Si (111) by gas source molecular beam epitaxy. *Journal of Crystal Growth*, 436:1–11, 2016.

[181] D. L. Rode. Electron mobility in direct-gap polar semiconductors. *Physical Review B*, 2(4):1012, 1970.

[182] D. L. Rode. Electron transport in InSb, InAs, and InP. *Physical Review B*, 3(10):3287–3299, 1971.

[183] A. Rogalski, P. Martyniuk, and M. Kopytko. Inas/gasb type-ii superlattice infrared detectors: Future prospect. *Applied physics Reviews*, 4(3):031304, 2017.

[184] J. C. Rojas-Sánchez, S. Oyarzún, Y. Fu, A. Marty, C. Vergnaud, S. Gambarelli, L. Vila, M. Jamet, Y. Ohtsubo, A. Taleb-Ibrahimi, P. Le Fèvre, F. Bertran, N. Reyren, J. M. George, and A. Fert. Spin to Charge Conversion at Room Temperature by Spin Pumping into a New Type of Topological Insulator: α -Sn Films. *Physical Review Letters*, 116(9):1–6, 2016.

[185] M. Rosini, M. C. Righi, P. Kratzer, and R. Magri. Indium surface diffusion on InAs (2Œ4) reconstructed wetting layers on GaAs(001). *Physical Review B - Condensed Matter and Materials Physics*, 79(7):1–7, 2009.

[186] I. Roy, S. Dutta, A. N. Roy Choudhury, S. Basistha, I. MacCari, S. Mandal, J. Jesudasan, V. Bagwe, C. Castellani, L. Benfatto, and P. Raychaudhuri. Melting of the Vortex Lattice through Intermediate Hexatic Fluid in an a-MoGe Thin Film. *Physical Review Letters*, 122(4):47001, 2019.

[187] F. Sánchez-Bajo and F. L. Cumbrera. The Use of the Pseudo-Voigt Function in the Variance Method of X-ray Line-Broadening Analysis. *Journal of Applied Crystallography*, 30(4):427–430, 1997.

[188] F. Sánchez-Ochoa, F. Hidalgo, M. Pruneda, and C. Noguez. Unfolding method for periodic twisted systems with commensurate moiré patterns. *Journal of Physics: Condensed Matter*, 32(2):025501, 2019.

[189] M. A. T. Sandoval, E. A. d. A. e Silva, A. F. da Silva, and G. C. La Rocca. Electron g factor anisotropy in asymmetric iii–v semiconductor quantum wells. *Semiconductor Science and Technology*, 31(11):115008, 2016.

[190] C. Santori, D. Fattal, J. Vučković, G. S. Solomon, and Y. Yamamoto. Indistinguishable photons from a single-photon device. *Nature*, 419(6907):594–597, 2002.

[191] M. Sato and Y. Ando. Topological superconductors: A review. *Reports on Progress in Physics*, 80(7):1–45, 2017.

[192] M. Schäfer, W. Naumann, T. Finnberg, M. Hannss, A. Dutschke, and R. Anton. UV/ozone-activated growth of oxide layers on InAs(001) surfaces and oxide desorption under arsenic pressure. *Applied Surface Science*, 158(1):147–158, 2000.

[193] C. Schmetterer, J. Polt, and H. Flandorfer. The phase equilibria in the Sb-Sn system Part II: Experimental results. *Journal of Alloys and Compounds*, 743:523–536, 2018.

[194] M. Schneider-Ramelow and C. Ehrhardt. The reliability of wire bonding using ag and al. *Microelectronics Reliability*, 63:336–341, 2016.

[195] W. Seifert, M. Borgström, K. Deppert, K. A. Dick, J. Johansson, M. W. Larsson, T. Mårtensson, N. Sköld, C. P. T. Svensson, B. A. Wacaser, et al. Growth of one-dimensional nanostructures in movpe. *Journal of crystal growth*, 272(1-4):211–220, 2004.

[196] W. Seifert, M. Borgström, K. Deppert, K. A. Dick, J. Johansson, M. W. Larsson, T. Mårtensson, N. Skold, C. P. T. Svensson, B. A. Wacaser, L. R. Wallenberg, and L. Samuelson. Growth of one-dimensional nanostructures in MOVPE. *Journal of Crystal Growth*, 272(1-4 SPEC. ISS.):211–220, 2004.

[197] S. Sellner, A. Gerlach, F. Schreiber, M. Kelsch, N. Kasper, H. Dosch, S. Meyer, J. Pflaum, M. Fischer, B. Gompf, and G. Ulbricht. Mechanisms for the enhancement of the thermal stability of organic thin films by aluminum oxide capping layers. *Journal of Materials Research*, 21(2):455–464, 2006.

[198] J. Shen, S. Heedt, F. Borsoi, B. van Heck, S. Gazibegovic, R. L. Op het Veld, D. Car, J. A. Logan, M. Pendharkar, S. J. Ramakers, G. Wang, D. Xu, D. Bouman, A. Geresdi, C. J. Palmstrøm, E. P. Bakkers, and L. P. Kouwenhoven. Parity transitions in the superconducting ground state of hybrid InSbAl Coulomb islands. *Nature Communications*, 9(1):1–8, 2018.

[199] Shiintaro Kobayashi. The "sphincter" corer: A wide-diameter corer with watertight core-catcher. *The Rigaku Journal*, 4(2):149–162, 2010.

[200] D. Shindo and T. Oikawa. Energy dispersive x-ray spectroscopy. In *Analytical electron microscopy for materials science*, pages 81–102. Springer, 2002.

[201] H. Song, J. Yao, Y. Ding, Y. Gu, Y. Deng, M. H. Lu, H. Lu, and Y. F. Chen. Thermal Stability Enhancement in Epitaxial Alpha Tin Films by Strain Engineering. *Advanced Engineering Materials*, 21(10):1–7, 2019.

[202] M. S. Song, T. Koren, M. Załuska-Kotur, R. Buczko, N. Avraham, P. Kacman, H. Shtrikman, and H. Beidenkopf. Sub-Band Spectrum Engineering via Structural Order in Tapered Nanowires. *Nano Letters*, 21(24):10215–10221, 2021.

[203] S. M. Song, Y. H. Song, T. L. Yang, S. H. Jia, Y. Q. Xin, and Y. H. Li. Effect of homo-buffer layer on the properties of indium tin oxide thin films. *Rengong Jingti Xuebao/Journal of Synthetic Crystals*, 42(12):1–6, 2013.

[204] A. Steffen Schlör. Dilution refrigerator — Wikipedia, the free encyclopedia, 2022. [Online; accessed 6-July-2022].

[205] W. Sun, Y. Guo, H. Xu, Q. Gao, H. Hoe Tan, C. Jagadish, and J. Zou. Polarity driven simultaneous growth of free-standing and lateral GaAsP epitaxial nanowires on GaAs (001) substrate. *Applied Physics Letters*, 103(22):1–5, 2013.

[206] H. K. Sung, C. Wang, and N. Y. Kim. Reliability study of Au-in solid-liquid interdiffusion bonding for GaN-based vertical LED packaging. *Journal of Micromechanics and Microengineering*, 25(12):127002, 2015.

[207] M. Tchernycheva, L. Travers, G. Patriarche, F. Glas, J. C. Harmand, G. E. Cirlin, and V. G. Dubrovskii. Au-assisted molecular beam epitaxy of InAs nanowires: Growth and theoretical analysis. *Journal of Applied Physics*, 102(9), 2007.

[208] R. Tessler, C. Saguy, O. Klin, S. Greenberg, E. Weiss, R. Akhvlediani, R. Edrei, and A. Hoffman. Oxide-free InSb (100) surfaces by molecular hydrogen cleaning. *Applied Physics Letters*, 88(3):1–3, 2006.

[209] R. Tessler, C. Saguy, O. Klin, S. Greenberg, E. Weiss, R. Akhvlediani, R. Edrei, and A. Hoffman. Desorption of InSb(001) native oxide and surface smoothing induced by low temperature annealing under molecular hydrogen flow. *Journal of Applied Physics*, 101(2), 2007.

[210] M. Tian, J. Wang, J. Snyder, J. Kurtz, Y. Liu, P. Schiffer, T. E. Mallouk, and M. H. Chan. Synthesis and characterization of superconducting single-crystal Sn nanowires. *Applied Physics Letters*, 83(8):1620–1622, 2003.

[211] K. Tomioka, K. Ikejiri, T. Tanaka, J. Motohisa, S. Hara, K. Hiruma, and T. Fukui. Selective-area growth of iii-v nanowires and their applications. *Journal of Materials Research*, 26(17):2127–2141, 2011.

[212] J. Y. Tsao. *Materials fundamentals of molecular beam epitaxy*. Academic Press, 2012.

[213] A. R. Ullah, H. J. Joyce, A. M. Burke, J. Wong-Leung, H. H. Tan, C. Jagadish, and A. P. Micolich. Electronic comparison of InAs wurtzite and zincblende phases using nanowire transistors. *Physica Status Solidi - Rapid Research Letters*, 7(10):911–914, 2013.

[214] B. Van Heck, A. Akhmerov, F. Hassler, M. Burrello, and C. Beenakker. Coulomb-assisted braiding of majorana fermions in a josephson junction array. *New Journal of Physics*, 14(3):035019, 2012.

[215] R. Veresegyházy, I. Mojzes, and B. Pecz. Comparative mass spectrometric study of aiii-bv compounds covered with a gold layer. *Vacuum*, 36(7-9):547–549, 1986.

[216] R. Veresegyhazy, B. Pecz, and I. Mojzes. The influence of a gold layer on the thermal decomposition of inas. *Physica Status Solidi. A, Applied Research*, 94(1):K11–K12, 1986.

[217] V. B. Verma, A. E. Lita, M. R. Vissers, F. Marsili, D. P. Pappas, R. P. Mirin, and S. W. Nam. Superconducting nanowire single photon detectors fabricated from an amorphous Mo0.75Ge0.25 thin film. *Applied Physics Letters*, 105(2):0–5, 2014.

[218] R. S. Wagner and W. C. Ellis. Vapor-liquid-solid mechanism of single crystal growth. *Applied Physics Letters*, 4(5):89–90, 1964.

[219] H. Wang, M. Sun, K. Ding, M. T. Hill, and C.-Z. Ning. A top-down approach to fabrication of high quality vertical heterostructure nanowire arrays. *Nano Letters*, 11(4):1646–1650, 2011.

[220] J. Wang, S. Plissard, M. Hocevar, T. T. Vu, T. Zehender, G. G. Immink, M. A. Verheijen, J. Haverkort, and E. P. Bakkers. Position-controlled [100] InP nanowire arrays. *Applied Physics Letters*, 100(5):1–4, 2012.

[221] S. Wang, Z. Shan, and H. Huang. The mechanical properties of nanowires. *Advanced Science*, 4(4):1600332, 2017.

[222] Y. Wang, T. Šikola, and M. Kolíbal. Collector Droplet Behavior during Formation of Nanowire Junctions. *Journal of Physical Chemistry Letters*, 11(16):6498–6504, 2020.

[223] Y.-L. Wang, X. Ma, J. Xu, Z.-L. Xiao, A. Snezhko, R. Divan, L. E. Ocola, J. E. Pearson, B. Janko, and W.-K. Kwok. Switchable geometric frustration in an artificial-spin-ice–superconductor heterosystem. *Nature nanotechnology*, 13(7):560–565, 2018.

[224] B. E. Warren. *X-ray Diffraction*. Courier Corporation, 1990.

[225] P. Wei, F. Katmis, C.-Z. Chang, and J. S. Moodera. Induced superconductivity and engineered josephson tunneling devices in epitaxial (111)-oriented gold/vanadium heterostructures. *Nano Letters*, 16(4):2714–2719, 2016.

[226] S. P. West. *Substrate Cleaning Using a Remote Hydrogen Rf-Plasma*. PhD thesis, 2000.

[227] J. Westwater, D. P. Gosain, S. Tomiya, S. Usui, and H. Ruda. Growth of silicon nanowires via gold/silane vapor–liquid–solid reaction. *Journal of Vacuum Science & Technology B:*

Microelectronics and Nanometer Structures Processing, Measurement, and Phenomena, 15(3):554–557, 1997.

[228] wiki community. X-ray reflectivity — Wikipedia, the free encyclopedia, 2022. [Online; accessed 11-September-2022].

[229] Wikipedia. Voigt profile, 2022. [Online; accessed 4-September-2022].

[230] T. Wonglakhon and D. Zahn. Interaction potentials for modelling gan precipitation and solid state polymorphism. *Journal of Physics: Condensed Matter*, 32(20):205401, 2020.

[231] C. Z. Xu, Y. H. Chan, P. Chen, X. Wang, D. Flötotto, J. A. Hlevyack, G. Bian, S. K. Mo, M. Y. Chou, and T. C. Chiang. Gapped electronic structure of epitaxial stanene on InSb(111). *Physical Review B*, 97(3):1–5, 2018.

[232] H. Ye, L. Li, R. T. Hinkey, R. Q. Yang, T. D. Mishima, J. C. Keay, M. B. Santos, and M. B. Johnson. MBE growth optimization of InAs (001) homoepitaxy. *Journal of Vacuum Science & Technology B, Nanotechnology and Microelectronics: Materials, Processing, Measurement, and Phenomena*, 31(3):03C135, 2013.

[233] G. Yi and W. Schwarzacher. Single crystal superconductor nanowires by electrodeposition. *Applied Physics Letters*, 74(12):1746–1748, 1999.

[234] M. Yu, S. Yang, C. Wu, and N. Marom. Machine learning the hubbard u parameter in dft+u using bayesian optimization. *npj Computational Materials*, 6(1):180, 2020.

[235] P. Yu, J. Chen, M. Gomanko, G. Badawy, E. Bakkers, K. Zuo, V. Mourik, and S. Frolov. Non-majorana states yield nearly quantized conductance in proximatized nanowires. *Nature Physics*, 17(4):482–488, 2021.

[236] X. Yu, L. Li, H. Wang, J. Xiao, C. Shen, D. Pan, and J. Zhao. Two-step fabrication of self-catalyzed Ga-based semiconductor nanowires on Si by molecular-beam epitaxy. *Nanoscale*, 8(20):10615–10621, 2016.

[237] X. Yuan, P. Caroff, J. Wong-Leung, L. Fu, H. H. Tan, and C. Jagadish. Tunable Polarity in a III-V Nanowire by Droplet Wetting and Surface Energy Engineering. *Advanced Materials*, 27(40):6096–6103, 2015.

[238] X. Yuan, J. Yang, J. He, H. H. Tan, and C. Jagadish. Role of surface energy in nanowire growth. *Journal of Physics D: Applied Physics*, 51(28), 2018.

[239] H. Zeng, X. Yu, H. A. Fonseka, G. Boras, P. Jurczak, T. Wang, A. M. Sanchez, and H. Liu. Preferred growth direction of III-V nanowires on differently oriented Si substrates. *Nanotechnology*, 31(47), 2020.

[240] H. Zhang, Ö. Gül, S. Conesa-Boj, M. P. Nowak, M. Wimmer, K. Zuo, V. Mourik, F. K. De Vries, J. Van Veen, M. W. De Moor, et al. Ballistic superconductivity in semiconductor nanowires. *Nature communications*, 8(1):1–7, 2017.

[241] Y. Zhang, C. H. Wong, J. Shen, S. T. Sze, B. Zhang, H. Zhang, Y. Dong, H. Xu, Z. Yan, Y. Li, X. Hu, and R. Lortz. Dramatic enhancement of superconductivity in single-crystalline nanowire arrays of Sn. *Scientific Reports*, 6(August):1–10, 2016.

[242] Z. Zhang, Z. Lu, H. Xu, P. Chen, W. Lu, and J. Zou. Structure and quality controlled growth of inas nanowires through catalyst engineering. *Nano Research*, 7(11):1640–1649, 2014.

[243] Z. Zhang, Z. Y. Lu, P. P. Chen, W. Lu, and J. Zou. Controlling the crystal phase and structural quality of epitaxial InAs nanowires by tuning V/III ratio in molecular beam epitax. *Acta Materialia*, 92:25–32, 2015.

APPENDIX A

Supplementary data for Part I

A.1 Indium rich Au droplet

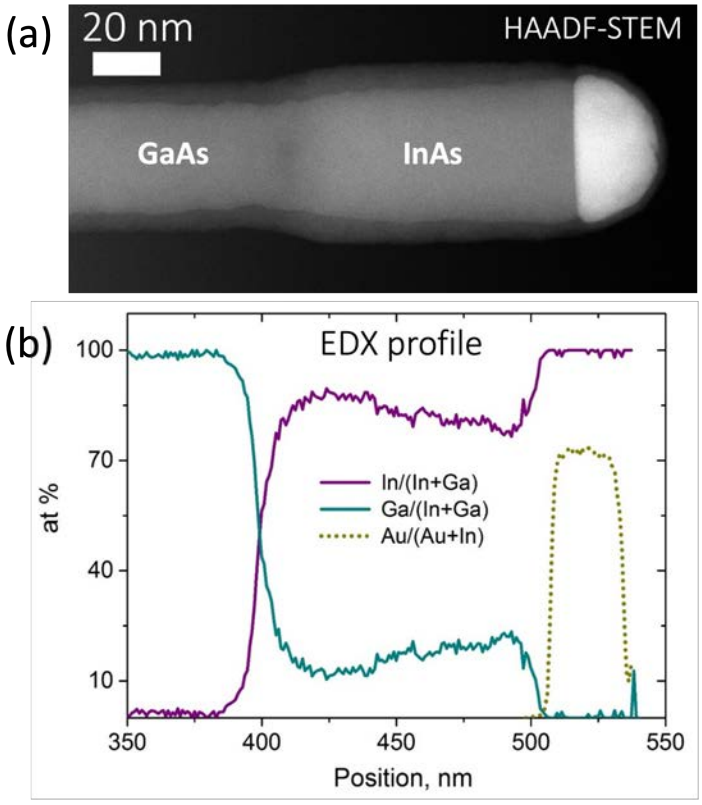

Figure A.1.1: STEM-EDS analysis of a GaAs/InAs nanowire top [20]. (a) HAADF-STEM image. (b) EDS analysis of the element percentage contained in nanowire versus the position along the nanowire.

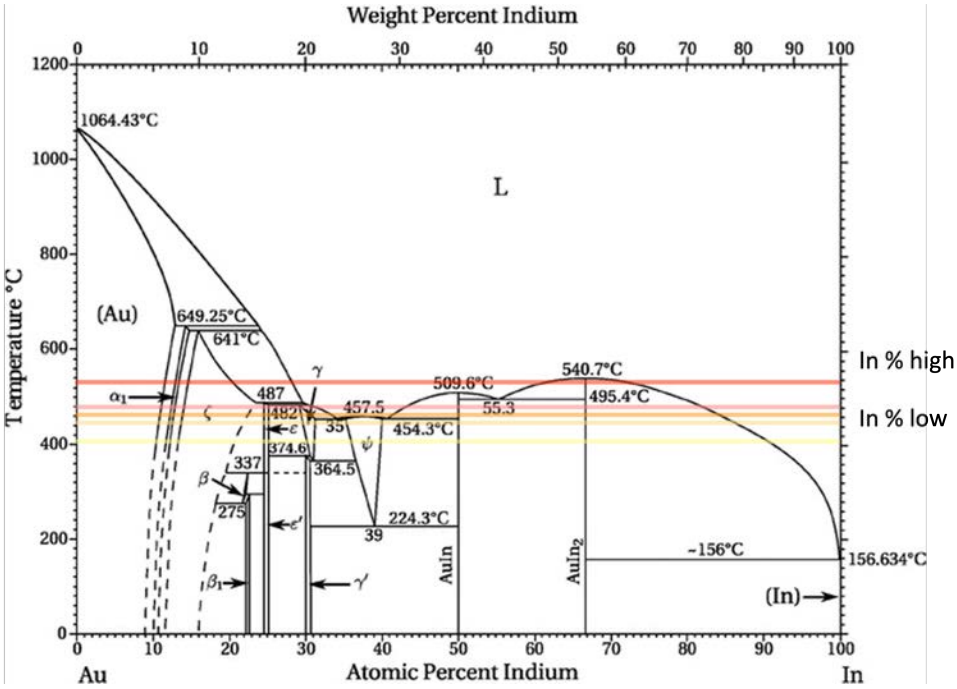

Figure A.1.2: Phase-diagram of In-Au [206].

A.2 Growth optimization

A.2.1 Annealing temperature

To evaluate the relation between size of Au-In droplet and T_a, we then measure droplet diameter for each T_a. Figure A.2.1 (a) demonstrates the definition of Au-In droplet in red dashed circle on a plan-view SEM image of 50 nm Au droplet. Figure A.2.1 (b)-(d) show the plots of diameter of Au-In droplet versus annealing temperature. We observe that there's no obvious trend or affect on the alloy size from T_a. Additionally, the top diameter of nanowires for 40 minutes growth time has similar values as the one of alloy droplets.

Used Au droplet diameter (nm)	T_a (°C)	**Length** (μm)	**Top diameter (nm)**
20	420	10.1 ± 2.9	64 ± 10
	460	9.7 ± 3.4	58 ± 11
	480	11.7 ± 1.4	56 ± 9
	500	-	-
	560	9.3 ± 3.3	43 ± 13
30	420	13.5 ± 1.8	55 ± 10
	460	10.7 ± 2.5	65 ± 15
	480	7.5 ± 2.2	53 ± 10
	500	7.9 ± 1.3	69 ± 11
	560	5.7 ± 2.3	48 ± 7
50	420	6.2 ± 2.5	85 ± 12
	460	6.1 ± 2.4	81 ± 15
	480	3.1 ± 0.9	75 ± 7
	500	4.1 ± 1.0	83 ± 7
	560	3.3 ± 1.8	80 ± 10
60	420	6.7 ± 2.5	93 ± 15
	460	5.5 ± 2.5	92 ± 16
	480	2.8 ± 0.8	80 ± 8
	500	3.5 ± 1.7	84 ± 14
	560	-	-

Table A.2.1: Nanowires dimensions (length and top diameter) versus T_a for different colloids sizes. We do not have enough data for nanowires grown from 20 nm and 60 nm colloids solutions and of a too low density of colloids, respectively.

Used Au droplet diameter (nm)	T_a °C	**Growth time (min)**	**Density of crater** (μm^{-2})
30	420	1	0.37 ± 0.09
	460	1	-
	480	1	-
	500	1	0.26 ± 0.10
	560	1	0.33 ± 0.20

Table A.2.2: Analysis of density of nanoparticles after 1 min growth after each T_a with 30 nm Au droplets

Used Au droplet diameter (nm)	T_a(°C)	Density of		
		Crater (μm^{-2})	Nanoparticle (μm^{-2})	Nanowire (μm^{-2})
30	420	0.20 ± 0.04	0.001 ± 0.003	0.02 ± 0.02
	460	0.60 ± 0.07	0.01 ± 0.01	0.01 ± 0.01
	480	0.10 ± 0.06	0.40 ± 0.30	0.06 ± 0.05
	500	0.01 ± 0.02	0.05 ± 0.08	0.08 ± 0.06
	560	0.40 ± 0.10	0.40 ± 0.20	0.004 ± 0.010
50	420	0.04 ± 0.02	0.01 ± 0.01	0.01 ± 0.01
	460	0.40 ± 0.10	0.01 ± 0.02	0.02 ± 0.02
	480	0.05 ± 0.03	0.06 ± 0.04	0.03 ± 0.03
	500	0.03 ± 0.04	0.03 ± 0.05	0.05 ± 0.05
	560	0.30 ± 0.03	0.10 ± 0.07	0.03 ± 0.02
60	420	0.20 ± 0.03	0.01 ± 0.01	0.04 ± 0.05
	460	0.50 ± 0.06	0.01 ± 0.02	0.02 ± 0.02
	480	0.05 ± 0.06	0.02 ± 0.03	0.07 ± 0.04
	500	0.02 ± 0.02	0.003 ± 0.004	0.02 ± 0.01
	560	0.20 ± 0.20	0.06 ± 0.05	0.003 ± 0.010

Table A.2.3: Table of density analysis for T_a ratio study, categorized into craters, nanoparticles and nanowires. The density analysis doesn't applied on 20 nm because we diluted the colloid solution before deposition. There's a possibility that the inhomogeneous dilution process bias the density distribution.

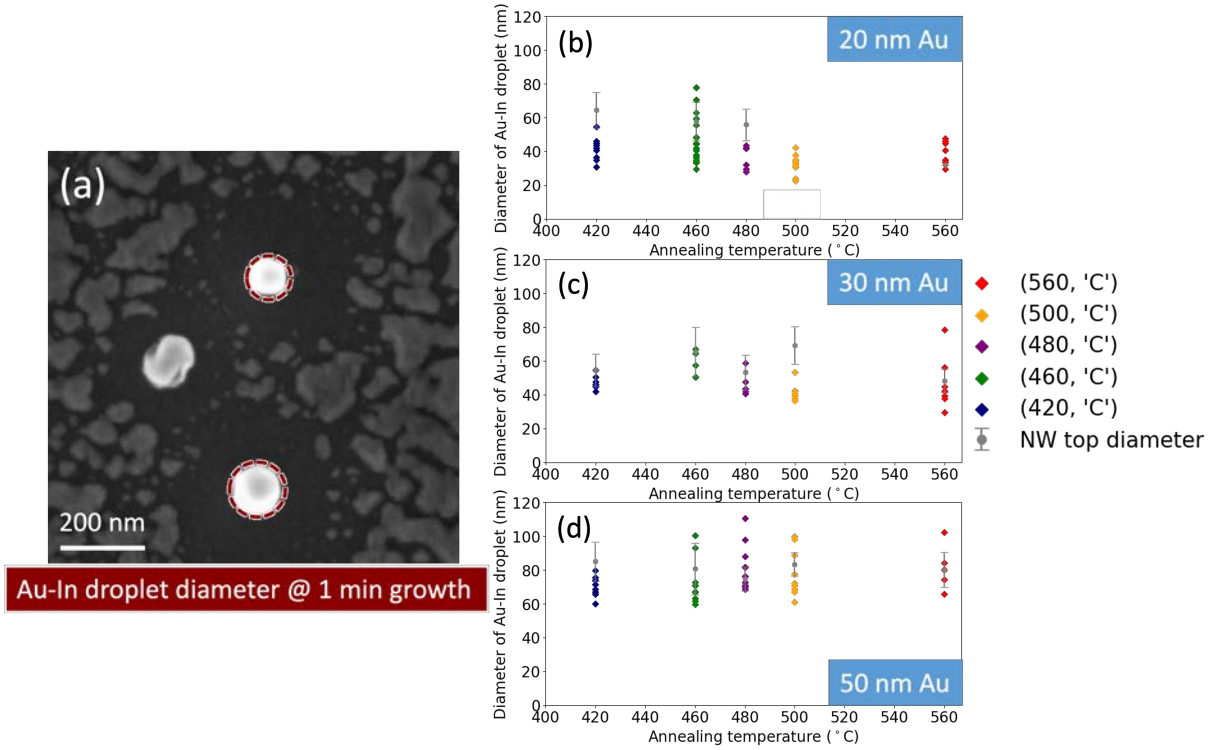

Figure A.2.1: Diameter evolution of Au-In droplet of InAs nanowire growth for 1 minute after each T_a. (a) Plan-view SEM image indicates the diameter of Au-In droplet in red dashed circles. Plots of Au-In alloy droplet diameter versus T_a for (b) 20 nm, (c) 30 nm and (d) 50 nm Au catalyst.

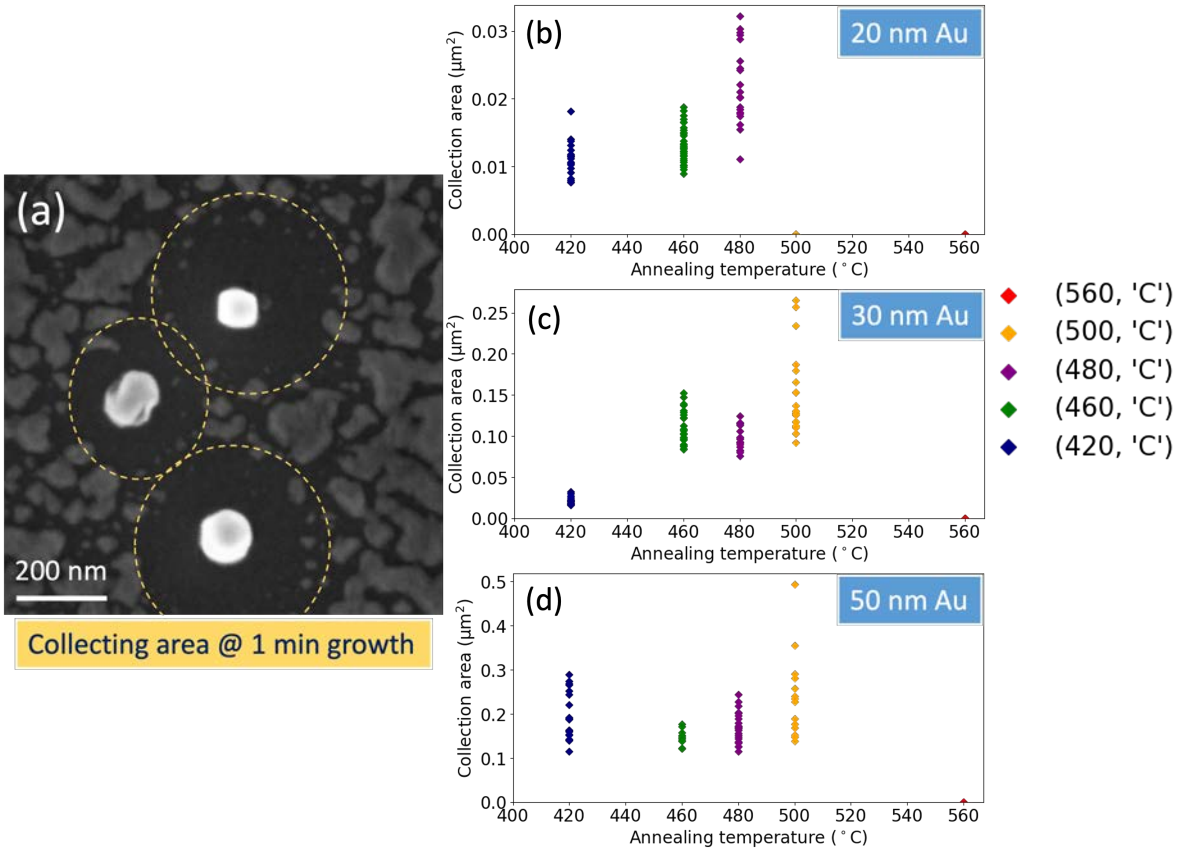

Figure A.2.2: Collecting area radius of Au-In alloy for 1 minute growth after each T_a. (a) Definition of collecting area is indicated in yellow dashed circles. Plots of collecting area versus T_a for (b) 20 nm, (c) 30 nm and (d) 50 nm Au droplet. The NW top diameter states the top diameter of nanowire after 40 minutes growth time with same growth parameters.

Next, we observe the collecting area surrounding droplets thus we study whether the size of collecting area is related to T_a. Figure A.2.2 (b)-(d), the evolution of collecting area versus T_a is demonstrated for each size of Au droplet. We observe that the collecting area increases with elevating T_a till 500 °C for most of Au catalyst. For example, 30 nm catalyst has 0.023 μm^2 at T_a = 420 °C and increases to 0.15 μm^2 at T_a = 500 °C. For higher T_a, the collecting area disappear for all the size of catalyst. For 20 nm catalyst, the collecting area disappears at T_a = 500 – 560 °C; for larger catalyst, it disappears at higher T_a = 560 °C. We also observe that larger Au catalyst results in bigger collection area regardless T_a. For example, 20 nm catalyst has 0.01–0.022 μm^2, 30 nm catalyst 0.023–0.14 μm^2 and 50 nm catalyst ranges 0.20–0.23 μm^2.

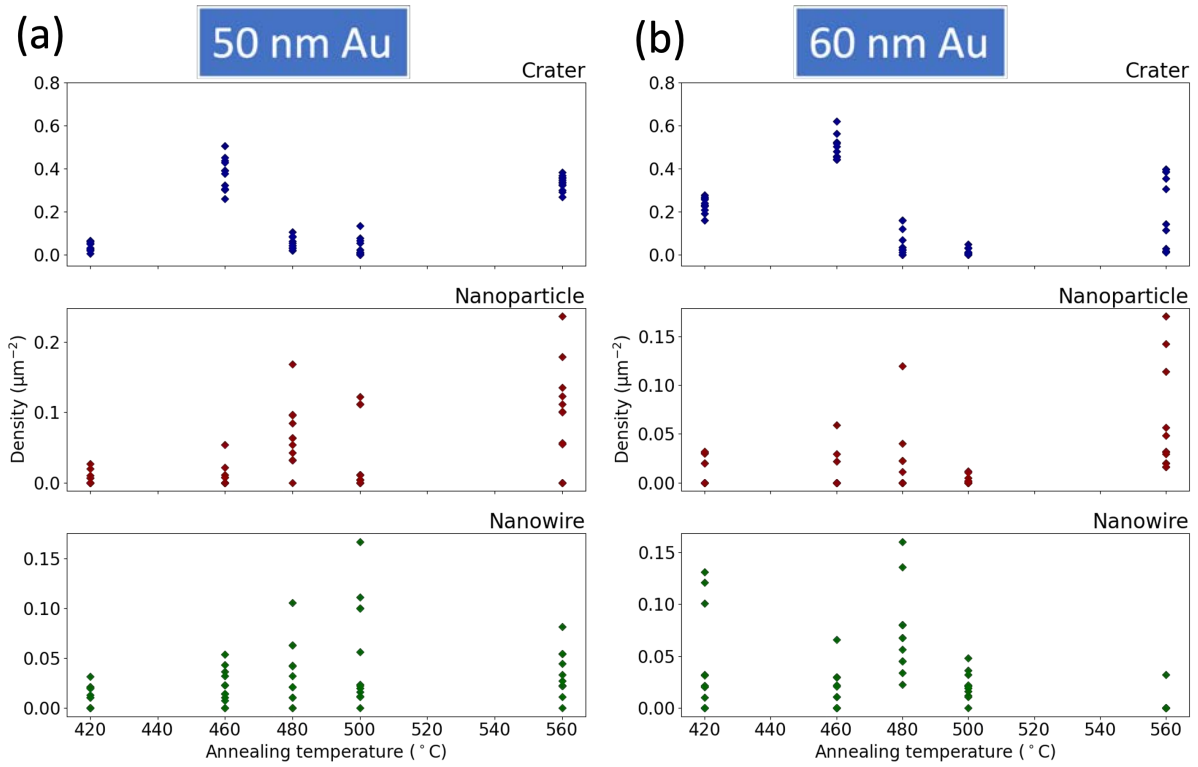

Figure A.2.3: Density analysis on (a) 50 nm and (b) 60 nm Au catalyzed nanowire samples in the annealing temperature (T_a) study.

Crater study

Next, we study the craters depth evolution with T_a. We observe the sample and look at a freshly cut edge using a 90° tilt in SEM. The observation is realized around the middle of the cut edge to avoid effect from the border of sample. Figure A.2.4 shows two craters from samples annealed at 420 °C and 560 °C. We observe that the craters have the same shape: the V-shaped facets of the craters oriented orthogonally to the viewing direction have the 35.26° angle with [001] which corresponds to {111}B planes. We observe that the craters have a minimum depth in the range, between 300 nm to 500 nm, for nanowire samples growth after T_a = 420 °C and 560 °C. It is difficult to measure accurately the craters depth because it depends where the cleavage takes place. The plot of the crater minimum depth as the function of T_a is shown on Figure A.2.4 (c). The depth of craters seems to be independent of T_a except in the 480 °C–500 °C window where the craters seems to be either very small or absent.

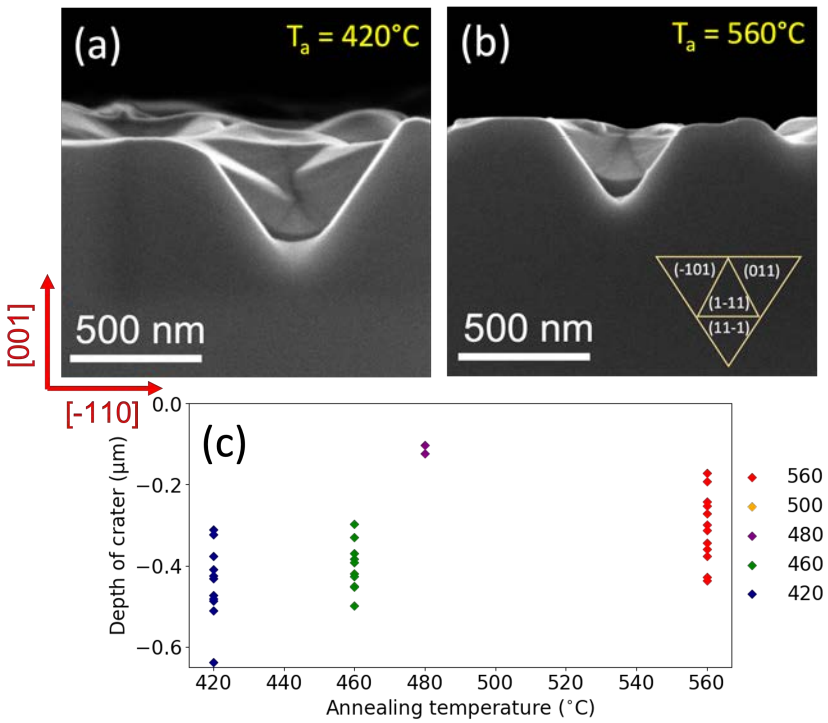

Figure A.2.4: Side-view SEM images of craters for samples grown after different T_a. (a) T_a = 420 °C and (b) T_a = 560 °C. The orientation of the samples is indicated in red: the y-axis corresponds to the [001] direction and the x-axis corresponds to the [$\bar{1}$10] direction. (c) Plot of the crater minimum depth versus T_a measured on side-view SEM images. At T_a = 500 °C, we could not see any craters on the SEM images taken at 90°.

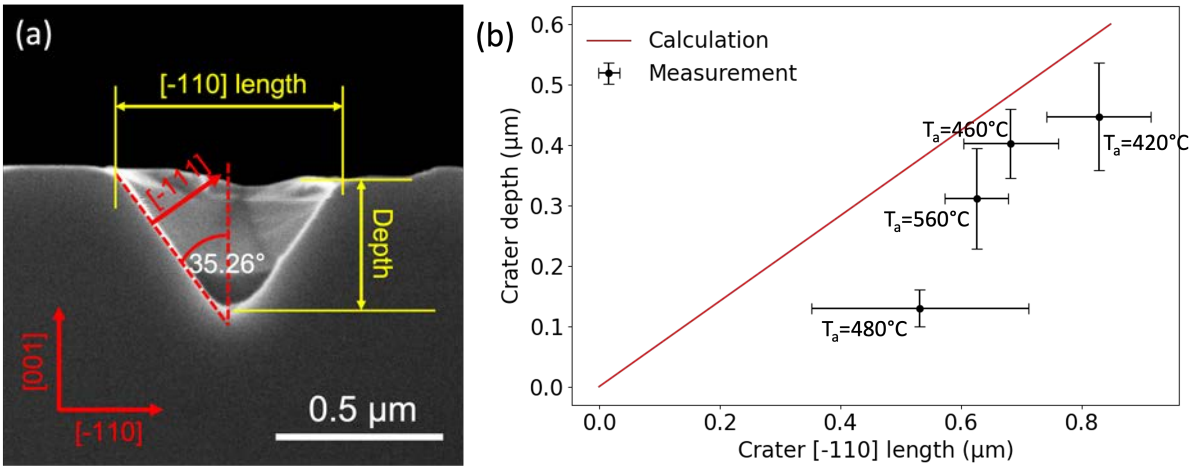

Figure A.2.5: Geometrical analysis of the crater. (a) Side-view SEM image of a crater labeled with relevant measures: [$\bar{1}$10] length, depth, angle between [111]B and [$\bar{1}$10] direction. (b) Calculated and measured values of its depth plotted versus the crater length in the [$\bar{1}$10] direction depends on T_a.

Due to the facetting of the crater, there's a geometrical relation between the crater's depth and length. The angle between the [111]B and the [110] is 35.26°, obtained from trigonometric

functions. Considering a $1 \times 1 \times 1$ cubic,

$$\cos^{-1}\left(\frac{[110]\ \text{length} = \sqrt{2}}{[111]\text{B}\ \text{length} = \sqrt{3}}\right) = 35.26^{\circ} \tag{A.1}$$

So then the depth can be calculated from the $[\bar{1}10]$ length,

$$\text{depth} = \frac{[\bar{1}10]\,\text{length}}{\tan(35.26^{\circ})} \tag{A.2}$$

Figure A.2.5 shows the evolution of $[\bar{1}10]$ length versus depth. We see that (1) larger $[\bar{1}10]$ gives deeper craters both theory and measurements, (2) there is a discrepancy between theory and measure because crater has a flat bottom or we never cut at the center of the crater.

A.2.2 Growth temperature

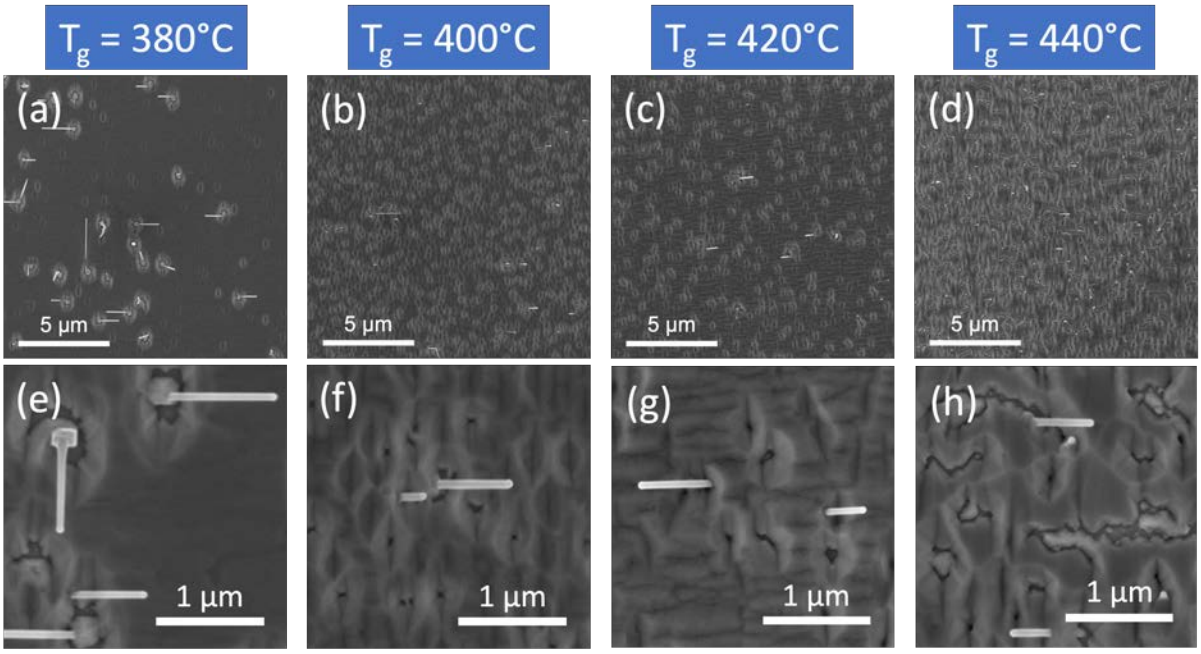

Figure A.2.6: Plane-view SEM images of InAs nanowire sample grown with 50 nm Au droplets in the growth temperature study. Plane-view SEM images (a)-(d) in a lower magnification, (e)-(h) in a higher magnification.

Used Au droplet diameter (nm)	T_g (°C)	**Length** (μm)	**Top diameter (nm)**	**Bottom diameter (nm)**
30	380	1.9 ± 0.8	45 ± 4	50 ± 4
	400	1.2 ± 0.5	45 ± 8	51 ± 9
	420	1.3 ± 0.2	40 ± 4	44 ± 4
	440	1.2 ± 0.6	50 ± 4	54 ± 4
50	380	1.2 ± 0.5	70 ± 4	79 ± 5
	400	0.6 ± 0.2	71 ± 11	78 ± 12
	420	1.0 ± 0.4	66 ± 7	73 ± 9
	440	0.5 ± 0.2	74 ± 4	79 ± 5

Table A.2.4: Table of nanowires dimensions in T_g study for each used Au droplet size, including nanowires' length, top diameter and bottom diameter.

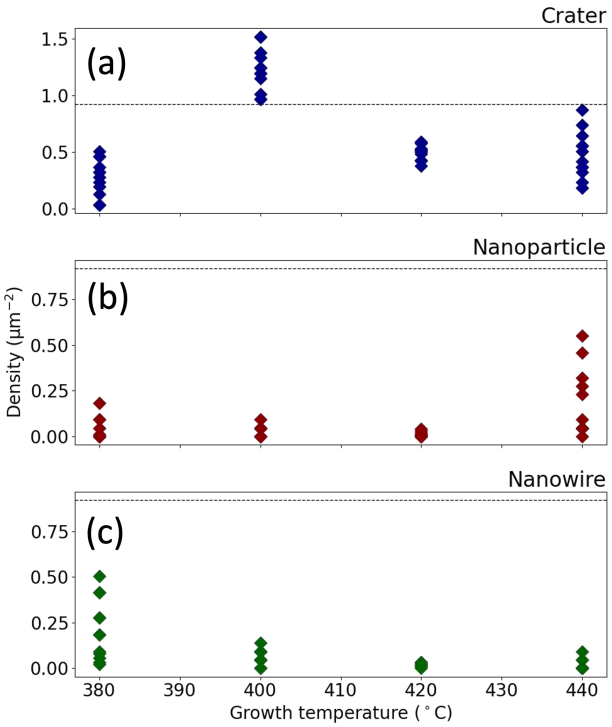

Figure A.2.7: Density analysis of the nanowire samples grown with 50 nm Au droplets. The black dashed horizontal line indicates the initial seeding density.

Used Au droplet diameter (nm)	T_g	**Density of**		
		Crater (μm^{-2})	**Nanoparticle** (μm^{-2})	**Nanowire** (μm^{-2})
30	380	0.4 ± 0.1	0.08 ± 0.05	0.3 ± 0.1
	400	1.3 ± 0.2	0.07 ± 0.05	0.1 ± 0.1
	420	0.01 ± 0.02	0.1 ± 0.1	0.3 ± 0.1
	440	0.03 ± 0.05	0.9 ± 0.3	0.2 ± 0.2
50	380	0.3 ± 0.2	0.04 ± 0.06	0.2 ± 0.2
	400	1.3 ± 0.2	0.03 ± 0.03	0.06 ± 0.04
	420	0.5 ± 0.07	0.01 ± 0.01	0.02 ± 0.01
	440	0.48 ± 0.2	0.2 ± 0.2	0.02 ± 0.03

Table A.2.5: Table of density analysis for T_g study, categorized into craters, nanoparticles and nanowires.

A.2.3 V/III ratio

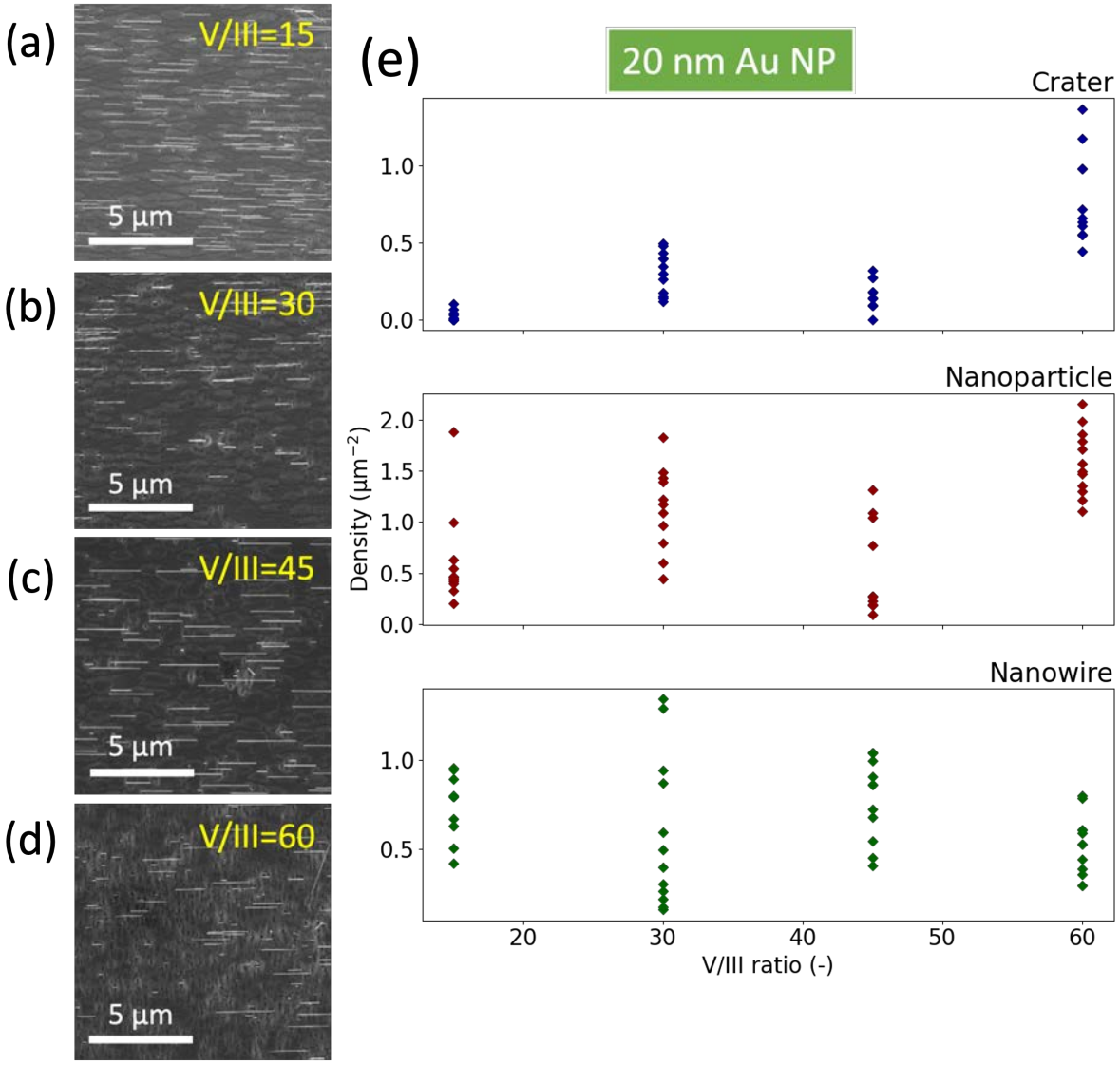

Figure A.2.8: Plane-view SEM images and density analysis of nanowire samples grown with 20 nm droplets in the V/III ratio study. (a)-(d) Plane-view SEM images of InAs nanowire samples grown with different V/III ratios. (e) Density analysis.

Used Au droplet diameter (nm)	V/III ratio (-)	Length (μm)	Top diameter (nm)	Bottom diameter (nm)
20	15	1.5 ± 0.6	30 ± 7	35 ± 6
	30	1.1 ± 0.5	33 ± 9	36 ± 10
	45	2.4 ± 1.2	29 ± 6	32 ± 4
	60	1.5 ± 1.0	31 ± 6	34 ± 4
30	15	1.3 ± 0.2	40 ± 4	44 ± 4
	30	2.5 ± 0.8	38 ± 5	44 ± 5
	45	3.0 ± 0.8	44 ± 8	51 ± 5
	60	3.2 ± 0.7	40 ± 4	47 ± 4
50	15	1.0 ± 0.4	66 ± 8	73 ± 9
	30	1.1 ± 0.2	66 ± 5	77 ± 7
	45	1.3 ± 0.4	72 ± 10	80 ± 10
	60	1.5 ± 0.3	62 ± 7	67 ± 9

Table A.2.6: Table of nanowires dimensions in V/III ratio study for each used Au droplet size, including length, top diameter and bottom diameter.

Used Au droplet diameter (nm)	V/III ratio	Density of	
		Nanoparticle (μm^{-2})	Nanowire (μm^{-2})
20	15	0.6 ± 0.4	0.7 ± 0.2
	30	1.1 ± 0.4	0.6 ± 0.4
	45	0.5 ± 0.2	0.8 ± 0.2
	60	1.6 ± 0.3	0.5 ± 0.2
30	15	0.1 ± 0.1	0.3 ± 0.1
	30	0	0.4 ± 0.1
	45	0	0.3 ± 0.1
	60	0	0.5 ± 0.1
50	15	0.01 ± 0.01	0.02 ± 0.01
	30	0.02 ± 0.03	0.2 ± 0.06
	45	0	0.2 ± 0.09
	60	0	0.1 ± 0.06

Table A.2.7: Table of density analysis for V/III ratio study, categorized into craters, nanoparticles and nanowires.

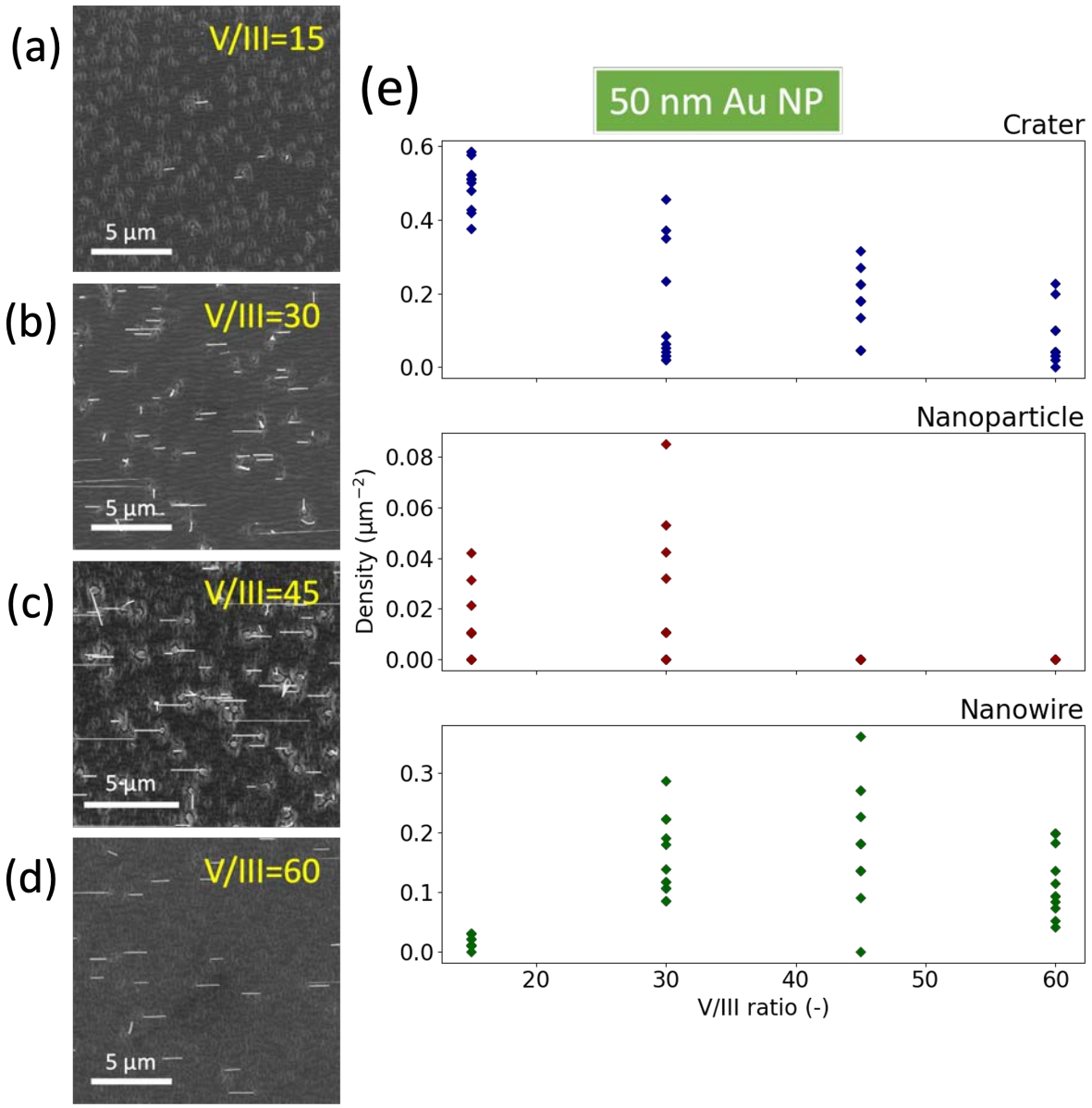

Figure A.2.9: Plane-view SEM images and density analysis of nanowire samples grown with 50 nm droplets in the V/III ratio study. (a)-(d) Plane-view SEM images of InAs nanowire samples grown with different V/III ratios. (e) Density analysis.

A.2.4 Growth time

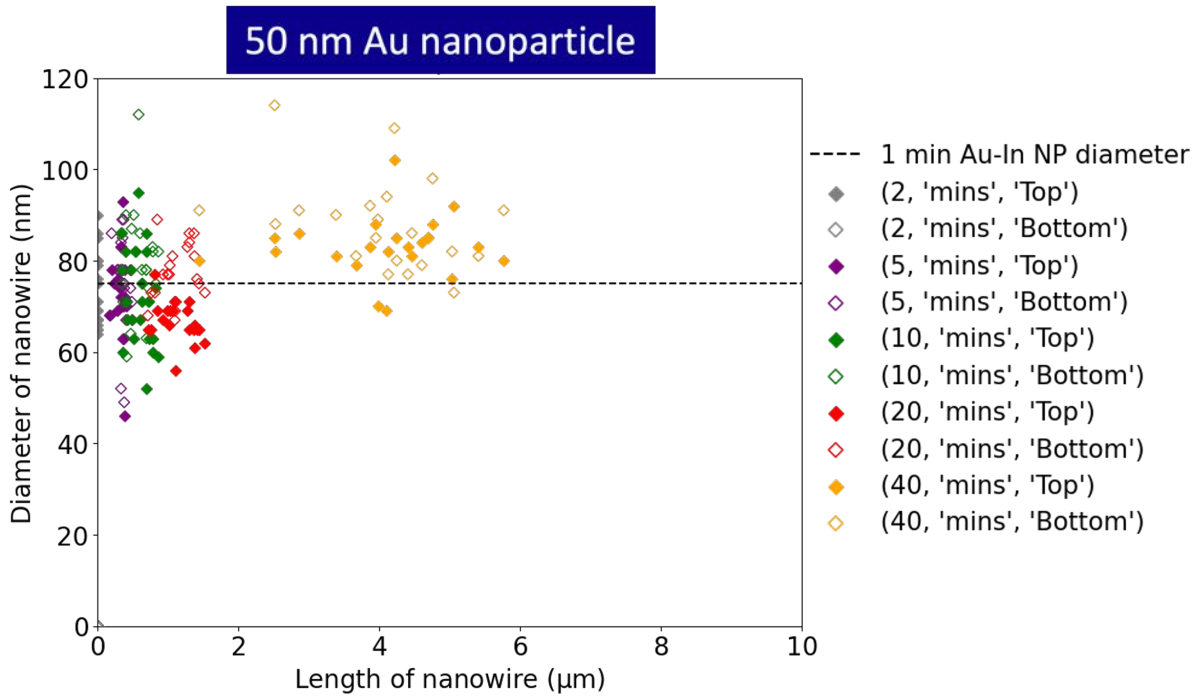

Figure A.2.10: Time evolution of nanowires' dimensions grown with 50 nm Au droplets. Black horizontal dashed line represents the Au-In droplets' diameter after 1 minute growth.

Used Au droplet diameter (nm)	**Growth time (minute)**	**Length (μm)**	**Top diameter (nm)**	**Middle diameter (nm)**	**Bottom diameter (nm)**
30	1	0	42 ± 6	-	-
	2	0.2 ± 0.03	43 ± 6	-	44 ± 7
	5	0.4 ± 0.07	46 ± 6	49 ± 4	51 ± 5
	10	0.6 ± 0.2	45 ± 3	45 ± 3	47 ± 3
	20	2.5 ± 0.8	41 ± 3	46 ± 4	47 ± 4
	40	7.9 ± 1.3	41 ± 9	76 ± 11	57 ± 21

Table A.2.8: Table of nanowires dimensions grown with 30 nm Au droplet in growth time study for each used Au droplet size, including nanowires' length, top, middle and bottom diameter.

APPENDIX **B**

Supplementary data for Part II

B.1 2D Sn thin film on InSb substrate

B.1.1 TEM lamella failure

The Sn/InSb lamella was prepared using the cryo-FIB, which cooled down the sample to –190 °C during ion milling process. Figure B.1.1 showed the STEM-EDS analysis of 38 nm-thick Sn layer grown on a InSb(110) substrate. We observed the intermixing of Sn and InSb, particularly the In diffused into the top of the surface of the InSb. There was no pure Sn observed from this lamella.

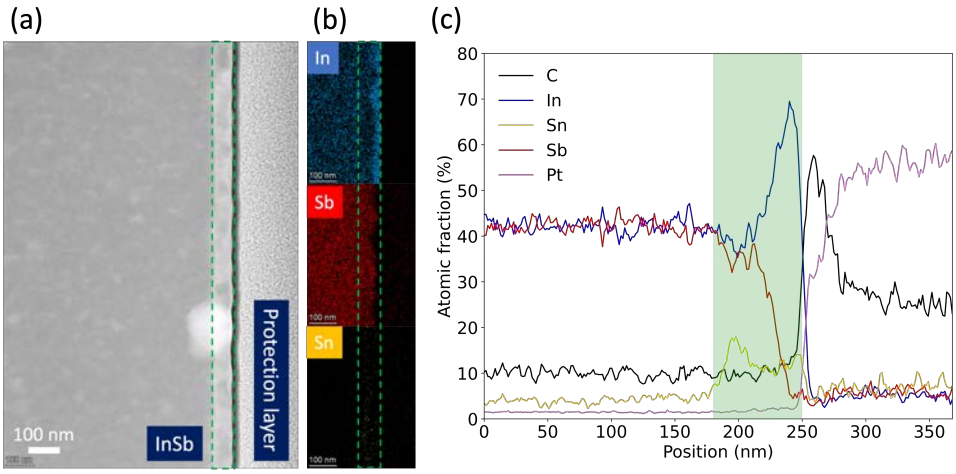

Figure B.1.1: [Tin4W-110] STEM-EDS analysis of Sn thin film grown on InSb substrate. (a) HAADF-STEM image of the cross section of Sn/InSb sample. (b) EDS analysis of element composition mapping. (c) Plot of the atomic fraction of element versus the position in the cross section of the lamella.

B.1.2 Reciprocal space map

Figure B.1.2 shows the deformation of RSM from the setup and X-rays beam.

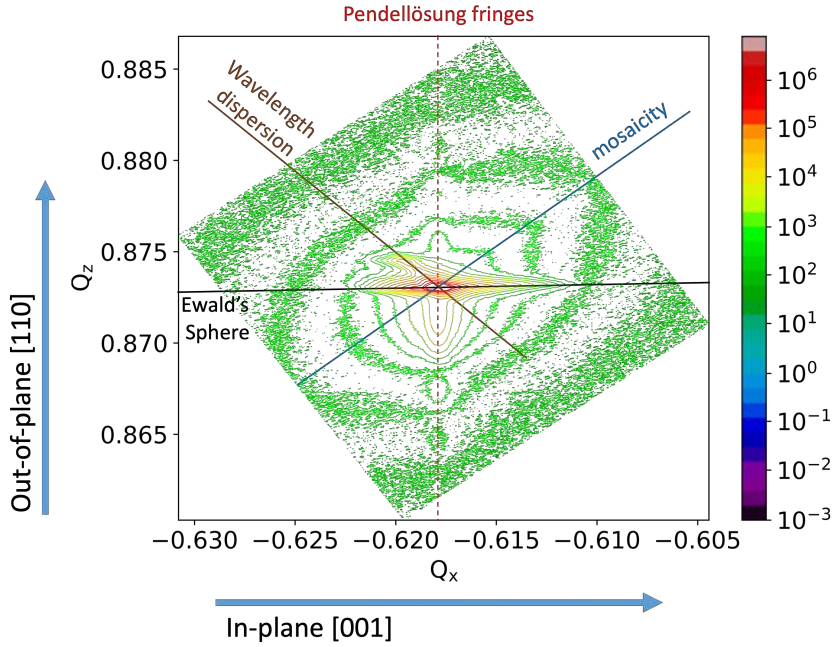

Figure B.1.2: [Tin4W-110] Reciprocal space map of 38 nm-thick Sn/InSb. The deformation of the diffraction point (444) were indicated by lines.

B.1.3 Thickness effect

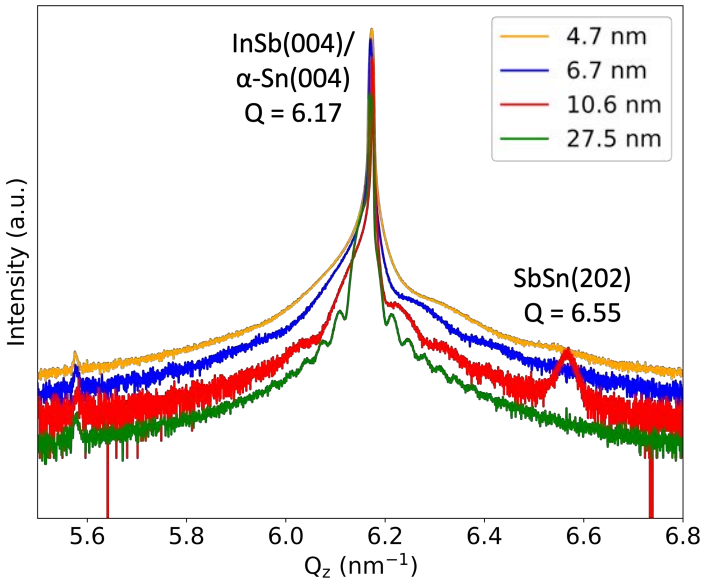

Figure B.1.3: [Tin1W-100, Tin2W-100,Tin3W-100, Tin4W-100] Out-of-plane scans on InSb(004) with different Sn thickness grown on InSb(100) substrates.

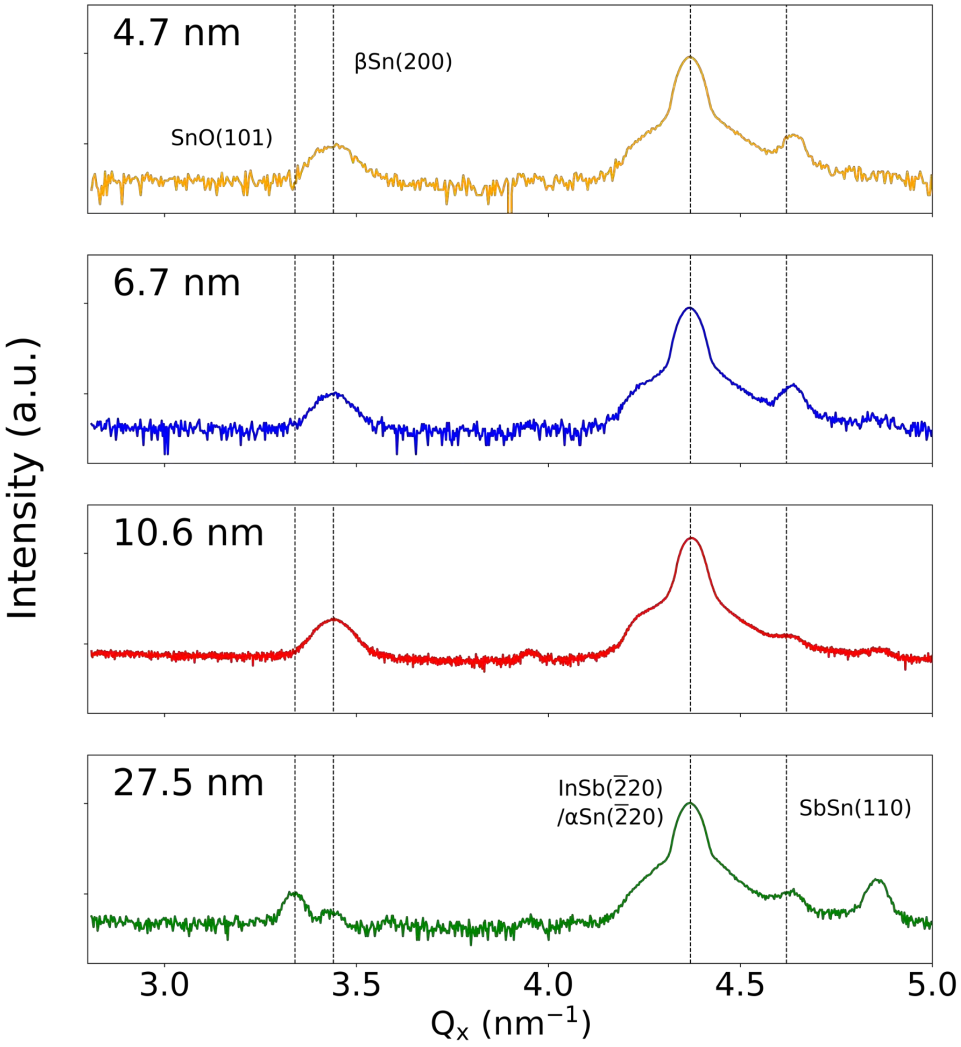

Figure B.1.4: [Tin1W-100, Tin2W-100,Tin3W-100, Tin4W-100] In-plane scans on InSb($\bar{2}$20) with different Sn thickness grown on InSb(100) substrates.

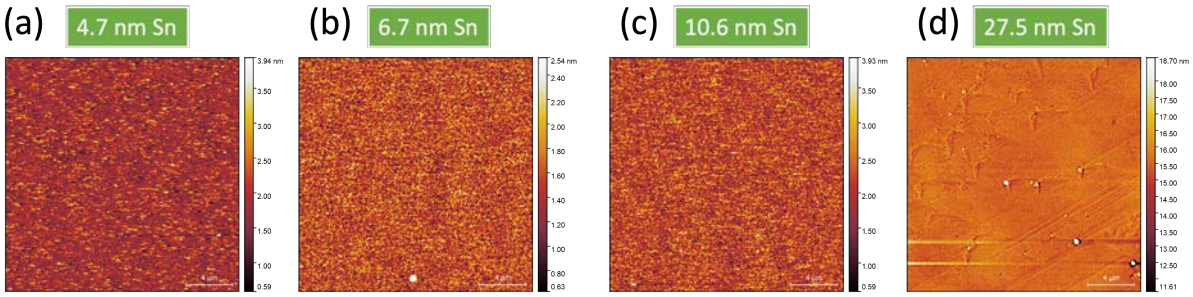

Figure B.1.5: [Tin1W-100, Tin2W-100,Tin3W-100, Tin4W-100] AFM analysis of Sn thin films with different thickness grown on InSb(100) substrates.

Sample	Capping	RMS roughness (nm)
Tin1W-100	AlO_x	0.49 ± 0.09
Tin2W-100	AlO_x	0.30 ± 0.00
Tin3W-100	AlO_x	0.58 ± 0.16
Tin4W-100	AlO_x	0.61 ± 0.20
CPD166-100	AlO_x	0.64 ± 0.30
CPD167-100	Al oxidized	0.96 ± 0.47
CPD168-100	Sn oxidized	1.48 ± 1.13

Table B.1.1: The list of the RMS roughness for each studied Sn/InSb(100).

B.1.4 Stability over time: Capping layers

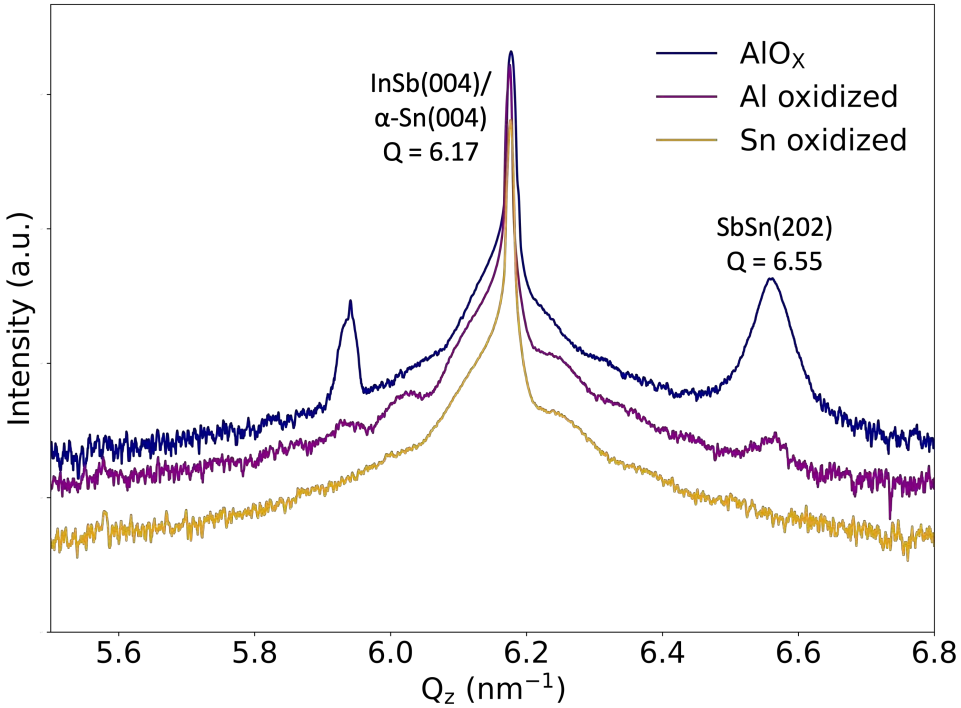

Figure B.1.6: [CPD166-100, CPD167-100, CPD168-100] Out-of-plane scans on InSb(004) grown on InSb(100) substrates with different capping layers, including AlO_x, deposited Al oxidized, and deposited Sn oxidized. The diffraction peaks of InSb(004)/α-Sn(004) and SbSn(202) were indicated with the labels.

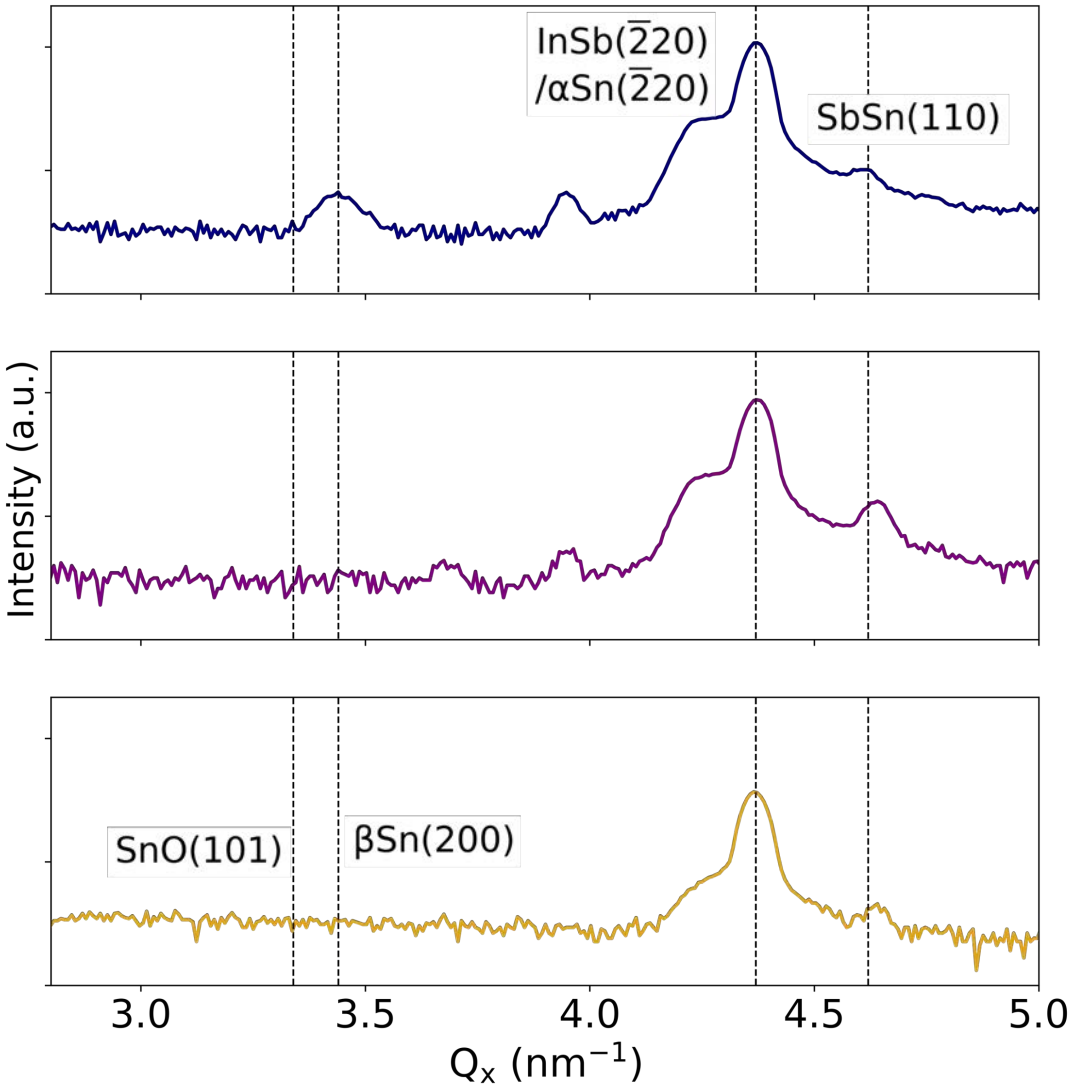

Figure B.1.7: [CPD166-100, CPD167-100, CPD168-100] In-plane scans on InSb($\bar{2}20$) with different Sn thickness grown on InSb(100) substrates. The vertical dashed lines indicated the positions of SnO(101), β-Sn(200), InSb($\bar{2}20$)/α-Sn($\bar{2}20$), and SbSn(110).

We discussed the morphology of Sn thin films with different capping layers, as seen in Figure B.1.8. We observe that the grains emerged on the surface in all the capping methods. The grains are smaller in the AlO_x capped Sn thin film than in the others. For example, the radius of grains in the AlO_x capped sample is 111 nm, in the Al oxidized sample is 152 nm, and in Sn oxidized sample is 159 nm. The RMS roughness of all the capping methods is less than 1 nm, and AlO_x capping resulted in the smoothest surface (0.45 nm). The AFM analysis values are listed in Table 5.3.1. There's no significant change of morphology from the capping methods.

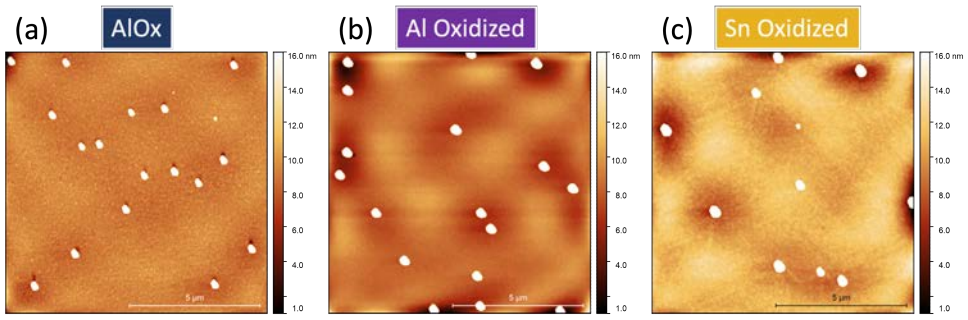

Figure B.1.8: [CPD166-110, CPD167-110, CPD168-110] AFM images of the morphology of Sn thin film with different capping layer. The scanning area is 10 μm $\times$ 10 μm for each.

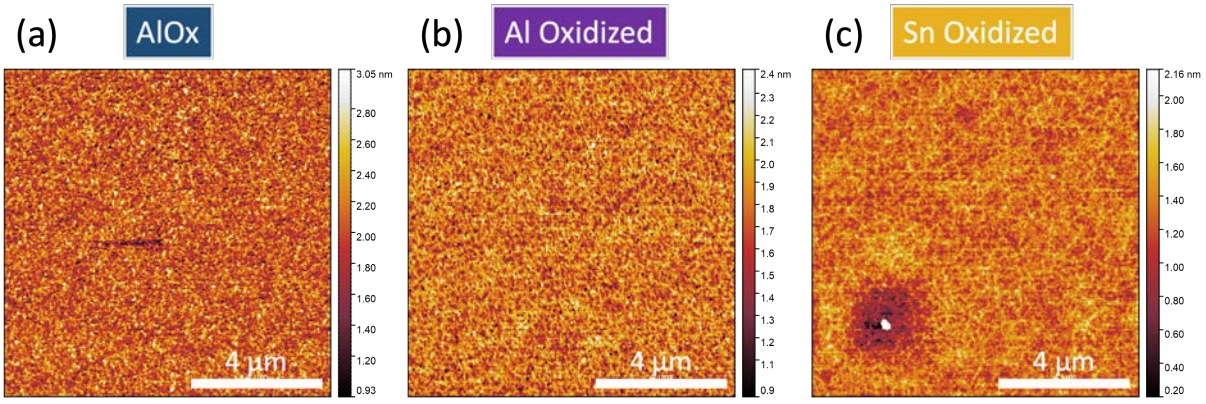

Figure B.1.9: [CPD166-100, CPD167-100, CPD168-100] AFM analysis of Sn thin films grown on InSb(100) substrates with different capping layers.

B.2 Sn shell on InSb nanowire

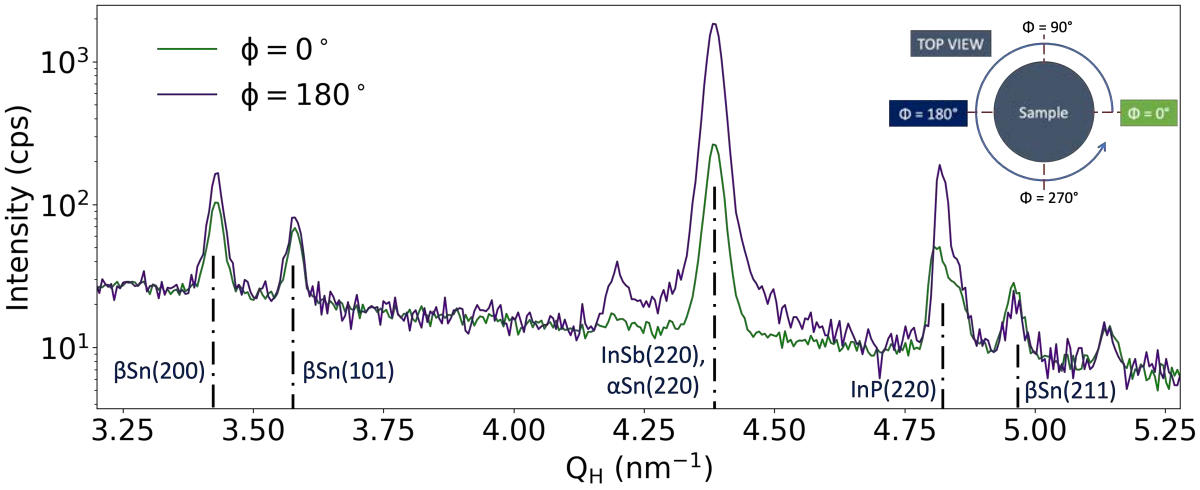

Figure B.2.1: Out-of-plane scans from $\phi = 0°$ and $\phi = 180°$ of sample along the InSb[110] direction.

B.3 Superconductivity of Sn/InSb nanowire

We also have a Sn/InSb nanowire device fabricated with the conventional baking resist process. We are interested in seeing if the heating affects the superconductivity of the device. The same configuration (4-probes) is applied on the heated device. Figure B.3.1 shows the resistance of the heated device versus the temperature during cooling down. We observe that the R of the heated nanowire device decreases initially from 30 to 6 Ω at 1.2 K; it decreases again to zero at 0.6 K.

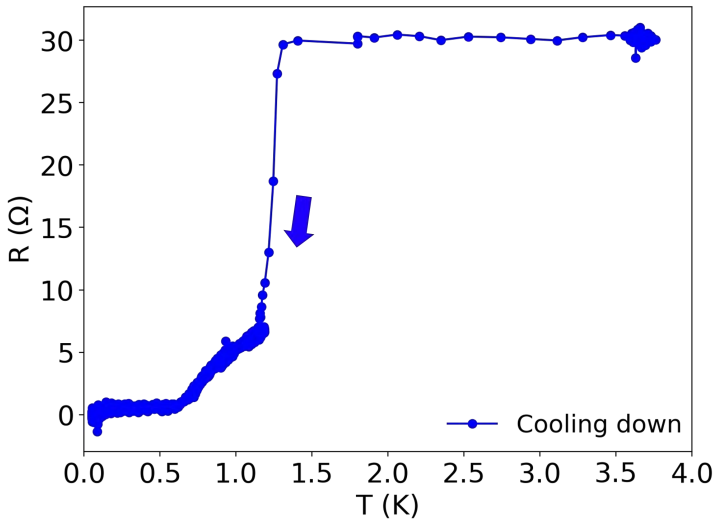

Figure B.3.1: [ESRF4-Chip05] Superconductivity measurement of the heated Sn/InSb nanowire device performed in the dilution refrigerator, the device resistance R versus the measurement temperature T. The sweeping direction indicated with a blue arrow is from a higher T 3.75 K to a lower T 0.05 K.

We observe that T_c in the unheated Sn/InSb hybrid nanowire device is around 3.2 – 3.45 K, which is lower than the T_c in bulk β-Sn, 3.7 K [241]. We first consider if the 1D shape of β-Sn would affect the T_c. Y. J. Hsu and S. Y. Lu showed that the T_c of single-crystalline β-Sn nanowire has a similar T_c as the bulk value [100]. M. Tian et al. reported that the different diameters of single-crystal β-Sn nanowire won't change the value of T_c [210]. So the low dimension and the shape of β-Sn won't affect T_c. However, the crystal quality of superconductor can affect T_c. The polycrystalline superconductor nanowire has a lower T_c than the single-crystalline one [233]. The reason is that the disorder reduces the density of states at the Fermi level, which is detrimental to form the superconductivity states [99]. With the TEM images, we did observe the polycrystalline nature of our Sn shell. We thus attribute the decrease of T_c in our Sn shell to the polycrystalline crystal structure.

For the heated Sn/InSb nanowire device, its T_c is around 1.2 K and 0.6 K, which are both distinguishably lower than the unheated one. We suspected that the resist baking process had changed the properties of Sn/InSb nanowires in terms of the composition or interface of the Sn shell on InSb nanowire. According to the capping study on 2D Sn/InSb, we observe that the

SbSn(110) diffraction appears intensively in the AlO_x capped sample. SbSn has been reported as a stable binary phase in Sn-Sb system, and is also a superconductor, whose bulk T_c is 1.5 K [193, 137]. J. D. McBrayer et al showed that an increasing temperature can enhance the diffusivity of metal atoms in a solid material [149]. We know that the heating from the AlO_x capping process induces the formation of β-Sn and can probably favor the formation of SbSn. Thus, we suggest that the baking process enhances the inter-diffusivity of Sn shell and InSb nanowire, which triggers SbSn formation that makes the nanowire device superconducting with a lower T_c. We can use the TEM analysis or XRD spectrum to confirm the existence of SbSn in heated Sn/InSb nanowire.

Publications

Publications as a first author

- **A.-H. Chen**, M. Rossi, T. van Schijndel, M. A. Verheijen, E. P. A. M. Bakkers, B. Kousar, F. Gay, B. Sacépé, J. Rubio-Zuazo, J.Eymery, E. Bellet-Amalric, and M. H., In-situ Structural Study of Sn growth on InSb Nanowires by synchrotron X-Ray Diffraction, (In preparation)

- **A.-H. Chen**, C.P. Dempsey, M. Pendharkar, S. Tan, A. Sharma, B. Zhang, S.M. Frolov, C.J. Palmstrom, L. Bellon, E. Bellet-Amalric, and M. H., Role of a capping layer on the crystalline structure of Sn thin films grown at cryogenic temperatures on InSb substrates, (In preparation)

- **A.-H. Chen**, and M. H. (2022) Influence of annealing temperature on inclined InAs nanowire growth on (001) substrates, (In preparation)

Publications as a contributor

- Pendharkar, M., B. Zhang, H. Wu, A. Zarassi, P. Zhang, C. P. Dempsey, J. S. Lee, S. D. Harrington, G. Badawy, S. Gazibegovic, R. L. M. Op het Veld, M. Rossi, J. Jung, **A.-H. Chen**, M. A. Verheijen, M. Hocevar, E. P. A. M. Bakkers, C. J. Palmstrøm, and S. M. Frolov. 2021. Parity-Preserving and Magnetic Field-Resilient Superconductivity in InSb Nanowires with Sn Shells. Science 372(6541):508-11.

- Jardine, M., Dardzinski, D., Yu, M., Purkayastha, **A.-H, Chen**, A.-H., Hocevar, M., Frolov, S. and Marom, N. First Principles Assessment of CdTe as a Tunnel Barrier at the α-Sn/InSb Interface. (In preparation)

- P. Zhang, A. Zarassi, M. Pendharkar, J.S. Lee, L. Jarjat, V. Van de Sande, B. Zhang, S. Mudi, H. Wu, C.P. Dempsey, A.P. McFadden, S.D. Harrington, **A.-H. Chen**, G. Badawy,

S. Gazibegovic, R. Op het Veld, S. Tan, E.P.A.M. Bakkers, M. Hocevar, C.J. Palmstrøm, and S.M. Frolov, Planar Josephson junctions templated by nanowire shadowing. (In preparation)

- P. Zhang, A. Zarassi, M. Pendharkar, J.S. Lee, L. Jarjat, V. Van de Sande, C.P. Dempsey, A.P. McFadden, S.D. Harrington, **A.-H. Chen**, G. Badawy, S. Gazibegovic, R. Op het Veld, E.P.A.M. Bakkers, M. Hocevar, C.J. Palmstrøm, and S.M. Frolov, Large Second-Order Josephson Effect in Planar Superconductor-Semiconductor Junctions. (In preparation)

- P. Zhang, A. Zarassi, M. Pendharkar, J.S. Lee, V. Van de Sande, S. Mudi, C.P. Dempsey, A.P. McFadden, S.D. Harrington, **A.-H. Chen**, G. Badawy, S. Gazibegovic, R. Op het Veld, E.P.A.M. Bakkers, M. Hocevar, C.J. Palmstrøm, and S.M. Frolov, Mimicking the fractional Josephson effect: patterns of missing Shapiro steps in non-topological junctions. (In preparation)